

TALLINN UNIVERSITY OF TECHNOLOGY  
DOCTORAL THESIS  
61/2019

**Severe Plastic Deformation of Metals  
by Using High Pressure  
Torsion Extrusion**

BABAK OMRANPOUR SHAHREZA



TALLINN UNIVERSITY OF TECHNOLOGY

School of Engineering

Department of Mechanical and Industrial Engineering

This dissertation was accepted for the defense of the degree of Doctor of Philosophy in Engineering on 22/10/2019

**Supervisor:** Dr. Lembit Kommel  
School of Engineering, Tallinn University of Technology  
Tallinn, Estonia

**Co-supervisor:** Dr. Julia Ivanisenko  
Karlsruhe Institute of Technology  
Karlsruhe, Germany

**Opponents:** Prof. Alexei Vinogradov  
Department of Engineering Design and Materials  
Norwegian University of Science and Technology  
Trondheim, Norway

Prof. Boris Straumal  
Institute of Solid State Physics  
Russian Academy of Sciences  
Chernogolovka, Russia

**Defense of the thesis:** 17/12/2019, Tallinn

**Declaration:**

Hereby I declare that this doctoral thesis, my original investigation and achievement, submitted for the doctoral degree at Tallinn University of Technology has not been submitted for doctoral or equivalent academic degree.

Babak Omranpour Shahreza

.....

signature



European Union  
European Regional  
Development Fund



Investing  
in your future



Karlsruhe Institute of Technology



Deutscher Akademischer Austausch Dienst  
German Academic Exchange Service

Copyright: Babak Omranpour Shahreza, 2019

ISSN 2585-6898 (publication)

ISBN 978-9949-83-500-3 (publication)

ISSN 2585-6901 (PDF)

ISBN 978-9949-83-501-0 (PDF)



TALLINNA TEHNIKAÜLIKOOL  
DOKTORITÖÖ  
61/2019

# **Metallide süvoplastne deformeerimine kõrgsurve-väändeekstrusiooni meetodil**

BABAK OMRANPOUR SHAHREZA





# CONTENTS

<b>LIST OF PUBLICATIONS .....</b>	<b>7</b>
<b>AUTHOR'S CONTRIBUTION TO THE PUBLICATIONS .....</b>	<b>8</b>
<b>PREFACE.....</b>	<b>9</b>
<b>LIST OF ABBREVIATIONS AND SYMBOLS.....</b>	<b>10</b>
<b>1. INTRODUCTION: AN OVERVIEW OF THE THESIS.....</b>	<b>12</b>
1.1. Aims and objectives .....	12
1.2. Outlines of the thesis .....	12
1.3. Approbation.....	12
1.3.1. Publications and conferences .....	12
1.3.2. Proposals.....	13
1.3.3. On-going projects.....	13
<b>2. STATE OF THE ART .....</b>	<b>14</b>
2.1. Literature review.....	14
2.1.1. Bulk nanostructured materials .....	14
2.1.2. Multifunctional properties of nanostructured and UFG materials.....	15
2.1.3. The advent of Severe Plastic Deformations (SPD) .....	16
2.2. Motivation .....	18
2.3. Principles of High Pressure torsion Extrusion (HPTE) .....	20
<b>3. MODELING AND SIMULATION OF HPTE BY FINITE ELEMENT ANALYSIS .....</b>	<b>24</b>
3.1. Modeling and simulations.....	24
3.1.1. Drafting and modeling .....	24
3.1.2. Simulation of the process .....	24
<b>4. SPD PROCESSING OF ALUMINUM .....</b>	<b>28</b>
4.1. Methodology of experiments .....	28
4.1.1. Materials and characterization techniques .....	28
4.1.2. HPTE processing of aluminum .....	29
4.1.3. ECAP processing of aluminum .....	29
4.2. Results of experiments.....	30
4.2.1. Compressive strength of HPTE samples.....	30
4.2.2. Hardness evolution .....	31
4.2.3. Microstructural refinement .....	32

4.3.	Discussion and interpretation of results .....	40
<b>5.</b>	<b>SPD PROCESSING OF NIOBIUM .....</b>	<b>48</b>
5.1.	Methodology of experiments .....	48
5.1.1.	Materials and characterization methods .....	48
5.1.2.	HPTE experiments .....	48
5.1.3.	ECAP experiments .....	48
5.2.	Results of experiments .....	50
5.2.1.	Microhardness evolution .....	50
5.2.2.	Microstructural refinement .....	50
5.3	Discussion and interpretation of results .....	55
<b>6.</b>	<b>CONCLUSION .....</b>	<b>58</b>
6.1.	Concluding remarks .....	58
6.2.	Scientific novelty .....	59
6.3.	Recommendations and future plans .....	59
	<b>LIST OF FIGURES .....</b>	<b>61</b>
	<b>LIST OF TABLES .....</b>	<b>62</b>
	<b>REFERENCES .....</b>	<b>63</b>
	<b>ACKNOWLEDGEMENT .....</b>	<b>73</b>
	<b>ABSTRACT .....</b>	<b>74</b>
	<b>LÜHIKOKKUVÕTE .....</b>	<b>76</b>
	<b>APPENDIX.....</b>	<b>79</b>
	<b>CURRICULUM VITAE .....</b>	<b>161</b>
	<b>ELULOOKIRJELDUS .....</b>	<b>162</b>

## LIST OF PUBLICATIONS

The author of this thesis published eight peer reviewed articles as part of his research activities in the field of Severe Plastic Deformations. Those articles whose contents/materials were used in the design and preparation of this thesis are listed below. These articles are referred by “Paper I”, “Paper II”, etc. in the thesis.

- Paper I        **Omranpour B**, Ivanisenko Y, Kulagin R, Kommel L, Garcia Sanchez E, Nugmanov D, et al. Evolution of microstructure and hardness in aluminum processed by High Pressure Torsion Extrusion. *Mater Sci Eng A* 2019;762:138074.
- Paper II        **Omranpour B**, Kommel L, Mikli V, Garcia E, Huot J. Nanostructure development in refractory metals: ECAP processing of Niobium and Tantalum using indirect-extrusion technique. *Int J Refract Met Hard Mater* 2019;79:1–9.
- Paper III        **Omranpour B**, Kommel L, Sanchez EG, Ivanisenko Y, Huot J. Enhancement of Hydrogen Storage in Metals by Using a New Technique in Severe Plastic Deformations. *Key Eng Mater* 2019;799:173–8.
- Paper IV        Kommel L, **Omranpour B**, Mikli V. Structuration of Refractory Metals Tantalum and Niobium Using Modified Equal Channel Angular Pressing Technique. *Key Eng Mater* 2019;799:103–8.
- Paper V        **Omranpour B**, Kulagin R, Ivanisenko Y, Garcia Sanchez E. Experimental and numerical analysis of HPTE on mechanical properties of materials and strain distribution. *IOP Conf Ser Mater Sci Eng* 2017;194:012047.
- Paper VI        Djavanroodi F, **Omranpour B**, Sedighi M. Artificial Neural Network Modeling of ECAP Process. *Mater Manuf Process* 2013;28:276–81.
- Paper VII        Djavanroodi F, **Omranpour B**, Ebrahimi M, Sedighi M. Designing of ECAP parameters based on strain distribution uniformity. *Prog Nat Sci Mater Int* 2012;22:452–60.

All published articles are presented in the appendix section at the end of this thesis.

## **AUTHOR'S CONTRIBUTION TO THE PUBLICATIONS**

The author of this thesis conceived of the plan and performed all the SPD processes, ran the simulations and took the lead in writing the publications where he was the first author. In the publications as a second author, he carried out the SPD processes, assisted in materials characterization techniques and ran the simulations, if any.

## PREFACE

Increasing demand on high-strength and light materials led to the development of bulk Ultra-Fine Grained (UFG) materials with superior mechanical properties. UFG materials produced by Severe Plastic Deformation (SPD) have distinguished characteristics such as high strength along with retaining the ductility up to certain levels, owing to the process of grain refinement. Nonetheless, industrial applications of these materials are still limited because of the cost, shape, or the efficiency of the process. For instance, HPT as a conventional and famous SPD technique, although efficient in imposing large amounts of strains up to 90 mm/mm, is limited to fabricating thin-disk samples which are not eminently practical for industrial use. In the case of ECAP, another famous SPD technique, imposing high amounts of strains on the materials is time consuming because each pass of ECAP applies a strain value in the order of  $\sim 1$  mm/mm, and as a result, it needs a repetition of a couple of times to press the same sample to achieve a strain value of the order of 10 mm/mm.

To overcome the aforementioned flaws, a new technique called “High Pressure Torsion Extrusion” was introduced at the Institute of Nanotechnology in Karlsruhe-Germany to facilitate inducing large amount of deformation in bulk samples within one pass of processing. This technique favors the benefit of the combination of conventional method of HPT and extrusion, and is capable of producing bulk UFG materials with considerable improvement in mechanical properties. The main focus in the present study is dedicated to the experimental analysis of HPTE and its process parameters on the evolution of microstructure and mechanical behavior of materials.

The main advantage of this technique over other SPD techniques such as ECAP and HPT is that process parameters e.g. extrusion speed ( $v$ ) and rotational speed ( $\omega$ ) are variable even during the process, and therefore, a variety of properties can be expected from different samples. Another distinctive characteristic of HPTE is the gradient distribution of strain and hardness in the cross section of the processed billets as a consequence of torsion. Accordingly, materials in the central zone of the billet are softer and at the periphery, are harder. This fact makes this technique suitable when costly surface hardening of a billet is required while ductility should retain in the core. Considering the market-oriented media with an approach to improve the mechanical properties of materials without using costly alloying elements, this technique seems to be a time-efficient method to fabricate UFG materials only within one pass of extrusion with improved mechanical properties.

## LIST OF ABBREVIATIONS AND SYMBOLS

### Abbreviations:

ABR	Accumulative Roll Bonding
BCC	Body-Centered Cubic
BNS	Bulk Nano-Structured
CAD	Computer Aided Design
CEE	Cyclic-Expansion Extrusion
CP	Commercially Pure
CP-Al	Commercially Pure Aluminum
Cryo-T	Cryogenic Temperature
DHPT	Dynamic-High Pressure Torsion
EBSD	Electron Backscattered Diffraction
ECAP	Equal Channel Angular Pressing
FCC	Face-Centered Cubic
FEA	Finite Element Analysis
FEM	Finite Element Method
FWHM	Full Width at Half Maximum
HAGB	High Angle Grain Boundary
HC-HPT	Hollow-Cone High Pressure Torsion
HPT	High Pressure Torsion
HPTE	High Pressure Torsion Extrusion
IE-ECAP	Indirect Extrusion Equal Channel Angular Pressing
LAGB	Low Angle Grain Boundary
RPM	Revolution per minute
R.T	Room Temperature
SEM	Scanning Electron Microscopy
SPD	Severe Plastic Deformation
TEM	Transmission Electron Microscopy
UCS	Ultimate Compressive Strength
UFG	Ultra-Fine Grained
XRD	X-ray Diffraction
YS	Yield Strength



## Symbols

### Greek:

$\beta$	Peak broadening (XRD)
$\varepsilon$	Lattice Strain
$\bar{\varepsilon}$	Equivalent strain
$\vartheta$	Bragg angle (XRD)
$\lambda$	Wavelength (XRD)
$u$	Extrusion speed (HPTE)
$\sigma_y$	Yield strength
$\varphi$	Cross-section angle (ECAP die)
$\psi$	Corner angle (ECAP die)
$\omega$	Rotational Speed (HPTE)

### Latin:

D	Grain diameter
$D_{ave}$	Average grain diameter
e	Elongation
ECAP1	ECAP regime in which sample is extruded for one pass
ECAP4	ECAP regime in which sample is extruded for four passes
ECAP8	ECAP regime in which sample is extruded for eight passes
N	Number of passes
R	The radial distance from the central axis of the HPTE processed billet
v7w1	HPTE regime with an extruding speed of 7 mm/min and rotational speed of 1 rpm
v1w1	HPTE regime, extruding speed of 1 mm/min and rotational speed of 1 rpm
v1w3	HPTE regime, extruding speed of 1 mm/min and rotational speed of 1 rpm
$V_{HAGB}$	Volume fraction of high angle grain boundaries

# **1. INTRODUCTION: AN OVERVIEW OF THE THESIS**

## **1.1. Aims and objectives**

The primary aim of this study is to evaluate the effect of HPTE on the evolution of materials, particularly on hardness and microstructure. Special attention will be devoted to the process parameters of this technique to examine their influence on the materials properties after processing. Moreover, in order to better understand the effectiveness of this technique, HPTE will be compared with ECAP. The provided knowledge shall offer new insights in Severe Plastic Deformation fields and provide the reader with a detailed understanding of this process as well as the effect of process parameters on the microstructure and mechanical properties of materials.

Based on what has been mentioned, the main objectives of this study are established upon experimental and numerical analysis of HPTE for evaluation of this technique. Furthermore, a comparative study between HPTE and ECAP comes within the scope of this thesis to provide further evidence about the effectiveness of HPTE on materials evolution. Simulation of HPTE by Finite Element Method (FEM) is utilized to demonstrate the materials flow and the strain distribution in this technique.

Two types of materials, aluminum (Al) and niobium (Nb) with fcc and bcc crystal structures have been used for experimentations, and hardness and microstructural evolution of materials will be evaluated in this study. Microstructural refinement will be examined by observation of the grain size in materials using electron microscopy techniques as well as studying the X-ray diffraction patterns. Eventually, some comparisons will be drawn between the results obtained in this work and the previous studies available in the literature about SPD processing of the same materials for further analysis and discussion.

## **1.2. Outlines of the thesis**

This thesis contains six chapters along with one appendix in which author's publications are presented. The contents of the thesis include literature review, simulations, and experiments. After this introduction section, the state of the art will be presented in chapter 2. Chapter 3 illustrates the simulation of HPTE processing via FEM. Chapter 4 is devoted to SPD processing of aluminum including the methodology of experiments, results, and discussion. Chapter 5 deals with SPD processing of niobium. Eventually, the outcomes of this thesis along with some recommendations will be summarized in chapter 6.

## **1.3. Approbation**

### **1.3.1. Publications and conferences**

In addition to having published the results of this study in peer-reviewed journals presented in the appendix section, the author of this thesis has participated in six different symposiums and seminars and delivered lectures or presented posters.

### **1.3.2. Proposals**

Two proposals related to the topics of this thesis were submitted and approved for financial/technical support.

1. German academic research service (DAAD), research proposal for financial support of the project and conducting the experiments in Karlsruhe-Germany, 2016.
2. Karlsruhe Nano-Micro Facility center (KNMF), Helmholtz association-Germany, research proposal as a collaborative project between KNMF and Tallinn University of Technology for technical support in microstructural studies of SPD processed materials, 2016

### **1.3.3. On-going projects**

A cooperative research project has been launched at the University of Quebec -Trois Rivieres, Canada to study the functional properties of HPTE processed materials to be applied to industrial applications.

## 2. STATE OF THE ART

This chapter provides a brief overview of the studies about Severe Plastic Deformation (SPD) and the importance of nanostructured materials. Then, the deficiency of traditional SPD techniques and the motivation for introducing a new technique to fabricate bulk nanostructured materials with appropriate properties will be discussed; finally, the principles of HPTE, geometrical parameters of the die, process parameters, and the equivalent strain in HPTE will be elaborated.

### 2.1. Literature review

#### 2.1.1. Bulk nanostructured materials

Grain size is a key factor in polycrystalline metals which may affect different properties including chemical, physical or mechanical aspects [1]. According to Hall-Petch relationship (Eq. 1), yield strength of metals increases by decreasing the grain size [2,3].

$$\sigma_y = \sigma_0 + \frac{k}{\sqrt{d}} \quad (1)$$

In this equation,  $\sigma_y$  is the yield stress,  $\sigma_0$  is the lattice friction stress,  $k$  is a constant, and  $d$  is the grain size. According to this relationship, metals with finer microstructures are expected to possess higher strength compared to the coarse grains [4].

The dependence of strength on the grain size, according to the Hall-Petch equation, led to an increasing interest in the fabrication of Bulk Nanostructured (BNS) materials [5]. Processing of BNS materials can be fundamentally divided by two main methods: “Bottom-up” procedures in which atoms or molecules are assembled into nanoscale clusters and they require subsequent consolidation processes to form bulk materials. In contrast, in “Top-down” procedures, structural decomposition applies to a bulk solid to obtain a nanostructured composition while retaining the original integrity [6]. Bottom-up procedures are basically cost-effective in large scale productions, although they may induce porosity or contamination into the materials during fabrication [5]. Inert gas condensation and electro-deposition are the two famous methods in bottom-up procedures where the process starts with the assembly of atoms and ends with materials in small volumes, usually on a surface layer [7]. Severe Plastic Deformation (SPD) techniques and ball milling are two examples of top-down procedures where the process starts with bulk samples and it does not affect the overall shape of the product. Materials processed by SPD, in comparison to ball milling, generally retain the initial dimensions and show better resistance to air contamination during processing [8].

SPD has some distinctive characteristics [9]:

- It can impose extremely high amounts of strain on the materials, sometimes up to 20 or even more, leading to exceptional grain refinement.
- Although this process is categorized as a deformation technique, the overall dimensions of the workpiece remain the same after processing.
- Due to the unique attribute of SPD in processing without changing the dimensions, materials are able to be processed through the same die for several times and thereby, receive more strain and achieve further grain refinement after each pass.

Grain refinement in SPD starts with plastic deformation in metals which results in changes in crystallographic orientations and the formation of dislocation cells. By increasing the plastic straining and accumulation of misorientations, the dislocation cells gradually transform into new fine grains [10]. This transformation can lead to the formation of High-angle grain boundaries due to the accumulation of dislocations between cells at high values of strains [11]. Several techniques and equipment have been utilized to characterize the grain refinement in nanostructured materials. A direct approach to detect the dimensions of grain refinement is using electron microscopy techniques, such as Scanning Electron Microscopes (SEM), Electron Backscattered Diffraction (EBSD) and Transmission Electron Microscopes (TEM) [12]. An indirect approach to this study is using X-Ray Diffraction (XRD) patterns where the evidence of grain refinement can emerge in peak broadening of the XRD patterns [Paper II]. As a matter of fact, the origin of peak broadening comes from two main factors: (1) refinement of microstructure in crystalline materials; (2) accumulation of micro-strains in materials due to lattice distortions [13,14]. There are some techniques that can quantify the values of these parameters by evaluating the peak broadening in XRD patterns. Williamson-Hall method is one of the famous techniques which is frequently used for this purpose [14–17].

Grain refinement and the accumulation of high density of dislocations in SPD processed materials are known to be the main mechanisms for promoting mechanical strength in materials [18]. Grain size in SPD processed materials is usually in sub-micron scales ( $D < 1 \mu\text{m}$ ); thus, they are referred to as Bulk Nanostructured (BNS) or Ultra-fine Grained (hereinafter UFG) materials. UFG materials are distinctive of improved mechanical, physical and functional properties [5,19,20]. The most outstanding characteristics are considered as “enhanced yield and ultimate strength” which enable them to be utilized in light structures with strong mechanical properties in manufacturing. UFG materials have also shown high-cycle fatigue resistance, enhanced fracture toughness at low temperatures, uniform corrosion, improved biocompatibility and enhanced diffusivity [12,21]. These attributes help them to demonstrate long-term potentials for a variety of engineering and industrial applications such as superplastic forming and diffusion bonding processes, cryogenic and outer space applications, biological tissues, hydrogen storage in metal hydrides for green energy applications, etc. [22]. Such prominent features of UFG materials absorbed the researchers’ attention to study and to devote their effort towards the development of new methods for fabricating UFG materials with enhanced properties.

Nowadays, production of BNS and UFG materials is changing from laboratory-scale research into commercial applications. The evidence of this shift can be revealed by considering the facts that firstly, recent studies on UFG materials are shifting from pure metals to commercial alloys; and Secondly, more research studies have been dedicated to the development of new SPD techniques towards economical production of such materials [12].

### **2.1.2. Multifunctional properties of nanostructured and UFG materials**

The main goal of grain refinement in SPD processing of metals is to improve mechanical properties such as yield strength and hardness. However, in the case of alloys, SPD not only provides the grain refinement but also leads to other hardening mechanisms such as formation of nano-twins, segregations and secondary phase precipitations in materials [23–27].

In addition to tensile strength and hardness improvements, other enhancements in mechanical properties of materials have been noticed in UFG materials. Wear resistance of materials may increase after SPD processing since this parameter is closely correlated with hardness [28,29]. Fatigue life in UFG materials is usually enhanced owing to the presence of high density of grain boundaries which impedes crack propagation [30]. Enhancement of such properties makes these metals superior compared to their coarse-grain counterparts in the market, especially in terms of critical design parameters like strength to weight ratio and fatigue life [31].

Besides mechanical-property improvement which is the primary purpose of using severe plastic deformations, UFG metals have represented notable improvements in other aspects such as physical and technological properties. Superplasticity, which is the ability of polycrystalline materials to receive extremely high amounts of deformations, namely elongations in the order of 400% in tension [32], has been reported in UFG materials. In some commercial aluminum alloys processed by SPD, elongations up to 1000% were recorded at strain rates of  $10^{-2}$ /sec [21]. Hydrogen storage in metal hydrides is another interesting application of UFG materials as energy carriers. Hydrogen storage in metals has been recently used for mobile applications, but the main issues arise from poor kinetics of absorption-desorption and high hydrogen desorption temperatures. Grain refinement in metals may accelerate the kinetics of H-sorption due to the increased volume fraction of grain boundaries [8]; particularly in the case of magnesium hydrides, hydrogen desorption temperature can decrease to 100 °C [33]. Production of nanostructured biomaterials is an outstanding example whereby SPD technologies represent industrial applications for medical implants such as bone replacement and dental applications [20]. Pure titanium is among the best selections of biomaterials possessing good biocompatibility and biocorrosion properties, but with the downside of low strength. Nanostructured titanium processed by SPD has overcome this weakness owing to the improved mechanical properties [34]. UFG materials processed via SPD contain large amounts of dislocation densities and point defects in microstructure because of receiving extreme plastic straining. These defects act as a barrier against the thermal conductivity and as a result, thermal resistivity will increase which is a drawback to copper alloys and other conductors [35]. However, this effect of SPD can be utilized in thermoelectric materials and thermoelectric generators for producing electricity by increasing the thermal resistivity and thereby enhancing the thermoelectric efficiency in materials [36,37].

Due to the abovementioned benefits, UFG materials are made more famous in different industrial sectors such as aerospace technology, renewable energy, medical implants and micro-manufacturing, and more investigations have been conducted towards SPD techniques either to modify the conventional methods or to devise new methods for fabricating materials with superior properties. The following section will review the most well-known SPD techniques which are frequently used in research studies.

### **2.1.3. The advent of Severe Plastic Deformations (SPD)**

Early efforts towards severe deformation of metals started by Bridgman in the 1940s, when he studied about “torsion combined with compression” [38], and later during the 1980s, his research ended to the invention of “High Pressure Torsion” or briefly HPT [39]. In HPT, a disk-shape sample is located between two anvils and receives compressive pressure, and rotation of one anvil applies torsional stress to the disk (Figure 1). The equivalent strain imposed on the disk depends on the number of rotations (N),

disk thickness ( $h$ ), and radial distance from the center ( $r$ ) (see Eq. 2 [39]). Accordingly, points with different distances from the center encounter with different amounts of strain during processing, and subsequently, materials will show a non-homogeneous distribution of grain refinement and mechanical properties along the radius of the disk after processing.

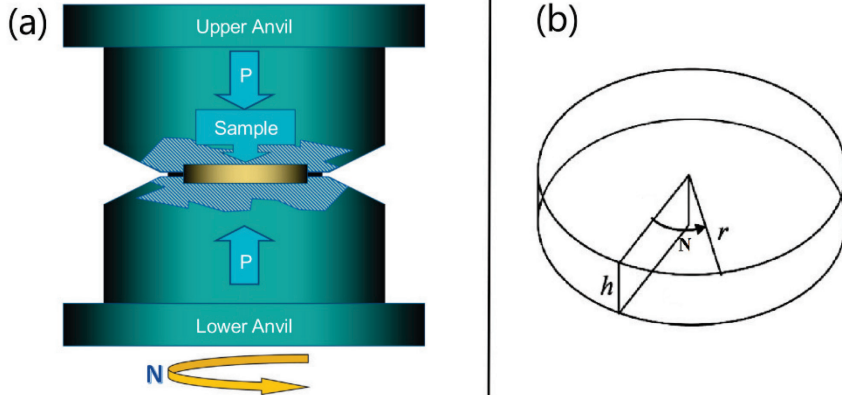


Figure 1. (a) Illustration of HPT die [40]; (b) parameters of an HPT disk.

$$\bar{\epsilon}_{HPT} = \frac{2\pi Nr}{\sqrt{3}h} \quad (2)$$

Increasing demand for polycrystalline materials with more homogeneous and equiaxed microstructure led to the invention of another SPD technique so-called “Equal Channel Angular Pressing” (ECAP) [41]. Afterwards, ECAP turned into the most popular batch process among SPD techniques [42].

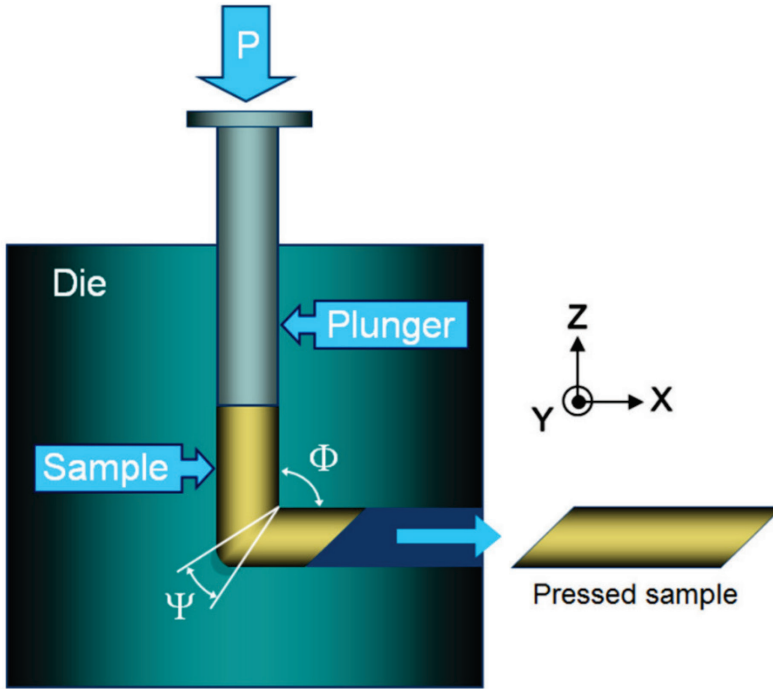


Figure 2. Illustration of ECAP [43].

Equivalent strain in ECAP relies on the die parameters shown in Figure 2 (the angle between the two channels  $\phi$ , and the corner angle  $\psi$ ), and can be measured by Eq. 3 [44]. Repetition of extrusion in ECAP die by  $N$  times, may accumulate the strain in the sample.

$$\bar{\epsilon}_{ECAP} = \frac{N}{\sqrt{3}} \left[ 2 \cdot \cot \left( \frac{\phi + \psi}{2} \right) + \psi \cdot \operatorname{cosec} \left( \frac{\phi + \psi}{2} \right) \right] \quad (3)$$

In addition to ECAP and HPT, more SPD techniques have been introduced to the society of Nano-SPD researchers, including Cyclic Extrusion-Compression (CEC) [45], Accumulative Roll Bonding (ARB) [46], Repetitive Corrugation and Straightening (RCS) [47], Twist extrusion (TE) [48] and some others. The main common characteristic in these techniques is to retain the original shape of the sample unchanged during processing and therefore, keep repeating the process on the same sample for a number of times to achieve a certain level of grain refinement or to obtain the desired properties.

## 2.2. Motivation

HPT and ECAP are probably the most attractive and famous SPD techniques up to date [30]; each of them has its own advantages and disadvantages in materials processing. For instance, HPT can impose high amounts of strains such as 90 mm/mm or even more and fabricate UFG materials with extreme grain-refinement and improved mechanical properties. Due to the nature of torsional deformation and its dependency on the distance from the central axis, a non-uniform distribution of strain is applied to the



materials by HPT [39]; however, this method imposes the restriction of fabricating thin-disk samples with an approximate diameter of 10 mm and a thickness of less than 1mm [30], which impedes its development for commercial use [10]. In contrast, ECAP may produce UFG materials in bulk shapes with homogeneous microstructure, depending on the ECAP route [44] and die geometry [Paper VII]; nonetheless, the main drawback in ECAP is the non-continuous nature of the process [30], because each pass of extrusion imposes a certain amount of strain on the sample that barely reaches 2. In order to obtain higher values of strain in materials, samples should be re-inserted into the die and extruded for several times. This endeavor makes the process labor-intensive and time-consuming for industrial use. These limitations urged researchers to conduct more research to fix these flaws in SPD techniques.

Subsequent to introducing ECAP in the 1970s and 1980s by Segal [44], several modified versions of ECAP have been developed to overcome those limitations and to enhance the efficiency of the process. *Rotary-die ECAP* was introduced to facilitate the process for several passes without any need to remove the sample from the die [49,50]. *Multi-pass ECAP facility* was introduced to produce the materials in several passes of ECAP in one press [51]. *ECAP with Parallel-Channel* kept the metal flow undistorted in one full pass, thereby strain distribution in the whole sample-length remained uniform [52]. *Continuous processing of ECAP* is another subject that has been widely developed to form metals in a variety of shapes including wires and stripes [53]. *Equal Channel Angular Swaging (ECAS)* is a cost-efficient method which is a combination of ECAP and incremental rotary swaging and has this potential to be extended as a continuous SPD process [54]. These techniques mainly have the benefit of applying several passes of ECAP by inserting the sample only for one time and thereby, increasing the efficiency of the process.

Recently, a modified method of ECAP called “Indirect Extrusion ECAP” (IE-ECAP) has been developed by implementing the principles of indirect extrusion in order to reduce the friction between the die and workpiece for processing of hard materials [Paper II, Paper IV]. It has been proved that the extrusion load of tantalum reduced by 23 % during the first pass using this modified technique, and as a result, it made it possible to extrude the sample to a higher number of passes; whereas using the conventional method of ECAP, the punch broke after the third pass [55]. Section 5.1.3 will demonstrate this technique with details.

The main limitation in all ECAP-based techniques is the low amount of strain that can be applied to the materials in one pass, even in multi-pass ECAP facility where the highest strain values barely exceed 6 [51]. This limitation is an opportunity for HPT and its new generations in which strain values of 20 mm/mm and higher are readily attainable. There are several reports in the literature which have tried to scale up HPT for industrial purposes such as HPT using ring-shaped samples [56], High pressure tube twisting [57], continuous HPT-processing of wires [58], and Incremental HPT [59].

In comparison to ECAP processed materials which are in bulk shapes and can be used for general-purpose applications, modified HPT techniques are mainly useful when materials in special shapes or specific purposes are required to be used such as in tubes or thin wires. This fact initiates the idea of fabricating HPT processed materials in bulk shapes if they can be extruded as a rod. This idea generated the fundamental concepts of “**High Pressure Torsion Extrusion**” or **HPTE**. As it will be shown in the following, in addition to the mechanism of torsional straining, this technique benefits by imposing extra strain through the mechanisms of expansion and extrusion. The concept of

expansion and extrusion was primarily implemented by Pardis et al [60] in a modified SPD technique called “Cyclic Expansion-Extrusion” (CEE) which was a variation of the conventional method of “Cyclic Extrusion-Compression” (CEC) [45]. It has been shown that CEE can evolve the microstructure and hardness of materials by means of consecutive expansion and extrusion in several passes without any need for back-pressure [61]; the same concept has also been implemented in HPTE.

As it will be illustrated in the next section, HPTE has the advantage of using variable process parameters (such as extrusion speed which directly affects the amount of deformation) while in other conventional SPD methods, process parameters are usually dependent on die geometry and are not changeable during processing. For instance, in the case of ECAP, the main process parameters are the channel angle  $\phi$ , and corner angle  $\psi$  (see Figure 2); and they are fixed after die manufacture. This fact makes HPTE more attractive in terms of applying a wider range of deformation to the materials. In order to better understand the effect of HPTE on materials, HPTE experiments are accompanied by ECAP in this study to employ a comparative approach to the effect of SPD processing on materials. ECAP is believed to be the most predominant SPD technique in the processing of bulk nanostructured materials owing to its simplicity and rather low-cost productivity. A large number of research studies are available in the literature using this technique for processing of different materials. Both ECAP and HPTE share some common aspects such as processing of bulk billets, extruding the materials to apply deformation, and the possibility of re-extruding the same sample for further deformation; nevertheless, the amount of strain, mechanics of deformation, and the resulting properties in materials are different in each technique. Methodology of the experiments and the results of experiments obtained by each technique will be elaborated in the following chapters.

### **2.3. Principles of High Pressure torsion Extrusion (HPTE)**

The Principal mechanism of deformation in HPTE is based on torsion. That is to say, compressive torsional strain in the deformation zone is applied to the materials. By extruding the sample, each section of the billet passes through the deformation zone and undergoes this torsional straining. Additionally, due to the special shape of the deformation zone which is conical, materials will experience two additional deformations of expansion and extrusion (see Figure 3).

HPTE facility is a computer-controlled machine (manufactured by W. Klement GmbH) and is composed of upper die, lower die, and punch which are made of tool steel. The upper die is fixed, but the lower die is attached to an electromotor by a chain and can rotate with a rotational speed of  $\omega$  to apply torsional stress to the material. The punch is attached to a hydraulic press to extrude the specimen (with an extruding speed of  $v$ ) through the channel. This channel varies in diameter within different sections:  $D_0=12$  mm, the diameter at the inlet channel;  $D_1=14$  mm, the diameter at the deformation zone; and  $D_2= 10.6$  mm, the diameter at the outlet channel (see Figure 3-b).

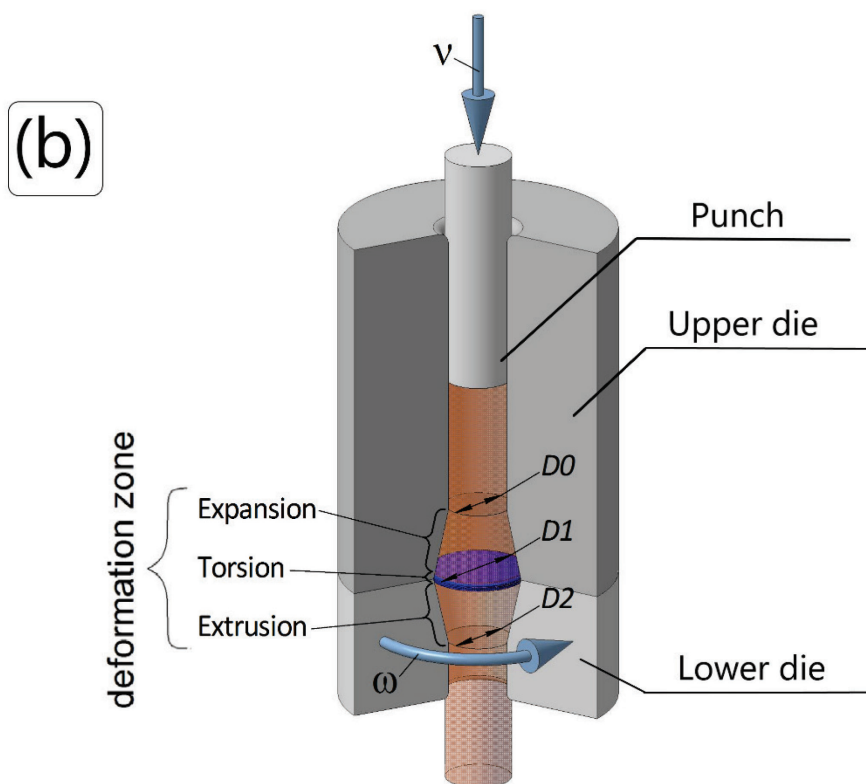
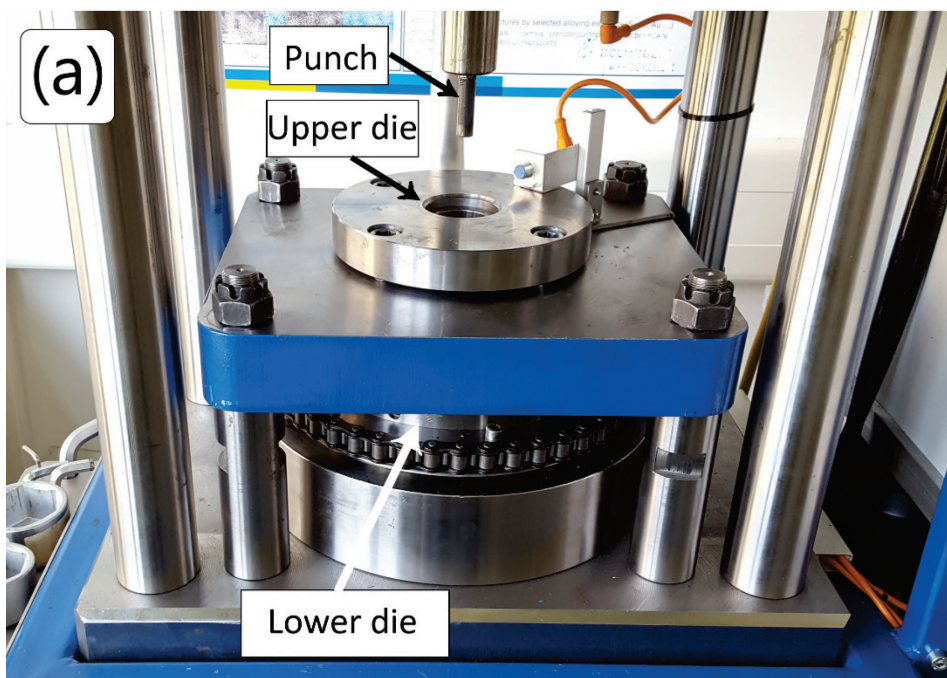


Figure 3. (a) HPTE die components; (b) Schematic illustration of HPTE die and the parameters [paper I].

Torsional straining of the specimen is possible by rotating the die only if the frictional torque (provided by the die) is enough to prevent the specimen from slipping on the surface of the die. To meet such conditions, some jutting elements have been provided in the deformation zone of the channel to provide this engagement and to restrain the specimen (Figure 4).

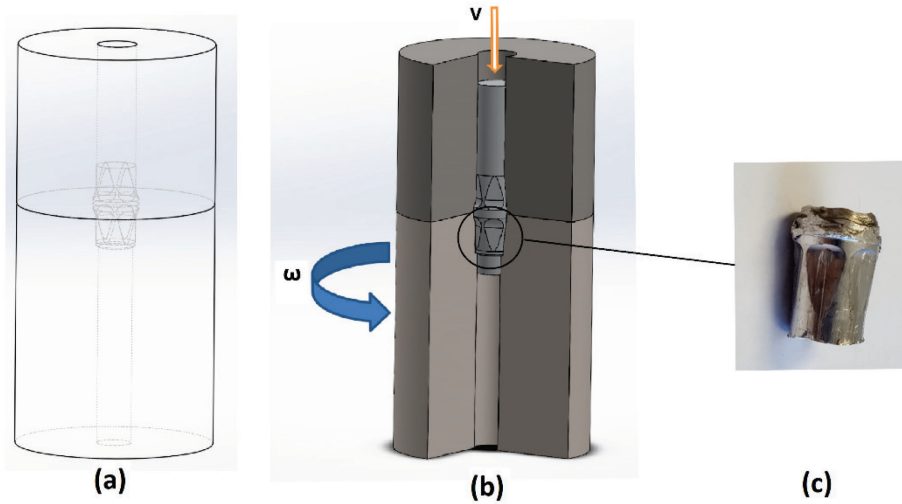


Figure 4. (A) Wireframe representation of the die demonstrating the jutting elements inside the die; (B) Cross-section of the die; (C) A piece of workpiece extracted in the middle of the process; the effect of the jutting elements can be seen on the workpiece [Paper V].

Once the punch extrudes one specimen, the process stops, the punch rises from the die; a new specimen will be inserted and then, the process starts over. In this way, the whole length of the specimen gradually passes through the deformation zone and experiences torsional straining as well as expansion and extrusion.

Equivalent strain in HPTE depends on the rotational speed of the die ( $\omega$ ), the inverse value of extruding speed ( $1/v$ ), the radial distance from the central axis of the billet ( $R$ ), the ratio of the channel diameters ( $D_1/D_0$ ), ( $D_1/D_2$ ), and can be calculated by Eq. 4 [62].

$$\bar{\epsilon}_{HPTE} = 2 \ln \frac{D_1}{D_0} + 2 \ln \frac{D_1}{D_2} + \frac{2\pi \cdot \omega \cdot R \cdot D_1}{\sqrt{3} \cdot v \cdot D_2} \quad (4)$$

In this Equation, the first and second terms come from expansion and extrusion, and since the diameters are fixed, their corresponding values will not change. The third term is resulted from torsion and may vary depending on the extruding speed ( $v$ ), rotational speed ( $\omega$ ), and the distance from the central axis of the billet ( $R$ ). Theoretically, in a specific specimen, the strain caused by torsion in the center is zero since  $R=0$ , and the only imposed strain originates from expansion and extrusion. The maximum deformation is applied to the area near to the edge of the specimen, where  $R$  obtains its maximum value (the farthest points from the center). Increasing the amount of  $\omega$  or reducing the amount of  $v$  results in increasing the total value of strain ( $\bar{\epsilon}$ ) imposed on the specimen.

As it is demonstrated in Figure 5, one advantage of HPTE due to the presence of torsion is the steep gradient velocity in materials flow during processing which makes it possible to fabricate hybrid materials with helical architecture [62].

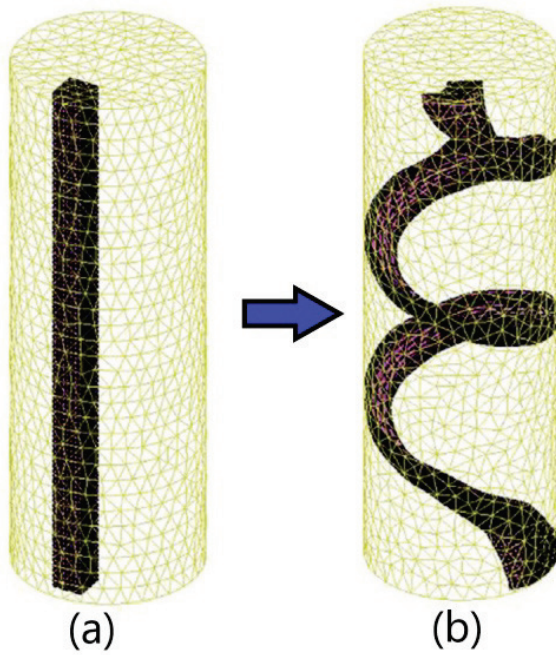


*Figure 5. Demonstration of fabricating helical architecture by HPTE; (a) sample before processing, (b) sample after processing [62].*

### 3. MODELING AND SIMULATION OF HPTE BY FINITE ELEMENT ANALYSIS

This chapter will focus on CAD modeling of HPTE as well as simulation of the process by Finite Element Analysis (FEA). The aim of this chapter is to study the effect of HPTE processing on materials flow and imposed strain. Subsequently, the correlation between the strain and radius in the cross section of the HPTE specimens will be presented.

#### 3.1. Modeling and simulations

##### 3.1.1. Drafting and modeling

CAD modeling of the die was made by SOLIDWORKS®2016 based on the exact dimensions of the die. Then, the drafts were imported to Deform-3D, Ver11 for FEA simulations. Assumptions for simulations rest on the following conditions: Neglecting the generated deformation-heat during processing, considering the die as a rigid body, and friction coefficient of 0.4 [Paper V].

##### 3.1.2. Simulation of the process

3D modeling of the die and workpiece were imported to DEFORM for simulations. Tetrahedral elements (4 nodes) were selected for meshing procedure. However, mesh size should be selected carefully as this parameter directly affects the accuracy of the results [63]. As a rule, the smaller is the mesh size, the more accurate is the result. However, decreasing the mesh size will sharply increase the computation time. Hence, there should be an optimal value for the mesh size where the results are good enough, but computation time is not too long. The optimum value can be found by the mesh convergence study as presented below. Using DEFORM, the operator may control the mesh size by changing the total number of elements (see Figure 6). In this study, different element numbers ranging from 8000 to 25000 have been selected, and extruding load as the target was evaluated to analyze the mesh sensitivity. Table 1 shows the predicted values of force and the required time for running the simulations.

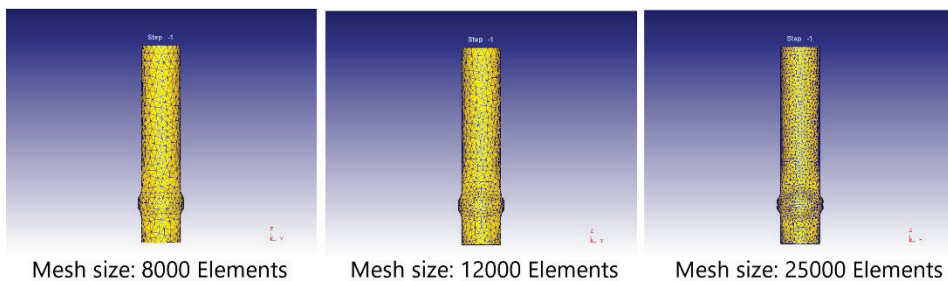


Figure 6. Demonstration of three different mesh sizes in simulations.

Table 1: Effect of meshing procedure on extrusion force and running time for simulation

Number of elements	Predicted force [kN]	Required time for simulation [h]
8000	23	0.5
10000	32	0.8
12000	41	1
15000	43	1.5
20000	41	2
25000	42	2.5

Mesh sensitivity diagram is plotted in Figure 7. As it can be seen, the sensitivity of the mesh size after selecting 12000 elements disappeared. Therefore, this mesh size (with an average length of 2mm for each element) has been chosen as the optimum value for the simulations in this work.

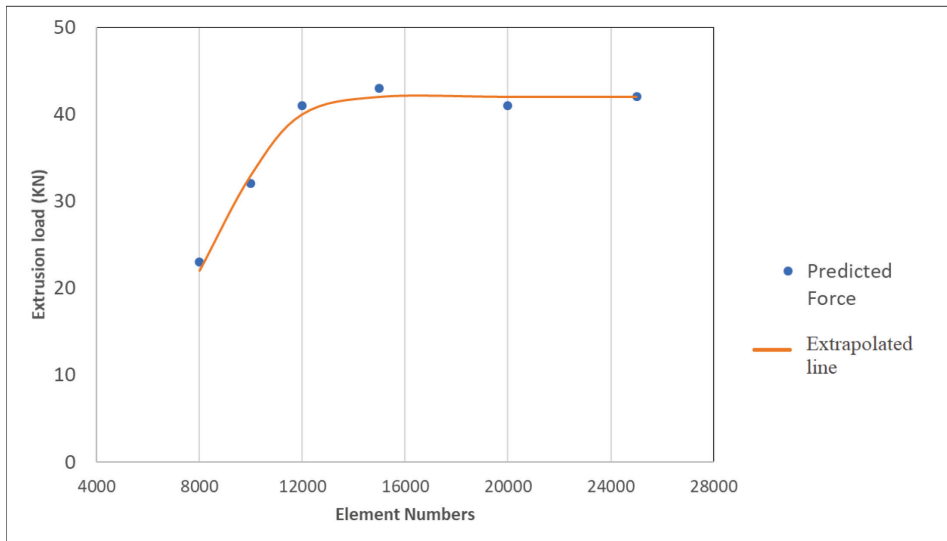


Figure 7. Mesh sensitivity diagram.

In order for validating the simulation results, one experiment with the extrusion speed of  $v=7$  mm/min and rotational speed of  $\omega=1$  rpm was performed to measure the required force for extrusion of the sample through the die; and validation was satisfied by comparison between the experiment and simulations with a relative error of 6 %.

Figure 8 shows the simulated models of HPTE in which the side view and cross section of the specimens are shown to illustrate the distribution of stress, strain and strain rate in HPTE. As it can be seen in the distribution of strain, the highest values of strain are located at the periphery of the specimen, near to the edge, which are in conformity with the equation of strain in HPTE (Eq. 4).

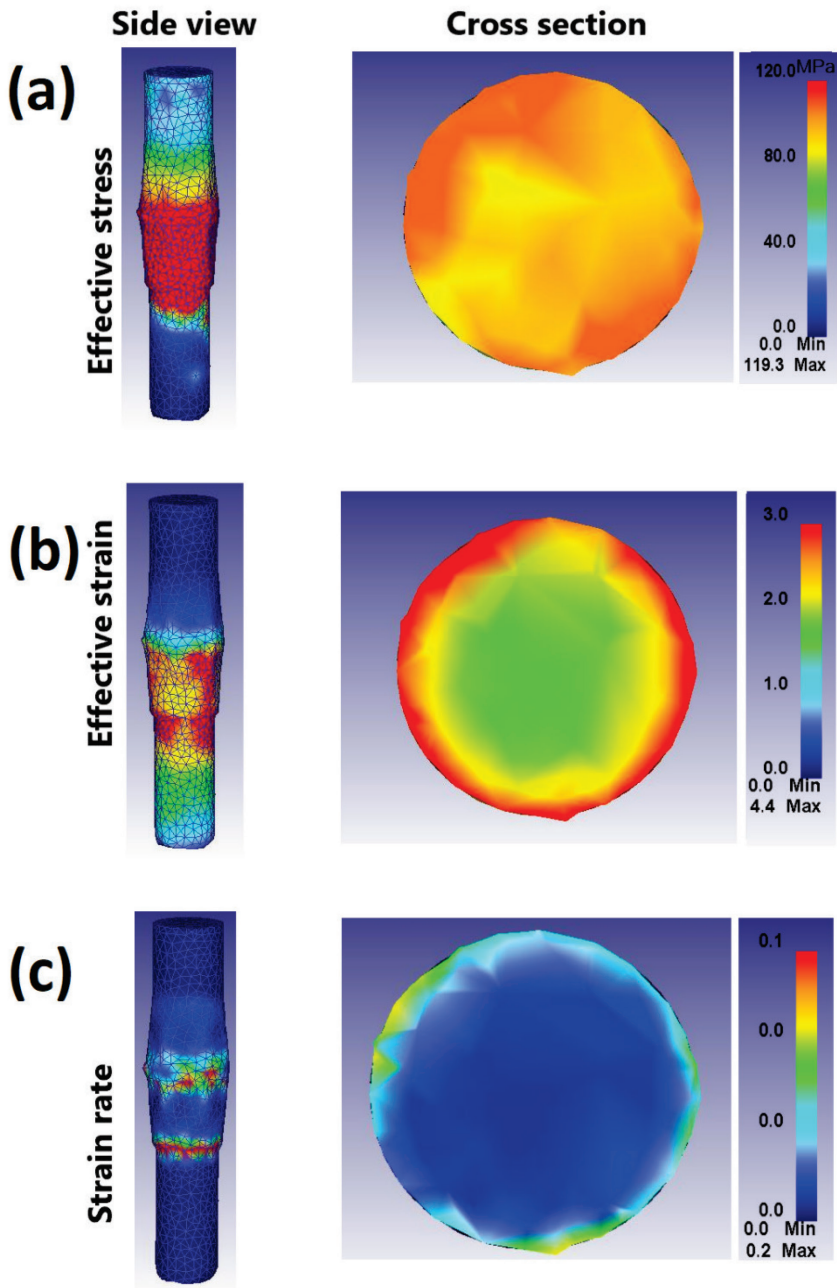


Figure 8. Illustration of stress (a), strain (b), and strain rate (c) in HPTE specimen.

In order to compare the results of simulation with theoretical values obtained by Eq.4, twenty nodes from the cross section of the specimen were selected through a line, evenly spaced apart from each other (see Figure 9), and the corresponding value of each node along with its theoretical counterpart was plotted in Figure 10.



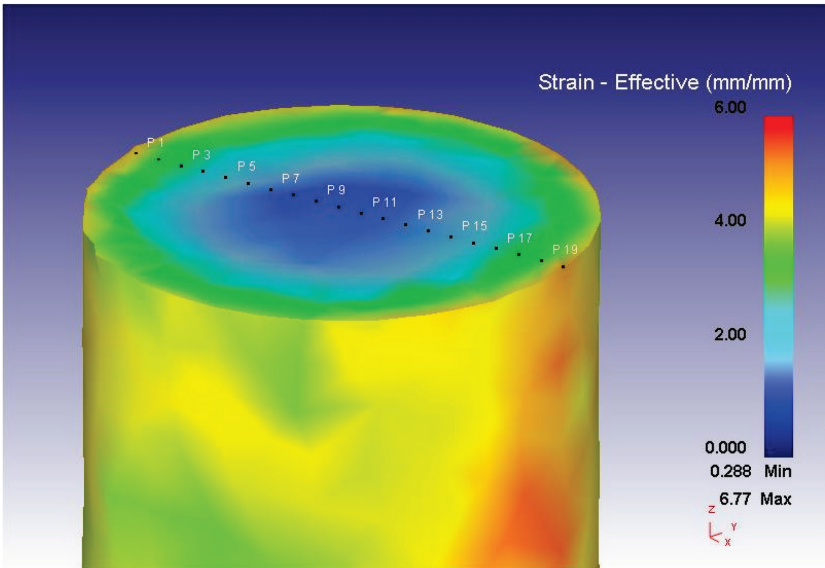


Figure 9. Selection of random nodes from the cross section of the specimen.

As it is demonstrated in Figure 10, the two graphs show the same increasing trend, confirming the intrinsic nature of torsional straining in HPTE specimens. Nonetheless, there is a slight discrepancy between the two graphs that is related to the effect of friction which was not taken into account in the theoretical equation of strain (Eq. 4), while this friction was considered in the simulations between the material and the die.

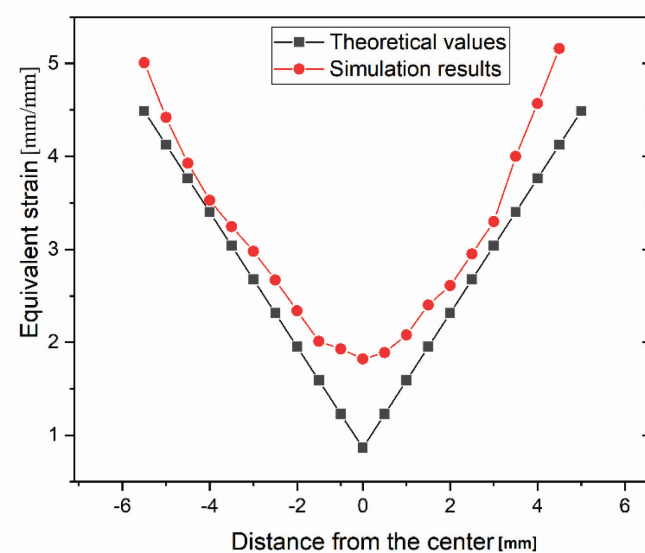


Figure 10. Distribution of strain in the cross section of HPTE specimen; simulation vs. theory.

## 4. SPD PROCESSING OF ALUMINUM

This chapter presents the experimental procedures performed on aluminum by HPTE and ECAP. The main aim of this chapter is to establish a detailed analysis about the effect of HPTE versus ECAP on the microstructure and hardness of materials. Moreover, a comparative analysis will be conducted to evaluate the results obtained here compared to the results reported in the literature about SPD processing of aluminum.

### 4.1. Methodology of experiments

#### 4.1.1. Materials and characterization techniques

Commercially-Pure (CP) aluminum AA1050 (Al 99.5) with the purity of 99.5 wt% was annealed at 345°C for 30 minutes and then cooled to room temperature. In order for microstructural observations, samples were mechanically polished and then electropolished at 20 V and 1 A for 8 seconds at room temperature using a solution of 70 vol.% ethanol, 20 vol.% perchloric acid, and 10 vol.% glycerin. The images were taken from the cross section of the billets (transversal direction) in ECAP and HPTE samples. Microstructural observation of HPTE samples was performed at three different locations on the cross section of the samples: in the center, in the mid-radius region ( $\approx 2.7$  mm from the central axis of the samples) and in the edge zone ( $\approx 4.5$  mm from the central axis).

An optical microscope of “Nikon Eclipse Ci-L” was implemented to take an image from the annealed sample. SEM images were obtained by using “Ultra-55 Zeiss” microscope running at 15 kV in electron-backscattered mode. Electron backscatter diffraction (EBSD) imaging was carried out by using FEI Quanta 3D scanning electron microscopes operating at 20 kV. The images were taken from the cross section of the samples, perpendicular to the extrusion direction. The scanning step size in EBSD was about 25 nm, which corresponds to one-pixel size. To eliminate disputable orientations caused by orientation noise, a  $2^\circ$  criterion was used as the lowest limit for misorientation. A cut-off value of  $15^\circ$  was employed to differentiate between the low-angle grain boundaries (LAGBs) and high-angle grain boundaries (HAGBs).

X-ray Diffraction (XRD) patterns of the samples were obtained by a “PANalytical Empyrean” facility with a copper anode ( $\text{CuK}\alpha$  radiation of  $\lambda=1.5406\text{\AA}$ ), operated at 45 kV, and 40 mA with a pixel detector in Bragg-Brentano geometry. Scans were carried out in a  $2\theta$  range from  $36^\circ$  to  $120^\circ$  with a scan step of  $0.013^\circ$  and 10 seconds per step in continuous rotating mode. PANalytical Highscore Plus-Version 3.0 was used for refinement and analysis of the patterns. Williamson-Hall method [64] was employed to predict the microstructural parameters of the processed materials, and thereby, estimating the values of crystallite size and dislocation densities.

Microhardness of the samples was measured by a “Micromet-5104” in Vickers scale with a load of 1.96 N (200 gr) and a dwell time of 15 s. Indentation was applied in several points along two perpendicular diameters in the cross section of the samples (Figure 13-a), each point spaced apart from the other one evenly with a distance of 0.9 mm.

Compressive strength of HPTE processed samples was measured by a “SHIMADZU” universal testing machine on the samples in accordance with ASTM E9-89a [65]. It should be noted that although tensile test is a common technique for mechanical-property evaluation, in this scenario since the HPTE processed billets are supposed to be soft in the core and hard at the peripheral zone, preparation of dumbbell-shaped specimens and performing the tensile test on these samples might not be a good choice to represent

the whole characteristics of the material as a unique feature. In this regard, compressive test was selected and performed on the samples at a compressive speed of 2 mm/min and a Teflon sheet was used as a solid lubricant; the criterion of the maximum length-reduction of 66.67 % ( $e=2/3$ ) was established in the test.

The relative errors for the measured values of microhardness, volume fraction of high-angle grain boundaries ( $V_{HAGB}$ ), compressive strength, grain size, and dislocation densities were 2, 5, 5, 10, 20 %, respectively.

#### 4.1.2. HPTE processing of aluminum

Aluminum samples were cut into a length of 35 mm and a diameter of 11.8 mm to obtain the desired dimensions for HPTE processing.

HPTE experiments were performed at room temperature and Molybdenum Disulfide ( $MoS_2$ ) was used as a lubricant in all experiments to reduce the friction between the die and workpiece. The main process parameters of HPTE (extrusion speed,  $v$ ; and rotational speed,  $\omega$ ) are variable and user may choose different values to apply different range of strains to the materials. Due to the mechanism of deformation in torsion, the imposed strain on the material varies depending on the distance from the center ( $R$ ) in the cross section of the sample. In this set of experiments, three different regimes were selected as shown in Table 2 with their corresponding strain values. All samples were processed in one pass of HPTE.

Table 2: Notation of HPTE regimes and the corresponding process parameters

HPTE									
Sample ID	$v$ [mm/min]	$\omega$ [rpm]	Equivalent strain [mm/mm]						
			$R$ [mm]						
			0	0.9	1.8	2.7	3.6	4.5	
v7w1	7	1	0.9	1.5	2.1	2.7	3.3	3.9	
v1w1	1	1	0.9	5.2	9.5	13.8	18.1	22.4	
v1w3	1	3	0.9	13.8	26.7	39.7	52.6	65.5	

#### 4.1.3. ECAP processing of aluminum

Aluminum samples in the annealed conditions with a length of 130 mm and a diameter of 15.8 mm were processed for ECAP. The ECAP die used here was a parallel-channel ECAP die shown in Figure 11 with the die parameters of  $\varphi=110^\circ$  and  $\psi=70^\circ$ .

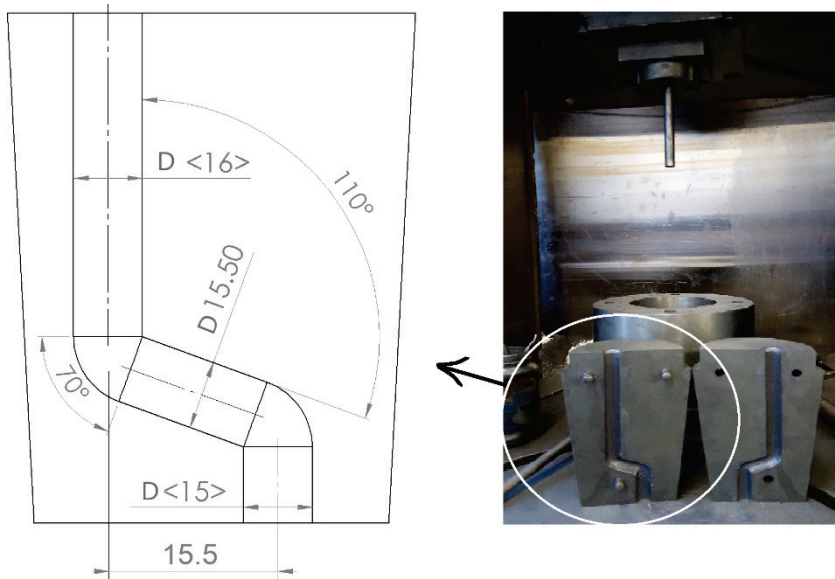


Figure 11. Parallel channel ECAP die.

The equivalent strain that can be obtained by extruding the sample through each ECAP channel is equal to  $\bar{\epsilon} = 0.78$  mm/mm. Samples were processed for 4 and 8 passes of ECAP at room temperature by using route B<sub>c</sub> by which the sample is rotated for 90 degrees between consecutive passes and thereby produces fairly homogeneous properties in the material [Paper VI, Paper VII]. The following table shows the process IDs along with the corresponding equivalent values of strain in each regime.

Table 3: Notation of ECAP regimes and the corresponding imposed strain

Process ID	Notes	Equivalent strain [mm/mm]
ECAP4	after 4 passes	3.1
ECAP8	after 8 passes	6.2

## 4.2. Results of experiments

### 4.2.1. Compressive strength of HPTE samples

Results of compressive testing of HPTE processed aluminum are presented in Figure 12. According to this graph, HPTE substantially improved the compressive yield strength and ultimate strength of materials after processing.

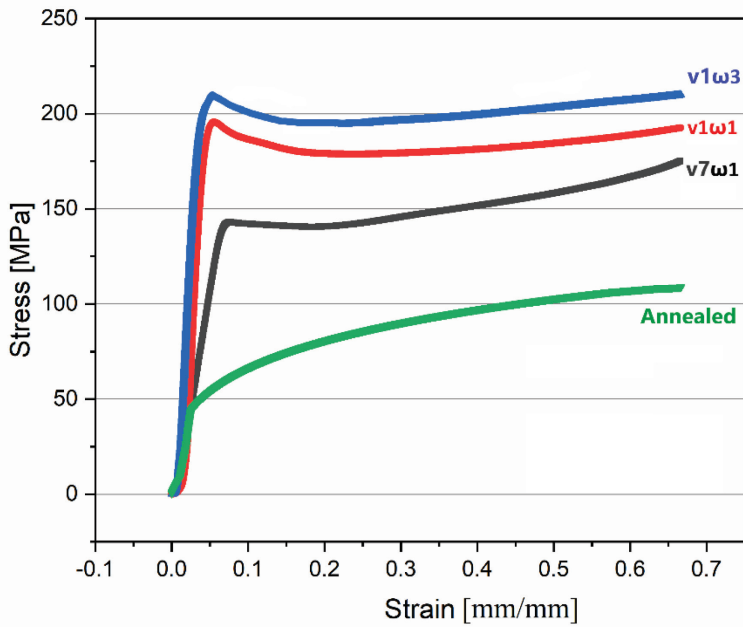


Figure 12. Stress-strain diagram obtained from compression test.

Table 4 illustrates the corresponding values obtained by compression test for the processed samples beside the initial one. The yield strength in aluminum improved from the initial value of ~44 MPa to ~141, ~194, and ~207 MPa, in v7w1, v1w1, and v1w3 samples, respectively, after processing. Sample v7w1 demonstrated a significant difference between the yield strength and ultimate strength in compression, whereas the other two samples (v1w1, v1w3) represented almost similar values in yield and ultimate compressive strength.

Table 4: Compressive strength of HPTE processed aluminum

Sample	Yield Strength [MPa]	Improvement rate in Y.S <sup>†</sup> [%]	Ultimate Compressive strength [MPa]	Improvement rate in U.C.S [%]
Initial	44	–	109	–
v7w1	141	220	175	60
v1w1	194	340	195	79
v1w3	207	370	209	92

†. The improvement rates in Yield strength and Ultimate strength for each sample are measured based on comparison with the initial sample.

#### 4.2.2. Hardness evolution

Hardness testing is a useful tool to demonstrate the effect of a hardening mechanism in metallic materials, especially when it comes into the evaluation of the effect of strain distribution on mechanical properties. Results of microhardness testing performed on the samples are shown in Figure 13.

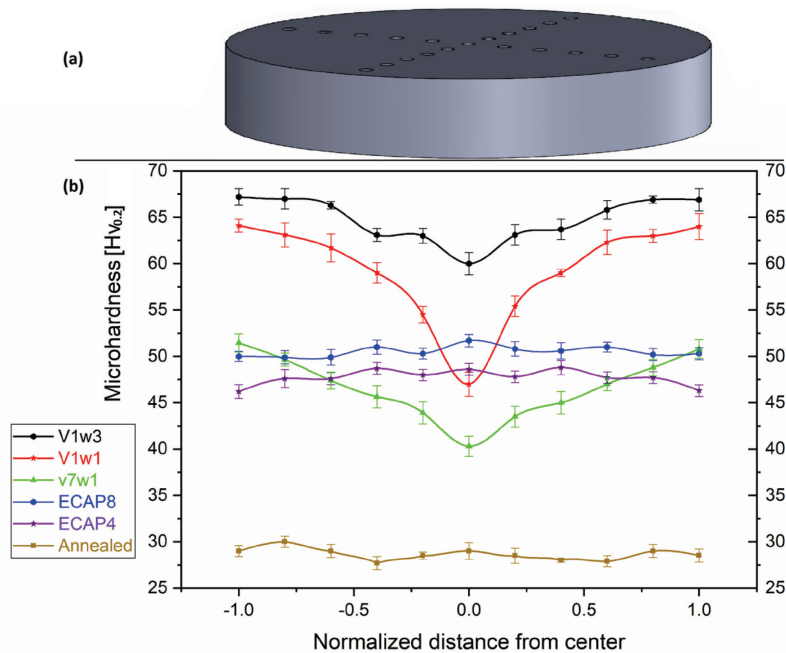
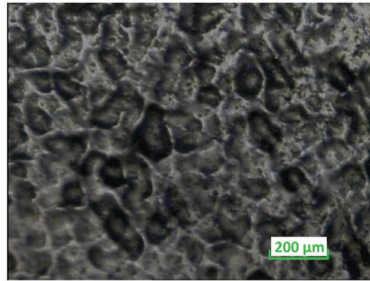


Figure 13. a) Illustration of a specimen exposed to microhardness; b) Microhardness distribution in HPT processed samples.

The most homogeneous hardness distribution in this figure is found in the initial sample (annealed) with an average value of 28 HV0.2. ECAPed samples also showed rather a homogeneous distribution with the average hardness values of 47 and 51 HV0.2 in ECAP4 and ECAP8, respectively. However, hardness distribution in the cross section of HPT samples is basically inhomogeneous and represents a V-shape distribution; lower values of hardness are found in the central zone and higher values are distributed near to the edge (the peripheral zone). The minimum hardness values in the HPT samples are 40, 46, and 60 HV0.2 located in the center, and the maximum values are 51, 64, and 67 HV0.2 in the peripheral zone for the samples v7w1, v1w1, and v1w3, respectively. This V-shape distribution of hardness in the HPT samples is in agreement with the distribution of strain along the diameter of HPT sample shown in Figure 10.

#### 4.2.3. Microstructural refinement

As indicated before, the primary purpose of each SPD process is to reduce the grain size in metallic materials with the intention of improvement in material properties. Figure 14 shows the microstructure of aluminum samples in annealed conditions (obtained by optical microscope) and ECAP processed conditions (obtained by SEM-Backscattered electron imaging).



**Initial case (Annealed)**

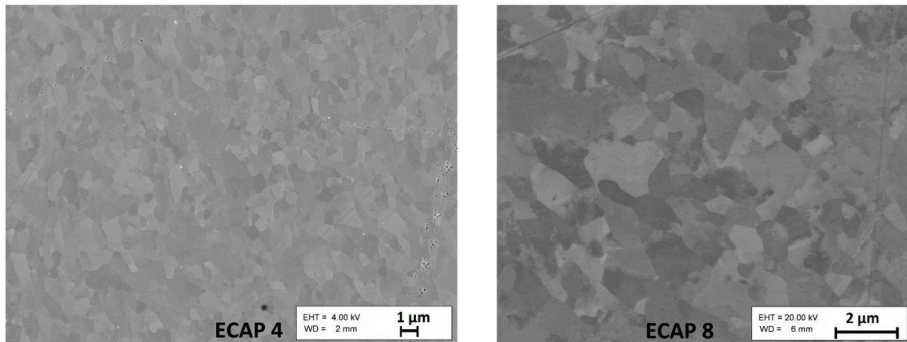


*Figure 14. Microstructural observation of annealed and ECAPed aluminum.*

The average grain size in the annealed case was measured as  $130\ \mu\text{m}$  and this value reduced to  $1.1\ \mu\text{m}$  in ECAP4 and  $0.9\ \mu\text{m}$  in ECAP8.

As mentioned before, HPTE is supposed to present a gradient distribution of properties across the cross section of the sample due to the mechanism of torsion which was applied to the materials. In order to demonstrate this gradient in the microstructure of the samples graphically, EBSD technique was implemented and three different sections for each regime (e.g. the center, the mid-radius, and the edge zone) were assessed for microstructural evolution. As it can be observed in Figure 15, HPTE made different levels of grain refinement in the materials, depending on the regime and distance from the center.



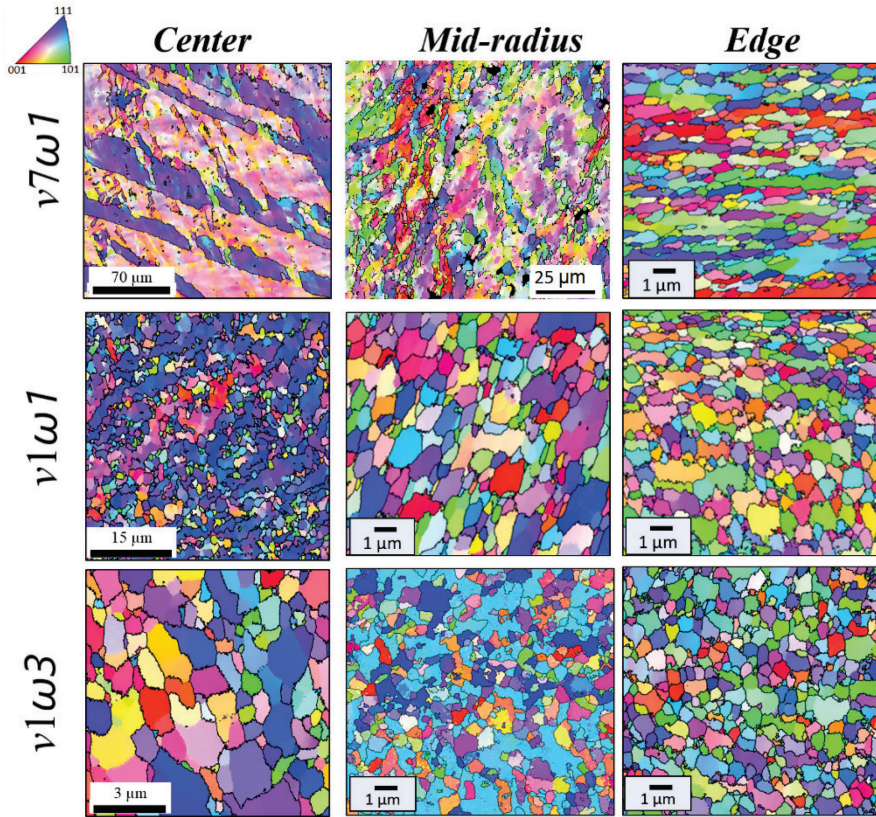


Figure 15. EBSD mapping of HPT processed samples.

As expected, coarse grains are located in the center and finer grains are distributed near to the periphery. Figure 16, Figure 17, and Figure 18 represent the statistical analysis of the EBSD maps regarding the grain size and misorientation angles for each regime and each section. The values of average grain diameter ( $D_{ave}$ ) and volume fraction of High Angle Grain Boundaries (percentage of grain boundaries with the misorientation angle of above  $15^\circ$  -  $V_{HAGB}$ ) are inset into the graphs.



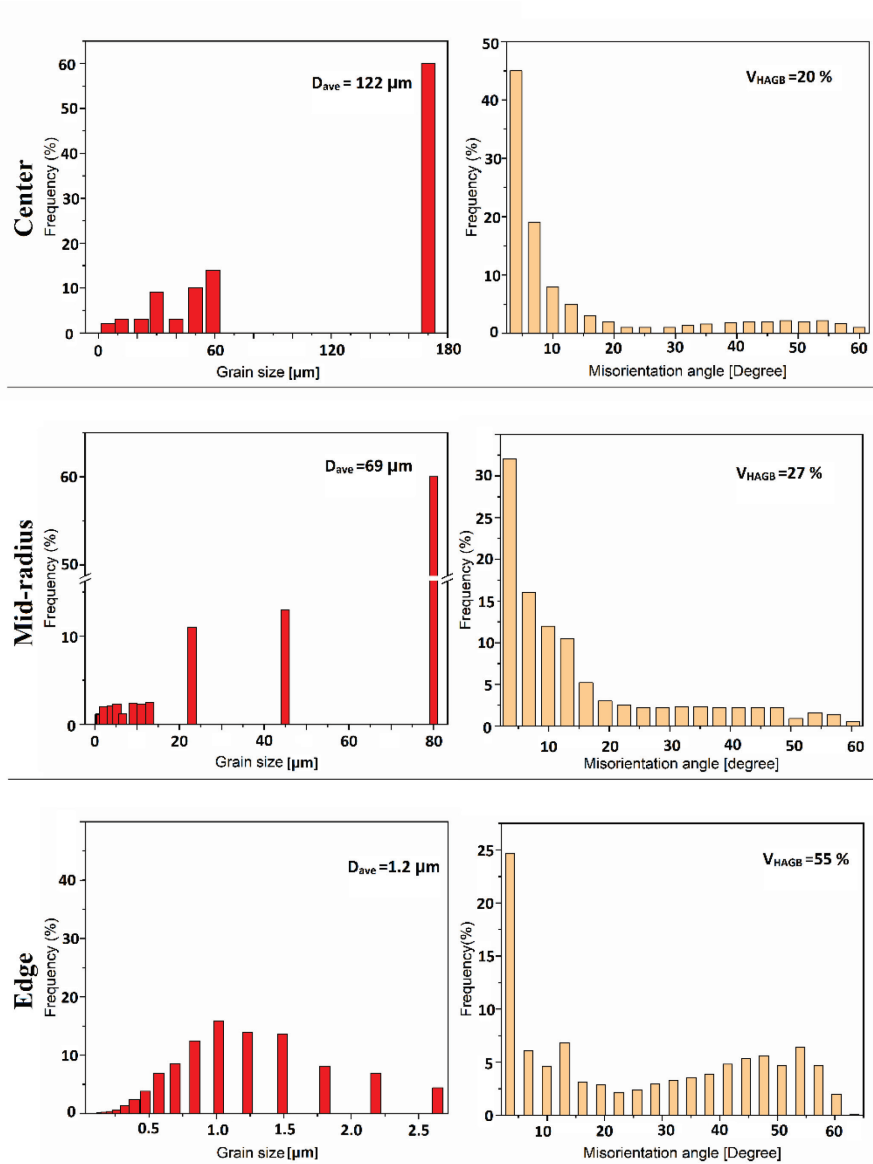


Figure 16. Distribution of grain size (left) and grain-boundary misorientation angles (right) for the v7w1 sample.

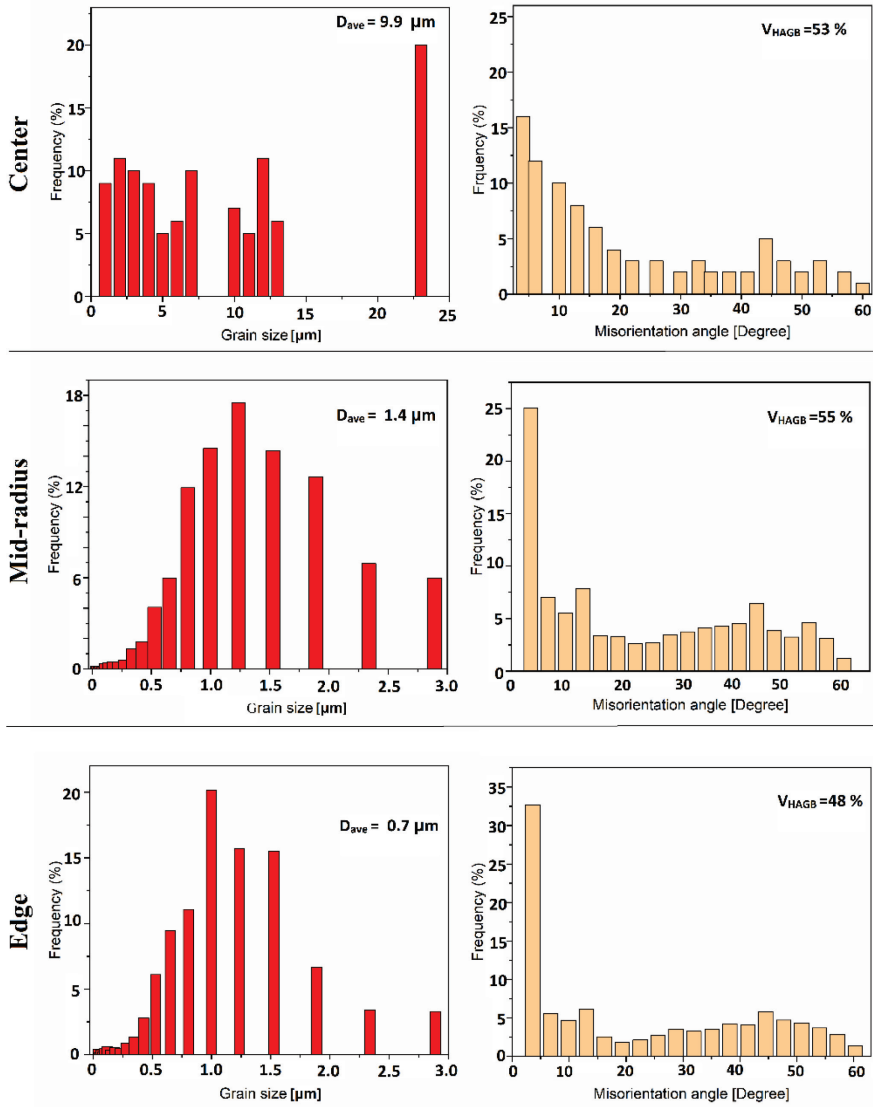


Figure 17. Distribution of grain size (left) and grain-boundary misorientation angles (right) for the v1w1 sample.

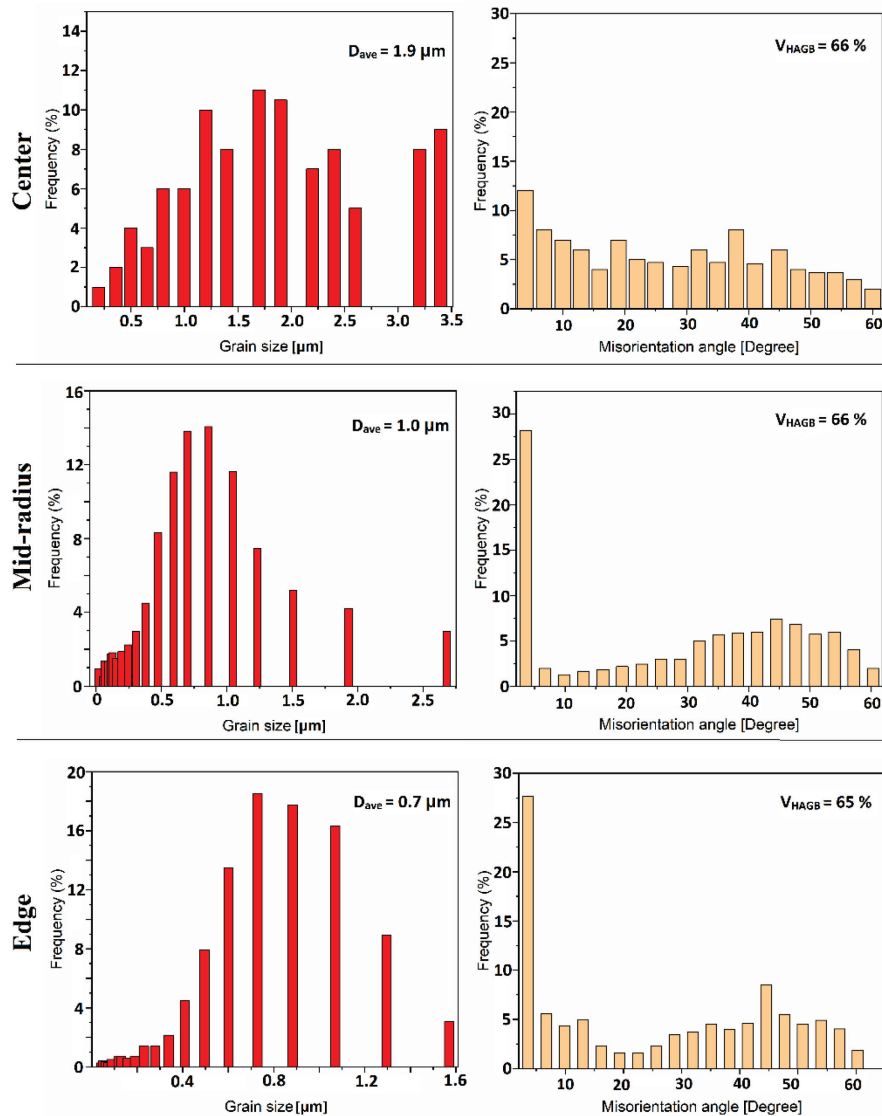


Figure 18. Distribution of grain size (left) and grain-boundary misorientation angles (right) for the v1w3 sample.

In general, the average grain size decreased after processing in all cases. According to the results, there is a wide variation in the microstructure and volume fraction of HAGBs ( $V_{\text{HAGB}}$ ) in v7w1 sample by moving along the radius from center to edge ( $D_{\text{ave}}=1.2 - 122 \mu\text{m}$ ,  $V_{\text{HAGB}} = 20 - 55 \%$ ). This variation is fairly smaller in v1w1 sample ( $D_{\text{ave}}= 0.7- 9.9 \mu\text{m}$ ,  $V_{\text{HAGB}} = 48 - 55 \%$ ). Sample v1w3, however, showed the smallest variation in grain-size distribution and  $V_{\text{HAGB}}$  along the radius ( $D_{\text{ave}}= 0.7 - 1.9 \mu\text{m}$ ,  $V_{\text{HAGB}} = 65 - 66 \%$ ) and thereby representing more homogeneity in microstructure.

Results of X-ray diffraction (XRD) patterns of the samples are presented in Figure 19. The patterns are presented on a normalized intensity basis.

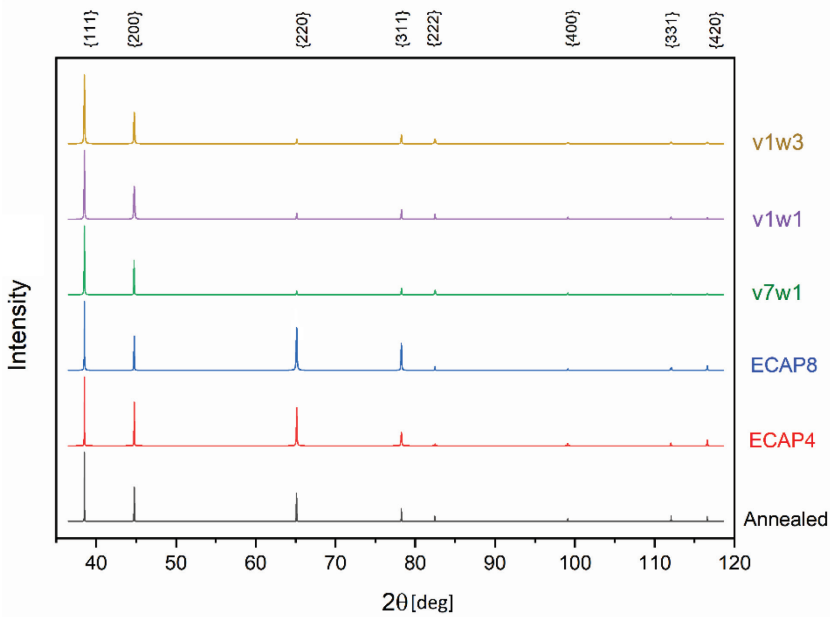


Figure 19. XRD patterns of processed and annealed aluminum.

Peak broadening of the diffraction patterns in the processed samples may be noticed in this image. This peak broadening, as mentioned in chapter 2, is a consequence of microstructural deformation [66] and can be employed to identify the crystallite size, micro-strains (lattice strain) and the dislocation densities which are retained in the materials. These parameters can be estimated by measuring the Full Width at Half-Maximum (FWHM) of the peaks and implementing Williamson-Hall equation (Eq. 5) [17,67]:

$$\beta \cos\theta = \frac{K\lambda}{D_{cr}} + 4\varepsilon \cdot \sin\theta \quad (5)$$

In this equation,  $\beta$  is the peak broadening (FWHM) in radians,  $\lambda$  is the wavelength of the X-ray beam ( $\lambda=0.1542$  nm for Cu- $\kappa\alpha$ ),  $K$  is the Scherrer constant ( $K\approx 0.94$ ) [15,68],  $D_{cr}$  is the crystallite size,  $\varepsilon$  is the lattice strain, and  $\vartheta$  is the Bragg angle.

The experimental value of FWHM ( $\beta_{exp}$ ) encompasses the intrinsic value ( $\beta$ ) and instrumental profile ( $\beta_{ins}$ ) and it can be unfolded by using Eq. 6 [15] in which the instrumental profile is considered to be  $\beta_{ins}=0.026^\circ$ :

$$\frac{\beta}{\beta_{exp}} = 1 - \left( \frac{\beta_{ins}}{\beta_{exp}} \right)^2 \quad (6)$$

Eq. 5 can be modeled as the equation of a line ( $y= ax + b$ ); thereby, from the linear plot of  $4\sin\theta$  in X-axis, and  $\beta \cdot \cos\theta$  in Y-axis (Figure 20), the crystallite size ( $D_{cr}$ ) and lattice strain ( $\varepsilon$ ) can be extracted from the intercept and slope of the line, respectively [69,70]. Figure 20 shows the Williamson-Hall plots along with the extracted equations of linear curve fitting and corresponding R-squared values for each regression model.

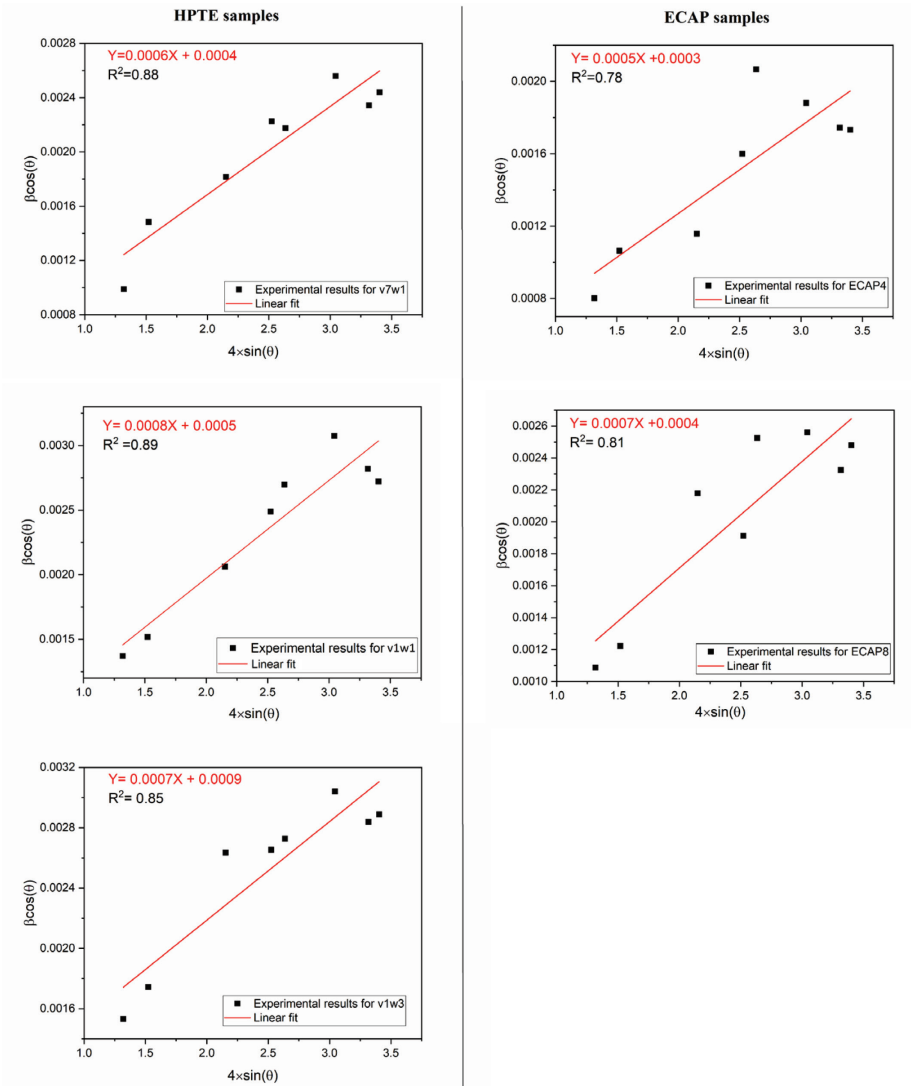


Figure 20. Williamson-Hall plots obtained from XRD patterns; sample IDs are shown as insets within each graph.

Using the estimated values of lattice strain and crystallite size, dislocation density ( $\rho$ ) in the processed samples can be calculated by Eq. 7 [67,71,72]:

$$\rho = \frac{2\sqrt{3}(\varepsilon^2)^{\frac{1}{2}}}{b \times D_{cr}} \quad (7)$$

In this equation,  $b$  is the burgers vector and is equal to  $b = 0.286$  nm in aluminum [66]. Accordingly, by substituting all known values, crystallite size, lattice strain, and dislocation density can be estimated as follows.

Table 5: Structural parameters of processed samples obtained by Williamson-Hall method

Sample ID	Crystallite size [nm]	Lattice strain [%]	Dislocation density [ $10^{13} \text{ m}^{-2}$ ]
V7w1	362	0.06	2.0
V1w1	290	0.08	3.34
V1w3	161	0.07	5.26
ECAP4	483	0.05	1.25
ECAP8	362	0.07	2.33

According to Table 5, v1w3 encompasses the maximum amount of dislocation density as this sample received the highest amount of deformation (equivalent strain of 65 mm/mm at the edge zone; see Table 2), and ECAP4 contains the lowest amount of dislocation density compared with all other samples.

### 4.3. Discussion and interpretation of results

Results of experiments presented above showed that ECAP processing provides a homogeneous distribution of hardness in materials whereas HPTE makes a gradient distribution. This variation (from the center to edge) was also observed in the simulation of strain distribution (Figure 10). The trend of simulated strain distribution was in conformity with the trend of theoretical values of strain expressed by Eq. 4 (see section 2.3). Results of hardness measurement clearly demonstrated this variation as well. Microstructural observation of the samples confirmed the fact that the finest grains in each regime are located in the edge zones, and coarse grains are found in the center (see Figure 15). The main mechanism of deformation in the center is basically affected by extrusion as the component of torsion in this zone is zero in theory and the equivalent strain is 0.9 mm/mm in all samples (see Table 2). Nonetheless, the level of grain refinement in the center is totally different in each regime. According to the results, the average grain size in the center for the HPTE regime v7w1 is about 122  $\mu\text{m}$  while this value for v1w1 is 9.9  $\mu\text{m}$  and for v1w3 is 1.9  $\mu\text{m}$ . The grains in the central zone of v7w1 are distorted and heterogeneous whereas in the other two regimes, and especially in v1w3, grains are looked like to be more equiaxed and homogeneous. This phenomenon can be explained by "strain gradient plasticity modeling" [73] by which plasticity can spread into the center from the neighboring regions during processing depending on the process parameters. In the case of v1w3, extrusion is slow enough so that there will be enough time for the deformed materials affected by torsion to spread out the influence of torsion from the edge zone to the neighboring zones. In fact, the contribution of shear strain on deformation of the central zone increased by increasing the ratio of  $\omega/v$  as the level of grain refinement in the central zone of the samples increased in the order of v7w1, v1w1, and v1w3. Effect of gradient plasticity is also evident in the results of hardness distribution (see Figure 13), where an extraordinary increase in hardness was observed in the central zone of v1w3 and hardness distribution along the radius was rather homogeneous but the other two samples showed a big difference in hardness between the center and the edge. The evolution of misorientations from low angle to high angle in the central zones of the samples can also reflect the gradient-plasticity

effect. An inspection of the volume fraction of HAGBs ( $V_{\text{HAGB}}$ ) in Figure 16, Figure 17, and Figure 18 showed that  $V_{\text{HAGB}}$  increased from 20 % to 66 % in the central zones by increasing the ratio of  $\omega/v$ . Table 6 collects all structural parameters and demonstrates this increasing trend clearly.

The impact of gradient plasticity in the central zone of HPTE samples can also be traced in an earlier study accomplished on HPTE processing of copper, whereby increasing the ratio of  $\omega/v$  from  $\frac{1}{10}$  to 1, noticeably increased the homogeneity of microstructure and hardness distribution from the center to edge [62]. These results imply this fact that changing the ratio of  $\omega/v$  in HPTE, regardless of materials, may result in a heterogeneous or homogeneous structure in materials, depending on the chosen process-parameters and desired properties.

Table 6: Results of experimental procedures on SPD processed aluminum

Sample, location	Strain [mm/mm]	Average grain size ( $D_{\text{ave}}$ ) [ $\mu\text{m}$ ]	Average crystallite size <sup>†</sup> [nm]	Lattice strain [%]	Dislocation density [ $10^{13}/\text{m}^2$ ]	Hardness [HV0.2]
v7w1, center	0.9	122				40
v7w1, mid-radius	2.7	69	362	0.06	2.0	46
v7w1, edge	3.9	1.2				51
v1w1, center	0.9	9.9				47
v1w1, mid-radius	13.8	1.4	290	0.08	3.34	60
v1w1, edge	22.4	0.7				64
v1w3, center	0.9	1.9				60
v1w3, mid-radius	39.7	1.0	161	0.07	5.26	65
v1w3, edge	65.5	0.7				67
ECAP4	3.1	1.1	483	0.05	1.25	47
ECAP8	6.2	0.9	362	0.07	2.33	51

<sup>†</sup>. The values of FWHM in different sections of each HPTE regime were obtained the same; accordingly, the corresponding values of crystallite size, lattice strain, and dislocation densities are equal in the center, mid-radius and edge zone of each sample.

Analysis of the microstructure of HPTE processed materials reveals that each sample experienced different levels of grain refinement and different grain size distribution across the cross section of the samples. Distribution of grain size in v7w1 varied widely along the radius of the sample (Figure 15). The average grain size of 122, 69, and 1.2  $\mu\text{m}$  in the center, in the mid-radius ( $R \approx 2.7\text{mm}$ ), and in the edge zone ( $R \approx 4.5\text{mm}$ ) of the sample were observed respectively (see Figure 16). The volume fraction of HAGB ( $V_{\text{HAGB}}$ ) in the edge zone was considerably higher (55 %) than the ones in the mid-radius zone

(27 %) and in the center (27 %), suggesting this fact that the strain imposed on the sample v7w1 was not enough to introduce any microstructural saturation in this sample.

The evolution of microstructure in the mid-radius and in the edge zone of the sample v1w1 showed similar levels of grain refinement, while having coarse grains in the central zone (see Figure 15). The average values of grain size in the center, in the mid-radius, and in the edge zone were 9.9, 1.4 and 0.7  $\mu\text{m}$ , respectively. Volume fractions of HAGBs obtained from the three zones of this sample were fairly similar (48-55%; see Figure 17). In comparison with the results of v7w1, this sample showed less variation in the microstructural distribution.

The most uniform distribution in HPTE microstructure was formed in v1w3 (see Figure 15). The average grain size in the center, in the mid-radius, and in the edge zones were 1.9, 1, and 0.7  $\mu\text{m}$ , respectively, showing the least variation in grain size among all three samples (see Table 6). It is noticeable that the highest HAGB fractions were measured in the sample v1w3 with nearly identical values from the center to the edge (65-66 %; Figure 18).

Results of microstructural evolution in ECAP also showed a considerable grain refinement in materials in comparison with the initial case (see Figure 14). The average values of grain size in the ECAPed samples were measured as 1.1  $\mu\text{m}$  and 0.9  $\mu\text{m}$  in ECAP4 and ECAP8 respectively.

Evaluation of results on the grain refinement of aluminum in the present work showed that the finest grain size that can be achieved by SPD processing of aluminum is 0.7  $\mu\text{m}$ . This value was obtained by HPTE and by means of two different regimes: v1w3 regime and applying an equivalent strain of  $\sim 65$  mm/mm; and v1w1 regime at a lower strain of  $\sim 22$  mm/mm. These results imply that although HPTE may provide extremely high amounts of strains, further grain refinement may not be possible due to approaching the saturation level in grain refinement of aluminum [Paper I]. In the case of ECAP, this level did not achieve even after eight passes of extrusion. Other research studies about SPD processing of aluminum AA1050 also agree with these findings. Two different studies about ECAP processing reported nearly similar values of grain size (0.85-1.1  $\mu\text{m}$ ) for the same aluminum alloy (AA1050) after eight passes of extrusion [74,75], while a research work about HPT of aluminum reported the grain size of 0.7  $\mu\text{m}$  achieved in an equivalent strain value of  $\sim 95$  mm/mm processed at room temperature [76]. It has been reported that grain refinement in pure metals and single-phase alloys, reach the saturation level within a strain range of 5 to 50 mm/mm [77]. However, in the case of dilute aluminum alloys processed by SPD at room temperature, it seems that the saturation level of 0.7  $\mu\text{m}$  can be achieved within the strain range of 10-20 mm/mm.

One subtle point that is worth to note here is the difference between the grain-size values obtained by electron microscopy and the crystallite-size values measured by XRD analysis. Although both methods showed the same descending order of size in HPTE and ECAP, the crystallite-size values are considerably smaller (see Table 6 for comparison). This difference was also noticed in other studies on SPD processed materials [15,70]. This phenomenon can be explained by considering the fact that applying SPD processing on crystalline materials considerably increases the amounts of crystalline defects. Accumulation of these defects can form dislocations cells with small misorientations inside the grains [78]. Therefore, each grain may consist of different misorientations which are referred to as subgrains or dislocation cells [7]. In general, subgrains are not considered as a complete grain by electron microscopy analysis, though they are detectable by XRD analysis [79].



The main expectation of SPD processed materials after grain refinement is to come up with an enhancement in mechanical properties, although some other physical/chemical properties such as thermo-electric properties [80], hydrogen-storage [81], [Paper III], and biocorrosion resistance [82] may also be improved. It has been approved that grain size in polycrystalline materials is the major factor in dictating the properties of materials [43]. A striking feature of this correlation between the grain size and strength is the hall-Petch relationship (Eq. 1) [2,3] which was discussed in section 2.1. Reportedly, grain refinement by SPD in pure metals or dilute alloys can improve the strength by a factor of 3-8 [21]. In the present work, a considerable improvement occurred in the compressive strength of materials after HPTE processing as yield Strength of aluminum improved by the factor of 3.7 for the HPTE sample v1w3 (see Table 4). This improvement is evident in the stress-strain diagrams in Figure 12. Another point that is noticeable in this figure is the saturation of work hardening. The initial sample (Annealed) showed a big difference between the Yield Strength and Ultimate Compressive Strength (44 MPa vs. 109 MPa), while this difference reduced in the processed sample v7w1 (141 MPa vs. 175 MPa). This difference between the yield and ultimate strength almost vanished away in the other two processed samples as it was 194 MPa vs. 195 MPa in v1w1, and 207 MPa vs. 209 MPa in v1w3, indicative of approaching the saturation level in strain hardening in the two HPTE samples v1w1 and v1w3.

Results of hardness testing shown in Figure 13 reflected a significant improvement after applying both SPD techniques, although the rate of increase was different in ECAP and HPTE. This figure shows that the maximum hardness achievable by HPTE (67 HV0.2) is 1.3 times higher than the maximum hardness measured in ECAP (51 HV0.2). However, hardness distribution in the cross section of HPTE samples is basically inhomogeneous and has a V-shape pattern. In HPTE regime v7w1, the hardness in the center (40 HV0.2) is even lower than the hardness values measured in ECAP4 sample; while in the edge zone, the hardness value reaches 51 HV0.2 and the curve coincides with ECAP4 and ECAP8 in several points.

Distribution of hardness in the sample v1w1 shows a range of variation from 47 HV0.2 in the center to 64 HV0.2 in the edge zone. This graph also coincides with the hardness-distribution graphs of ECAP4 and ECAP8 in the center zone.

Hardness distribution in v1w3 is rather homogeneous within the range of 60 to 67 HV0.2. The lowest hardness value measured in the center zone (60 HV0.2) is remarkably higher than the highest value of hardness obtained by ECAP (51 HV0.2).

It is noteworthy that the V-shape pattern of hardness distribution in HPTE processed aluminum can be observed in another study about copper [62] because of the inherent effect of torsional deformation [83]; as we will see in the following chapter, this pattern is also evident in hardness distribution of HPTE niobium samples. Due to the same reason, a similar V-shape pattern of hardness distributions can be found in earlier studies about conventional HPT processing in different materials such as aluminum [40,84–87], steel [88], and nickel [89].

A detailed observation of the hardness graph in Figure 13, implies that hardness of the samples enhanced until a certain point and then approached a saturation level. In order to identify the saturation level of hardness and correlating the strain with hardness in HPTE, strain values corresponding to each point of the graph for the processed samples in Figure 13 were plotted against hardness, and a curve fitting

procedure was employed to extrapolate the data points (see Figure 21). The fitted curve in this figure is shown as a solid line.

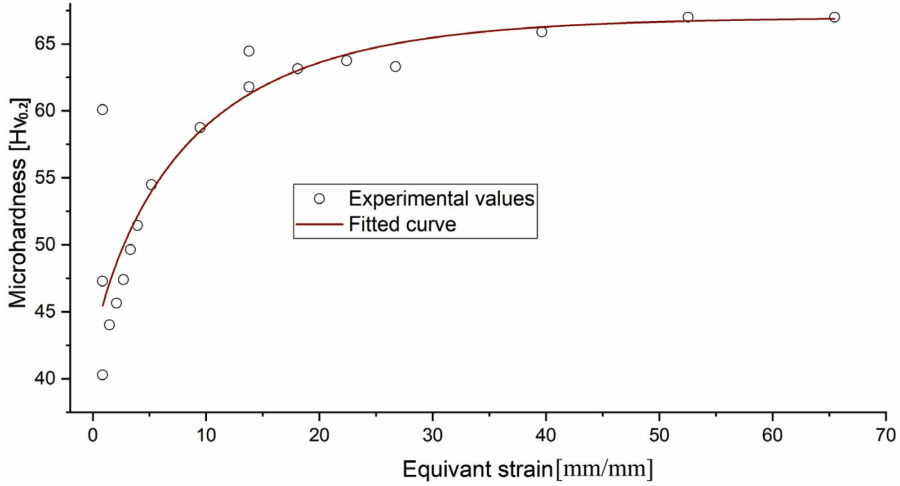


Figure 21. Microhardness vs. equivalent strain in HPTE samples.

The following non-linear regression function (Eq. 8) was implemented to identify the fitted curve [90].

$$HV_R = HV_{max} - (HV_{max} - HV_{min}) \times e^{(-a\varepsilon^b)} \quad (8)$$

where  $HV_R$  is the non-linear regression function of hardness,  $HV_{max} = 67$  HV0.2 (the maximum experimental value of hardness),  $HV_{min} = 42$  HV0.2 (the minimum experimental value of hardness); “ $a$ ” and “ $b$ ” are the fitting parameters and can be determined by minimization of the sum of squared differences of the experimental data points and the model. The algorithm of minimization is shown in Eq. 9:

$$A = \Sigma(HV_{exp} - HV_R)^2 \mid \text{Min } A \quad (9)$$

where  $HV_{exp}$  is the set of data points calculated by experiments; and  $A$  is the least possible value of sum of squared differences. Using the algorithm introduced in Eq. 9 and iterative minimization of  $A$ , “ $a$ ” and “ $b$ ” were determined as “ $a = 0.17$ ” and “ $b = 0.83$ ”.

By substituting the known parameters in Eq. 8, it can be rewritten as:

$$Hv = 67 - 25 * e^{(-0.17\varepsilon^{0.83})} \quad (10)$$

Eq. 10 represents an empirical relationship between hardness and strain in aluminum processed by HPTE, regardless of the HPTE regimes. However, some data points in this model which correspond to the central zone of the sample v1w3 showed some deviation from the curve at low values of strain (see Figure 21). This phenomenon can be explained by considering the effect of gradient plasticity. As mentioned earlier, at higher ratios of  $\omega/v$ , the plastic deformation may spread out from the surrounding areas into the central region and affects the microstructure and hardness of materials, although the nominal value of torsional strain is near to zero in the central zone. Accordingly, the hardness

values obtained from the central zone of the sample v1w3 are extraordinarily higher than expected and do not match the fitted curve [Paper I].

There are two subtle points here to notice about the saturation hardness. First, Figure 21 offers that the trend of hardness in HPTE processed aluminum approaches the saturation level of 67 HV0.2 and this level is achievable already at strain values of  $\sim 20$  mm/mm, and imposing any further strain on the material does not make any noticeable change in the hardness results.

Second, the saturation hardness in HPTE processed aluminum, which was obtained at 67 HV0.2, is significantly higher than the maximum value obtained by ECAP (51 HV0.2; see Table 6). A detailed review in the literature about the hardness evolution of commercially pure aluminum (CP-Al) in ECAP and other SPD techniques may clarify this fact. The following tables have summarized the hardness evolution of CP-Al processed by ECAP and HPT presented in the previous studies. As shown in Table 7, the maximum achievable value of hardness by ECAP barely exceeded 56 HV, while this value in the conventional HPT (Table 8) extended to the range of 62-65 HV.

This difference in hardness properties can be explained by considering the microstructural evolution of materials undergone during each process. In the present work, extreme grain refinement up to  $0.7 \mu\text{m}$  with high amounts of dislocation densities up to  $5.3 \times 10^{13}/\text{m}^2$  was achieved by HPTE whereas the maximum grain refinement in ECAP occurred at  $0.85 \mu\text{m}$  with the dislocation densities of  $2.3 \times 10^{13}/\text{m}^2$  (see Table 6). In addition, volume fraction of HAGBs in HPTE increased up to  $V_{\text{HAGB}} = 66\%$ , while microstructural studies accomplished earlier on ECAP showed lower HAGB fractions (40-58 %) and relatively larger grain size (in the range of  $1 \mu\text{m}$ ) [74,75]. Indeed, smaller grain size along with higher dislocation densities and higher fraction of HAGBs act as barriers against the dislocation movements and increase the strength of the material and thereby promising the higher hardness values in HPTE.

Table 7: Maximum hardness values obtained by ECAP and miscellaneous SPD techniques

	Material	Process	Process parameter	Number of passes	Route	Temp.	Reported hardness value [HV]	Ref.
1	AA1050	ECAP	$\phi = 110$ $\psi = 70$	8	Bc	R.T	51	Current study
2	AA1050	ECAP	$\phi = 90$ $\psi = 20$	8	Bc	R.T	54	[91]
3	AA1050	ECAP	$\phi = 90$ $\psi = 20$	8	Bc	R.T	51	[92]
4	AA1050	ECAP	$\phi = 90$ $\psi = 20$	8	Bc	Cryo T.	53	[92]
5	AA1050	ECAP	$\phi = 90$ $\psi = 20$	8	Bc	Cryo T.	54	[93]
6	AA1050	ECAP	$\phi = 90$ $\psi = 20$	6	Bc	R.T	56	[94]
7	AA1050	ECAP	$\phi = 90$ $\psi = 0$	8	Bc	R.T	60	[74]
8	Pure aluminum (99.99 wt%)	ECAP	$\phi = 90$ $\psi = 20$	8	Bc	R.T	44	[95]
9	AA1050	ECAP	$\phi = 120$ $\psi = 20$	8	A	R.T	52	[96]
10	AA1050	CEE	-	1 cycle	-	R.T	52	[60]
11	AA1050	ARB	50% reduction in each cycle	5 cycles	-	R.T	63	[97]
12	AA1050	Incremental (I-ECAP)	$\phi = 90$ -	8	Bc	R.T	59	[98]
13	AA1050	Ultrasonic-assisted ECAP	$\phi = 90$ $\psi = 3$	1	-	R.T	51	[99]
14	AA1080	Integrated ECAP and direct-Extrusion die	$\phi = 90$ $\psi = 20$ Extrusion ratio: 8	1	-	R.T	52	[100]
15	AA1070	ECAP	$\phi = 90$ $\psi = 20$	8	Bc	R.T	52	[101]
16	AA1050	Dual-Equal Channel Lateral Extrusion (DECL)	$\phi = 90$ -	6	-	R.T	55	[102]
17	AA1050	T-ECAP, Integration of ECAP and torsion	$\phi = 90$ $\psi = 36$ $\omega = 0.9$ rad/sec	1	-	R.T	50	[103]
18	AA1050	Cyclic forward-backward Extrusion (CFBE)	D=10mm d=2.5mm	No of cycles: 1	-	R.T	52	[104]
19	AA1050	Cold rolling	-	92% reduction ratio	-	R.T	52	[105]
20	AA1050	Accumulative Back Extrusion (ABE)	-	3	-	R.T	67	[106]
21	AA1050	Repetitive Tube Expansion and Shrinking (RTES)	-	One cycle	-	R.T	55	[107]

Table 8: Maximum hardness values reported in the literature about CP-aluminum processed by HPT

	Material	Process	Number of rotations [N]	Pressure [GPa]	Temperature	Reported hardness value [HV]	Ref.
1	AA1050	HPT	5 turns	6	R.T	65	[108]
2	AA1050	HPT	5 turns	6	R.T	65	[109]
3	AA1050	HPT	15 turns	1	R.T	53	[110]
4	AA1050	HPT	8 turns	1	R.T	62	[87]
5	AA1060	DHPT	5/72 turns (25 deg.)	1.33	R.T	55	[111]
6	CP-Al (99.9 wt%)	HC-HPT	1/2 turns	-	R.T	53	[112]

It should also be noticed is that according to the results obtained in this work, increasing the hardness by ECAP up to 51 HV0.2 required eight times of extrusion through the ECAP die; whereas achieving higher level of hardness (67 HV0.2) with finer grain size was readily attainable by HPTE and within one pass of extrusion. These results signify the effectiveness and time efficiency of HPTE in the improvement of hardness and grain refinement in materials.

The last point that is worth to note here is that the nominal equivalent strain in ECAP is basically constant in each pass since it only depends on the die geometrical parameters,  $\phi$  and  $\psi$  (see Eq. 3, section 2.1.3), while in HPTE, strain not only depends on the geometry but also on the process parameters of  $\nu$  and  $\omega$  (see Eq. 4, section 2.3). In other words, the main effective process parameters in ECAP are fixed after die manufacture and operator can increase the amount of strain only by increasing the pass number of ECAP whereas in HPTE, the main process parameters are changeable, and operator has this possibility to choose a wide range of strains (from 0.9 to 65 mm/mm) within one pass of HPTE.

## 5. SPD PROCESSING OF NIOBIUM

This chapter describes the experiments performed on niobium via HPTE and ECAP. The aim of this chapter, in parallel to the previous chapter, is to evaluate the effect of HPTE in comparison with ECAP, on the microstructure and hardness in a different material (niobium) with different crystal structure. Firstly, the methodology of experiments will be delineated and then, the results of experiments comprising microhardness testing and microstructural refinement will be demonstrated and discussed in detail.

### 5.1. Methodology of experiments

#### 5.1.1. Materials and characterization methods

Niobium samples with the purity of 98.5 wt.% were received in bulk shapes and then prepared for processing. Materials characterization methods for SEM, hardness testing and X-ray diffraction patterns were described earlier in section 4.1. EBSD analysis was performed by Esprit-2.1 Bruker operating at 20 kV. The EBSD image of the HPTE sample was taken from the edge zone (a distance of  $R \approx 4.5$  mm from the center).

The relative errors for the values of microhardness,  $V_{HAGB}$ , grain size, and dislocation densities were 3, 5, 5, and 15 %, respectively.

#### 5.1.2. HPTE experiments

Samples were cut and prepared in the exact dimensions described in section 4.1.2 for HPTE. Experiments were performed at room temperature for one pass of HPTE and extrusion speed of  $v=7$  mm/min and rotational speed of  $\omega=1$  rpm ( $v7w1$ ) was applied to the samples.

#### 5.1.3. ECAP experiments

ECAP processing of niobium samples was accomplished by using a modified ECAP die called Indirect-Extrusion ECAP (IE-ECAP) with the channel angle of  $\phi=90^\circ$  and corner angle of  $\psi=0^\circ$ . This technique takes advantage of indirect extrusion for extruding the samples through the die and thereby, decreasing the friction during extrusion [Paper II], [55]. IE-ECAP is useful when extruding hard materials such as tantalum particularly at higher pass numbers of extrusion [Paper II]. Figure 22 shows the sequence of extrusion through the die.

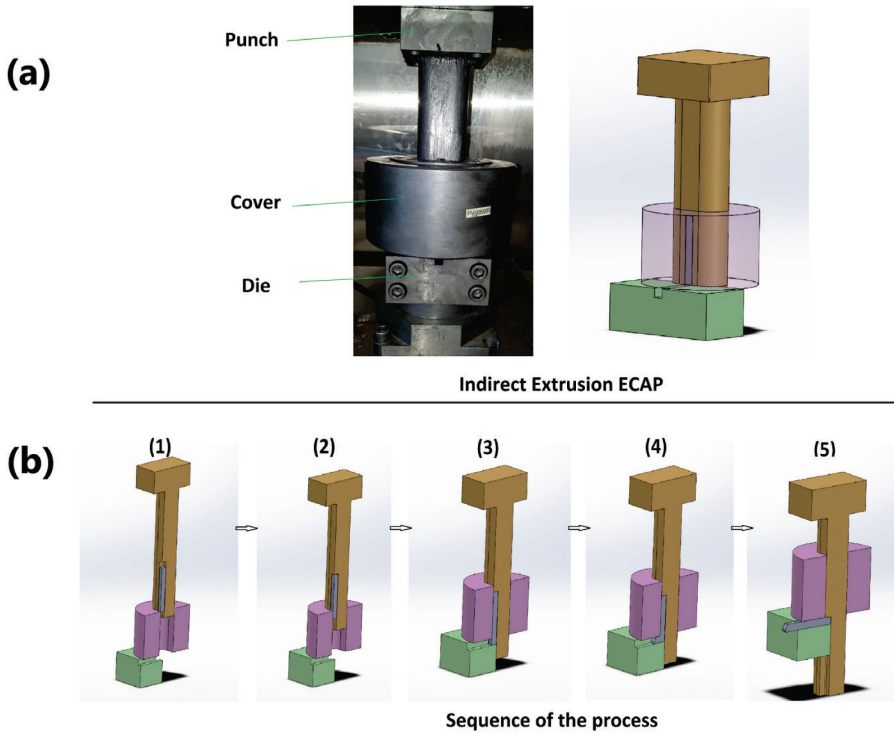


Figure 22. a) Die components of IE-ECAP in assembled configuration; b) Illustration of the progress of ECAP through the cross section of the die [Paper II].

Specimens of niobium were cut into the dimensions of 12×12×120 mm and then processed for one pass (ECAP1) and four passes (ECAP4) of ECAP using route B<sub>c</sub>.

Table 9 shows the sample IDs for HPTE and ECAP processed samples along with the corresponding equivalent-strain value in each regime.

Table 9: HPTE and ECAP regimes for niobium and corresponding equivalent strain

Sample ID	Notes	Equivalent strain [mm/mm]
As-received	Initial sample	-
ECAP1	ECAPed sample after 1 pass	1.15
ECAP4	ECAPed sample after 4 passes	4.62
HPTE	HPTE regime v7w1 - Equivalent strain at R≈4.5 mm from the center	3.9

## 5.2. Results of experiments

### 5.2.1. Microhardness evolution

Results of microhardness testing on niobium samples are presented in Figure 23. The initial hardness value of 81 HV0.2 in the as-received sample increased by 35 % in ECAP1 with an average value of 109 HV0.2 and increased by 91% in ECAP4 with an average value of 155 HV0.2. The hardness distribution in the HPTE sample showed a V-shape distribution which is in agreement with the hardness distribution in HPTE processed aluminum, as shown in section 4.2, and HPTE processed copper presented in another research study [62]. The minimum hardness-increase of 198 % was obtained in the center of the HPTE processed niobium with a value of 241 HV0.2, and the highest hardness-increase of 252 % was achieved in the edge zone with the maximum value of 285 HV0.2.

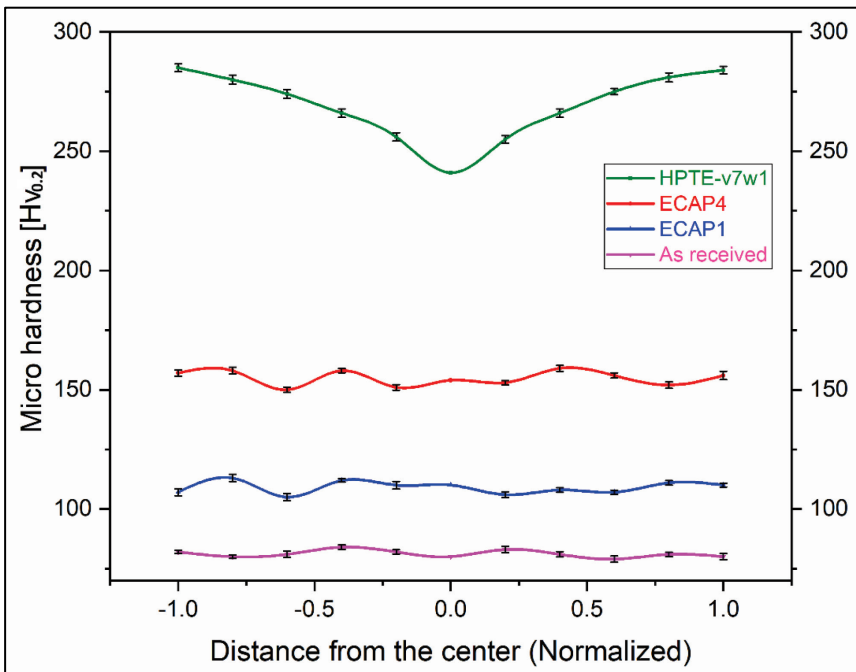


Figure 23. Microhardness distribution in niobium samples.

### 5.2.2. Microstructural refinement

Results of grain refinement can basically demonstrate the impact of SPD processing on materials. Figure 24 shows an SEM image of the niobium sample in initial conditions, before processing with an average grain size of 12.6  $\mu\text{m}$ .



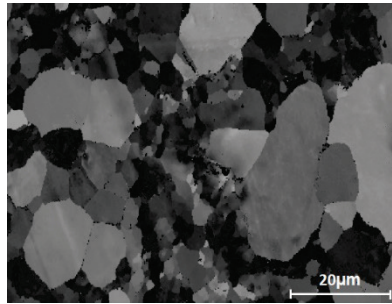


Figure 24. Microstructure of as-received niobium revealed by Backscattered-SEM.

The following figure illustrates the crystallographic orientation maps obtained by EBSD from the niobium samples after processing.

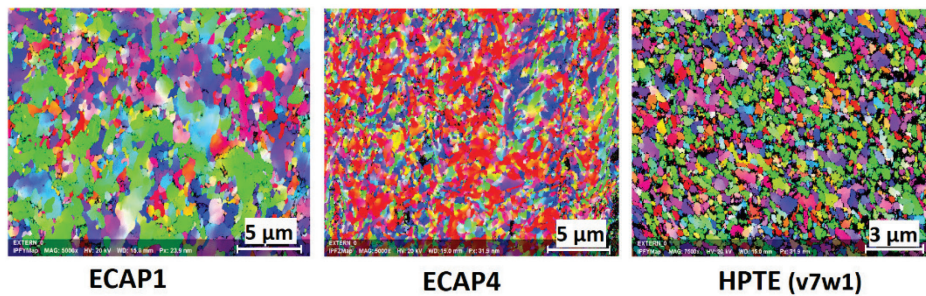


Figure 25. EBSD mapping of niobium processed by different regimes.

Statistical analysis of EBSD mapping including the grain size and misorientation-angle distributions are presented in Figure 26. According to these results, the initial grain size of 12.6  $\mu\text{m}$  decreased considerably after processing to the average grain size of 2.26  $\mu\text{m}$ , 0.67  $\mu\text{m}$ , and 0.49  $\mu\text{m}$  in ECAP1, ECAP4, and HPTE, respectively. Moreover, HAGBs in these specimens constituted a high fraction of misorientation angles ( $V_{\text{HAGB}}$ ) with the values of 76 %, 86 %, and 84 % in ECAP1, ECAP4 and HPTE, respectively.

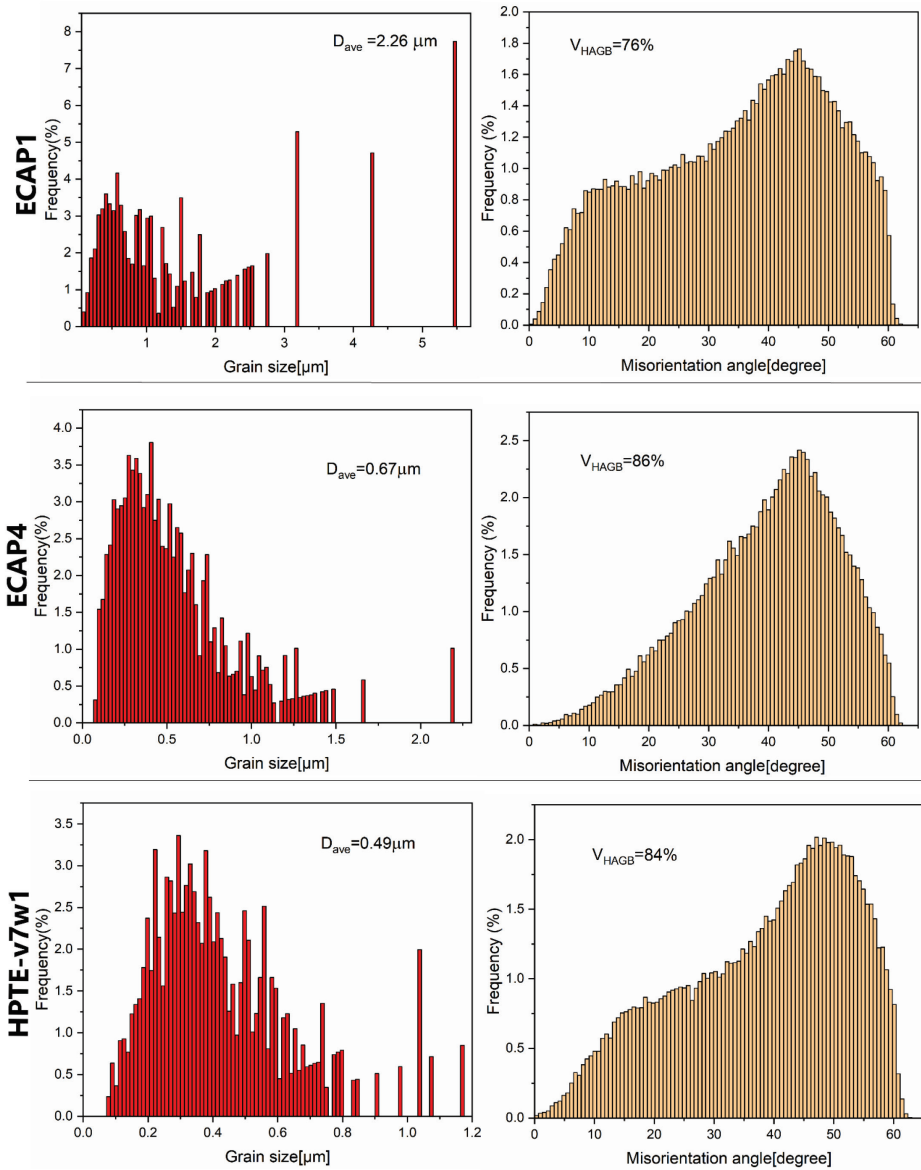


Figure 26. Distribution of grain size and misorientation angles in niobium samples; the average values of grain size ( $D_{ave}$ ) and volume fraction of HAGBs ( $V_{HAGB}$ ) are inset into the graphs.

Results of XRD patterns may also confirm the trend of microstructural refinement in the niobium samples. Figure 27 shows the results of XRD patterns where peak broadening of the patterns is evident in the processed samples.

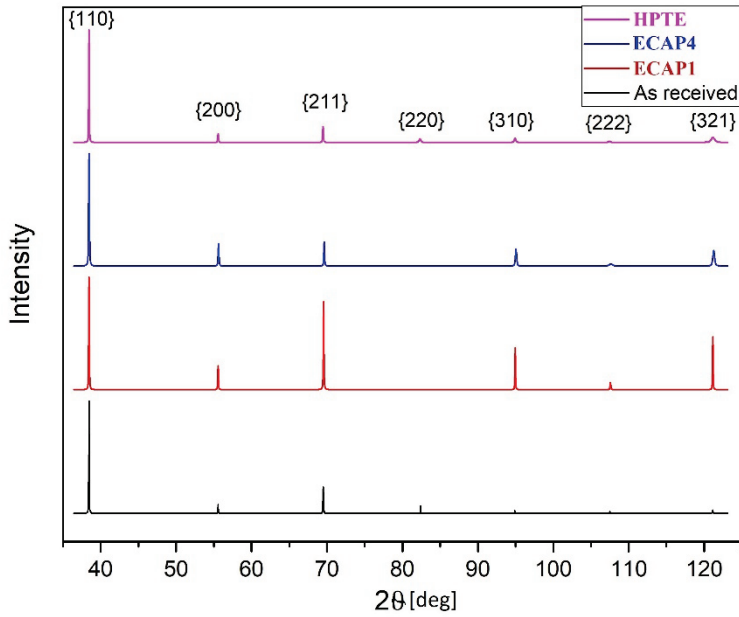


Figure 27. XRD pattern of niobium samples.

In order to quantify the dislocation densities in the samples, Williamson-Hall method was implemented as explained earlier (see Eq. 5, section 4.2.3). Dislocation density in each sample was measured using Eq. 7 (see section 4.2.3) and considering the burgers vector as  $b=0.2858$  nm in niobium [113].

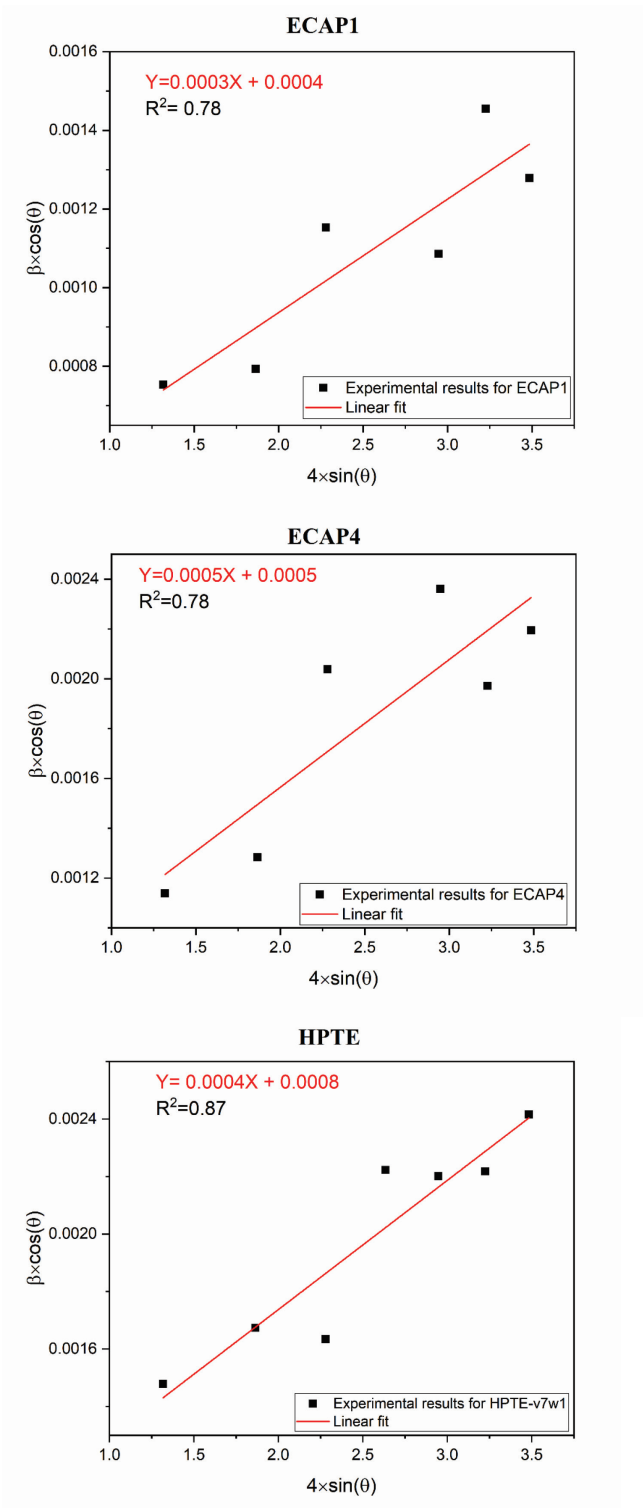


Figure 28. Williamson-Hall plots for niobium samples.

Table 10 collects the information obtained by the analysis of XRD patterns of niobium samples using Williamson-Hall plots shown in Figure 28.

Table 10: Crystallographic parameters of niobium samples obtained by Williamson-Hall method

Sample ID	Crystallite size [nm]	Lattice strain [%]	Dislocation Density [ $10^{13} m^{-2}$ ]
ECAP1	362	0.03	1.00
ECAP4	290	0.05	2.09
HPTE-v7w1	181	0.04	2.68

As it can be seen in this table, the trend of microstructural refinement in terms of crystallite size is in conformity with that of grain refinement represented in Figure 26. Moreover, the amount of dislocation density in the processed samples which is indicative of accumulation of defects in materials, clarifies the trend of hardness-increase in SPD processed niobium shown in Figure 23.

### 5.3 Discussion and interpretation of results

Table 11 summarizes the results of experiments performed on niobium. These results confirmed the effect of HPTE on grain refinement in materials. As we saw in Figure 24 and Figure 25, the initial grain size of 12.6  $\mu m$  reduced to 2.26  $\mu m$  and 0.67  $\mu m$  in ECAP1 and ECAP4 respectively; and the finest grain size was achieved in HPTE with an average value of 0.49  $\mu m$ . In a similar manner, results of XRD analysis and peak broadening of the patterns indicated the refinement of microstructure in the processed samples. Analysis of XRD patterns showed an increasing trend in the dislocation densities by imposing further strain on the materials (see Table 11).

Table 11: Results of experimental procedures on SPD processed niobium

Sample ID	Equivalent Strain [mm/mm]	Average grain size [ $\mu m$ ]	Average crystallite size [nm]	Lattice strain [%]	Dislocation density [ $10^{13}/m^2$ ]	Hardness [HV0.2]
ECAP1	1.2	2.26	362	0.03	1.0	109
ECAP4	4.6	0.67	290	0.05	2.0	155
HPTE-v7w1	3.9	0.49	181	0.04	2.7	285

It should be noticed that the ultra-fine grain size of 0.49  $\mu m$  in niobium via HPTE was achieved by one pass of extrusion, and the grain size of 0.67  $\mu m$  was obtained after 4 times of extrusion through ECAP die indicating more demands on time and effort for processing of the samples. Other studies about ECAP processing of niobium reported similar range of grain size after several passes of extrusions. An earlier study about ECAP processing of niobium with 1.4 wt% Y and 0.15 wt% of Ni showed the grain refinement of materials to an average level of 0.42  $\mu m$  after 8 passes of ECAP [Paper II]. A research

study about ECAP processing of niobium with 1 wt% of zirconium reported an average grain size of 0.40  $\mu\text{m}$  after 16 times of ECAP extrusions [114]. Another study on HPT processing of niobium showed the mean grain size of 378 nm after 10 rotations with a nominal pressure of 5.6 GPa in HPT die [115]. A comprehensive study about ECAP processing of CP-niobium up to 24 passes claimed that this material reached the saturated grain size of 300nm after 8 passes of ECAP [113]. These results show that the new technique of HPTE was successful in grain refinement of niobium and approaching the saturation level as within one pass of HPTE extrusion and applying low amounts of strains into the material, an average size of 0.49  $\mu\text{m}$  was achieved.

Results of hardness testing provided in section 5.2.1 showed the effectiveness of HPTE on increasing the strength of niobium. As it was shown in Figure 23, the hardness of materials from the initial value of 81HV0.2 increased to the average value of 109 HV0.2 in ECAP1 and to 155 HV0.2 in ECAP4, while the lowest hardness value in HPTE was measured as 241 HV0.2 in the central zone and it increased up to 285 HV0.2 in the edge zone. As expected, ECAPed samples exhibited a homogeneous distribution, and the HPTE-sample presented a V-shape distribution in hardness. The additional hardness-increase in HPTE can be explained by considering the finer size of grains in niobium as well as higher dislocation densities retained in the materials (see Table 11). As a matter of fact, decreasing the grain size in materials leads to an increase in the density of grain boundaries, and these grain boundaries along with the accumulation of dislocations pose as obstacles to dislocation slip; accordingly, materials will show more resistance to any further deformation [116].

It is also noticeable that the maximum value of hardness (285 HV0.2) which was achieved here by one pass of HPTE may require a couple of times of extrusion by ECAP to obtain a similar level of hardness. A quick review in the literature can confirm this fact. Table 12 shows the previous studies on SPD processing of niobium and the reported hardness values obtained by each process.

*Table 12: Maximum hardness values reported in the literature about SPD processed niobium*

	Material	Process	Number of passes/rotations	Pressure (in HPT) [GPa]	Temp.	Reported hardness value [HV]	Ref.
1	98.5% Nb	HPTE	1 P	-	R.T	285	Current work
2	98%Nb	ECAP	8 P	-	R.T	176	[Paper II]
3	CP Nb	HPT	10 R	5.6	R.T	256	[115]
4	CP Nb	ECAP	24 P	-	R.T	149* <sup>1</sup>	[117]
5	High-purity Nb	HPT	3 R	8	Cryo-T	490*	[118]
6	CP Nb	HPT	5 R	6	R.T	255*	[119]
7	99% Nb, 1%Zr	ECAP	8 P	-	R.T	240	[120]
8	High-Purity Nb	ECAP	8 P	-	R.T	140	[121]

1. The starred values were reported in different scales (SI units, HB, etc.) but their equivalent Vickers values are shown here for consistency of the table.

According to the table above, the range of hardness values in the SPD processed niobium is near to the range of hardness in the HPTE processed sample (from the center to edge; see Figure 23) or even lower. There is only one exception in this table where cryogenic-HPT processing of niobium resulted in the maximum hardness of 490 HV. This extraordinary increase in hardness value can be associated with processing of the material at cryogenic temperature ( $T=80$  K) which led to the presence of high density of defects and extreme grain-refinement to nanoscale (75 nm) with a non-equilibrium state in grain boundaries [118].

The results of this chapter together with the results of the previous chapter about aluminum revealed that HPTE is a powerful technique in reducing the grain size in materials to ultra-fine levels with enhanced mechanical properties. These achievements can be obtained only within one pass of HPTE implying its efficiency in labor- and time- consumption for processing of materials. On the other hand, ECAP in both cases of aluminum and niobium proved to be a promising technique in providing a homogeneous structure in materials along with some enhancement in mechanical properties.

## 6. CONCLUSION

### 6.1. Concluding remarks

This study carried out an investigation on a new technique of Severe Plastic Deformation (SPD) with the name of High Pressure Torsion Extrusion (HPTE) and compared it with ECAP which is one of the most well-known techniques in the society of SPD researchers. FEM simulations along with several experiments were performed on materials and the effect of this technique on the microstructure and hardness of materials was studied. The following outcomes can be addressed from this work:

- Simulation of the HPTE process by Finite Element Method (FEM) demonstrated a gradient distribution in strain from the center to edge in the cross section of the specimens. This distribution was in conformity with the distribution of theoretical values of strain obtained by the equation of strain in HPTE.
- It has been shown that the main process parameters in HPTE (rotational speed,  $\omega$ , and extrusion speed,  $\nu$ ) are variable and by changing these parameters, it is possible to apply a wide range of strain ( $\bar{\epsilon}= 0.9$  to 65 mm/mm) to materials just within one pass of extrusion, whereas the main process parameters in ECAP ( $\phi$  and  $\psi$  angles) depend on the die geometry and are fixed after die manufacture. However, it is possible to increase the amount of strain in ECAP by increasing the pass numbers of extrusion in order to accumulate more deformation in materials.
- Due to the nature of torsion, HPTE imposed a gradient distribution in grain refinement and hardness in the cross section of the samples along the radius, from the central axis of the billets to the edge. Microstructural analysis of the samples showed that coarse grains are located in the central zone and ultra-fine grains can be observed in the edge zone, the farthest distance from the center. It was also found that the ratio of rotational speed to extrusion speed ( $\omega/\nu$ ) can affect this gradient in microstructure from the center to edge. The higher is this ratio, the finer are the grains in the center, and consequently, the less is the variation of grain size. In fact, increasing this ratio makes the grain-size distribution more homogeneous in HPTE. This correlation between the ratio of  $\omega/\nu$  and homogeneity is also valid in the hardness distribution of HPTE samples along the radius.
- Comparison between HPTE and ECAP processing of commercially pure aluminum revealed that HPTE was able to reach the saturation level in grain refinement and hardness of materials only within one pass while ECAP was not capable of approaching this level even after eight passes of extrusion. The saturation levels of grain refinement and hardness achieved by HPTE were measured as 0.7  $\mu\text{m}$  and 67 HV0.2, respectively, whereas these values were limited to 0.9  $\mu\text{m}$  and 51 HV0.2 in ECAP after eight passes.
- Analysis of the results obtained by HPTE and ECAP processing of commercially pure niobium showed that applying nearly the same amount of strain using the two techniques, HPTE was able to achieve finer microstructure and higher hardness value in materials. The finest grain size and largest hardness value were achieved in the edge zone of HPTE sample with the values of 0.49  $\mu\text{m}$  and 285 HV0.2, respectively,



while these values were measured as 0.67  $\mu\text{m}$  and 155 HV0.2 in ECAP after four passes of extrusion.

- Results of experiments showed that ECAP fabricates Ultra-Fine Grained (UFG) materials with homogeneous structure, whereas HPTE induces inhomogeneity at the cross section of the samples due to the mechanism of torsion. On the other hand, HPTE is capable of inducing large amount of deformation in materials along with enhanced mechanical properties only in one pass; in contrast, ECAP requires a couple of times of extrusion to obtain similar properties in materials and thereby, consuming more time and labor. In the final analysis, it can be concluded that HPTE appeared to be a time-efficient technique to fabricate UFG materials with enhanced properties to be considered for industrial applications.

## 6.2. Scientific novelty

A new technique in Severe Plastic Deformations (SPD) has been studied and evaluated in different aspects. It has been proved that this technique is able to impose high amounts of strains (above 60 mm/mm) on bulk materials just in one pass. This level of deformation was heretofore achievable by the conventional method of HPT and only in thin-disk samples.

The main novelty outputs of this work can be addressed as follows:

- For the first time, the effect of HPTE process-parameters on microstructure and mechanical behavior of materials was studied.
- For the first time, a comparative analysis of ECAP and HPTE in microstructure and hardness evolution was conducted.
- A non-linear regression model was developed to predict the hardness evolution with respect to the strain in aluminum regardless of the processing regimes.
- The impact of process parameters of HPTE on materials evolution was studied, and a correlation between the ratio of rotational speed to extrusion speed ( $\omega/v$ ) and homogeneity of materials was proposed.

## 6.3. Recommendations and future plans

This study proved that HPTE made a substantial improvement in microstructural refinement and mechanical properties of materials. Compared to the conventional HPT, this new technique brings the advantage of fabricating nanostructured materials in bulk samples which makes it more suitable for practical applications. However, due to the relatively lower pressures used in this new technique ( $\approx 1$  GPa) as compared to HPT, it might be problematic to process brittle or high-strength materials [Paper I]. Nevertheless, increasing the processing temperature may reduce the flow stress in materials and help the process to overcome the lack of high working-pressure.

Processing of functional materials (such as metal hydrides for hydrogen storage or thermo-electric materials for automotive applications) is another interesting topic with great potentials for industrial applications. Although these materials have been studied and processed by HPT in the form of thin disks, fabrication of such bulk materials on a larger scale seems to be more suitable for practical applications. One part of this scheme

is under investigation to explore the influence of HPTE on metal hydrides and their absorption kinetics.

Considering the fact of gradient distribution of hardness in the cross section of HPTE processed billets, research studies about the wear and tribological properties of these materials can be stunningly attractive since the processed samples are fairly hard at the periphery of the billet whereas the core is softer. As a result, it is expected that the periphery should be wear-resistant while the core retains the ductility. This subject requires further studies as it may open up new horizons for industries to avoid extra costs for abrasion resistant coating-technologies and produce high-strength materials with considerable wear resistance on the surface and yet, ductile in the core.

## LIST OF FIGURES

Figure 1. (a) Illustration of HPT die [40]; (b) parameters of an HPT disk. ....	17
Figure 2. Illustration of ECAP [43]. ....	18
Figure 3. (a) HPTE die components; (b) Schematic illustration of HPTE die and the parameters [paper I]. ....	21
Figure 4. (A) Wireframe representation of the die demonstrating the jutting elements inside the die; (B) Cross-section of the die; (C) A piece of workpiece extracted in the middle of the process; the effect of the jutting elements can be seen on the workpiece [Paper V]. ....	22
Figure 5. Demonstration of fabricating helical architecture by HPTE; (a) sample before processing, (b) sample after processing [62]. ....	23
Figure 6. Demonstration of three different mesh sizes in simulations. ....	24
Figure 7. Mesh sensitivity diagram. ....	25
Figure 8. Illustration of stress (a), strain (b), and strain rate (c) in HPTE specimen. ....	26
Figure 9. Selection of random nodes from the cross section of the specimen. ....	27
Figure 10. Distribution of strain in the cross section of HPTE specimen; simulation vs. theory. ....	27
Figure 11. Parallel channel ECAP die. ....	30
Figure 12. Stress-strain diagram obtained from compression test. ....	31
Figure 13. a) Illustration of a specimen exposed to microhardness; b) Microhardness distribution in HPTE processed samples. ....	32
Figure 14. Microstructural observation of annealed and ECAPed aluminum. ....	33
Figure 15. EBSD mapping of HPTE processed samples. ....	34
Figure 16. Distribution of grain size (left) and grain-boundary misorientation angles (right) for the v7 $\omega$ 1 sample. ....	35
Figure 17. Distribution of grain size (left) and grain-boundary misorientation angles (right) for the v1 $\omega$ 1 sample. ....	36
Figure 18. Distribution of grain size (left) and grain-boundary misorientation angles (right) for the v1 $\omega$ 3 sample. ....	37
Figure 19. XRD patterns of processed and annealed aluminum. ....	38
Figure 20. Williamson-Hall plots obtained from XRD patterns; sample IDs are shown as insets within each graph. ....	39
Figure 21. Microhardness vs. equivalent strain in HPTE samples. ....	44
Figure 22. a) Die components of IE-ECAP in assembled configuration; b) Illustration of the progress of ECAP through the cross section of the die [Paper II]. ....	49
Figure 23. Microhardness distribution in niobium samples. ....	50
Figure 24. Microstructure of as-received niobium revealed by Backscattered-SEM. ....	51
Figure 25. EBSD mapping of niobium processed by different regimes. ....	51
Figure 26. Distribution of grain size and misorientation angles in niobium samples; the average values of grain size ( $D_{ave}$ ) and volume fraction of HAGBs ( $V_{HAGB}$ ) are inset into the graphs. ....	52
Figure 27. XRD pattern of niobium samples. ....	53
Figure 28. Williamson-Hall plots for niobium samples. ....	54

## LIST OF TABLES

Table 1: Effect of meshing procedure on extrusion force and running time for simulation .....	25
Table 2: Notation of HPTE regimes and the corresponding process parameters .....	29
Table 3: Notation of ECAP regimes and the corresponding imposed strain .....	30
Table 4: Compressive strength of HPTE processed aluminum.....	31
Table 5: Structural parameters of processed samples obtained by Williamson-Hall method.....	40
Table 6: Results of experimental procedures on SPD processed aluminum.....	41
Table 7:Maximum hardness values obtained by ECAP and miscellaneous SPD techniques	46
Table 8: Maximum hardness values reported in the literature about CP-aluminum processed by HPT .....	47
Table 9: HPTE and ECAP regimes for niobium and corresponding equivalent strain .....	49
Table 10: Crystallographic parameters of niobium samples obtained by Williamson-Hall method.....	55
Table 11: Results of experimental procedures on SPD processed niobium.....	55
Table 12:Maximum hardness values reported in the literature about SPD processed niobium .....	56

## REFERENCES

- [1] Faraji G, Kim HS. Review of principles and methods of severe plastic deformation for producing ultrafine-grained tubes. *Mater Sci Technol* 2017;33:905–23. <https://doi.org/10.1080/02670836.2016.1215064>.
- [2] Hall EO. The Deformation and Ageing of Mild Steel: III Discussion of Results. *Proc Phys Soc Sect B* 1951;64:747–53. <https://doi.org/10.1088/0370-1301/64/9/303>.
- [3] N. J. Petch. The cleavage strength of polycrystals. *J Iron Steel Inst* 1953;174:25–28.
- [4] Görtan MO. Severe plastic deformation of metallic materials by equal channel angular swaging: Theory, experiment and numerical simulation. PhD thesis, Technische Universität Darmstadt, 2014.
- [5] Sabirov I, Enikeev NA, Murashkin MY, Valiev RZ. Bulk Nanostructured Materials with Multifunctional Properties. 2015. <https://doi.org/10.1007/978-3-319-19599-5>.
- [6] Koch CC. Nanostructured Materials: An Overview. *Bulk Nanostructured Mater.*, Weinheim, Germany: Wiley-VCH Verlag GmbH & Co. KGaA; n.d., p. 1–20. <https://doi.org/10.1002/9783527626892.ch1>.
- [7] Toth LS, Gu C. Ultrafine-grain metals by severe plastic deformation. *Mater Charact* 2014;92:1–14. <https://doi.org/10.1016/j.matchar.2014.02.003>.
- [8] Huot J. Enhancing Hydrogen Storage Properties of MH:By Mechanical Deformations. Springer; 2016. <https://doi.org/10.1007/978-3-319-35107-0>.
- [9] Aliofkhaezrai M. Handbook of Mechanical Nanostructuring. vol. 1. wiley; 2015. <https://doi.org/10.1002/9783527674947>.
- [10] Estrin Y, Vinogradov A. Extreme grain refinement by severe plastic deformation: A wealth of challenging science. *Acta Mater* 2013;61:782–817. <https://doi.org/10.1016/j.actamat.2012.10.038>.
- [11] Baik SC, Estrin Y, Hellmig RJ, Kim HS. Modeling of Deformation Behavior and Texture Development in Aluminium under Equal Channel Angular Pressing. *Nanomater. by Sev. Plast. Deform.*, Wiley-VCH Verlag GmbH & Co. KGaA; 2005, p. 233–8. <https://doi.org/10.1002/3527602461.ch4c>.
- [12] Zehetbauer MJ, Zhu YT. *Bulk Nanostructured Materials*. Wiley-VCH; 2009. <https://doi.org/10.1002/9783527626892>.
- [13] Khodabakhshi F, Gerlich AP. Accumulative fold-forging (AFF) as a novel severe plastic deformation process to fabricate a high strength ultra-fine grained layered aluminum alloy structure. *Mater Charact* 2018;136:229–39. <https://doi.org/10.1016/j.matchar.2017.12.023>.
- [14] Das Bakshi S, Sinha D, Ghosh Chowdhury S. Anisotropic broadening of XRD peaks of  $\alpha'$ -Fe: Williamson-Hall and Warren-Averbach analysis using full width at half maximum (FWHM) and integral breadth (IB). *Mater Charact* 2018;142:144–53. <https://doi.org/10.1016/j.matchar.2018.05.018>.

- [15] Gashti SO, Fattah-alhosseini A, Mazaheri Y, Keshavarz MK. Microstructure, mechanical properties and electrochemical behavior of AA1050 processed by accumulative roll bonding ( ARB ). *J Alloys Compd* 2016;688:44–55. <https://doi.org/10.1016/j.jallcom.2016.07.177>.
- [16] Dutta A, Gayathri N, Neogy S, Mukherjee P. Microstructural characterisation of proton irradiated niobium using X-ray diffraction technique. *Philos Mag* 2018;98:1031–52. <https://doi.org/10.1080/14786435.2018.1425555>.
- [17] Dai W, Liang S, Luo Y, Yang Q. Effect of W powders characteristics on the Ti-rich phase and properties of W-10 wt.% Ti alloy. *Int J Refract Met Hard Mater* 2015;50:240–6. <https://doi.org/10.1016/j.ijrmhm.2015.02.003>.
- [18] Valiev RZ, Nazarov AA. *Bulk Nanostructured Materials by SPD Processing: Techniques, Microstructures and Properties*. Bulk Nanostructured Mater., Weinheim, Germany: Wiley-VCH Verlag GmbH & Co. KGaA; n.d., p. 21–48. <https://doi.org/10.1002/9783527626892.ch2>.
- [19] Zehetbauer M, Grössinger R, Krenn H, Krystian M, Pippan R, Rogl P, et al. Bulk nanostructured functional materials by severe plastic deformation. *Adv Eng Mater* 2010;12:692–700. <https://doi.org/10.1002/adem.201000119>.
- [20] Valiev RZ, Estrin Y, Horita Z, Langdon TG, Zehetbauer MJ, Zhu Y. Producing Bulk Ultrafine-Grained Materials by Severe Plastic Deformation: Ten Years Later. *JoM* 2016;68:1216–26. <https://doi.org/10.1007/s11837-016-1820-6>.
- [21] Valiev RZZ, Estrin Y, Horita Z, Langdon TGG, Zehetbauer MJJ, Zhu YTT. Fundamentals of Superior Properties in Bulk NanoSPD Materials. *Mater Res Lett* 2015;3831:1–21. <https://doi.org/10.1080/21663831.2015.1060543>.
- [22] Rosochowski A. *Severe Plastic Deformation Technology*. vol. 38. Whittles Publishing; 2017. <https://doi.org/10.1016/j.jallcom.2003.10.065>.
- [23] Liddicoat P V., Liao X-Z, Zhao Y, Zhu Y, Murashkin MY, Lavernia EJ, et al. Nanostructural hierarchy increases the strength of aluminium alloys. *Nat Commun* 2010;1:1–7. <https://doi.org/10.1038/ncomms1062>.
- [24] Langdon TG. Twenty-five years of ultrafine-grained materials: Achieving exceptional properties through grain refinement. *Acta Mater* 2013;61:7035–59. <https://doi.org/10.1016/j.actamat.2013.08.018>.
- [25] Zhu YT, Liao XZ, Wu XL. Deformation twinning in nanocrystalline materials. *Prog Mater Sci* 2012;57:1–62. <https://doi.org/10.1016/J.PMATSCI.2011.05.001>.
- [26] Zhao Y, Zhu Y, Lavernia EJ. Strategies for Improving Tensile Ductility of Bulk Nanostructured Materials. *Adv Eng Mater* 2010;12:769–78. <https://doi.org/10.1002/adem.200900335>.
- [27] Valiev RZ, Enikeev NA, Murashkin MY, Kazykhanov VU, Sauvage X. On the origin of the extremely high strength of ultrafine-grained Al alloys produced by severe plastic deformation. *Scr Mater* 2010;63:949–52. <https://doi.org/10.1016/J.SCRIPTAMAT.2010.07.014>.

- [28] Jafari M, Enayati MH, Abbasi MH, Karimzadeh F. Compressive and wear behaviors of bulk nanostructured Al2024 alloy. *Mater Des* 2010;31:663–9. <https://doi.org/10.1016/J.MATDES.2009.08.020>.
- [29] Wang CT, Gao N, Wood RJK, Langdon TG. Wear behavior of an aluminum alloy processed by equal-channel angular pressing. *J Mater Sci* 2011;46:123–30. <https://doi.org/10.1007/s10853-010-4862-0>.
- [30] Valiev RZ, Langdon TG. Achieving Exceptional Grain Refinement through Severe Plastic Deformation: New Approaches for Improving the Processing Technology. *Metall Mater Trans A* 2011;42:2942–51. <https://doi.org/10.1007/s11661-010-0556-0>.
- [31] Lowe TC, Zhu YT. Commercialization of nanostructured metals produced by severe plastic deformation processing. *Adv Eng Mater* 2003;5:373–8. <https://doi.org/10.1002/adem.200310076>.
- [32] Langdon TG. Seventy-five years of superplasticity: historic developments and new opportunities. *J Mater Sci* 2009;44:5998–6010. <https://doi.org/10.1007/s10853-009-3780-5>.
- [33] Barkhordarian G, Klassen T, Bormann R. Effect of Nb2O5 content on hydrogen reaction kinetics of Mg. *J Alloys Compd* 2004;364:242–6. [https://doi.org/10.1016/S0925-8388\(03\)00530-9](https://doi.org/10.1016/S0925-8388(03)00530-9).
- [34] Mishnaevsky L, Levashov E, Valiev RZ, Segurado J, Sabirov I, Enikeev N, et al. Nanostructured titanium-based materials for medical implants: Modeling and development. *Mater Sci Eng R Reports* 2014;81:1–19. <https://doi.org/10.1016/J.MSER.2014.04.002>.
- [35] Gendelman OV, Shapiro M, Estrin Y, Hellmig RJ, Lekhtmakher S. Grain size distribution and heat conductivity of copper processed by equal channel angular pressing. *Mater Sci Eng A* 2006;434:88–94. <https://doi.org/10.1016/J.MSEA.2006.06.091>.
- [36] Rogl G, Setman D, Schafner E, Horáky J, Kerber M, Zehetbauer M, et al. High-pressure torsion, a new processing route for thermoelectrics of high ZTs by means of severe plastic deformation. *Acta Mater* 2012;60:2146–57. <https://doi.org/10.1016/J.ACTAMAT.2011.12.023>.
- [37] Rogl G, Rogl P, Bauer E, Zehetbauer M. Severe Plastic Deformation, A Tool to Enhance Thermoelectric Performance. *Thermoelectr. Nanomater.*, Springer, Berlin, Heidelberg; 2013, p. 193–254. [https://doi.org/10.1007/978-3-642-37537-8\\_10](https://doi.org/10.1007/978-3-642-37537-8_10).
- [38] Bridgman PW. On Torsion Combined with Compression. *J Appl Phys* 1943;14:273–83. <https://doi.org/10.1063/1.1714987>.
- [39] ZHILYAEV A, LANGDON T. Using high-pressure torsion for metal processing: Fundamentals and applications. *Prog Mater Sci* 2008;53:893–979. <https://doi.org/10.1016/j.pmatsci.2008.03.002>.

- [40] Xu C, Horita Z, Langdon TG. The evolution of homogeneity in an aluminum alloy processed using high-pressure torsion. *Acta Mater* 2008;56:5168–76. <https://doi.org/10.1016/J.ACTAMAT.2008.06.036>.
- [41] Segal V, Reznikov V, Drobysheskiy A, Kopylov V. Plastic working of metals by simple shear. *Russ Metall* 1981:99–105.
- [42] Rosochowski A, Olejnik L, Richert M. 3D-ECAP of Square Aluminium Billets. *Adv. Methods Mater. Form.*, Berlin, Heidelberg: Springer Berlin Heidelberg; 2007, p. 215–32. [https://doi.org/10.1007/3-540-69845-0\\_13](https://doi.org/10.1007/3-540-69845-0_13).
- [43] Huang Y, Langdon TG. Advances in ultrafine-grained materials. *Mater Today* 2013;16:85–93. <https://doi.org/10.1016/j.mattod.2013.03.004>.
- [44] Valiev RZ, Langdon TG. Principles of equal-channel angular pressing as a processing tool for grain refinement. *Prog Mater Sci* 2006;51:881–981. <https://doi.org/10.1016/j.pmatsci.2006.02.003>.
- [45] Richert J, Richert M. A new method for unlimited deformation of metals and alloys. *Aluminium* 1986;62:604–7.
- [46] Saito Y, Utsunomiya H, Tsuji N, Sakai T. Novel ultra-high straining process for bulk materials—development of the accumulative roll-bonding (ARB) process. *Acta Mater* 1999;47:579–83. [https://doi.org/10.1016/S1359-6454\(98\)00365-6](https://doi.org/10.1016/S1359-6454(98)00365-6).
- [47] Huang J, Zhu YT, Alexander DJ, Liao X, Lowe TC, Asaro RJ. Development of repetitive corrugation and straightening. *Mater Sci Eng A* 2004;371:35–9. [https://doi.org/10.1016/S0921-5093\(03\)00114-X](https://doi.org/10.1016/S0921-5093(03)00114-X).
- [48] Beygelzimer Y, Varyukhin V, Synkov S, Orlov D. Useful properties of twist extrusion. *Mater Sci Eng A* 2009;503:14–7. <https://doi.org/10.1016/J.MSEA.2007.12.055>.
- [49] Nishida Y, Arima H, Kim J-C, Ando T. Rotary-die equal-channel angular pressing of an Al – 7 mass% Si – 0.35 mass% Mg alloy. *Scr Mater* 2001;45:261–6. [https://doi.org/10.1016/S1359-6462\(01\)00985-X](https://doi.org/10.1016/S1359-6462(01)00985-X).
- [50] Ma A, Nishida Y, Suzuki K, Shigematsu I, Saito N. Characteristics of plastic deformation by rotary-die equal-channel angular pressing. *Scr Mater* 2005;52:433–7. <https://doi.org/10.1016/j.scriptamat.2004.11.014>.
- [51] Nakashima K, Horita Z, Nemoto M, Langdon TG. Development of a multi-pass facility for equal-channel angular pressing to high total strains. *Mater Sci Eng A* 2000;281:82–7. [https://doi.org/10.1016/S0921-5093\(99\)00744-3](https://doi.org/10.1016/S0921-5093(99)00744-3).
- [52] Raab GI. Plastic flow at equal channel angular processing in parallel channels. *Mater Sci Eng A* 2005;410–411:230–3. <https://doi.org/10.1016/j.msea.2005.08.089>.
- [53] Raab GJ, Valiev RZ, Lowe TC, Zhu YT. Continuous processing of ultrafine grained Al by ECAP–Conform. *Mater Sci Eng A* 2004;382:30–4. <https://doi.org/10.1016/j.msea.2004.04.021>.



- [54] Görtan MO, Groche P. Tool design guidelines for the equal channel angular swaging (ECAS) process. *J Mater Process Technol* 2014;214:2220–32. <https://doi.org/10.1016/j.jmatprotec.2014.04.023>.
- [55] Kommel L, Shahreza BO, Mikli V. Microstructure and physical-mechanical properties evolution of pure tantalum processed with hard cyclic viscoplastic deformation. *Int J Refract Met Hard Mater* 2019;83:104983. <https://doi.org/10.1016/j.IJRMHM.2019.104983>.
- [56] Edalati K, Horita Z. Scaling-Up of High Pressure Torsion Using Ring Shape. *Mater Trans* 2009;50:92–5. <https://doi.org/10.2320/matertrans.MD200822>.
- [57] Toth L, ARZAGHI M, FUNDENBERGER J, BEAUSIR B, BOUAZIZ O, ARRUFFATMASSION R. Severe plastic deformation of metals by high-pressure tube twisting. *Scr Mater* 2009;60:175–7. <https://doi.org/10.1016/j.scriptamat.2008.09.029>.
- [58] Edalati K, Lee S, Horita Z. Continuous high-pressure torsion using wires. *J Mater Sci* 2012;47:473–8. <https://doi.org/10.1007/s10853-011-5822-z>.
- [59] Hohenwarter A. Incremental high pressure torsion as a novel severe plastic deformation process: Processing features and application to copper. *Mater Sci Eng A* 2015;626:80–5. <https://doi.org/10.1016/j.msea.2014.12.041>.
- [60] Pardis N, Talebanpour B, Ebrahimi R, Zomorodian S. Cyclic expansion-extrusion (CEE): A modified counterpart of cyclic extrusion-compression (CEC). *Mater Sci Eng A* 2011;528:7537–40. <https://doi.org/10.1016/j.msea.2011.06.059>.
- [61] Pardis N, Chen C, Ebrahimi R, Toth LS, Gu CF, Beausir B, et al. Microstructure, texture and mechanical properties of cyclic expansion–extrusion deformed pure copper. *Mater Sci Eng A* 2015;628:423–32. <https://doi.org/10.1016/j.msea.2015.01.003>.
- [62] Ivanisenko Y, Kulagin R, Fedorov V, Mazilkin A, Scherer T, Baretzky B, et al. High Pressure Torsion Extrusion as a new severe plastic deformation process. *Mater Sci Eng A* 2016;664:247–56. <https://doi.org/10.1016/j.msea.2016.04.008>.
- [63] Guo L, Xiang J, Latham J-P, Izzuddin B. A numerical investigation of mesh sensitivity for a new three-dimensional fracture model within the combined finite-discrete element method. *Eng Fract Mech* 2016;151:70–91. <https://doi.org/10.1016/J.ENGFRACMECH.2015.11.006>.
- [64] Williamson G., Hall W. X-ray line broadening from filed aluminium and wolfram. *Acta Metall* 1953;1:22–31. [https://doi.org/10.1016/0001-6160\(53\)90006-6](https://doi.org/10.1016/0001-6160(53)90006-6).
- [65] ASTM. Standard Test Methods of Compression Testing of Metallic Materials at Room Temperature. 1990 Annu B ASTM Stand 1990;E9:98–105.
- [66] Zhu Z, Han J, Gao C, Liu M, Song J, Wang Z, et al. Microstructures and mechanical properties of Al-Li 2198-T8 alloys processed by two different severe plastic deformation methods: A comparative study. *Mater Sci Eng A* 2017;681:65–73. <https://doi.org/10.1016/j.msea.2016.10.108>.

- [67] Patra A, Saxena R, Karak SK. Combined effect of Ni and nano-Y<sub>2</sub>O<sub>3</sub> addition on microstructure, mechanical and high temperature behavior of mechanically alloyed W-Mo. *Int J Refract Met Hard Mater* 2016;60:131–46. <https://doi.org/10.1016/j.ijrmhm.2016.07.017>.
- [68] Li P, Lin Q, Wang X, Tian Y, Xue KM. Recrystallization behavior of pure molybdenum powder processed by high-pressure torsion. *Int J Refract Met Hard Mater* 2018;72:367–72. <https://doi.org/10.1016/j.ijrmhm.2018.01.002>.
- [69] Yogamalar R, Srinivasan R, Vinu A, Ariga K, Bose AC. X-ray peak broadening analysis in ZnO nanoparticles. *Solid State Commun* 2009;149:1919–23. <https://doi.org/10.1016/j.ssc.2009.07.043>.
- [70] Tański T, Snopiński P, Prusik K, Sroka M. The effects of room temperature ECAP and subsequent aging on the structure and properties of the Al-3%Mg aluminium alloy. *Mater Charact* 2017;133:185–95. <https://doi.org/10.1016/j.matchar.2017.09.039>.
- [71] Slama C, Abdellaoui M, Boulaares MD. Microstructure characterization of nanocrystalline (Ti<sub>0.9</sub>W<sub>0.1</sub>)C prepared by mechanical alloying. *Int J Refract Met Hard Mater* 2016;54:270–8. <https://doi.org/10.1016/j.ijrmhm.2015.07.018>.
- [72] Liu MP, Roven HJ, Murashkin MY, Valiev RZ, Kilmametov A, Zhang Z, et al. Structure and mechanical properties of nanostructured Al–Mg alloys processed by severe plastic deformation. *J Mater Sci* 2013;48:4681–8. <https://doi.org/10.1007/s10853-012-7133-4>.
- [73] Estrin Y, Molotnikov A, Davies CHJ, Lapovok R. Strain gradient plasticity modelling of high-pressure torsion. *J Mech Phys Solids* 2008;56:1186–202. <https://doi.org/10.1016/J.JMPS.2007.10.004>.
- [74] El-Danaf EA, Soliman MS, Almajid AA, El-Rayes MM. Enhancement of mechanical properties and grain size refinement of commercial purity aluminum 1050 processed by ECAP. *Mater Sci Eng A* 2007;458:226–34. <https://doi.org/10.1016/J.MSEA.2006.12.077>.
- [75] Cao Y, He L, Zhou Y, Wang P, Cui J. Contributions to yield strength in an ultrafine grained 1050 aluminum alloy after DC current annealing. *Mater Sci Eng A* 2016;674:193–202. <https://doi.org/10.1016/J.MSEA.2016.06.084>.
- [76] Naderi M, Peterlechner M, Divinski S V., Wilde G. The effect of pre-annealing on defects, microstructure and recrystallization of ultra-fine grained Al produced by high-pressure torsion. *Mater Sci Eng A* 2017;708:171–80. <https://doi.org/10.1016/J.MSEA.2017.09.126>.
- [77] Pippan R, Wetscher F, Hafok M, Vorhauer A, Sabirov I. The Limits of Refinement by Severe Plastic Deformation. *Adv Eng Mater* 2006;8:1046–56. <https://doi.org/10.1002/adem.200600133>.
- [78] Wang YB, Ho JC, Liao XZ, Li HQ, Ringer SP, Zhu YT. Mechanism of grain growth during severe plastic deformation of a nanocrystalline Ni-Fe alloy. *Appl Phys Lett* 2009;94. <https://doi.org/10.1063/1.3065025>.

- [79] Ungár T, Balogh L, Zhu YT, Horita Z, Xu C, Langdon TG. Using X-ray microdiffraction to determine grain sizes at selected positions in disks processed by high-pressure torsion. *Mater Sci Eng A* 2007;444:153–6. <https://doi.org/10.1016/j.msea.2006.08.059>.
- [80] Satyala N, Norouzzadeh P, Vashaee D. *Nano Bulk Thermoelectrics: Concepts, Techniques, and Modeling*. *Nanoscale Thermoelectr.*, Springer, Cham; 2013, p. 141–83. [https://doi.org/10.1007/978-3-319-02012-9\\_4](https://doi.org/10.1007/978-3-319-02012-9_4).
- [81] Cesario Asselli AA, Bourbeau Hébert N, Huot J. The role of morphology and severe plastic deformation on the hydrogen storage properties of magnesium. *Int J Hydrogen Energy* 2014;39:12778–83. <https://doi.org/10.1016/j.ijhydene.2014.06.042>.
- [82] Hoseini M, Shahryari A, Omanovic S, Szpunar JA. Comparative effect of grain size and texture on the corrosion behaviour of commercially pure titanium processed by equal channel angular pressing. *Corros Sci* 2009;51:3064–7. <https://doi.org/10.1016/J.CORSCI.2009.08.017>.
- [83] Kulagin R, Beygelzimer Y, Estrin Y, Ivanisenko Y, Baretzky B, Hahn HA. Mathematical Model of Deformation under High Pressure Torsion Extrusion. *Metals (Basel)* 2019;9:306. <https://doi.org/10.3390/met9030306>.
- [84] Sabbaghianrad S, Wongsan-Ngam J, Kawasaki M, Langdon TG. An examination of the saturation microstructures achieved in ultrafine-grained metals processed by high-pressure torsion. *J Mater Res Technol* 2014;3:319–26. <https://doi.org/10.1016/J.JMRT.2014.10.002>.
- [85] Sabbaghianrad S, Langdon TG. An evaluation of the saturation hardness in an ultrafine-grained aluminum 7075 alloy processed using different techniques. *J Mater Sci* 2015;50:4357–65. <https://doi.org/10.1007/s10853-015-8989-x>.
- [86] Bazarnik P, Huang Y, Lewandowska M, Langdon TG. Structural impact on the Hall–Petch relationship in an Al–5Mg alloy processed by high-pressure torsion. *Mater Sci Eng A* 2015;626:9–15. <https://doi.org/10.1016/J.MSEA.2014.12.027>.
- [87] Zhilyaev AP, Oh-ishi K, Langdon TG, McNelley TR. Microstructural evolution in commercial purity aluminum during high-pressure torsion. *Mater Sci Eng A* 2005;410–411:277–80. <https://doi.org/10.1016/j.msea.2005.08.044>.
- [88] Song Y, Wang W, Gao D, Kim H-S, Yoon E-Y, Lee D-J, et al. Inhomogeneous Hardness Distribution of High Pressure Torsion Processed IF Steel Disks. *Mater Sci Appl* 2012;3:234–9. <https://doi.org/10.4236/msa.2012.34034>.
- [89] Rathmayr GB, Pippan R. Influence of impurities and deformation temperature on the saturation microstructure and ductility of HPT-deformed nickel. *Acta Mater* 2011;59:7228–40. <https://doi.org/10.1016/J.ACTAMAT.2011.08.023>.
- [90] Fu J, Barlat F, Kim J-H, Pierron F. Identification of nonlinear kinematic hardening constitutive model parameters using the virtual fields method for advanced high strength steels. *Int J Solids Struct* 2016;102–103:30–43. <https://doi.org/10.1016/J.IJSOLSTR.2016.10.020>.

- [91] Koprowski P, Bogucki R, Bieda M, Kawałko J, Sztwiertnia K. Thermal Stability of AA1050 Aluminum Alloy after Equal Channel Angular Pressing. *Arch Metall Mater* 2017;62:777–86. <https://doi.org/10.1515/amm-2017-0116>.
- [92] Su LH, Lu C, He LZ, Zhang LC, Guagliardo P, Tieu AK, et al. Study of vacancy-type defects by positron annihilation in ultrafine-grained aluminum severely deformed at room and cryogenic temperatures. *Acta Mater* 2012;60:4218–28. <https://doi.org/10.1016/j.actamat.2012.04.003>.
- [93] Chen Y, Li Y, He L, Lu C, Ding H, Li Q. The influence of cryoECAP on microstructure and property of commercial pure aluminum. *Mater Lett* 2008;62:2821–4. <https://doi.org/10.1016/j.matlet.2008.01.091>.
- [94] Alhajeri SN, Gao N, Langdon TG. Hardness homogeneity on longitudinal and transverse sections of an aluminum alloy processed by ECAP. *Mater Sci Eng A* 2011;528:3833–40. <https://doi.org/10.1016/j.msea.2011.01.074>.
- [95] Xu C, Langdon TG. The development of hardness homogeneity in aluminum and an aluminum alloy processed by ECAP. *J Mater Sci* 2007;42:1542–50. <https://doi.org/10.1007/s10853-006-0899-5>.
- [96] Vega MCV, Bolmaro RE, Ferrante M, Sordi VL, Kliuga AM. The influence of deformation path on strain characteristics of AA1050 aluminium processed by equal-channel angular pressing followed by rolling. *Mater Sci Eng A* 2015;646:154–62. <https://doi.org/10.1016/j.msea.2015.07.083>.
- [97] Su L, Lu C, Li H, Deng G, Tieu K. Investigation of ultrafine grained AA1050 fabricated by accumulative roll bonding. *Mater Sci Eng A* 2014;614:148–55. <https://doi.org/10.1016/J.MSEA.2014.07.032>.
- [98] Salamati M, Tamimi S, Moturu S, Sivaswamy G, Qarni M, Rosochowski A. Microstructure and mechanical properties of Al-1050 during incremental ECAP. *IOP Conf Ser Mater Sci Eng* 2017;194:012009. <https://doi.org/10.1088/1757-899X/194/1/012009>.
- [99] Bagherzadeh S, Abrinia K, Han Q. Ultrasonic assisted equal channel angular extrusion (UAE) as a novel hybrid method for continuous production of ultra-fine grained metals. *Mater Lett* 2016;169:90–4. <https://doi.org/10.1016/j.matlet.2016.01.095>.
- [100] Abd El Aal MI, Yong Um H, Yoo Yoon E, Seop Kim H. Microstructure evolution and mechanical properties of pure aluminum deformed by equal channel angular pressing and direct extrusion in one step through an integrated die. *Mater Sci Eng A* 2015;625:252–63. <https://doi.org/10.1016/j.msea.2014.11.089>.
- [101] Tolaminejad B, Dehghani K. Microstructural characterization and mechanical properties of nanostructured AA1070 aluminum after equal channel angular extrusion. *Mater Des* 2012;34:285–92. <https://doi.org/10.1016/j.matdes.2011.08.003>.

- [102] Talebanpour B, Ebrahimi R, Janghorban K. Microstructural and mechanical properties of commercially pure aluminum subjected to Dual Equal Channel Lateral Extrusion. *Mater Sci Eng A* 2009;527:141–5. <https://doi.org/10.1016/j.msea.2009.07.040>.
- [103] Mani B, Jahedi M, Paydar MH. A modification on ECAP process by incorporating torsional deformation. *Mater Sci Eng A* 2011;528:4159–65. <https://doi.org/10.1016/j.msea.2011.02.015>.
- [104] Alihosseini H, Asle Zaeem M, Dehghani K. A cyclic forward-backward extrusion process as a novel severe plastic deformation for production of ultrafine grains materials. *Mater Lett* 2012;68:204–8. <https://doi.org/10.1016/j.matlet.2011.10.037>.
- [105] Lee JC, Seok HK, Suh JY. Microstructural evolutions of the Al strip prepared by cold rolling and continuous equal channel angular pressing. *Acta Mater* 2002;50:4005–19. [https://doi.org/10.1016/S1359-6454\(02\)00200-8](https://doi.org/10.1016/S1359-6454(02)00200-8).
- [106] Alihosseini H, Faraji G, Dizaji AF, Dehghani K. Characterization of ultra-fine grained aluminum produced by accumulative back extrusion (ABE). *Mater Charact* 2012;68:14–21. <https://doi.org/10.1016/j.matchar.2012.03.004>.
- [107] Jafarzadeh H, Abrinia K. Fabrication of ultra-fine grained aluminium tubes by RTES technique. *Mater Charact* 2015;102:1–8. <https://doi.org/10.1016/j.matchar.2014.12.025>.
- [108] Kawasaki M, Alhajeri SN, Xu C, Langdon TG. The development of hardness homogeneity in pure aluminum and aluminum alloy disks processed by high-pressure torsion. *Mater Sci Eng A* 2011;529:345–51. <https://doi.org/10.1016/j.msea.2011.09.039>.
- [109] Kawasaki M, Lee HJ, Ahn B, Zhilyaev AP, Langdon TG. Evolution of hardness in ultrafine-grained metals processed by high-pressure torsion. *J Mater Res Technol* 2014;3:311–8. <https://doi.org/10.1016/j.jmrt.2014.06.002>.
- [110] Ito Y, Edalati K, Horita Z. High-pressure torsion of aluminum with ultrahigh purity (99.9999%) and occurrence of inverse Hall-Petch relationship. *Mater Sci Eng A* 2017;679:428–34. <https://doi.org/10.1016/j.msea.2016.10.066>.
- [111] Lanjewar H, Kestens L, Verleysen P. A novel method for severe plastic deformation at high strain rate. *EPJ Web Conf* 2018;183:03008. <https://doi.org/10.1051/epjconf/201818303008>.
- [112] Guo J, Zhang X, Kong D, Joo SH, Kim W, Kim HS, et al. Microstructure, Micro-Hardness, and Corrosion Resistance of Commercial Purity Al Processed by Hollow-Cone High-Pressure Torsion. *Adv Eng Mater* 2019;21:1–7. <https://doi.org/10.1002/adem.201800905>.
- [113] Pan Z, Xu F, Mathaudhu SN, Kecskes LJ, Yin WH, Zhang XY, et al. Microstructural evolution and mechanical properties of niobium processed by equal channel angular extrusion up to 24 passes. *Acta Mater* 2012;60:2310–23. <https://doi.org/10.1016/j.actamat.2011.12.019>.

- [114] Niendorf T, Canadinc D, Maier HJ, Karaman I, Yapici GG. Microstructure–mechanical property relationships in ultrafine-grained NbZr. *Acta Mater* 2007;55:6596–605. <https://doi.org/10.1016/J.ACTAMAT.2007.08.015>.
- [115] Hohenwarter A, Wurster S, Völker B. Fracture of severely plastically deformed Ta and Nb. *Int J Refract Met Hard Mater* 2017;64:143–50. <https://doi.org/10.1016/j.ijrmhm.2016.12.009>.
- [116] Cao Y, Ni S, Liao X, Song M, Zhu Y. Structural evolutions of metallic materials processed by severe plastic deformation. *Mater Sci Eng R Reports* 2018;133:1–59. <https://doi.org/10.1016/j.mser.2018.06.001>.
- [117] Mathaudhu SN, Blum S, Barber RE, Hartwig KT. Severe plastic deformation of bulk Nb for Nb3Sn superconductors. *IEEE Trans. Appl. Supercond.*, vol. 15, 2005, p. 3438–41. <https://doi.org/10.1109/TASC.2005.849044>.
- [118] Popov VV, Popova EN, Stolbovskiy AV, Pilyugin VP. Thermal stability of nanocrystalline structure in niobium processed by high pressure torsion at cryogenic temperatures. *Mater Sci Eng A* 2011;528:1491–6. <https://doi.org/10.1016/J.MSEA.2010.10.052>.
- [119] Guo YZ, Behm NA, Ligda JP, Li YL, Pan Z, Horita Z, et al. Critical issues related to instrumented indentation on non-uniform materials: Application to niobium subjected to high pressure torsion. *Mater Sci Eng A* 2013;586:149–59. <https://doi.org/10.1016/J.MSEA.2013.08.015>.
- [120] Rubitschek F, Niendorf T, Karaman I, Maier HJ. Microstructural stability of ultrafine-grained niobium–zirconium alloy at elevated temperatures. *J Alloys Compd* 2012;517:61–8. <https://doi.org/10.1016/J.JALLCOM.2011.11.150>.
- [121] Sandim HRZ, Bernardi HH, Verlinden B, Raabe D. Equal channel angular extrusion of niobium single crystals. *Mater Sci Eng A* 2007;467:44–52. <https://doi.org/10.1016/J.MSEA.2007.02.086>.

## **ACKNOWLEDGEMENT**

This work was mainly accomplished at the Institute of Nano-technology in Karlsruhe Institute of Technology (KIT)-Germany and in part in Tallinn University of Technology (TalTech)-Estonia.

Firstly, I would like to express my sincere gratitude towards my supervisors, Dr Lembit Kommel from Tallinn University of Technology and Dr Julia Ivanisenko from Karlsruhe Institute of Technology for their support, patience and tolerance.

I am truly thankful to professor Fjodor Sergejev for his valuable pieces of advice on my PhD career.

I would like to extend my sincere thanks to Professor Jeno Gubicza from Hungary and Professor Edgar Garcia from Mexico for their valuable and insightful comments.

Finally, I would like to express my deep gratitude towards my parents for their love, support, and patience, without whom I would not have been able to deal with the hardships in my life.

Financial support for this project was sponsored in part by Archimedes Foundation-Estonia, and in part by Deutscher Akademischer Austauschdienst (DAAD)-Germany.

Babak Omranpour

Tallinn, 01.09.2019

## ABSTRACT

### Severe Plastic Deformation of Metals by Using High Pressure Torsion Extrusion

This doctoral thesis presents a study on evaluation of a new technique in Severe Plastic Deformations namely High Pressure Torsion Extrusion (HPTE) and investigates the impact of its process parameters on the microstructure and mechanical properties of materials. Two types of metals, aluminum and niobium with fcc and bcc crystal structures were employed for processing in this study. In order to better understand the effectiveness of this technique, some experiments were performed on materials by using ECAP, and the results were compared with each other. HPTE takes advantage of the combination of the conventional method of HPT and extrusion. HPT as a famous SPD method for enhancing the microstructure and mechanical properties of materials, imposes the restriction on the thickness of the samples (maximum thickness of 1-2 mm); whereas the new technique fabricates bulk ultrafine-Grained (UFG) materials with similar attractive mechanical properties in cylindrical shapes.

Due to the nature of torsional deformation applied by HPTE, there is a gradient distribution in the strain imposed on the cross-section of the samples, increasing from the central axis of the billet to the edge. This strain may vary in a wide range from 0.9 to 65.5 mm/mm depending on the process parameters. Simulation of the process by Finite Element Analysis (FEA) demonstrated this gradient distribution graphically.

SPD processing of aluminum alloy AA1050 (Al 99.5) was conducted by HPTE and ECAP at room temperature via different regimes. HPTE experiments were performed with three different regimes using different rotational speeds ( $\omega$ , rpm) and extrusion speeds ( $u$ , mm/min) as follows:  $u7\omega1$ ,  $u1\omega1$ ,  $u1\omega3$ . ECAP experiments were conducted in two regimes, ECAP4 after 4 passes, and ECAP8 after 8 passes of ECAP via route Bc. Microstructural analysis of the samples showed different levels of grain refinement from the initial grain size of 130  $\mu\text{m}$  in the annealed sample to the final grain size of 1.1  $\mu\text{m}$  and 0.9  $\mu\text{m}$  in ECAP4 and ECAP8, respectively. Grain refinement in HPTE occurred in a wide range depending on the regime and the distance from center in each sample. However, the maximum grain refinement was achieved in the periphery-zone of the samples (near to the edge) with the final grain size of 1.2, 0.7, 0.7  $\mu\text{m}$ , in  $u7\omega1$ ,  $u1\omega1$ ,  $u1\omega3$ , respectively.

In a similar manner, the hardness of materials increased after processing depending on the processing conditions. The initial hardness value of 28 HV0.2 increased to the average values of 47 HV0.2 in ECAP4 and to 51 HV0.2 in ECAP8. The highest hardness values in HPTE were measured in the edge zone of the samples with the values of 51, 64, 67 HV0.2 in  $u7\omega1$ ,  $u1\omega1$ ,  $u1\omega3$ , respectively. Results of XRD analysis also confirm the presence of higher dislocation densities in HPTE samples compared to ECAP. Results of hardness distribution in HPTE samples showed a gradual decrease by moving from the edge to the center, which is in conformity with the distribution of strain at the cross-section of the samples. Evaluation of the results of hardness with respect to strain revealed that saturation level in hardness occurred near to the strain value of 20 although HPTE was able to impose higher values of strains up to 65.5 mm/mm in materials. The saturation levels of hardness and grain size in aluminum were measured as 67 HV0.2 and 0.7  $\mu\text{m}$ , respectively.



In studying the effect of process parameters of HPTE on materials evolution, it was found that the ratio of  $\omega/u$  had a great impact on the homogeneity of the samples. Increasing this ratio increased the induced plastic deformation in the center zone and consequently, increased the homogeneity in the distribution of hardness and grain size at the cross-section of the samples.

SPD processing of niobium was performed by using the HPTE regime v7w1 and ECAP regimes ECAP1 and ECAP4 through route B<sub>c</sub>. Considerable grain refinement occurred in the processed sample as the initial grain size of 12.6  $\mu\text{m}$  reduced to 2.26  $\mu\text{m}$  in ECAP1 and to 0.67  $\mu\text{m}$  in ECAP4. The finest microstructure, however, was observed in HPTE with an average grain size of 0.49  $\mu\text{m}$  in the edge zone. Correspondingly, the hardness values increased after processing, from the initial value of 81 HV0.2 to 109, 155, 285 HV0.2 in ECAP1, ECAP4, and HPTE (in the edge zone) respectively. However, the hardness distribution in HPTE showed a downward gradient from edge to center, similar to the case of aluminum, which is related to the inherent effect of torsion on strain distribution in materials. The lowest hardness value in HPTE processed niobium was measured as 241 HV0.2 in the central zone of HPTE which is still higher than the highest hardness value in ECAP4. XRD analysis of the results proved the presence of higher dislocation densities in the HPTE sample as compared to the ECAPed ones.

In an overall assessment, it can be concluded that HPTE is an effective technique in fabricating bulk-nanostructured metals. Increasing rate of 140% in the hardness of aluminum and 252 % in that of niobium confirm the striking effect of HPTE on the improvement of mechanical properties. Compared to the other SPD counterparts such as HPT and ECAP, this technique takes advantage of fabricating bulk samples with extreme grain-refinement, as well as providing a substantial improvement in mechanical properties within only one pass of extrusion.

# LÜHIKOKKUVÕTE

## Metallide süvoplastne deformeerimine kõrgsurve- väändeekstrusiooni meetodil

Käesolevas doktoritöös uuriti metallide süvoplastse deformeerimise uutset tehnikat, nimelt kõrgsurve-väändeekstrudeerimist (HPTE) ja selle protsessi mõju puhaste metallide mikrostruktuurile ja omadustele. Doktoritöös uuriti kahte tüüpi kristallivõrega metalle: tahkesendatud kuupvõrega alumiiniumi ja ruumkesendatud kuupvõrega niobiumi. HPTE meetodi tõhususe paremaks mõistmiseks viidi samuti läbi paralleelselt võrdkanalilise nurkpressimise (ECAP) katsed ja tulemusi võrreldi omavahel. HPTE kujutab endast tavapärase kõrgsurve-väände (HPT) ja ekstrusiooni meetodi kombinatsiooni. Materjalide mikrostruktuuri ja mehaaniliste omaduste parandamiseks tuntud SPD meetodist HPT korral on piiravaks katsekehade paksus (maksimaalne paksus 1-2 mm), samal ajal kui uus HPTE tehnoloogia võimaldab toota silindrikujulisi ülipeenteralisi (UFG) materjale, millel on sarnased atraktiivsed mehaanilised omadused. Kasutatavat väändedeformatsiooni HPTE meetodit iseloomustab silindrilise katsekehade ristlõikes struktuuri ja omaduste gradientjaotus keskpunktist servani, kuna deformatsioon võib varieeruda laias vahemikus alates 0,9 kuni 65,5 sõltuvalt katsekeha raadiusest ja protsessi parameetritest. Protsessi modelleerimine lõplike elementide analüüsi (FEA) meetodiga võimaldas seda gradientjaotust esitada graafiliselt.

Puhta alumiiniumi töötlus HPTE ja ECAP meetoditel erinevatel parameetritel viidi läbi toatemperatuuril. HPTE katsed viidi läbi kolmel erinevatel parameetrite kombinatsioonidel kasutades erinevaid pöörlemiskiirusi ( $\omega$ , 1 / min) ja ekstrusiooni kiirusi ( $u$ , mm / min) järgmiselt:  $u7\omega1$ ,  $u1\omega1$ ,  $u1\omega3$ . ECAP katsed viidi läbi kahel pressimiste arvul: ECAP4 (4 pressimist) ja ECAP8 (8 pressimist)  $B_c$  marsruudil. Katsekehade mikrostruktuuri analüüs näitas terade peenenemise erinevaid tasemeid, alates lõõmutatud proovi algsest tera suuruselt  $\sim 130 \mu\text{m}$  kuni lõpliku tera suuruseni  $1.1 \mu\text{m}$  ja  $0.9 \mu\text{m}$  vastavalt. Sõltuvalt parameetritest ja kaugusest silindrilise katsekeha keskpunktist servani toimus terade mõõtmete vähenemine HPTE ajal laias vahemikus. Proovide perifeerses tsoonis (serva lähedal) saavutati tera keskmiseks suurusks  $1.2$ ,  $0.7$ , ja  $0.7 \mu\text{m}$  parameetritel  $u7\omega1$ ,  $u1\omega1$ ,  $u1\omega3$  vastavalt.

Materjalide kõvadus suureneb töötlemise ajal sõltuvalt töötlemistingimustest. Mikrokõvaduse algväärtus  $28 \text{HV}0.2$  tõusis keskmistele väärtustele ECAP4 ajal kuni  $47 \text{HV}0.2$  ja ECAP8 korral kuni  $51 \text{HV}0.2$  vastavalt. Kõrgeimad kõvadusväärtusi HPTE ajal mõõdeti katsekehade serva piirkonnas  $51$ ,  $64$ , ja  $67 \text{HV}0.2$ , töötlemisrežiimide korral  $u7\omega1$ ,  $u1\omega1$ , ja  $u1\omega3$  vastavalt. Röntgendifraktsiooni analüüs (XRD ja EBSD) tulemused kinnitavad ka suuremat dislokatsioonide tihedust HPTE katsekehadel, võrreldes ECAP katsekehadega. Kõvaduse jaotuse tulemused HPTE katsekehadel näitasid servast keskele liikudes järkjärgulist vähenemist, mis on kooskõlas deformatsioonide jaotumisega katsekeha ristlõikes. Deformatsiooniastme tulemuste hindamine näitas, et küllastustase oli maksimaalsete väärtuste lähedal, ehkki HPTE korral materjalides oli võimalus kasutada kõrgemaid deformatsiooniastmeid (kuni 65,5). Alumiiniumi mikrokõvaduse ja tera suuruse mõõtmed olid  $67 \text{HV}0.2$  ja  $0,7 \mu\text{m}$  vastavalt. Uurides HPTE protsessi parameetrite mõju materjalide struktuuri kujunemisele, leiti, et suhe  $\omega / u$  avaldab suurt mõju katsekehade homogeensusele. Selle suhte kasv suurendas indutseeritud plastset deformatsiooni kesktsoonis ja sellega kõvaduse ja tera suuruse jaotuse ühtsust katsekehade ristlõikes.

Puhta nioobiumi SPD töötlemine viidi läbi HPTE-töötuse  $u7\omega1$  režiimil ja ECAP režiimidel ECAP4 ja ECAP8 marsruudil B<sub>c</sub> vastavalt. Töödeldud katsekehades täheldati olulist tera mõõtmete vähenemist: algse tera suurus 12.6  $\mu\text{m}$  vähenes ECAP4 juures kuni 2.26  $\mu\text{m}$ -ni ja ECAP8 juures kuni 0,67  $\mu\text{m}$ -ni. Kõige peenemat mikrostruktuuri täheldati aga HPTE meetodil kuni keskmise tera suurusega 0,49  $\mu\text{m}$  servatsoonis. Sellest tulenevalt kasvasid kõvaduse väärtused pärast töötlemist ECAP4, ECAP8 ja HPTE korral: algväärtusest 81 HV0.2 väärtusteni 109 HV0.2, 155 HV0.2, ja 285 HV0.2 (servatsoonis) vastavalt. Kõvaduse jaotumine HPTE korral näitas nioobiumi puhul sarnast servast allapoole suunatud gradienti, mis on tingitud materjali deformatsiooni jaotumisele omase väändeteguri mõjust. HPTE-meetodil töödeldud puhta nioobiumi madalaimaks kõvaduse keskmiseks väärtuseks mõõdeti 241 HV0.2 katsekeha kesktsoonis, mis on siiski kõrgem kui ECAP8 kõrgeim kõvadusväärtus. Tulemuste röntgendifraktsioonanalüüs kinnitas suuremat dislokatsioonide tihedust HPTE katsekehades võrreldes ECAP katsekehadega.

Üldiselt võime järeldada, et HPTE on tõhus meetod nanokristallilise struktuuriga puhaste metallide tootmiseks. Alumiiniumi kõvadusindeks tõusis 1.5 korda ja nioobiumil 2.5 korda, mis kinnitab HPTE olulist mõju metallide mehaanilitele omadustele. Võrreldes teiste SPD protsessidega, näiteks HPT-ga ja ECAP-ga, realiseerub selle meetodi korral maksimaalne terade peenendumisvõime materjalis, ning võimaldab ka nende mehaaniliste omaduste olulist paranemist vaid ühekordse ekstrusiooni tulemusena.



**APPENDIX**  
**Publications**



**Article I:**

B. Omranpour, Y. Ivanisenko, R. Kulagin, L. Kommel, E. Garcia Sanchez, D. Nugmanov, T. Scherer, A. Heczal, J. Gubicza, Evolution of microstructure and hardness in aluminum processed by High Pressure Torsion Extrusion, *Mater. Sci. Eng. A.* 762 (2019) 138074.

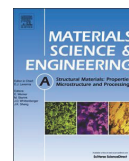






Contents lists available at ScienceDirect

## Materials Science &amp; Engineering A

journal homepage: [www.elsevier.com/locate/msea](http://www.elsevier.com/locate/msea)

## Evolution of microstructure and hardness in aluminum processed by High Pressure Torsion Extrusion



Babak Omranpour<sup>a,b,c,\*</sup>, Yulia Ivanisenko<sup>a</sup>, Roman Kulagin<sup>a</sup>, Lembit Kommel<sup>b</sup>, E. Garcia Sanchez<sup>c</sup>, Dayan Nugmanov<sup>a</sup>, Torsten Scherer<sup>a,d</sup>, Anita Heczal<sup>e</sup>, Jenő Gubicza<sup>e</sup>

<sup>a</sup> Institute of Nanotechnology (INT), Karlsruhe Institute of Technology (KIT), 76021, Karlsruhe, Germany

<sup>b</sup> Department of Mechanical and Industrial Engineering, Tallinn University of Technology (TALTECH), 19086, Tallinn, Estonia

<sup>c</sup> Facultad de Ingeniería Mecánica y Eléctrica (FIME), Universidad Autónoma de Nuevo León (UANL), 66455, San Nicolás de los Garza, Mexico

<sup>d</sup> Karlsruhe Nano Micro Facility (KNMF), Karlsruhe Institute of Technology (KIT), 76021, Karlsruhe, Germany

<sup>e</sup> Department of Materials Physics, Eötvös Loránd University, Budapest, P.O.B. 32, H-1518, Hungary

## ARTICLE INFO

## Keywords:

High pressure torsion extrusion  
Aluminum  
Ultrafine-grained materials  
Microstructure  
Hardness

## ABSTRACT

An investigation was conducted on aluminum samples (AA1050) to study the microstructure and hardness evolution during processing by High Pressure Torsion Extrusion (HPTE). The equivalent strain accumulated in the samples after one pass of HPTE varied in a wide range between 0.9 and 65.5, depending on the processing parameters. HPTE led to the formation of a gradient microstructure in which the grain size decreased by increasing the distance from the central axis of the billets. This gradient decreased significantly by increasing the ratio of rotational speed to extrusion speed. Most of the grain refinement and hardness-increase occurred up to the equivalent strain of  $\sim 5$  but saturation level was achieved at the strain of  $\sim 20$ . Saturation levels in grain size and hardness were  $\sim 0.7 \mu\text{m}$  and  $\sim 67 \text{HV}$ , respectively. HPTE technique can provide similar saturation in microstructure and hardness as those obtained by HPT but in much larger samples. Therefore, HPTE can be named as a suitable candidate for practical applications to produce bulk ultrafine-grained materials with considerable enhancement in hardness.

## 1. Introduction

Fully dense bulk ultrafine-grained (UFG) materials with superior mechanical properties can be produced by Severe Plastic Deformation (SPD) techniques [1,2]. One key factor in SPD is that the shape of the sample remains unchanged during the whole process while enduring large plastic deformations [3], therefore there is a possibility to reach high plastic strains by repeating the same SPD process on the sample. Early efforts towards SPD were started with the proposition of “torsion combined with compression” by Bridgman in Harvard in the 1940s [4] and later developed in Russia in the 1980s [5]. Subsequently, different SPD techniques were proposed due to the increasing demand for polycrystalline materials with very fine microstructure and large fraction of high-angle grain boundaries (HAGBs), including equal channel angular pressing (ECAP) [6], cyclic extrusion compression (CEC) [7] and cyclic expansion extrusion (CEE) [8]. During CEE, the material experiences consecutive expansion and extrusion in several passes without any need for back pressure [9]. Recently, it was suggested to combine conventional HPT with an expansion-extrusion technique.

This new method was called High Pressure Torsion Extrusion (HPTE) [10].

It was shown for pure copper that one of the most striking microstructural features after HPTE is a strong grain refinement except the specimen area close to the center. Another research on niobium also confirmed a remarkable improvement in the hardness of HPTE-processed samples [11]. According to these studies, the resulting microstructure and hardness distribution after HPTE are similar to the ones made by conventional HPT [10,11]. These attributes are basically related to the gradient of shear strain along the sample radius. However, HPTE has the advantage of producing bulk samples as compared to HPT. It has been proved that the compressive yield strength of bulk samples of pure aluminum considerably improved after HPTE processing [12]. In addition to the improvement in mechanical properties, the case study on niobium revealed that HPTE can make a substantial enhancement in hydrogen-storage capacity in materials [11]. Therefore, this technique can also be used as a potential tool to fabricate functional materials for industrial applications.

During the past years, researchers tried to analyze and compare

\* Corresponding author. Institute of Nanotechnology (INT), Karlsruhe Institute of Technology (KIT), 76021, Karlsruhe, Germany.  
E-mail address: [omranpou@uqtr.ca](mailto:omranpou@uqtr.ca) (B. Omranpour).

<https://doi.org/10.1016/j.msea.2019.138074>

Received 18 March 2019; Received in revised form 23 June 2019; Accepted 24 June 2019

Available online 25 June 2019

0921-5093/© 2019 Elsevier B.V. All rights reserved.

different SPD techniques to find optimal methods for practical applications. For example, a comparison of hardness and electrical conductivity of pure copper processed by ECAP and HPT was conducted in Ref. [13]. The effect of different SPD techniques, such as ECAP and HPT, on the microstructure was investigated for a Siclanic alloy (Cu-Ni-Si) [14], pure copper [15] and 7075 Al alloy [16].

Process parameters in SPD techniques are mainly affected by the die; thereby, the amount of strain applied to the material is basically invariant after die manufacture since these parameters are fixed (such as the angles of “ $\varphi$ ” and “ $\psi$ ” in ECAP) [17]. By contrast, process parameters in HPTE are not solely dependent on die parameters (e.g. extruding speed or rotational speed). Hence, a wide range of strain values are achievable simply by changing these parameters.

However, the effect of HPTE process parameters (regimes) on the microstructure has not been investigated yet. Therefore, the present study conducted a detailed analysis on HPTE by evaluating the evolution of microstructure and hardness in commercially pure aluminum, and the influence of process parameters on microstructure and hardness was investigated. The results obtained from HPTE-processed samples were compared with the available data in the literature about similar materials processed by traditional SPD techniques such as ECAP and HPT.

## 2. Materials and methods

### 2.1. Materials processing by HPTE

Commercially pure aluminum (CP-Al) samples containing 99.5 wt% Al (AA1050) were annealed for 30 min at 345 °C in order to get a homogeneous microstructure. Then, the annealed specimens were furnace cooled to room temperature. Cylindrical samples of aluminum with the diameter of  $D_0 = 11.8$  mm and the length of 35 mm were processed at room temperature using a computer controlled HPTE machine (manufacturer: W. Klement GmbH). Molybdenum Disulfide ( $\text{MoS}_2$ ) was used as a lubricant in all experiments to facilitate the extrusion process. The HPTE equipment used in this study was described in detail in a former paper [10]. A schematic representation of the HPTE die is shown in Fig. 1. Specimens were extruded through the die using a punch moving with an extrusion speed of  $v$ . Simultaneously, the lower die rotated with a rotational speed of  $\omega$ . As a result, the specimens experienced both expansion-extrusion deformation and torsional deformation in a narrow zone close to the middle of the die (see Fig. 1). For given values of  $v$  and  $\omega$ , the strain depends on the distance from the sample center (denoted as  $R$ ), providing a strain gradient from the

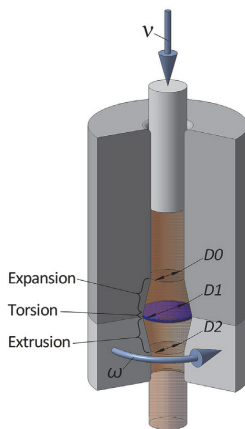


Fig. 1. Schematic illustration of HPTE and the process parameters.

Table 1

Notations of the studied samples and the corresponding equivalent strains obtained from eq. (1) for HPTE;  $v$ : extrusion speed,  $\omega$ : rotational speed of HPTE,  $R$ : distance from the central axis in the HPTE samples.

Sample notation	$v$ [mm/min]	$\omega$ [rpm]	HPTE					
			Equivalent strain for one pass					
			$R$ [mm]					
			0.0	0.9	1.8	2.7	3.6	4.5
v7w1	7	1	0.9	1.5	2.1	2.7	3.3	3.9
v1w1	1	1	0.9	5.2	9.5	13.8	18.1	22.4
v1w3	1	3	0.9	13.8	26.7	39.7	52.6	65.5

center to the edge of the specimen. Therefore, similar to the case of conventional HPT, it is expected that microstructure and hardness vary as a function of distance from the central axis of the billets. However, the homogeneity of samples along the longitudinal axis basically remains the same with a minor variation at the ends of the billet. More details about the homogeneity of processed billets over the whole length of the sample can be found in an earlier study [18].

The equivalent strain imposed during HPTE depends on the ratio of the channel diameters ( $D_1/D_0$ ), ( $D_1/D_2$ ), the extrusion speed of specimens ( $v$ ) and rotational speed of the die ( $\omega$ ). For one pass of HPTE, the equivalent strain can be calculated by Eq (1) [10]:

$$\epsilon_{\text{HPTE}} = 2 \ln \frac{D_1}{D_0} + 2 \ln \frac{D_1}{D_2} + \frac{2\pi \cdot \omega \cdot R \cdot D_1}{\sqrt{3} \cdot v \cdot D_2} \quad (1)$$

where  $D_0$ ,  $D_1$ , and  $D_2$  are fixed and equal to 12, 14 and 10.6 mm respectively.  $R$  is the distance from the center in the cross section of the specimen. The notations of the samples processed at different values of  $v$  and  $\omega$  are shown in Table 1. For each HPTE specimen, the studied locations along the radius were characterized with the values of  $R$ . The equivalent strain was calculated from eq. (1) and listed in Table 1 (each sample was processed by 1 pass of HPTE).

### 2.2. Characterization of microstructure

Microstructure evolution of the specimens processed by HPTE was investigated by electron backscatter diffraction (EBSD) using a Zeiss Auriga 60 and an FEI Quanta 3D scanning electron microscopes (SEM) operating at 20 kV. First, the samples were sectioned perpendicular to the extrusion axis, then grinded and mechanically polished. Finally, the samples were electropolished at the voltage of 20 V and current of 1 A for 8 s at room temperature using the solution of 70 vol.% ethanol, 20 vol.% perchloric acid, 10 vol.% glycerin. The images were taken from the planes normal to the extrusion direction (transversal section). The EBSD images were evaluated using the orientation imaging (OIM) software by EDAX. The scanning step size was about 25 nm, which corresponds to one-pixel size. The EBSD study was carried out at three different locations on the transversal section of the HPTE-processed specimens: in the center, in the mid-radius region ( $\sim 2.7$  mm from the central axis of the samples) and in the region close to the edge ( $\sim 4.5$  mm from the central axis of the samples). To ensure the reliability of EBSD data, all grains comprising four or fewer pixels were automatically removed from the EBSD maps using the grain-dilation cleanup and neighbor orientation correlation option in the OIM software (minimal grain tolerance angle of 15°). To eliminate disputable orientations caused by orientation noise, a lower limit boundary misorientation cut-off of 2° was used. A 15° criterion was employed to differentiate between the low-angle boundaries (LAGBs) and high-angle boundaries (HAGBs). The grain size was measured using the equal diameter method and only grains delineated by HAGBs and comprising at least 5 pixels were considered for study. Then, distribution of the area fraction of different grain sizes was constructed and the area-

weighted mean grain size ( $D_w$ ) was determined. More than 100 grains were analyzed for each sample.

Microstructural evolution in the center, in the mid-radius and in the peripheral zone of the HPTE-processed samples was studied by X-ray line Profile Analysis (XLP). The X-ray line profiles were measured by a high-resolution rotating anode diffractometer (type: RA-MultiMax9, manufacturer: Rigaku) using  $\text{CuK}\alpha_1$  (wavelength:  $\lambda = 0.15406$  nm) radiation. The diffraction profiles were evaluated by the Convolutional Multiple Whole Profile (CMWP) method [19]. In this method, the diffraction pattern is fitted by sum of a background spline and convolution of the instrumental pattern and theoretical line-profiles related to the diffraction domain size and dislocations. The instrumental diffraction peaks were measured on a  $\text{LaB}_6$  standard material (SRM 660). The instrumental broadening was similar to the profile breadths caused by the diffraction domain size. Therefore, only the dislocation density ( $\rho$ ) was determined from XLP. It is noted that the height of the X-ray beam spot on the sample surface was about 2 mm. Therefore, the results obtained in the center of the HPTE samples should be considered as an average distance between  $-1$  and  $+1$  mm from the center. The XLP measurement at the periphery of the disk was carried out at 1 mm from the edge, i.e., at a distance of 4 mm from the center.

### 2.3. Hardness testing

Microhardness of the samples was measured in Vickers scale using a Buehler Micromet-5104 tester. A load of 200 g with a dwell time of 15 s was applied to all samples. The indentation was performed in several points along two perpendicular diameters on the cross-section of the specimens, each point evenly spaced out from the previous one. The relative error of microhardness values was less than 2%.

## 3. Results

### 3.1. Microstructure evolution during HPTE

Fig. 2 shows crystallographic orientation maps obtained by EBSD for the center parts of the HPTE samples v7w1, v1w1 and v1w3. The grain-size and misorientation-angle distributions for the three samples are shown in Fig. 3. The average size of grains is listed in Table 2. This region was deformed mainly by extrusion as the nominal shear strain is zero in the center of the HPTE samples. It should be noted, however, that plasticity can spread into the center from the neighboring regions during HPTE processing similar to HPT deformation as it was shown by strain gradient plasticity modeling [20]. Although, the nominal equivalent strain is the same for the central zone of the three HPTE samples (0.9 according to eq. (1)), the average grain size in these specimens is very different. Namely, for the samples v7w1, v1w1 and v1w3, the grain size values were 122, 9.9 and 1.9  $\mu\text{m}$ , respectively.

Misorientation-angle distributions for the central zones of the samples v7w1, v1w1 and v1w3 are shown in Fig. 3a, b and c,

respectively. The fraction of HAGBs ( $V_{\text{HAGB}}$ ) were determined as 20, 53, and 66% for the samples v7w1, v1w1 and v1w3, respectively (see Table 2). These values show an increasing trend in HAGB fraction by increasing the deformation induced in the center due to the gradient plasticity.

Crystallographic orientation maps corresponding to the mid-radius zones ( $R \approx 2.7$  mm) and the edge zones ( $R \approx 4.5$  mm) of the specimens processed by HPTE are presented in Fig. 4. The grain size and misorientation-angle distribution histograms obtained from the orientation maps are shown in Fig. 5. Structural parameters such as average grain diameter and fraction of HAGBs are listed in Table 2. The microstructures formed in the mid-radius and in the edge zone of sample v7w1 are distinctly different. In the mid-radius zone, a complex bimodal microstructure is observed. Coarse grains elongated in shear direction are surrounded by fine-elongated grains (see Fig. 4a). The average grain size corresponding to this zone was  $\sim 69$   $\mu\text{m}$ , and the volume fraction of HAGBs was  $V_{\text{HAGB}} = 27\%$  (see Fig. 5a). In contrast, in the edge zone of sample v7w1, a fine-grained microstructure was observed by EBSD as shown in Fig. 4b. In this zone, elongated grains with a length of 2–3  $\mu\text{m}$  and thickness of 0.5–1.0  $\mu\text{m}$  were formed. The average grain size for this area was  $\sim 1.2$   $\mu\text{m}$ . The HAGB fraction at the edge ( $\sim 55\%$ ) is considerably higher than those of the mid-radius ( $\sim 27\%$ ) and the center (20%). Then, it can be concluded that in sample v7w1 a gradient microstructure was formed because the imposed strain was not enough for the achievement of microstructural saturation in this sample.

Microstructural observations for the sample v1w1 show a uniform grain refinement both at the mid-radius and the edge but with different values of grain size (see Fig. 4c and d). The grain size and misorientation-angle distributions are shown in Fig. 5b. The average grain size values in the mid-radius and in the edge-zone were 1.4 and 0.7  $\mu\text{m}$ , respectively (see Table 2). The fractions of HAGBs were very similar in the mid-radius and in the edge zone for this sample (48–55%), and it can be inferred that variation in microstructure in the two aforementioned zones of this sample is less than that of the sample v7w1.

For sample v1w3, a uniform grain structure was observed in both mid-radius and edge zones (see Fig. 4e and f). The average grain size values in these two sites were 1.0 and 0.7  $\mu\text{m}$ , respectively, which shows smaller variations than the values obtained in the samples v7w1 and v1w1, revealing more homogeneity in microstructure distribution (see Table 2). The highest HAGB fraction values were obtained from sample v1w3 as these values were about 65–66%.

Dislocation density for different HPTE processed samples was determined by XLP using CMWP fitting evaluation method. As an example, Fig. 6 shows the CMWP fitting for the edge of the sample v1w1. The dislocation densities obtained for the center, mid-radius and edge zones are listed in Table 2. The values of dislocation density were between  $(4$  and  $7) \times 10^{13} \text{ m}^{-2}$  in the center of the three HPTE samples which did not change significantly along the specimen radius. The relative error of dislocation density values was  $\sim 20\%$ . This observation

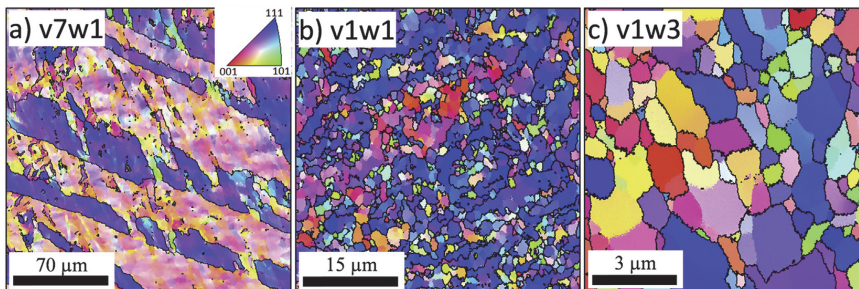


Fig. 2. Crystallographic orientation maps obtained by EBSD for the central zone of the HPTE samples (a) v7w1, (b) v1w1 and (c) v1w3.

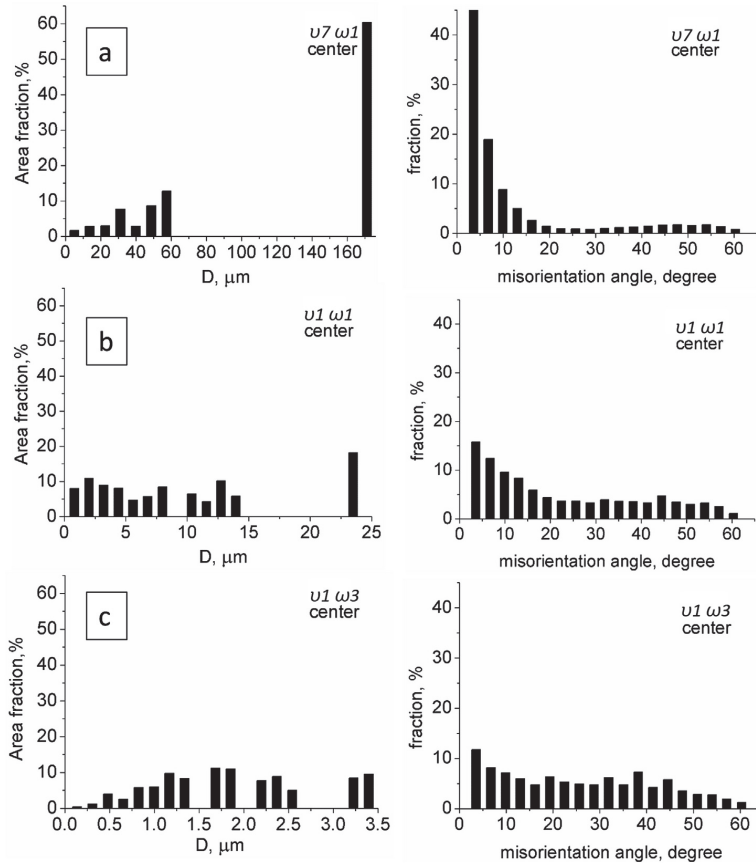


Fig. 3. Distribution of grain size (left) and grain-boundary misorientation angles (right) for the central zone of HPTE samples (a) v7w1, (b)v1w1, and (c) v1w3.

Table 2

Structural parameters and microhardness values for the samples processed by HPTE.  $D_a$ : area-weighted mean grain diameter,  $V_{HAGB}$ : fraction of HAGBs,  $\rho$ : dislocation density. The relative errors of  $V_{HAGB}$ , diameter and dislocation density are 5, 10 and 20%, respectively. The uncertainty of hardness values is 2%.

HPTE					
Sample, location	Strain	$D_a$ [ $\mu\text{m}$ ]	$V_{HAGB}$ [%]	$\rho$ [ $10^{13} \text{m}^{-2}$ ]	$Hv$
v7w1, center	0.9	122	20	7	40
v7w1, mid-radius	2.7	69	27	7	46
v7w1, edge	3.9	1.2	55	5	51
v1w1, center	0.9	9.9	53	4	47
v1w1, mid-radius	13.8	1.4	55	5	60
v1w1, edge	22.4	0.7	48	4	64
v1w3, center	0.9	1.9	66	5	60
v1w3, mid-radius	39.7	1.0	66	5	65
v1w3, edge	65.5	0.7	65	4	67

indicates an early saturation of dislocation density at the center where the theoretical equivalent strain is only  $\sim 0.9$ .

3.2. Microhardness

Fig. 7 shows microhardness distribution along the sample radius

(from the center to the edge) in the initial state and after processing by HPTE. The microhardness values are also listed in Table 2. It is evident that the HPTE specimens showed a gradual increase in hardness by moving from the center to the edge. HPTE showed a non-uniform increase in hardness from the initial hardness of  $\sim 28\text{HV}$  to  $\sim 40$ ,  $\sim 46$  and  $\sim 60$  HV at the center and to  $\sim 51$ ,  $\sim 64$ ,  $\sim 67$  HV at the edge for the samples v7w1, v1w1 and v1w3, respectively (see Table 2). It should also be noticed that the HPTE specimen v1w3 not only showed the highest hardness values in all zones, from the center to the edge, but also revealed the most homogenous hardness distribution among the HPTE samples.

4. Discussion

The experiments showed that HPTE can lead to a gradient in microstructure, depending on the regimes (v7w1, v1w1 or v1w3). Generally, in the very central zone of the specimen, a coarse-grained distorted microstructure was formed due to the direct extrusion. At the same time, owing to the gradient plasticity caused by torsion, the degree of grain refinement in the center depends significantly on HPTE regimes. Closer observation on Table 2 confirms this fact: the severer the torsion component, the smaller the grain size in the center. The efficiency of HPTE in grain refinement in the central zone increased in the following order: v7w1, v1w1 and v1w3. In the mid-radius zone of sample v7w1, microstructure is inhomogeneous comprising coarse- and



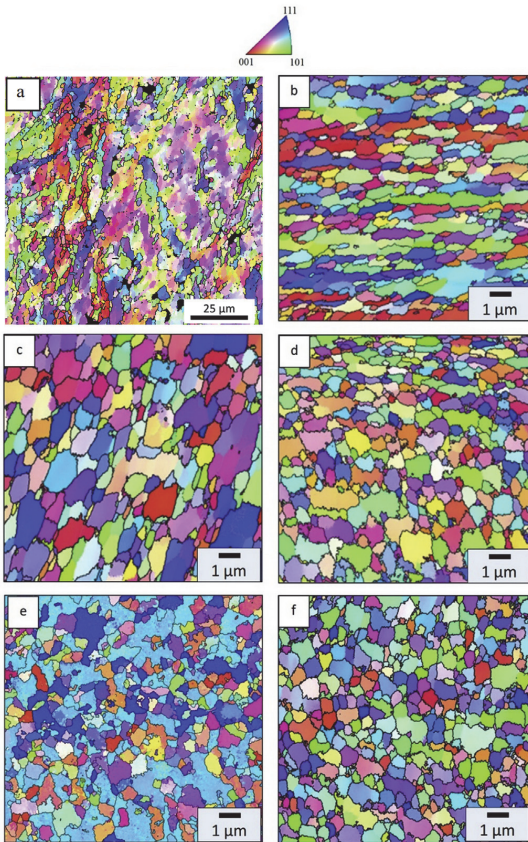


Fig. 4. Orientation maps taken at the mid-radius zones (a, c, e) and at the edge zones (b, d, f) of HPTE samples under the regimes of v7w1 (a,b), v1w1 (c,d), v1w3 (e,f).

fine-grained regions (see Fig. 4a) while sample v1w1 has a uniform UFG microstructure, as shown in Fig. 4c. In the areas close to the edge, the microstructure is homogeneously UFG for all HPTE-processed samples (see Fig. 4b, d and e). According to Table 2, the equivalent strain at the edge zone for the HPTE sample v1w3 is about three times larger than that of sample v1w1, and more than sixteen times larger than that of sample v7w1. The larger is the strain, the finer is the microstructure (compare Fig. 4b, d and f).

Fig. 8 shows the evolution of grain size and HAGB fraction as a function of equivalent strain for the three HPTE-processed samples. The data were taken from Table 2. At the lowest strain value of  $\sim 0.9$  which corresponds to the central zone, microstructural parameters showed different values in spite of applying the same nominal strain. This difference can be explained by gradient plasticity applied in the central zone. Indeed, the shear strain contribution out of the disk center increases by increasing the ratio of  $\omega/\nu$ . Therefore, the deformation caused by gradient plasticity increases in the order of v7w1, v1w1 and v1w3, leading to a further grain refinement. By increasing the nominal strain, the grain size decreased while the HAGB fraction increased, and most of these changes occurred up to the strain value of  $\sim 5$  (see Fig. 8). Between the strains of  $\sim 5$  to  $\sim 20$ , only a moderate decrease in grain size from  $\sim 1 \mu\text{m}$  to  $0.7 \mu\text{m}$  was observed, and a saturation in microstructures was achieved.

The present study demonstrates that HPTE provides an efficient

grain refinement comparable to that of ECAP and HPT processes. In the processed sample by HPTE regime v1w1, the mean grain size at the equivalent strain of  $\sim 20$  was about  $\sim 0.7 \mu\text{m}$ ; whereas further increase in strain via HPTE regime v1w3 did not change the grain size (see Table 2). El-Danaf [21] and Cao [22] reported that in Al-1050 alloy processed by 8 passes of ECAP the mean grain size was also  $\sim 0.7 \mu\text{m}$ . In another work, Naderi et al. [23] reported the same grain size obtained in an equivalent strain of  $\sim 95$  in AA1050 processed by HPT at room temperature. It seems that the minimum grain size achievable in dilute aluminum alloys processed by SPD at room temperature is approximately  $0.7 \mu\text{m}$ , and it can be obtained already at strain values of 10–20. It should be noticed, however, that ECAP requires about 10 passes to accumulate such amounts of strain in materials, whereas HPTE provides this strain level only within one pass, thereby simplifying and accelerating the processing of high-strength, bulk aluminum. So, it can be concluded that HPTE appears to be feasible for fabricating UFG aluminum with similarly small grain size as obtained by HPT but in bulk form. In addition, imposing high amounts of strain by HPTE is easier and faster than ECAP in term of the number of passes.

The limits of grain refinement in SPD-processing were studied systematically in Refs. [24–27]. It was reported that in pure metals and single-phase alloys, the microstructure refinement was saturated between the equivalent strain of 5 and 50 [25]. A set of external parameters that influence the strain corresponding to the onset of microstructure-refinement saturation were discussed, including the processing temperature, strain rate, strain path, applied pressure and also some features of materials such as alloying, presence of secondary phase particles, crystal structure and stacking fault energy [25,27]. For the present CP-Al, HPTE-processing at room temperature resulted in a saturation level in grain size with the value of  $\sim 0.7 \mu\text{m}$  at the equivalent strain of  $\sim 20$  (see Fig. 8). It seems that a change in the stress/strain conditions from pure shear in ECAP to a combination of shear and extrusion in HPTE has a minimal effect on the saturated grain size.

It should be noted that the minimum grain size achieved by HPTE in pure copper at a similar strain (320 nm) [10] was smaller than the value obtained in aluminum ( $\sim 0.7 \mu\text{m}$ ). It is well accepted that the microstructural evolution in SPD occurs as a sequence of several steps and begins with the formation of a cell structure with high dislocation density located in the cell boundaries [25,28–30]. When the deformation continues to increase to a higher range of strains, a non-homogeneous microstructure is formed with broad grain-size and grain-orientation distributions. Such microstructure is observed in the central areas of HPTE-processed samples (see Fig. 2). However, as discussed before, the mean cell and grain size gradually decrease by applying more strains, while the average misorientation angle increases due to the increased density of dislocations in the cell boundaries. Indeed, the lower is the homologous temperature of SPD, the more retarded is the annihilation of dislocations and thereby resulting in a faster approach to saturation of dislocation densities and reducing the grain size achievable by SPD [31].

On the other hand, the effect of SFE is not unequivocal. Former studies [32–34] have suggested that the minimum grain size obtained by SPD was reduced by decreasing the SFE. However, in these studies the reduction of SFE was achieved by increasing the solute content in alloys. Therefore, the decrease in grain size may be at least partly a consequence of the pinning effect of alloying elements on lattice defects, such as dislocations and grain boundaries. In addition, it was shown on pure materials that the minimum grain size in ECAP- or HPT-processed Cu was not higher than in Ag or Au with significantly lower SFE [35]. The negligible effect of SFE on the saturation grain size can be explained as follows: Low SFE retards the annihilation of dislocations (similar to the low homologous temperature of SPD), thereby causing a higher saturation dislocation density; however, the clustering of these dislocations into cell boundaries is hindered since the necessary climb and cross slip are more difficult in materials with lower SFE [35]. Thus, it is suggested that the smaller grain size in HPTE-processed Cu

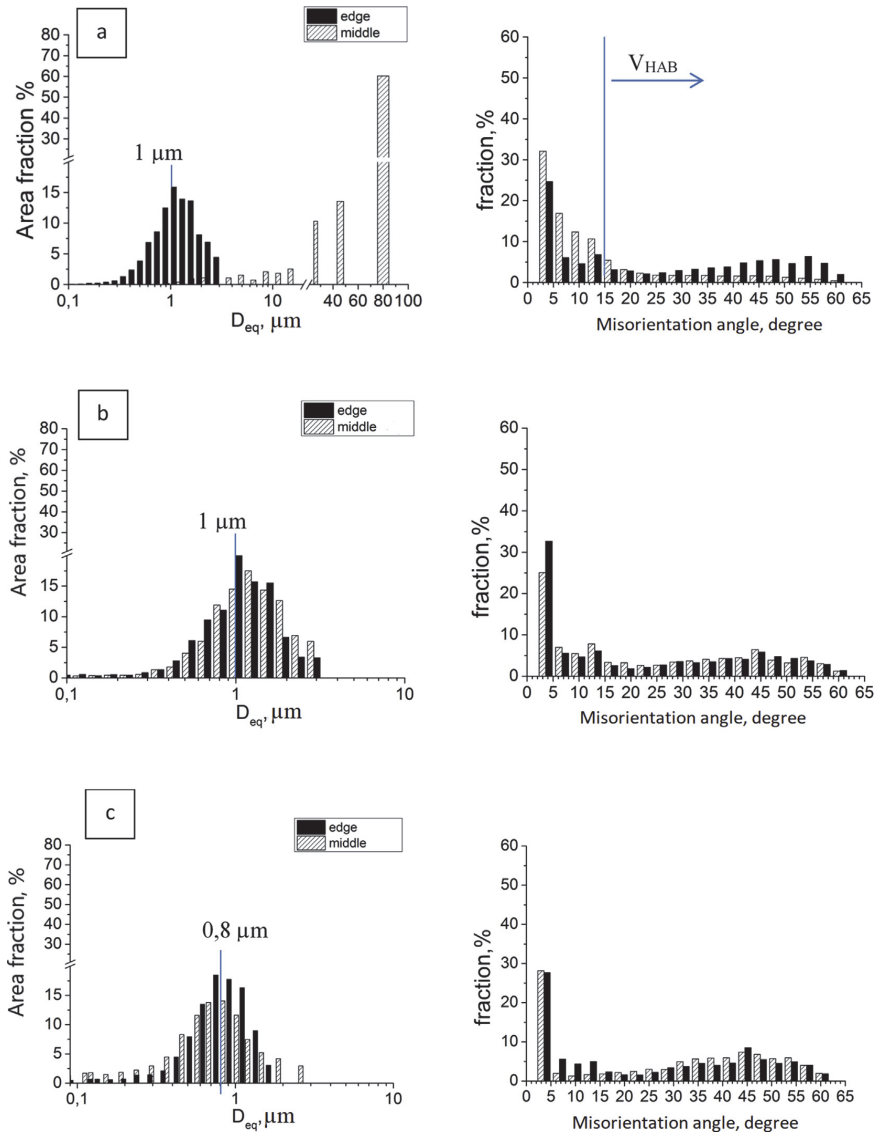


Fig. 5. Distribution of grain size (left) and grain-boundary misorientation angles (right) for the mid-radius and the edge zone of HPTE samples (a) v7w1, (b)v1w1 and (c) v1w3.

compared to Al is mainly caused by the higher melting point.

Fig. 8 indicates that most of the hardness increase during HPTE processing occurred up to the strain value of ~5, the same amount of strain in which grain size evolution took place. Thereafter, the rate of hardness-improvement decreased by increasing the strain, and a saturation hardness of ~67 HV was achieved at the strain value of ~20. In order to correlate the increasing trend of hardness with strain, the measured hardness values in each sample with the corresponding strain were mapped on the graph in Fig. 9, and then the experimental data points were fitted to a curve shown as a solid line. This curve was made by non-linear regression modeling using the following regression function of hardness ( $HV_R$ ) [36]:

$$HV_R = HV_{max} - (HV_{max} - HV_{min}) \times \exp(-a\varepsilon^b) \quad (2)$$

where  $HV_{max} = 67$  HV (the maximum experimental value of hardness),  $HV_{min} = 42$  HV (the minimum experimental value of hardness); “a” and “b” are the fitting parameters and can be determined by minimization of the sum of squared differences of the experimental data points and the model, as represented in the following equation:

$$A = \Sigma(HV_{exp} - HV_R)^2 \mid Min A \quad (3)$$

where  $HV_{exp}$  is the set of data points obtained by experiments, and A is the least possible value of sum of squared differences. Consequently, “a” and “b” are determined as “a = 0.17” and “b = 0.83” by iterative minimization of A.

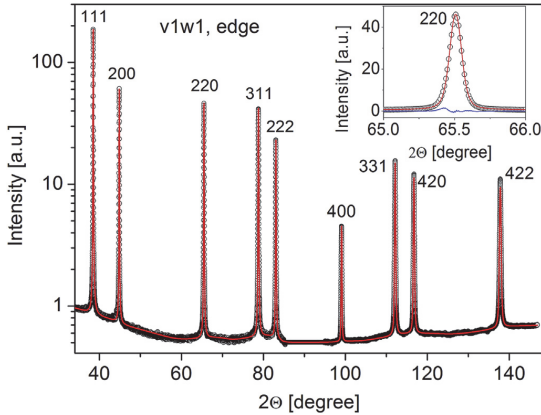


Fig. 6. CMWP evaluation of XRD patterns obtained at the edge of sample v1w1. The intensity is in logarithmic scale. The open circles and the solid line represent the measured and fitted diffractograms, respectively. The inset shows a part of the diffractogram (reflection 220) in linear intensity scale. The difference between the measured and fitted patterns is shown at the bottom of the inset.

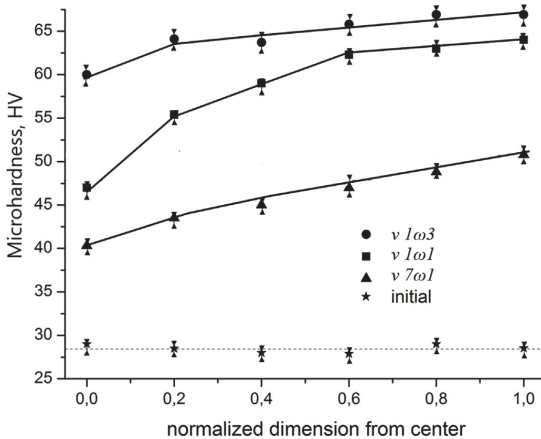


Fig. 7. Center-to-edge distribution of microhardness for the HPTE processed samples.

By substituting the known parameters, Eq. (2) can be rewritten as:

$$HV_R = 67 - 25 \times \exp(-0.17\varepsilon^{0.83}) \quad (4)$$

Eq. (4) can predict the hardness in the HPTE-processed AA1050 alloy, regardless of the regimes (v7w1, v1w1 or v1w3). However, some data points corresponding to the central region of sample v1w3 showed some deviations from the fitted curve at low values of strain. This phenomenon comes from the fact that the nominal shear strain in the center zone is close to zero whereas the real plastic deformation in this area, as mentioned earlier, is affected by the gradient plasticity which may spread out from the surrounding regions into the central zone and affects the microstructure and hardness of the material.

It is worth to note that the saturation value of hardness for HPTE-processed AA1050 (~67 HV) is significantly higher than that of obtained by ECAP in the literature (51–60 HV). Tables 3 and 4 provide a summary of the previously reported hardness values for commercially pure aluminum processed by SPD techniques such as ECAP and HPT.

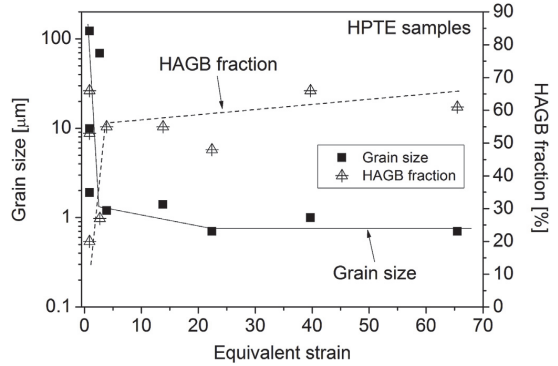


Fig. 8. Grain size and HAGB fraction versus equivalent strain for the HPTE processed samples; the data were taken from Table 2.

According to Table 3, the hardness values in ECAP rarely exceeded 56 HV; whereas this value in the conventional HPT (Table 4) appeared to be in the range of (62–65 HV).

The saturation hardness in HPTE was achieved at the edge of the specimen processed under the conditions of v1w3, but the hardness in the mid-radius zone had also a high value of ~65 HV (see Table 2). The higher saturation hardness in HPTE compared to ECAP can be explained by the smaller grain sizes achieved by HPTE, since ECAP at room temperature resulted in an average grain size of about 1.2 μm in AA1050 [21]. This reported grain size was determined by EBSD, similar to this study. It should be noticed, however, that there are studies in the literature which used transmission electron microscopy (TEM) for determination of the grain size in ECAP-processed AA1050 alloy [43]. These grain size values obtained by TEM are smaller than the ones determined by EBSD which can be related to the fact that in the bright-field TEM images, grain boundary misorientation is not measured, therefore the areas bounded by LAGBs may also be considered as grains whereas these areas could be only subgrains which are surrounded by the grains [60,61]. Nevertheless, the present work studied the grain size of HPTE-processed samples determined by EBSD, therefore the values should be compared with the grain size investigated also by EBSD for the ECAP-processed AA1050 alloy. EBSD also revealed that the fraction of HAGBs in AA1050 alloy processed by ECAP was significantly lower (40–58%) than that of obtained at the edge of sample v1w3 processed by HPTE (67%). The higher HAGB fraction for the HPTE samples may also contribute to the higher hardness values achieved in HPTE as compared to the ECAP samples because larger grain boundary misorientations usually increase the hardening effect of grain boundaries [62]. This is while the highest hardness values reported earlier on HPT-processed AA1050 alloy (see Table 4) are comparable with the saturation hardness obtained by HPTE in the present work; although HPT can produce only thin disks and HPTE is able to fabricate bulk UFG materials. Nonetheless, it should be noted that processing of brittle materials by HPTE may be technically difficult due to the relatively low pressures (up to 1 GPa) used in this technique. Due to the same reason, processing of high-strength materials can be problematic. However, increasing the processing temperature will reduce the flow stress, and allows HPTE to process harder materials. This scheme needs more investigation as it may initiate studies about processing of high-strength materials with commercial potentials for industrial applications.

### 5. Conclusions

An investigation was conducted to study the evolution of microstructure and hardness in bulk aluminum AA1050 samples processed by HPTE technique. The main conclusions of this research are summarized

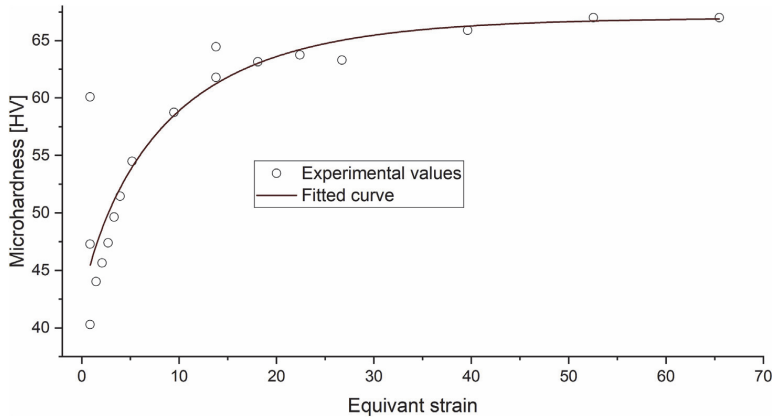


Fig. 9. Vickers microhardness versus equivalent strain for the HPTE processed samples.

below:

1. HPTE-processed samples exhibited gradient microstructures with coarser grains in the central zone and a finer microstructure in the periphery. This feature of HPTE is similar to that of conventional

HPT. It was found that the gradient in microstructure along the sample radius strongly depends on the ratio of the angular speed of rotation to extrusion speed ( $\omega/v$ ): the higher is this ratio, the larger is the shear strain in the center; accordingly, having higher values of this ratio resulted in a more homogeneous microstructure along the

Table 3

Summary table of hardness of commercially pure aluminum processed by ECAP and miscellaneous techniques reported in the literature.

Material	Process	Process parameter	Number of passes	Route	Temperature	Reported hardness value [HV]	Ref.
1 AA1050	ECAP	$\phi = 90$ $\psi = 20$	8	Bc	R.T	54	[37]
2 AA1050	ECAP	$\phi = 90$ $\psi = 20$	8	Bc	R.T	51	[38]
3 AA1050	ECAP	$\phi = 90$ $\psi = 20$	8	Bc	Cryo T.	53	[38]
4 AA1050	ECAP	$\phi = 90$ $\psi = 20$	8	Bc	Cryo T.	54	[39]
5 AA1050	ECAP	$\phi = 90$ $\psi = 20$	6	Bc	R.T	56	[40]
6 AA1050	ECAP	$\phi = 90$ $\psi = 0$	8	Bc	R.T	60	[21]
7 pure aluminum (99.99 wt%)	ECAP	$\phi = 90$ $\psi = 20$	8	Bc	R.T	44	[41]
8 AA1050	ECAP	$\phi = 120$ $\psi = 20$	8	A	R.T	52	[42]
9 AA1050	CEE	-	1 cycle	-	R.T	52	[8]
10 AA1050	ARB	50% reduction in each cycle	5 cycles	-	R.T	63	[43]
11 AA1050	Incremental ECAP	$\phi = 90$ -	8	Bc	R.T	59	[44]
12 AA1050	Ultrasonic-assisted ECAP	$\phi = 90$ $\psi = 3$	1	-	R.T	51	[45]
13 AA1080	Integrated ECAP and direct-Extrusion die	$\phi = 90$ $\psi = 20$	1	-	R.T	52	[46]
14 AA1070		Extrusion ratio: 8 $\phi = 90$ $\psi = 20$	8	Bc	R.T	52	[47]
15 AA1050	Dual-Equal Channel Lateral Extrusion (DECL)	$\phi = 90$ -	6	-	R.T	55	[48]
16 AA1050	T-ECAP, Integration of ECAP and torsion	$\phi = 90$ $\psi = 36$	1	-	R.T	50	[49]
17 AA1050	Cyclic forward-backward Extrusion (CFBE)	$\omega = 0.9$ rad/sec D = 10 mm d = 2.5 mm	No of cycles: 1	-	R.T	52	[50]
18 AA1050	Cold rolling	-	92% reduction ratio	-	R.T	52	[51]
19 AA1050	Accumulative Back Extrusion (ABE)	-	3	-	R.T	67	[52]
20 AA1050	Repetitive Tube Expansion and Shrinking (RTES)	-	One cycle	-	R.T	55	[53]



**Table 4**

Summary table of hardness values obtained by HPT processing of commercially pure aluminum reported in the literature.

	Material	Process	Number of rotations	Pressure [GPa]	Temperature	Reported hardness value [HV]	Ref.
1	AA1050	HPT	N = 1/4 turns; N = 5 turns	6	R.T	65	[54]
2	AA1050	HPT	N = 5 turns	6	R.T	65	[55]
3	AA1050	HPT	15 turns	1	R.T	53	[56]
4	AA1050	HPT	8 turns	1	R.T	62	[57]
5	AA1060	Dynamic HPT (DHPT)	25 deg.	1.33	R.T	55	[58]
6	C-pure Al (99.9 wt%)	Hollow-Cone HPT (HC-HPT)	N = 0.5 turns	–	R.T	53	[59]

sample radius. This fact is also valid for the hardness distribution along the radius of the HPTE samples.

- It was revealed that the evolution of grain size and hardness in the HPTE samples processed under different regimes can be described in a uniform way if the data were plotted as a function of equivalent strain. Nonetheless, this is not valid for the centers of the HPTE samples as in these zones the real strain differs significantly from the nominal value due to the gradient plasticity. Most of the grain refinement and hardness-increase occurred up to the equivalent strain of  $\sim 5$  but saturation was achieved only at the strain value of  $\sim 20$ . The saturation level in grain size and hardness were  $\sim 0.7 \mu\text{m}$  and  $\sim 67 \text{HV}$ , respectively.
- Processing of aluminum samples by HPTE resulted in a higher saturation hardness than that of obtained in ECAP due to fabricating smaller grain size and achieving a higher fraction of HAGBs as determined by EBSD. HPTE technique can provide a similar saturation level in microstructure and hardness to those obtained by HPT but in bulk samples. Therefore, the attractive mechanical properties obtained in thin disks after HPT processing can also be expected to appear in HPTE-processed billets. Another advantage of HPTE is that the very fine microstructure and the high hardness values are achievable only within one pass which makes it a time-efficient technique. Hence, HPTE has great opportunities for practical applications, especially for strength improvement in metals and alloys.

#### Data availability

The raw/processed data required to reproduce these findings cannot be shared at this time due to technical or time limitations.

#### Declaration of interest

None.

#### Contribution to authorship

B.O and Y.I conceived of the project plan. B.O and R.K performed the HPTE experiments. R.K developed the idea of using non-linear regression modeling. L.K and E.G.S supported the ECAP part of the project. D.N, A.H, T.S and J.G performed the EBSD analysis. A.H and J.G carried out the XLP test. E.G.S provided the access to hardness testing, and B.O performed the test. Y.I and J.G supervised the findings of this work. B.O coordinated the project and took the lead in writing the manuscript. All authors provided critical feedback and contributed to the final version of the manuscript.

#### Acknowledgment

This work was financially supported in part by *European social funds in the framework of "DoRa program" - Archimedes Foundation- Estonia*, and in part by *"Deutscher Akademischer Austauschdienst" (DAAD) - Germany*. Technical support by *Karlsruhe Nano-Micro Facility (KNMF)* is appreciated. L. Kommel would like to thank the Estonian Research Council-institutional research funding (Project No. IUT 1929). Yu. I., R.K. and D.N. acknowledge funding support from German Research Foundation

(DFG) under Grant No. IV98/8-1. J. Gubicza acknowledges financial support from the Ministry of Human Capacities of Hungary within the ELTE University Excellence program (1783-3/2018/FEKUTSRAT).

#### References

- T.G. Langdon, Twenty-five years of ultrafine-grained materials: achieving exceptional properties through grain refinement, *Acta Mater.* 61 (2013) 7035–7059, <https://doi.org/10.1016/j.actamat.2013.08.018>.
- R.Z.Z. Valiev, Y. Estrin, Z. Horita, T.G.G. Langdon, M.J.J. Zehetbauer, Y.T.T. Zhu, Fundamentals of superior properties in bulk NanoSPD materials, *Mater. Res. Lett.* 3831 (2015) 1–21, <https://doi.org/10.1080/21663831.2015.1060543>.
- R. Kocich, P. Lukáč, SPD processes - methods for mechanical nanostructuring, *Handb. Mech. Nanostructuring*, Wiley-VCH Verlag GmbH & Co. KGaA, Weinheim, Germany, 2015, pp. 235–262, <https://doi.org/10.1002/9783527674947.ch11>.
- P.W. Bridgman, On torsion combined with compression, *J. Appl. Phys.* 14 (1943) 273–283, <https://doi.org/10.1063/1.1714987>.
- A.P. Zhilyaev, T.G. Langdon, Using high-pressure torsion for metal processing: fundamentals and applications, *Prog. Mater. Sci.* 53 (2008) 893–979, <https://doi.org/10.1016/j.pmatsci.2008.03.002>.
- V. Segal, V. Reznikov, A. Drobyshevskiy, V. Kopylov, Plastic working of metals by simple shear, *Russ. Metall.* (1981) 99–105.
- J. Richert, M. Richert, A new method for unlimited deformation of metals and alloys, *Aluminium* 62 (1986) 604–607.
- N. Pardis, B. Talebanpour, R. Ebrahimi, S. Zomorodian, Cyclic expansion-extrusion (CEE): a modified counterpart of cyclic extrusion-compression (CEC), *Mater. Sci. Eng. A* 528 (2011) 7537–7540, <https://doi.org/10.1016/j.msea.2011.06.059>.
- N. Pardis, C. Chen, R. Ebrahimi, L.S. Toth, C.F. Gu, B. Beausir, L. Kommel, Microstructure, texture and mechanical properties of cyclic expansion-extrusion deformed pure copper, *Mater. Sci. Eng. A* 628 (2015) 423–432, <https://doi.org/10.1016/j.msea.2015.01.003>.
- Y. Ivanisenko, R. Kulagin, V. Fedorov, A. Mazilkin, T. Scherer, B. Baretzky, H. Hahn, High Pressure Torsion Extrusion as a new severe plastic deformation process, *Mater. Sci. Eng. A* 664 (2016) 247–256, <https://doi.org/10.1016/j.msea.2016.04.008>.
- B.S. Omranpour, L. Kommel, E.G. Sanchez, Y. Ivanisenko, J. Huot, Enhancement of hydrogen storage in metals by using a new technique in severe plastic deformations, *Key Eng. Mater.* 799 (2019) 173–178 [10.4028/www.scientific.net/KEM.799.173](https://doi.org/10.4028/www.scientific.net/KEM.799.173).
- B. Omranpour, R. Kulagin, Y. Ivanisenko, E. Garcia Sanchez, Experimental and numerical analysis of HPTE on mechanical properties of materials and strain distribution, *IOP Conf. Ser. Mater. Sci. Eng.* 194 (2017) 012047, <https://doi.org/10.1088/1757-899X/194/1/012047>.
- K. Edalati, K. Imamura, T. Kiss, Z. Horita, Equal-channel angular pressing and high-pressure torsion of pure copper: evolution of electrical conductivity and hardness with strain, *Mater. Trans.* 53 (2012) 123–127, <https://doi.org/10.2320/matertrans.MD201109>.
- A.Y. Khereddine, F.H. Larbi, M. Kawasaki, T. Baudin, D. Bradai, T.G. Langdon, An examination of microstructural evolution in a Cu–Ni–Si alloy processed by HPT and ECAP, *Mater. Sci. Eng. A* 576 (2013) 149–155, <https://doi.org/10.1016/j.msea.2013.04.004>.
- J. Li, F. Li, C. Zhao, H. Chen, X. Ma, J. Li, Experimental study on pure copper subjected to different severe plastic deformation modes, *Mater. Sci. Eng. A* 656 (2016) 142–150, <https://doi.org/10.1016/j.msea.2016.01.018>.
- S. Sabbaghianrad, T.G. Langdon, An evaluation of the saturation hardness in an ultrafine-grained aluminum 7075 alloy processed using different techniques, *J. Mater. Sci.* 50 (2015) 4357–4365, <https://doi.org/10.1007/s10853-015-8989-x>.
- F. Djavanroodi, B. Omranpour, M. Ebrahimi, M. Sedighi, Designing of ECAP parameters based on strain distribution uniformity, *Prog. Nat. Sci. Mater. Int.* 22 (2012) 452–460, <https://doi.org/10.1016/j.pnsc.2012.08.001>.
- R. Kulagin, Y. Beygelzimer, Y. Estrin, Y. Ivanisenko, B. Baretzky, H. Hahn, R. Kulagin, Y. Beygelzimer, Y. Estrin, Y. Ivanisenko, B. Baretzky, H. Hahn, A mathematical model of deformation under High Pressure Torsion Extrusion, *Metals (Basel)* 9 (2019) 306, <https://doi.org/10.3390/met9030306>.
- G. Ribárik, J. Gubicza, T. Ungár, Correlation between strength and microstructure of ball-milled Al–Mg alloys determined by X-ray diffraction, *Mater. Sci. Eng. A* 387–389 (2004) 343–347, <https://doi.org/10.1016/J.MSEA.2004.01.089>.
- Y. Estrin, A. Molotnikov, C.H.J. Davies, R. Lapovok, Strain gradient plasticity modelling of high-pressure torsion, *J. Mech. Phys. Solids* 56 (2008) 1186–1202, <https://doi.org/10.1016/J.JMPS.2007.10.004>.
- E.A. El-Danaf, M.S. Soliman, A.A. Almajid, M.M. El-Rayes, Enhancement of mechanical properties and grain size refinement of commercial purity aluminum 1050

- processed by ECAP, Mater. Sci. Eng. A 458 (2007) 226–234, <https://doi.org/10.1016/J.MSEA.2006.12.077>.
- [22] Y. Cao, L. He, Y. Zhou, P. Wang, J. Cui, Contributions to yield strength in an ultrafine grained 1050 aluminum alloy after DC current annealing, Mater. Sci. Eng. A 674 (2016) 193–202, <https://doi.org/10.1016/J.MSEA.2016.06.084>.
- [23] M. Naderi, M. Peterlechner, S.V. Divinski, G. Wilde, The effect of pre-annealing on defects, microstructure and recrystallization of ultra-fine grained Al produced by high-pressure torsion, Mater. Sci. Eng. A 708 (2017) 171–180, <https://doi.org/10.1016/J.MSEA.2017.09.126>.
- [24] F. Wetscher, A. Vorhauer, R. Pippan, Strain hardening during high pressure torsion deformation, Mater. Sci. Eng. A 410–411 (2005) 213–216, <https://doi.org/10.1016/J.MSEA.2005.08.027>.
- [25] R. Pippan, F. Wetscher, M. Hafok, A. Vorhauer, I. Sabirov, The limits of refinement by severe plastic deformation, Adv. Eng. Mater. 8 (2006) 1046–1056, <https://doi.org/10.1002/adem.200600133>.
- [26] A. Vorhauer, R. Pippan, On the onset of a steady state in body-centered cubic iron during severe plastic deformation at low homologous temperatures, Metall. Mater. Trans. A 39 (2008) 417–429, <https://doi.org/10.1007/s11661-007-9413-1>.
- [27] R. Pippan, S. Scheriau, A. Taylor, M. Hafok, A. Hohenwarter, A. Buchmaier, Saturation of fragmentation during severe plastic deformation, Ann. Rev. Mater. Res. 40 (2010) 319–343, <https://doi.org/10.1146/annurev-matsci-070909-104445>.
- [28] R. Valiev, R. Islamgaliev, I. Alexandrov, Bulk nanostructured materials from severe plastic deformation, Prog. Mater. Sci. 45 (2000) 103–189, [https://doi.org/10.1016/S0079-6425\(99\)00007-9](https://doi.org/10.1016/S0079-6425(99)00007-9).
- [29] R.Z. Valiev, Y.V. Ivanisenko, E.F. Rauch, B. Baudalet, Structure and deformation behaviour of Armco iron subjected to severe plastic deformation, Acta Mater. 44 (1996) 4705–4712, [https://doi.org/10.1016/S1359-6454\(96\)00156-5](https://doi.org/10.1016/S1359-6454(96)00156-5).
- [30] A.S. Edelstein, R.C. Cammarata, Nanomaterials: Synthesis, Properties, and Applications, Institute of Physics Pub, Bristol, 1998.
- [31] F.A. Mohamed, A dislocation model for the minimum grain size obtainable by milling, Acta Mater. 51 (2003) 4107–4119, [https://doi.org/10.1016/S1359-6454\(03\)00230-1](https://doi.org/10.1016/S1359-6454(03)00230-1).
- [32] Y.H. Zhao, X.Z. Liao, T.G. Langdon, Influence of stacking fault energy on nanostructure formation under high pressure torsion, Mater. Sci. Eng. A 410–411 (2005) 188–193, <https://doi.org/10.1016/J.MSEA.2005.08.074>.
- [33] Y.H. Zhao, X.Z. Liao, Z. Horita, T.G. Langdon, Influence of stacking fault energy on the minimum grain size achieved in severe plastic deformation, Mater. Sci. Eng. A 463 (2007) 22–26, <https://doi.org/10.1016/J.MSEA.2006.08.119>.
- [34] L. Kurmanaeva, Y. Ivanisenko, J. Markmann, C. Kübel, A. Chuvilin, S. Doyle, R.Z. Valiev, H.-J. Fecht, Grain refinement and mechanical properties in ultrafine grained Pd and Pd–Ag alloys produced by HPT, Mater. Sci. Eng. A 527 (2010) 1776–1783, <https://doi.org/10.1016/J.MSEA.2009.11.001>.
- [35] J. Gubicza, Defect Structure and Properties of Nanomaterials, Woodhead Publishing, Duxford, 2017, <https://doi.org/10.1016/B978-0-08-101917-7.05001-5>.
- [36] J. Fu, F. Barlat, J.-H. Kim, F. Pierron, Identification of nonlinear kinematic hardening constitutive model parameters using the virtual fields method for advanced high strength steels, Int. J. Solids Struct. 102–103 (2016) 30–43, <https://doi.org/10.1016/J.IJUSOLSTR.2016.10.020>.
- [37] P. Koprowski, R. Bogucki, M. Bieda, J. Kawalko, K. Sztwiertnia, Thermal stability of AA1050 aluminum alloy after equal channel angular pressing, Arch. Metall. Mater. 62 (2017) 777–786, <https://doi.org/10.1515/amm-2017-0116>.
- [38] L.H. Su, C. Lu, L.Z. He, L.C. Zhang, P. Guagliardo, A.K. Tieu, S.N. Samarin, J.F. Williams, H.J. Li, Study of vacancy-type defects by positron annihilation in ultrafine-grained aluminum severely deformed at room and cryogenic temperatures, Acta Mater. 60 (2012) 4218–4228, <https://doi.org/10.1016/j.actamat.2012.04.003>.
- [39] Y. Chen, Y. Li, L. He, C. Lu, H. Ding, Q. Li, The influence of cryoECAP on microstructure and properties of commercial pure aluminum, Mater. Lett. 62 (2008) 2821–2824, <https://doi.org/10.1016/j.matlet.2008.01.091>.
- [40] S.N. Alhajeri, N. Gao, T.G. Langdon, Hardness homogeneity on longitudinal and transverse sections of an aluminum alloy processed by ECAP, Mater. Sci. Eng. A 528 (2011) 3833–3840, <https://doi.org/10.1016/j.msea.2011.01.074>.
- [41] C. Xu, T.G. Langdon, The development of hardness homogeneity in aluminum and an aluminum alloy processed by ECAP, J. Mater. Sci. 42 (2007) 1542–1550, <https://doi.org/10.1007/s10853-006-0899-5>.
- [42] M.C.V. Vega, R.E. Bolmaro, M. Ferrante, V.L. Sordi, A.M. Kliauga, The influence of deformation path on strain characteristics of AA1050 aluminum processed by equal-channel angular pressing followed by rolling, Mater. Sci. Eng. A 646 (2015) 154–162, <https://doi.org/10.1016/j.msea.2015.07.083>.
- [43] L. Su, C. Lu, H. Li, G. Deng, K. Tieu, Investigation of ultrafine grained AA1050 fabricated by accumulative roll bonding, Mater. Sci. Eng. A 614 (2014) 148–155, <https://doi.org/10.1016/J.MSEA.2014.07.032>.
- [44] M. Salamati, S. Tamimi, S. Moturu, G. Sivaswamy, M. Qarni, A. Rosochowski, Microstructure and mechanical properties of Al-1050 during incremental ECAP, IOP Conf. Ser. Mater. Sci. Eng. 194 (2017) 012009, <https://doi.org/10.1088/1757-899X/194/1/012009>.
- [45] S. Bagherzadeh, K. Abrinia, Q. Han, Ultrasonic assisted equal channel angular extrusion (UAE) as a novel hybrid method for continuous production of ultra-fine grained metals, Mater. Lett. 169 (2016) 90–94, <https://doi.org/10.1016/j.matlet.2016.01.095>.
- [46] M.I. Abd El Aal, H. Yong Um, E. Yoo Yoon, H. Seop Kim, Microstructure evolution and mechanical properties of pure aluminum deformed by equal channel angular pressing and direct extrusion in one step through an integrated die, Mater. Sci. Eng. A 625 (2015) 252–263, <https://doi.org/10.1016/j.msea.2014.11.089>.
- [47] B. Tolaminejad, K. Dehghani, Microstructural characterization and mechanical properties of nanostructured AA1070 aluminum after equal channel angular extrusion, Mater. Des. 34 (2012) 285–292, <https://doi.org/10.1016/j.matdes.2011.08.003>.
- [48] B. Talebanpour, R. Ebrahimi, K. Janghorban, Microstructural and mechanical properties of commercially pure aluminum subjected to dual equal channel lateral extrusion, Mater. Sci. Eng. A 527 (2009) 141–145, <https://doi.org/10.1016/j.msea.2009.07.040>.
- [49] B. Mani, M. Jahedi, M.H. Paydar, A modification on ECAP process by incorporating torsional deformation, Mater. Sci. Eng. A 528 (2011) 4159–4165, <https://doi.org/10.1016/j.msea.2011.02.015>.
- [50] H. Alhosseini, M. Asle Zaem, K. Dehghani, A cyclic forward-backward extrusion process as a novel severe plastic deformation for production of ultrafine grains materials, Mater. Lett. 68 (2012) 204–208, <https://doi.org/10.1016/j.matlet.2011.10.037>.
- [51] J.C. Lee, H.K. Seok, J.Y. Suh, Microstructural evolutions of the Al strip prepared by cold rolling and continuous equal channel angular pressing, Acta Mater. 50 (2002) 4005–4019, [https://doi.org/10.1016/S1359-6454\(02\)00200-8](https://doi.org/10.1016/S1359-6454(02)00200-8).
- [52] H. Alhosseini, G. Faraji, A.F. Dizaji, K. Dehghani, Characterization of ultra-fine grained aluminum produced by accumulative back extrusion (ABE), Mater. Char. 68 (2012) 14–21, <https://doi.org/10.1016/j.matchar.2012.03.004>.
- [53] H. Jafarzadeh, K. Abrinia, Fabrication of ultra-fine grained aluminium tubes by RTES technique, Mater. Char. 102 (2015) 1–8, <https://doi.org/10.1016/j.matchar.2014.12.025>.
- [54] M. Kawasaki, S.N. Alhajeri, C. Xu, T.G. Langdon, The development of hardness homogeneity in pure aluminum and aluminum alloy disks processed by high-pressure torsion, Mater. Sci. Eng. A 529 (2011) 345–351, <https://doi.org/10.1016/j.msea.2011.09.039>.
- [55] M. Kawasaki, H.J. Lee, B. Ahn, A.P. Zhilyaev, T.G. Langdon, Evolution of hardness in ultrafine-grained metals processed by high-pressure torsion, J. Mater. Res. Technol. 3 (2014) 311–318, <https://doi.org/10.1016/j.jmrt.2014.06.002>.
- [56] Y. Ito, K. Edalati, Z. Horita, High-pressure torsion of aluminum with ultrahigh purity (99.9999%) and occurrence of inverse Hall-Petch relationship, Mater. Sci. Eng. A 679 (2017) 428–434, <https://doi.org/10.1016/j.msea.2016.10.066>.
- [57] A.P. Zhilyaev, K. Oh-ishi, T.G. Langdon, T.R. McNelley, Microstructural evolution in commercial purity aluminum during high-pressure torsion, Mater. Sci. Eng. A 410–411 (2005) 277–280, <https://doi.org/10.1016/j.msea.2005.08.044>.
- [58] H. Lanjewar, L. Kestens, P. Verleysen, A novel method for severe plastic deformation at high strain rate, EPJ Web Conf. 183 (2018) 03008, <https://doi.org/10.1051/epjconf/201818303008>.
- [59] J. Guo, X. Zhang, D. Kong, S.H. Joo, W. Kim, H.S. Kim, X. Zhang, Microstructure, micro-hardness, and corrosion resistance of commercial purity Al processed by hollow-cone high-pressure torsion, Adv. Eng. Mater. 21 (2019) 1–7, <https://doi.org/10.1002/adem.201809095>.
- [60] T. Ungár, G. Tichy, J. Gubicza, R.J. Hellmig, Correlation between subgrains and coherently scattering domains, Powder Diffr. 20 (2005) 366–375, <https://doi.org/10.1154/1.2135313>.
- [61] B. Omrانpour, L. Kommel, V. Mikli, E. García, J. Huot, Nanostructure development in refractory metals: ECAP processing of Niobium and Tantalum using indirect-extrusion technique, Int. J. Refract. Metals Hard Mater. 79 (2019), <https://doi.org/10.1016/j.ijrmhm.2018.10.018>.
- [62] J. Čížek, M. Janeček, T. Krajčák, J. Stráská, P. Hruška, J. Gubicza, H.S. Kim, Structural characterization of ultrafine-grained interstitial-free steel prepared by severe plastic deformation, Acta Mater. 105 (2016) 258–272, <https://doi.org/10.1016/J.ACTAMAT.2015.12.039>.

**Article II:**

B. Omranpour, L. Kommel, V. Mikli, E. Garcia, J. Huot, Nanostructure development in refractory metals: ECAP processing of Niobium and Tantalum using indirect-extrusion technique, *Int. J. Refract. Met. Hard Mater.* 79 (2019).





Contents lists available at ScienceDirect

# International Journal of Refractory Metals & Hard Materials

journal homepage: [www.elsevier.com/locate/IJRMHM](http://www.elsevier.com/locate/IJRMHM)

## Nanostructure development in refractory metals: ECAP processing of Niobium and Tantalum using indirect-extrusion technique

Babak Omranpour<sup>a,b,c,\*</sup>, Lembit Kommel<sup>a</sup>, Valdek Mikli<sup>a</sup>, Edgar Garcia<sup>b</sup>, Jacques Huot<sup>d</sup>

<sup>a</sup> Department of Materials Engineering, Tallinn University of Technology, 19086 Tallinn, Estonia

<sup>b</sup> Faculty of Mechanical and Electrical Engineering, Universidad Autónoma de Nuevo León (UANL), 66455 San Nicolás de los Garza, Mexico

<sup>c</sup> Institute of Nanotechnology (INT), Karlsruhe Institute of Technology (KIT), 76021 Karlsruhe, Germany

<sup>d</sup> Hydrogen Research Institute, Université du Québec à Trois-Rivières, Trois-Rivières G9A 5H7, QC, Canada

### ARTICLE INFO

#### Keywords:

Refractory metals  
Indirect-extrusion ECAP  
Nanostructured metals  
Hardness  
Finite element method

### ABSTRACT

A modified ECAP die by implementing the principles of indirect extrusion was fabricated to process refractory metals of Niobium and Tantalum. The main advantage of this modified technique over conventional method of ECAP is the reduction of frictional force during extrusion. Finite Element Method was utilized to demonstrate the difference between the extruding loads during the process. Several samples of Niobium and Tantalum were subjected to ECAP in different passes. Analysis of experimental results demonstrated a dramatic improvement in mechanical properties. Similarly, microstructure and XRD analyses of the samples showed noticeable enhancement in grain refinement of metals towards nanoscale.

### 1. Introduction

Severe Plastic Deformation (SPD) techniques have been the focus of attention during the last decades by virtue of their exceptional abilities in hardening, enhancement of mechanical properties and microstructural development. Compared with other methods of hardening mechanisms (precipitation hardening, solid solution hardening, etc) SPD gives a superior performance by using the mechanism of grain refinement, because the other mechanisms usually reduce ductility when improving hardness. However, some studies in this area showed that ductility could be retained in SPD processed materials [1,2]. Interestingly enough, other case studies showed that SPD can simultaneously improve ductility and strength in metals [3–5]. All these characteristics have inspired scientists to use SPD techniques for processing of metals and alloys towards improvement of mechanical properties or microstructure development. Among different materials, refractory metals hold a unique position in high performance applications because of high melting point (usually above 2000 K), low vapor pressure, creep resistance at high temperatures, and high corrosion resistance [6]. Niobium (Nb) and Tantalum (Ta), respectively, are two types of refractory/transition metals that attracted many attentions for research due to their applications in aerospace industries, electronics, telecommunications and semiconductors [7]. Particularly in the field of SPD, deformation mechanisms, microstructure evolution and mechanical properties of these metals were reported in different works [8–14].

These studies mainly used the two famous techniques of SPD for processing, namely Equal Channel Angular Pressing (ECAP) in the case of bulk metal processing, and High Pressure Torsion (HPT) in the case of thin-disk processing.

Equal Channel Angular Pressing or briefly ECAP is probably the most favorite technique for bulk-SPD materials because of its simplicity and straightforwardness [15,16]. This technique is based on extrusion of a sample through a bent channel by using a plunger [17]. Deformation in this process is simple shear which is applied at the cross section of the channel (Fig. 1). This method is a simple forward extrusion technique with the benefit of no change in the dimensions of the billet after extrusion, so there is a possibility to extrude the same sample again for several times and apply more deformation into the materials [18].

However, direct extrusion techniques in general, have a main drawback, that is the friction between the die and workpiece. Conventional ECAP as a type of direct extrusion, has the same inevitable consequence. Friction not only increases the deformation load during processing, but also it may affect the materials flow, inhomogeneity of deformation, surface finish of the workpiece, and die wear [20]. This problem would be more critical in practice when material is soft and tends to stick to the die, such as Niobium. All these issues came together to initiate the idea of indirect extrusion in ECAP in order to reduce the friction during the process.

In this scenario, the main idea of using Indirect Extrusion ECAP (IE-

\* Corresponding author at: Department of Materials Engineering, Tallinn University of Technology, 19086 Tallinn, Estonia.

E-mail address: [omranpou@uqtr.ca](mailto:omranpou@uqtr.ca) (B. Omranpour).

<https://doi.org/10.1016/j.ijrmhm.2018.10.018>

Received 14 July 2018; Received in revised form 21 October 2018; Accepted 27 October 2018

Available online 30 October 2018

0263-4368/ © 2018 Elsevier Ltd. All rights reserved.

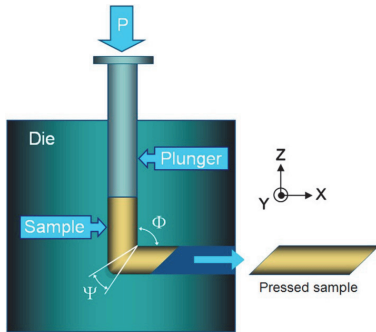


Fig. 1. Illustration of ECAP [19].

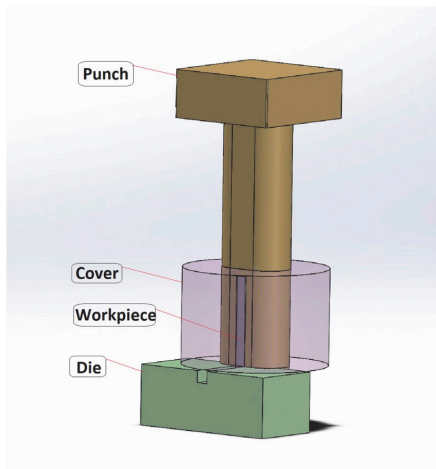


Fig. 2. Schematic representation of Indirect-Extrusion ECAP die.

ECAP) was drawn from the fact that in an earlier attempt, an ECAP die with conventional design of direct extrusion was employed to fabricate Ultra-fine grained Tantalum. This die failed during the third extrusion with a fracture in the punch since mechanical properties of materials

increased and the punch was not able to extrude the sample with a length of 120 mm through the channel during the third pass. However, as it is shown in the following, using indirect extrusion technique made it possible to process the same material up to twelve passes of ECAP.

Fundamental concept of IE-ECAP was proposed by Mathieu et al. [21]. They could successfully run the test on Copper and Titanium with a reduction in the required load for pressing the samples. Surendarnath et al. [22] used an Indirect extrusion die for ECAP processing of Aluminum alloys and reported considerable improvement in mechanical properties and reduction in friction. In another report, indirect extrusion technique was used in extrusion of tubular-shape samples to produce Aluminum tubes with Ultra-Fine Grained (UFG) microstructure [23]. Nonetheless, up to now, there has been no report about the effect of indirect-extrusion ECAP on refractory metals. This work, therefore, aims to apply indirect extrusion ECAP on refractory metals: Niobium and Tantalum with a focus on mechanical and microstructural properties. In addition to that, numerical analysis of direct and indirect extrusion methods has been carried out to compare the effect of friction force in each process.

## 2. Material and methods

### 2.1. Die setup and process parameters

An Indirect Extrusion ECAP (IE-ECAP) die was designed and manufactured for processing of materials. This die consists of three parts: Punch, Cover and channel die. The punch can move upward and downward freely but cover and die both are fixed (Fig. 2).

There is a narrow slot in the punch where the workpiece can be embedded in. Therefore, workpiece is surrounded from three sides by the punch and from one side by the interior surface of the cover. By pressing the punch and moving it downward, workpiece is therefore going down and there is no friction between the workpiece and punch as they move together. Below the cover is the channel die which provides a space to extrude the workpiece from the die. There is a jutting platform at the beginning of the channel which prevents the workpiece from further downward movement, making the materials change the direction and flow through the channel (Fig. 3).

The sequence of the process along with processed samples are represented in Fig. 4. In this figure, 3D modeling of the die is presented in cutaway view to show the middle section of assembly and the sequence of workpiece deformation during the process.

This ECAP die has the following geometrical parameters: channel angle ( $\phi$ ) of  $90^\circ$  and corner angle ( $\psi$ ) of  $0^\circ$ . Processing route Bc ( $90^\circ$  of clockwise rotation of workpiece billet between each pass [17])

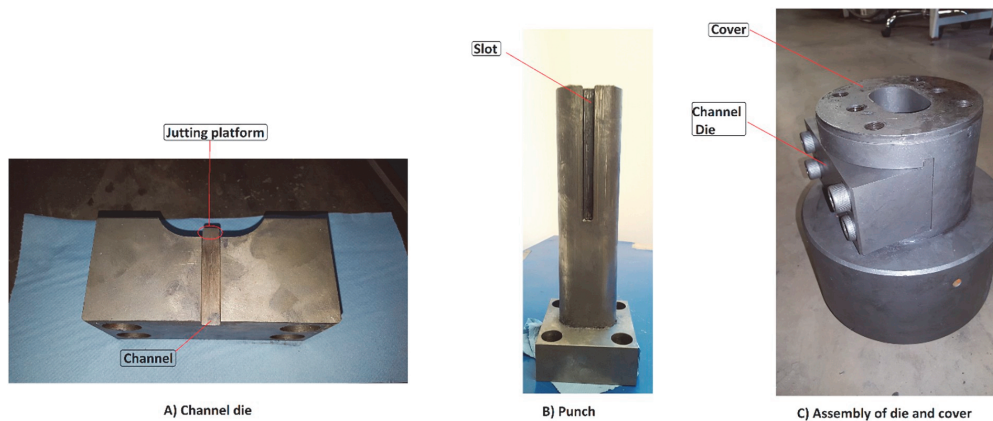


Fig. 3. ECAP die components.



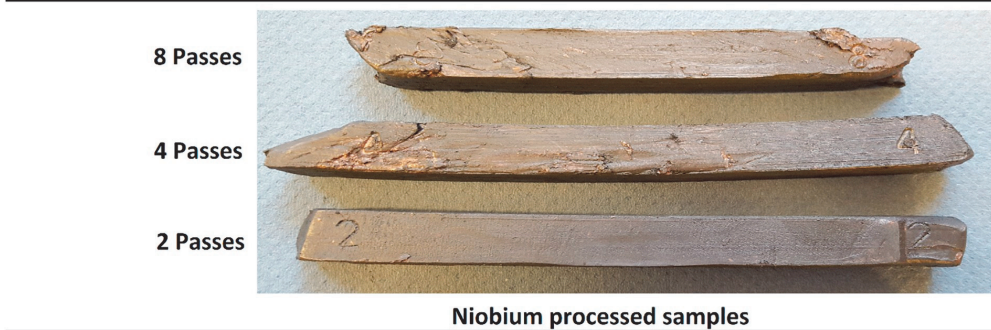
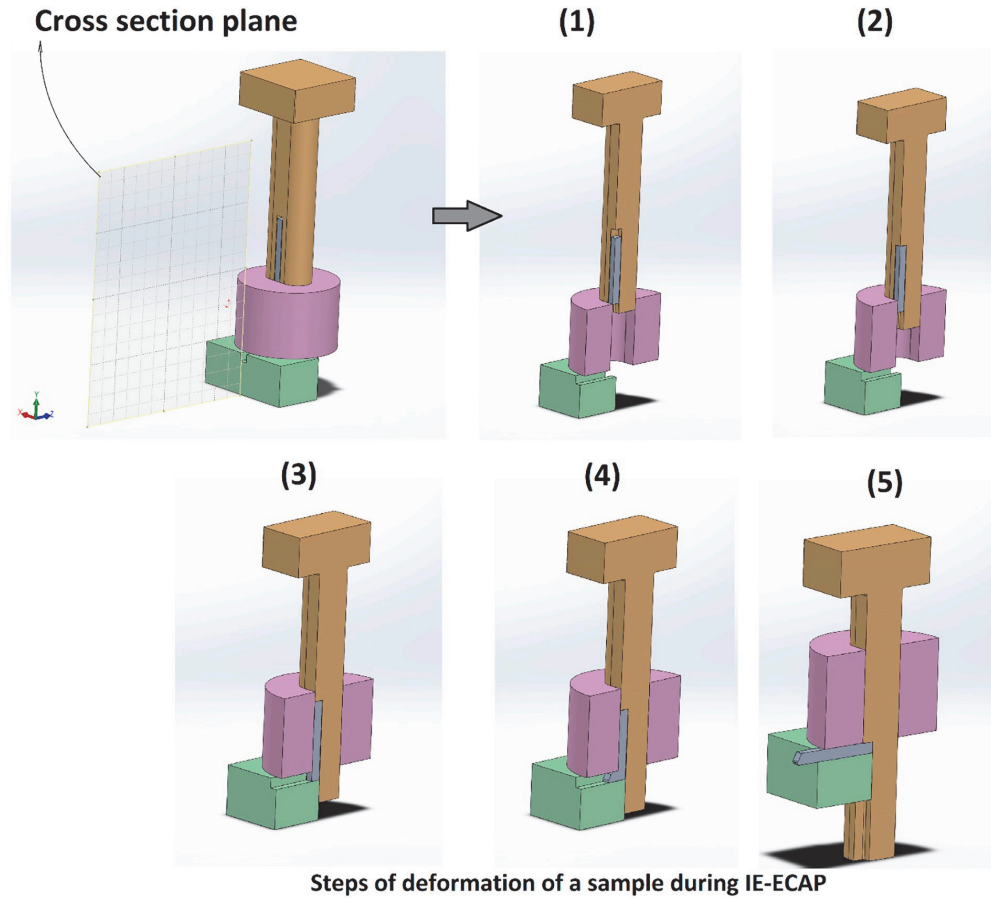


Fig. 4. Demonstration of deformation in IE-ECAP die & processed samples after 2, 4, and 8 passes of ECAP.

**Table 1**  
Chemical composition of samples.

	Chemical composition (%wt)		
Niobium samples	Niobium (Nb)	Yttrium (Y)	Nickel (Ni)
	Base	1.38	0.15
Tantalum samples	Tantalum (Ta)	Gallium (Ga)	Nickel (Ni)
	Base	0.98	0.12

conducted to all samples with extruding speed of 6 mm/s.

**2.2. Experimental method**

The two refractory metals, Niobium and Tantalum were studied for ECAP processing in this work. All samples were received in square cross-sections with the following chemical compositions (Table 1):

As-received materials of Niobium and Tantalum were cut and

**Table 2**  
Sample IDs and their specifications.

	ECAP pass no.	Sample ID
Niobium samples	As-received	Nb0
	1	Nb1
	2	Nb2
	4	Nb4
	8	Nb8
Tantalum samples	As-received	Ta0
	2	Ta2
	6	Ta6
	12	Ta12

prepared with precise dimensions of 12 mm × 12 mm × 120 mm. Niobium samples were foiled in copper sheets before ECAP processing to prevent them from cold welding to the ECAP die. All ECAP experiments were performed at room temperature.

The following IDs and numbers are assigned to the processed samples (Table 2):

During the process, pressure gage of the press machine was monitored to record the pressure applied to the punch in order for comparison and verification of simulation results.

A SHIMADZU HMV Micro-hardness tester conducted Vickers testing to the samples. Sixteen points through two perpendicular lines at transverse cross-section of samples were selected, and a pressing load of

200 g with a dwelling time of 15 s applied to the indenter to measure the hardness.

All samples of Niobium and Tantalum were initially polished with sand papers and then finely polished with highly concentrated diamond particles for metallography investigations. An Ultrasonic polishing machine (Buehler Vibromet) performed the final polishing process using Colloidal silica particles of 0.05 Microns for one hour. Microstructure images were obtained by an Ultra-55 Zeiss SEM machine using backscattered electron imaging. Image analysis of the results was obtained by using ImageJ Ver.1.51. A PANalytical Empyrean facility performed X-Ray Diffraction (XRD) test on the samples with CuK $\alpha$  radiation of  $\lambda = 1.5406 \text{ \AA}$ , operated at 45KV, and 40 mA with a pixel detector in Bragg-Brentano geometry. Scans were carried out in a  $2\theta$  range from  $35^\circ$  to  $125^\circ$  with a scan step of  $0.013^\circ$  and 10 s per step in continuous mode. PANalytical Highscore Plus software-Version 3.0 was used for refinement and analysis of the patterns. Microstrains and crystallite size were estimated from X-ray diffraction patterns using Williamson-Hall method.

2.3. Finite element modeling (FEM)

Both direct extrusion and Indirect extrusion processes were modeled and simulated by DEFORM™-Version 11. FEM modeling and analysis in this study rest on the following assumptions: Extruding speed of 6 mm/s; friction coefficient of  $\mu = 0.12$ ; neglecting heat generation which is

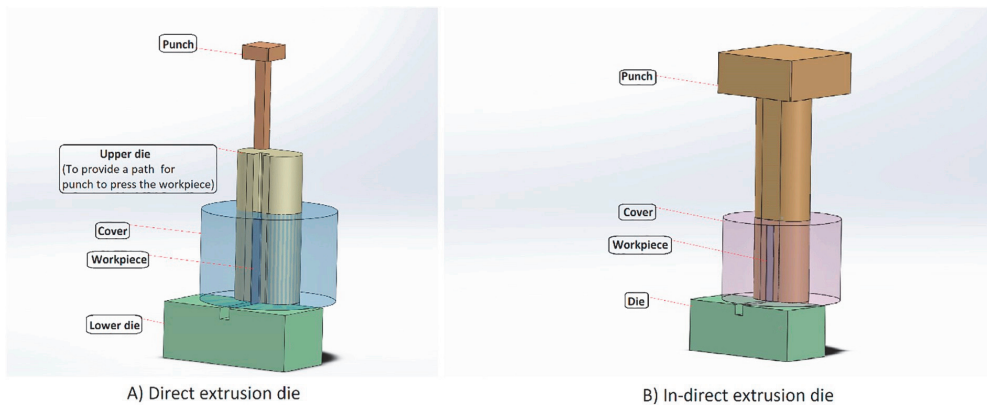


Fig. 5. Modeling of ECAP processing in direct extrusion vs. Indirect extrusion.

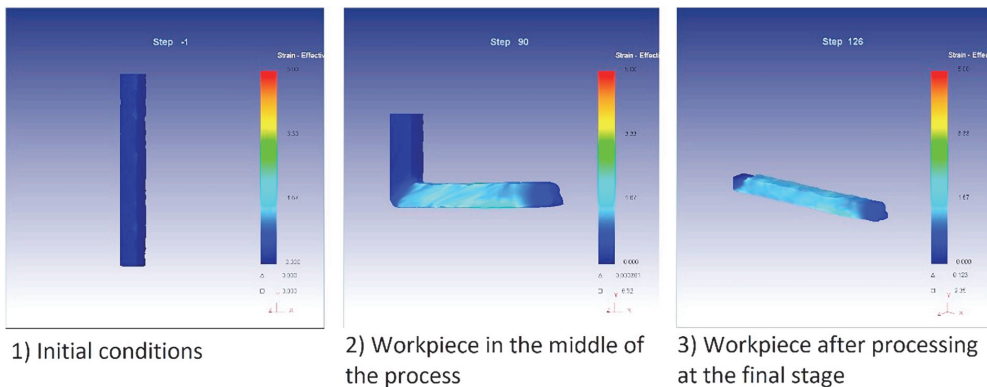


Fig. 6. Simulated process of IE-ECAP on a workpiece.



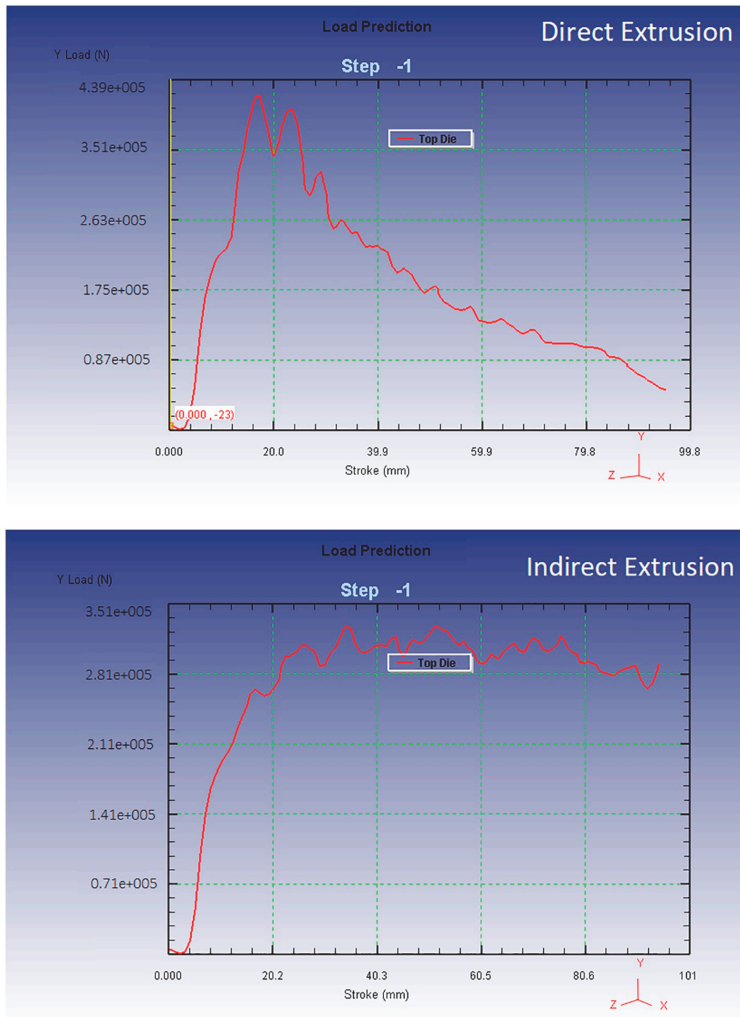


Fig. 7. Predicted load by FEM simulations for direct-extrusion and Indirect-extrusion ECAP.

associated with plastic deformation and assuming the die as a rigid body. In the first step, simulation results were verified by comparing the results of the load applied to extrude the workpiece during the experiments with that of force in FEM simulations; and validation was satisfied.

### 3. Results and discussion

#### 3.1. Simulation results and FEM analysis

CAD Modeling of the process in both direct extrusion and indirect extrusion dies is shown in Fig. 5.

As indicated in Introduction (Section 1), the idea of this simulation is to analyse the effect of indirect extrusion on friction and extruding load in ECAP with respect to its counterpart, direct extrusion method. Some stages of simulations are shown in Fig. 6.

Fig. 7 plots the results of simulations of load-displacement for both cases of direct extrusion and indirect extrusion. As a matter of fact, the

trends in the diagrams of Fig. 7 are fairly compatible with theoretical concepts and experimental force diagrams in literature [24,25]. According to the graphs, a peak load of  $\sim 420$  KN at the beginning of ECAP was required to extrude the punch for direct extrusion and it decreased with punch movement (Stroke). This peak load and succeeding decrease in the diagram are associated with friction of the workpiece and ECAP channel at the beginning of the process. By further processing, the length of undeformed workpiece which is in contact with the channel, will gradually decrease. Consequently, less friction will be generated between undeformed workpiece and ECAP channel [26]. By contrast, this diagram for indirect extrusion is almost constant ( $\sim 320$  KN) from the beginning of deformation to the end because this force is mainly dedicated to deformation of materials and not to overcome the friction force. Since the material was considered to be homogeneous for simulations, the required force for deformation at any stage of deformation is therefore relatively constant.

In an overall assessment, a decrease rate of  $\sim 23\%$  for the maximum load of extrusion can be observed in IE-ECAP due to reducing the

**Table 3**  
Vickers microhardness of Niobium and Tantalum before and after ECAP passes.

	Sample id	Hardness (HV)	Enhancement rate <sup>a</sup> (%)
Niobium	Nb0	81	–
	Nb1	109	35
	Nb2	131	20
	Nb4	155	18
	Nb8	176	14
Tantalum	Ta0	103	–
	Ta2	184	79
	Ta6	221	20
	Ta12	240	9

<sup>a</sup> Enhancement rate is measured based on the increase of hardness in each step in compared with the previous step.

friction between the workpiece and die.

3.2. Mechanical properties

Table 3 shows the results of Vickers hardness testing on the samples and the rate of enhancement in each step. These results show that hardness of niobium improved by 117% after eight passes of ECAP and for Tantalum the improvement was 133% after twelve passes.

Another point about hardness results is the enhancement rate in hardness. Fundamentally, microhardness values in metals tend to increase by increasing the pass numbers of ECAP but the rate of increase is different in each step. As it is shown in the results, niobium hardness increased by ~34% only after the first pass of ECAP from the initial harness value of 81 HV to 109 HV. With further processing, this rate of

increase changed to ~20% for the second pass from 109 HV to 131 HV; and this change was even smaller in higher pass numbers of ECAP, as it decreased to ~14% for the final step, from pass number 4 to pass number 8. This trend is also evident in Tantalum. Hardness of Tantalum samples improved by ~79% within one pass, whereas this change is smaller with additional ECAP processing; and in the last step, this rate is nearly ~9% from pass number 6 to pass number 12. Therefore, as it can be seen, hardness values approach to a saturation level by applying additional pass numbers of ECAP. This level is usually named 'saturation hardness' in ECAP [27]. Similar cases of saturation in mechanical properties and microstructure refinement were also reported for other materials in earlier studies such as aluminum [1,28] and copper [29,30].

3.3. Microstructural evolution

3.3.1. SEM

Evolution of microstructure by IE-ECAP is illustrated in Fig. 8. As it can be observed in the images, IE-ECAP effectively reduced the grain size in both metals. In the case of Niobium, grain refinement occurred in the samples from an average grain size of ~1280 nm towards final average grain size of ~420 nm after 8 passes of ECAP; and the same procedure happened to Tantalum from an average grain size of ~1170 nm to the final average size of ~469 nm after 12 passes. As expected, Aspect Ratio (the ratio of the greatest diameter to the smallest one in each grain, AR), increased after ECAP in both materials due to exerting severe deformation and increasing heterogeneity in microstructural shape of the grains. This ratio changed from an initial value of ~1.73 to the final value of ~1.91 in Niobium, and from ~1.71 to

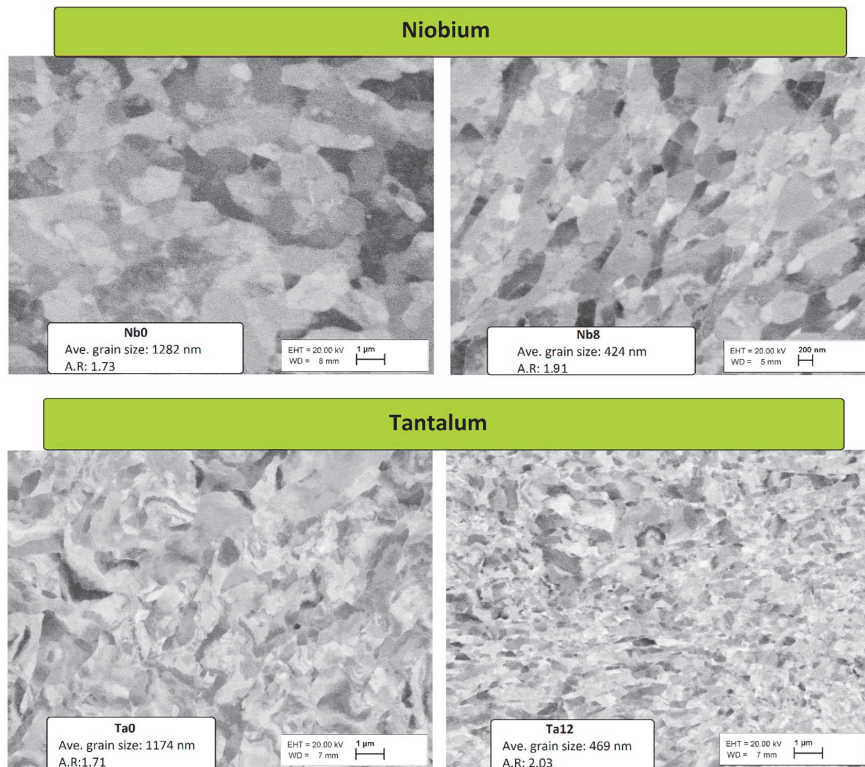


Fig. 8. SEM images of samples before and after ECAP.

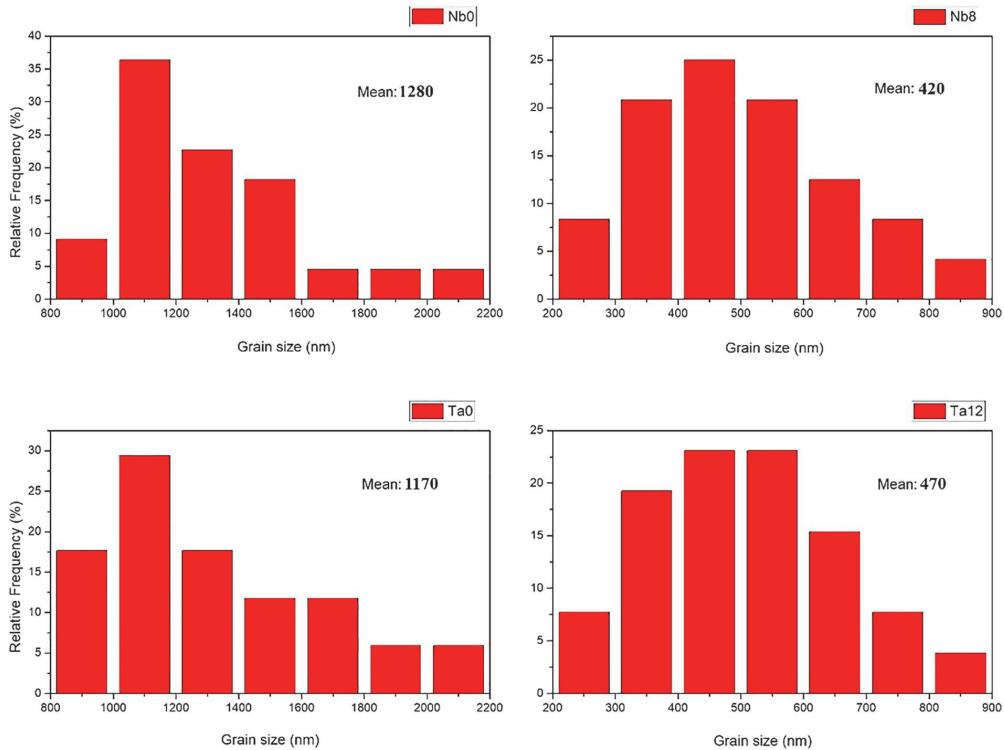


Fig. 9. Distribution of grains obtained from Fig. 8; measurements were made by ImageJ software.

~2.03 in Tantalum. Comparison of AR in both metals shows that the grains in Tantalum were more elongated during processing. But it should be noted that Tantalum samples were subjected to ECAP four times more than Niobium samples.

Analysis of grain size distribution is presented in Fig. 9. As it is displayed in the graphs, distribution pattern in the initial samples is mainly localized around the mean value (the average grain size); whereas distribution in the processed samples seems likely to be more uniform without presenting a lofty peak. According to these results, grain refinement in both metals occurred almost in the same order, from microscale towards submicron dimensions.

### 3.3.2. X-ray diffraction patterns

XRD patterns of Niobium and Tantalum are provided in Fig. 10. Peak broadening of samples after processing can be observed in Nb and Ta which are related to (1) refinement of microstructure and (2) accumulation of micro strains due to lattice distortions in the material [31–33]. Therefore, micro strain and crystallite size can be quantified by means of measuring Full Width at Half-Maximum (FWHM) of the peaks and following the principles of Williamson-Hall theory [34,35]:

$$\beta \cos\theta = \frac{K\lambda}{D} + 4\epsilon \cdot \sin\theta \tag{1}$$

where  $\beta$  is the peak broadening (FWHM) in rad,  $\lambda$  is the wavelength of the X-ray beam ( $\lambda = 0.1542$  nm for  $\text{Cu-K}\alpha$ ),  $K$  is the Scherrer factor ( $K=0.94$ ),  $D$  is the crystallite size,  $\epsilon$  is the lattice strain, and  $\theta$  is the Bragg angle.

The intrinsic value of  $\beta$  is different than experimental profile ( $\beta_{\text{exp}}$ ) measured in XRD patterns. The intrinsic value can be measured by stripping off the instrumental profile ( $\beta_{\text{ins}}$ ) from the experimental value

( $\beta_{\text{exp}}$ ) using Eq. (2) [36]:

$$\frac{\beta}{\beta_{\text{exp}}} = 1 - \left( \frac{\beta_{\text{ins}}}{\beta_{\text{exp}}} \right)^2 \tag{2}$$

Eq. (1) can be modeled as equation of a line: ( $Y = A + m \cdot X$ ) by considering  $\frac{K\lambda}{D}$  and  $\epsilon$  as the intersection and slope of the line, respectively, and plotting  $\beta \cos\theta$  versus  $4\sin\theta$ . Accordingly, values of  $D$  and  $\epsilon$  can be derived by applying linear extrapolation to this plot [37,38]. Fig. 11 shows this extrapolation for Niobium and Tantalum.

Table 4 summarizes the results of analysis and values of strain and crystallite size for the processed samples.

Comparison of results of XRD analysis and SEM reveals a slight difference between the crystallite size obtained by XRD and the grain size measured by SEM. As shown earlier in Fig. 8, the average grain size approximated to 420 nm for Nb8, and 470 nm for Ta12; whereas these values for crystallite size were estimated to be 180 nm and 290 nm for Nb8 and Ta12, respectively (Table 4). Earlier investigations about plastically deformed materials also reported the difference between grain size and crystallite size in materials where the average grain size measured by electron microscopy techniques was bigger than the crystallite size estimated by XRD analysis [36,38].

A quick observation on Fig. 12 may explain this difference better. In principle, Severe Plastic Deformations lead to the emergence of defects and misorientations in crystals. Applying excessive deformations may result in accumulation of defects at the grain boundaries, and also appearance of misorientations with Low Angle Boundaries (LAB) [39]. These misorientations inside the grains, are referred to as sub-grains in crystalline materials [40,41]. Studies on XRD analysis of SPD processed materials showed that crystallite size is basically equal to subgrain size

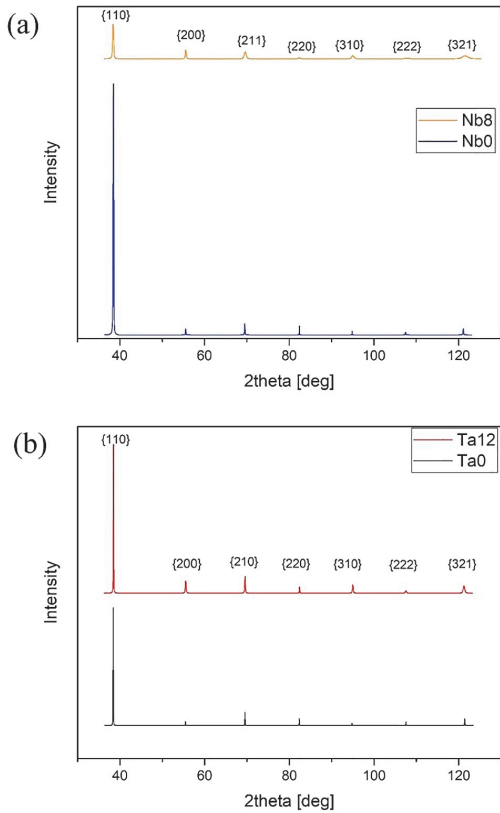


Fig. 10. XRD patterns of (a) Niobium, (b) Tantalum.

or dislocations cells formed by deformations but it could be smaller than the grain size values obtained by electron microscopes [42].

4. Conclusion

In the present work, two types of refractory metals, Niobium and Tantalum, were processed for the first time by Indirect Extrusion ECAP (IE-ECAP) to fabricate nanostructured metals. The main outcomes of this study are summarized below:

- IE-ECAP is a viable alternative to conventional ECAP. This technique is able to process the materials to higher numbers of ECAP passes by virtue of reducing the friction between the die and workpiece. The primary ECAP die with conventional direct extrusion method failed with a fracture in the punch during the third pass of extruding Tantalum, whereas the modified die (IE-ECAP) could extrude the same material up to twelve passes.
- FEM simulations proved considerable reduction of extruding load (~23%) for the first pass by using IE-ECAP compared to conventional ECAP. Moreover, the shape of load-stroke diagram changed from a peak-load form to a smooth curve with relatively constant values during the deformation process.
- Hardness of Niobium and Tantalum samples significantly improved after IE-ECAP processing. This improvement was about 117% in Niobium after eight passes, and about 133% for Tantalum after twelve passes.
- Microstructural development in the metals successfully occurred

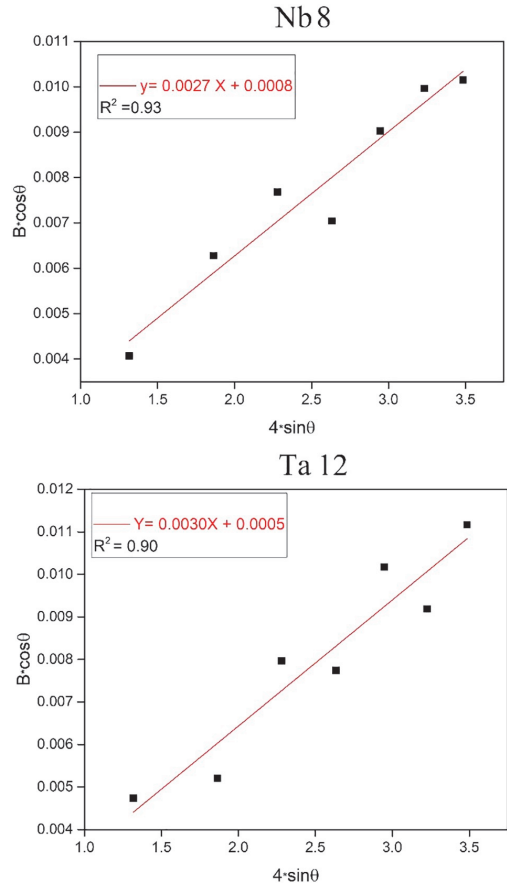


Fig. 11. Williamson-Hall plots for ECAPed Niobium and Tantalum.

Table 4

Results of XRD analysis.

	Micro strain (ε)%	Crystallite size (D) [nm]
Nb8	0.27	180
Ta12	0.30	290

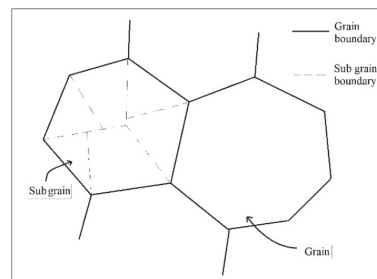


Fig. 12. Demonstration of grain Vs. sub grain.

after processing. Grain refinement in Niobium developed from an initial grain size of ~1280 nm to the final average grain size of ~420 nm, and for Tantalum occurred from the initial grain size of ~1170 nm to the final average grain size of ~470 nm. XRD results also showed peak broadening after ECAP which is related to the refinement in microstructure and accumulation of micro strains in the material.

## Declarations of interest

None.

## Acknowledgement

This project was funded in part by European social funds-DoraPlus-Estonia and in part by National Council of Science and Technology (CONACYT), Mexico. L. Kommel and V. Mikli would like to acknowledge the support from a collaborative project between Bulgarian Academy of Science and Estonian Academy of Science, (Estonian projects TAR16016, IUT1929 and IUT-T4).

## References

- [1] Z. Horita, T. Fujinami, M. Nemoto, T.G. Langdon, Equal-channel angular pressing of commercial aluminum alloys: grain refinement, thermal stability and tensile properties, *Metall. and Mater. Trans. A*. 31 (2000) 691–701, <https://doi.org/10.1007/s11661-000-0011-8>.
- [2] Y.T. Zhu, T.G. Langdon, The fundamentals of nanostructured materials processed by severe plastic deformation, *JOM* 56 (2004) 58–63, <https://doi.org/10.1007/s11837-004-0294-0>.
- [3] R.Z. Valiev, I.V. Alexandrov, Y.T. Zhu, T.C. Lowe, Paradox of strength and ductility in metals processed by severe plastic deformation, *J. Mater. Res.* 17 (2002) 5–8, <https://doi.org/10.1557/JMR.2002.0002>.
- [4] Y. Wang, M. Chen, F. Zhou, E. Ma, High tensile ductility in a nanostructured metal, *Nature* 419 (2002) 912–915, <https://doi.org/10.1038/nature01133>.
- [5] Z. Horita, K. Ohashi, T. Fujita, K. Kaneko, T.G. Langdon, Achieving high strength and high ductility in precipitation-hardened alloys, *Adv. Mater.* 17 (2005) 1599–1602, <https://doi.org/10.1002/adma.200500069>.
- [6] R. Grill, A. Gnadenberger, Niobium as mint metal: production-properties-processing, *Int. J. Refract. Met. Hard Mater.* 24 (2006) 275–282, <https://doi.org/10.1016/J.IJRMHM.2005.10.008>.
- [7] L. Kommel, UFG Microstructure processing by ecap from double electron-beam melted rare metal, *Mater. Sci. Forum* 584–586 (2008) 349–354, <https://doi.org/10.4028/www.scientific.net/MSF.584-586.349>.
- [8] Q. Wei, T. Jiao, S.N. Mathaudhu, E. Ma, K.T. Hartwig, K.T. Ramesh, Microstructure and mechanical properties of tantalum after equal channel angular extrusion (ECAE), *Mater. Sci. Eng. A* 358 (2003) 266–272, <https://doi.org/10.1016/j.msea.2003.03.005-8>.
- [9] H.R.Z. Sandim, H.H. Bernardi, B. Verlinden, D. Raabe, Equal channel angular extrusion of niobium single crystals, *Mater. Sci. Eng. A* 467 (2007) 44–52, <https://doi.org/10.1016/j.msea.2007.02.086>.
- [10] L. Zhu, M. Seefeldt, B. Verlinden, Three Nb single crystals processed by equal-channel angular pressing—part I: dislocation substructure, *Acta Mater.* 61 (2013) 4490–4503, <https://doi.org/10.1016/j.actamat.2013.04.018>.
- [11] L. Zhu, M. Seefeldt, B. Verlinden, Three Nb single crystals processed by equal-channel angular pressing—Part II: mesoscopic bands, *Acta Mater.* 61 (2013) 4504–4511, <https://doi.org/10.1016/j.actamat.2013.04.019>.
- [12] Y.R. Kolobov, B. Kieback, K.V. Ivanov, T. Weissgaerber, N.V. Girsova, Y.I. Pochivalov, G.P. Grabovetskaya, M.B. Ivanov, V.U. Kazhyanov, I.V. Alexandrov, The structure and microhardness evolution in submicrocrystalline molybdenum processed by severe plastic deformation followed by annealing, *Int. J. Refract. Met. Hard Mater.* 21 (2003) 69–73, [https://doi.org/10.1016/S0263-4368\(03\)00002-7](https://doi.org/10.1016/S0263-4368(03)00002-7).
- [13] Y. Wang, S. Goel, J.L. Sun, Y.M. Zhu, H. Yuan, J.T. Wang, The effect of temperature on activation volume of ultrafine grained tantalum, *Int. J. Refract. Met. Hard Mater.* 71 (2018) 232–238, <https://doi.org/10.1016/j.ijrmhm.2017.11.029>.
- [14] Z. Pan, F. Xu, S.N. Mathaudhu, L.J. Kecskes, W.H. Yin, X.Y. Zhang, K.T. Hartwig, Q. Wei, Microstructural evolution and mechanical properties of niobium processed by equal channel angular extrusion up to 24 passes, *Acta Mater.* 60 (2012) 2310–2323, <https://doi.org/10.1016/j.actamat.2011.12.019>.
- [15] A. de A. Mendes Filho, E.F. Prados, G.T. Valio, J.B. Rubert, V.L. Sordi, M. Ferrante, Severe plastic deformation by equal channel angular pressing: product quality and operational details, *Mater. Res.* 14 (2011) 335–339, <https://doi.org/10.1590/S1516-14392011005000045>.
- [16] F. Al-Mufadi, F. Djanvandroi, Equal-channel angular pressing of thin-walled copper tube, *Arab. J. Sci. Eng.* 40 (2015) 2785–2794, <https://doi.org/10.1007/s13369-015-1750-6>.
- [17] F. Djanvandroi, B. Omranpour, M. Sedighi, Artificial neural network modeling of ECAP process, *Mater. Manuf. Process.* 28 (2013) 276–281, <https://doi.org/10.1080/10426914.2012.667889>.
- [18] R.Z. Valiev, T.G. Langdon, Principles of equal-channel angular pressing as a processing tool for grain refinement, *Prog. Mater. Sci.* 51 (2006) 881–981, <https://doi.org/10.1016/j.pmatsci.2006.02.003>.
- [19] Y. Huang, T.G. Langdon, Advances in ultrafine-grained materials, *Mater. Today* 16 (2013) 85–93, <https://doi.org/10.1016/j.mattod.2013.03.004>.
- [20] C. Hu, Q. Yin, Z. Zhao, A novel method for determining friction in cold forging of complex parts using a steady combined forward and backward extrusion test, *J. Mater. Process. Technol.* 249 (2017) 57–66, <https://doi.org/10.1016/J.JMATPROTEC.2017.06.001>.
- [21] J.P. Mathieu, S. Suwas, A. Eberhardt, L.S. Tóth, P. Moll, A new design for equal channel angular extrusion, *J. Mater. Process. Technol.* 173 (2006) 29–33, <https://doi.org/10.1016/j.jmatprotec.2005.11.007>.
- [22] S. Surendarnath, K. Sankaranarayanan, B. Ravisankar, Experimental investigation on the performance of an improved equal channel angular pressing die, *IOP Conf. Ser. Mater. Sci. Eng.* 63 (2014) 1–8, <https://doi.org/10.1088/1757-899X/63/1/012011>.
- [23] S.H. Hosseini, K. Abrinia, G. Faraji, Applicability of a modified backward extrusion process on commercially pure aluminum, *Mater. Des.* 65 (2015) 521–528, <https://doi.org/10.1016/j.matdes.2014.09.043>.
- [24] A. García-Domínguez, J. Claver, A.M. Camacho, M.A. Sebastián, Comparative analysis of extrusion processes by finite element analysis, *Procedia Eng.* 100 (2015) 74–83, <https://doi.org/10.1016/j.proeng.2015.01.344>.
- [25] M.P. Groover, *Fundamentals of Modern Manufacturing: Materials, Processes, and Systems*, Fourth ed., J. Wiley & Sons, 2010, pp. 420–430.
- [26] A.V. Nagasekar, S.C. Yoon, Y. Tick-Hon, H.S. Kim, An experimental verification of the finite element modelling of equal channel angular pressing, *Comput. Mater. Sci.* 46 (2009) 347–351, <https://doi.org/10.1016/j.commatsci.2009.03.018>.
- [27] T.G. Langdon, Twenty-five years of ultrafine-grained materials: achieving exceptional properties through grain refinement, *Acta Mater.* 61 (2013) 7035–7059, <https://doi.org/10.1016/j.actamat.2013.08.018>.
- [28] S. Sabbaghianrad, T.G. Langdon, An evaluation of the saturation hardness in an ultrafine-grained aluminum 7075 alloy processed using different techniques, *J. Mater. Sci.* 50 (2015) 4357–4365, <https://doi.org/10.1007/s10853-015-8989-x>.
- [29] O.F. Higuera-Cobos, J.M. Cabrera, Mechanical, microstructural and electrical evolution of commercially pure copper processed by equal channel angular extrusion, *Mater. Sci. Eng. A* 571 (2013) 103–114, <https://doi.org/10.1016/j.msea.2013.01.076>.
- [30] K. Edalati, K. Imamura, T. Kiss, Z. Horita, Equal-channel angular pressing and high-pressure torsion of pure copper: evolution of electrical conductivity and hardness with strain, *Mater. Trans.* 53 (2012) 123–127, <https://doi.org/10.2320/matertrans.MD201109>.
- [31] F. Khodabakhshi, A.P. Gerlich, Accumulative fold-forging (AFF) as a novel severe plastic deformation process to fabricate a high strength ultra-fine grained layered aluminum alloy structure, *Mater. Charact.* 136 (2018) 229–239, <https://doi.org/10.1016/j.matchar.2017.12.023>.
- [32] Z. Zhu, J. Han, C. Gao, M. Liu, J. Song, Z. Wang, H. Li, Microstructures and mechanical properties of Al-Li 2198-T8 alloys processed by two different severe plastic deformation methods: a comparative study, *Mater. Sci. Eng. A* 681 (2017) 65–73, <https://doi.org/10.1016/j.msea.2016.10.108>.
- [33] S. Das Bakshi, D. Sinha, S. Ghosh Chowdhury, Anisotropic broadening of XRD peaks of  $\alpha$ -Fe: Williamson-Hall and Warren-Averbach analysis using full width at half maximum (FWHM) and integral breadth (IB), *Mater. Charact.* 142 (2018) 144–153, <https://doi.org/10.1016/j.matchar.2018.05.018>.
- [34] W. Dai, S. Liang, Y. Luo, Q. Yang, Effect of W powders characteristics on the Ti-rich phase and properties of W-10 wt.% Ti alloy, *Int. J. Refract. Met. Hard Mater.* 50 (2015) 240–246, <https://doi.org/10.1016/j.ijrmhm.2015.02.003>.
- [35] A. Dutta, N. Gayathri, S. Neogy, P. Mukherjee, Microstructural characterisation of proton irradiated niobium using X-ray diffraction technique, *Philos. Mag.* 98 (2018) 1031–1052, <https://doi.org/10.1080/14786435.2018.1425555>.
- [36] S.O. Gashit, A. Fattah-Alhosseini, Y. Mazaheri, M.K. Keshavaz, Microstructure, mechanical properties and electrochemical behavior of AA1050 processed by accumulative roll bonding (ARB), *J. Alloys Compd.* 688 (2016) 44–55, <https://doi.org/10.1016/j.jallcom.2016.07.177>.
- [37] R. Yogamalar, R. Srinivasan, A. Vinu, K. Ariga, A.C. Bose, X-ray peak broadening analysis in ZnO nanoparticles, *Solid State Commun.* 149 (2009) 1919–1923, <https://doi.org/10.1016/j.ssc.2009.07.043>.
- [38] T. Tański, P. Snopiński, K. Prusik, M. Sroka, The effects of room temperature ECAP and subsequent aging on the structure and properties of the Al-3%Mg aluminium alloy, *Mater. Charact.* 133 (2017) 185–195, <https://doi.org/10.1016/j.matchar.2017.09.039>.
- [39] Y.B. Wang, J.C. Ho, X.Z. Liao, H.Q. Li, S.P. Ringer, Y.T. Zhu, Mechanism of Grain Growth During Severe Plastic Deformation of a Nanocrystalline Ni-Fe Alloy, (2009), <https://doi.org/10.1063/1.3065205>.
- [40] R. Valiev, R. Islamgaliev, I. Alexandrov, Bulk nanostructured materials from severe plastic deformation, *Prog. Mater. Sci.* 45 (2000) 103–189, [https://doi.org/10.1016/S0079-6425\(99\)00007-9](https://doi.org/10.1016/S0079-6425(99)00007-9).
- [41] L.S. Toth, C. Gu, Ultrafine-grain metals by severe plastic deformation, *Mater. Charact.* 92 (2014) 1–14, <https://doi.org/10.1016/j.matchar.2014.02.003>.
- [42] T. Ungár, L. Balogh, Y.T. Zhu, Z. Horita, C. Xu, T.G. Langdon, Using X-ray micro-diffraction to determine grain sizes at selected positions in disks processed by high-pressure torsion, *Mater. Sci. Eng. A* 444 (2007) 153–156, <https://doi.org/10.1016/j.msea.2006.08.059>.



**Article III:**

B. Omranpour, L. Kommel, E.G. Sanchez, Y. Ivanisenko, J. Huot, Enhancement of Hydrogen Storage in Metals by Using a New Technique in Severe Plastic Deformations, *Key Eng. Mater.* 799 (2019) 173–178.







## Enhancement of Hydrogen Storage in Metals by Using a New Technique in Severe Plastic Deformations

Babak Omranpour<sup>1,2,3,a\*</sup>, Lembit Kommel<sup>1,b</sup>, E. Garcia Sanchez<sup>2,c</sup>,  
Julia Ivanisenko<sup>3,d</sup>, Jacques Huot<sup>4,e</sup>

<sup>1</sup>Department of Materials Engineering, Tallinn University of Technology (TalTech), 19086 Tallinn, Estonia

<sup>2</sup>Facultad de Ingeniería Mecánica y Eléctrica (FIME), Nuevo Leon State University (UANL), 66455 San Nicolás de los Garza, Mexico

<sup>3</sup>Institute of Nanotechnology (INT), Karlsruhe Institute of Technology (KIT), 76021 Karlsruhe, Germany

<sup>4</sup>Hydrogen Research Institute, Université du Québec à Trois-Rivières (UQTR), Trois-Rivieres, G9A 5H7 QC, Canada

<sup>a</sup>omranpou@uqtr.ca, <sup>b</sup>lembit.kommel@taltech.ee, <sup>c</sup>egs7710@gmail.com,  
<sup>d</sup>julia.ivanisenko@kit.edu, <sup>e</sup>jacques.huot@uqtr.ca

**Keywords:** Severe Plastic Deformation, High Pressure Torsion Extrusion, Hydrogenation

**Abstract.** Hydrogen is expected to be a viable solution for green-energy investment in future. However, hydrogen storage is a big challenge for stationary and mobile applications. Severe Plastic Deformation (SPD) techniques are well-known to be effective in enhancement of hydrogenation in metals hydrides. This paper shows the effect of a novel SPD technique named “High Pressure Torsion Extrusion-HPTE” on the hydrogenation of metal hydrides and compare it with the conventional method of ECAP. Results of mechanical testing and X-ray diffraction patterns showed significant enhancement in hardness and microstructural refinement in materials after HPTE. Accordingly, hydrogenation kinetics improved dramatically. This achievement could be an initiative to implement HPTE in synthesis of metal hydrides for clean energy applications.

### Introduction

Hydrogen as a safe alternative to fossil fuels, is believed to be solving the energy crisis in future with zero carbon emission. However, a real challenge on this technology is the storage of hydrogen, specifically with reversible storage systems [1]. There is plenty of research in this area which has been trying to solve this issue. Among various storage methods, solid-state storage of hydrogen is one of the safest ways for practical applications. A variety of materials such as composites and metals may absorb and store hydrogen. Among all these materials, metal hydrides have attracted considerable attention due to their high-volumetric and gravimetric capacities for hydrogen storage [2] and for their ability to absorb and desorb hydrogen with minor changes in hydrogen pressure [3]. Nonetheless, some of these materials have shown very slow kinetics; even in some cases, they may absorb hydrogen only at very high temperatures. Severe Plastic Deformations (SPD) are well-known to activate these materials and improve the kinetics of hydrogenation. In principle, SPD techniques apply tremendous amounts of deformation to the materials (strain values over 2) and reduce the grain size in metals towards nanoscale. This transformation in materials leads to higher volumetric density of grain boundaries, large accumulation of defects, and higher vacancy concentration in crystal structures [4]. These defects may act as the nucleation points for chemical reactions (like hydrogenation), whereas grain boundaries are the main pathways for diffusion[5]. Therefore, in this respect, SPD techniques may stand as promising candidates for the enhancement of hydrogen storage. Several studies proved the enhancement of hydrogenation in metals and alloys by employing different SPD techniques such as ECAP [6,7], HPT [8,9], ARB [10,11]. Recently, a new SPD technique named “High Pressure Torsion Extrusion” (HPTE) has been introduced to fabricate bulk nanostructured metals with enhanced mechanical and microstructural properties [12].

This technique is a variation of conventional HPT [13] with offering the advantage of producing bulk samples in rod shape, rather than fabricating thin disks with limited applications. Configuration of the die along with a processed sample is shown in Fig. 1.

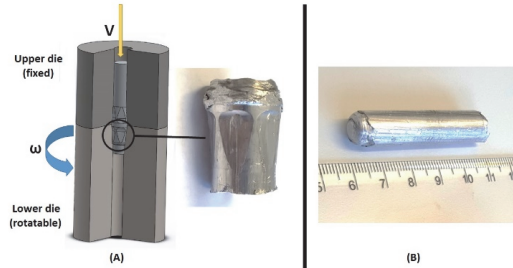


Fig. 1. High Pressure Torsion Extrusion (HPTE): (A) Schematic view of HPTE die with a sample during processing; (B) Processed sample

Deformation processing in this technique is based on torsion applied to the sample by the lower die with a rotational speed of  $\omega$ , along with extrusion applied by a punch with extruding speed of  $v$ . This extrusion helps the sample to experience a continuous deformation in each section of the rod during the process. Hence, HPTE can be compared with ECAP in terms of extrusion characteristics. More details about the process and die can be found in earlier reports [12,14].

This work, firstly, intends to evaluate the influence of HPTE on development of mechanical properties and microstructure in niobium. Furthermore, it has focused on evolution of capacity and hydrogenation kinetics of the samples processed by HPTE. In addition, some ECAP experiments are performed on niobium in order to highlight the effectiveness of HPTE in hydrogenation in contrast with one of the main traditional SPD methods which has been widely used for hydrogenation.

### Methodology of the Research

**SPD processing.** As-received niobium with purity of 98.5 wt% was processed by HPTE and ECAP at room temperature. HPTE die processed the samples at extruding speed of  $v=7$  mm/min and rotational speed of  $\omega=1$  rev/min.

ECAP processing was accomplished for two samples: ECAP processed sample after one pass of extrusion and after four passes. The ECAP die used in this set of experiments was an Indirect-Extrusion die with channel angle of  $\phi=90^\circ$  and corner angle of  $\psi=0^\circ$ . Route Bc was applied to the materials where sample is rotated  $90^\circ$  in the same direction between consecutive passes[15]. Details of the die and processing mechanism can be found in an earlier report [16]. Equivalent strain values of each regime along with processing parameters are summarized in Table 1.

A SHIMATZU HMW micro-hardness tester was used to run the Vickers hardness testing. The micro indenter applied an equivalent force of 200 gf with a dwelling time of 15 seconds to the points evenly spaced from each other on the cross section of the samples. A total number of 22 points lied in two diameters for each sample were selected for indentation (Fig. 3).

Table 1. Process parameters and corresponding equivalent strain in ECAP and HPTE

		Process parameter		Equivalent Strain*
SPD processed samples	HPTE	Distance from the center (R), [mm]	0	0.86
			1.8	2.10
			3.6	3.33
			4.5	3.94
	ECAP		Pass#1 (ECAP1)	1.15
			Pass#4 (ECAP4)	4.62

\*. Equivalent strain values were obtained from theoretical equations of strain for ECAP[17] and HPTE[12]

X-Ray Diffraction (XRD) patterns were recorded by PANalytical Empyrean facility with  $\text{CuK}\alpha$  radiation ( $\lambda = 1.5406 \text{ \AA}$ ) operated at 45 kV and 40 mA. The scans were performed in a  $2\theta$  range between  $36^\circ$  to  $122^\circ$  with a scanning step of  $0.013^\circ$  and 10 seconds per step in continuous mode. Scherrer method [18,19] was applied to XRD patterns to estimate the crystallite size in materials. Xpert Highscore Plus-Version 3.0 was utilized to refine the data.

**Hydrogenation process.** Kinetics of hydrogenation was measured by a homemade Sievert apparatus with calibrated volumes. Samples were cut into small chunks with an approximate weight of 100mg and exposed to hydrogen in a reactor at  $300^\circ\text{C}$  and 20 bars. Weight percentage of hydrogen absorbed by each sample was recorded during the synthesis to evaluate the kinetics of hydrogenation.

## Results and Discussion

**X-ray Diffraction (XRD) Pattern.** XRD results are presented in Fig. 2. The predominant peaks in all samples formed in  $\{110\}$  and  $\{210\}$  planes. Depending on the type of the process, some of the peaks faded away, such as the  $\{220\}$  peak which disappeared after ECAP and faded after HPTE. Peak broadening of the patterns which is caused by grain refinement [20,21] can be observed in the diffractogram of processed samples (Fig. 2-a). The average crystallite size in the samples was estimated from the peak broadening of XRD patterns by Scherrer method and presented in Fig. 2-b. Effect of SPD processing on microstructure refinement can be noticed in these results. The crystallites in HPTE and then in ECAP4, were able to reach sub-micrometer levels after processing.

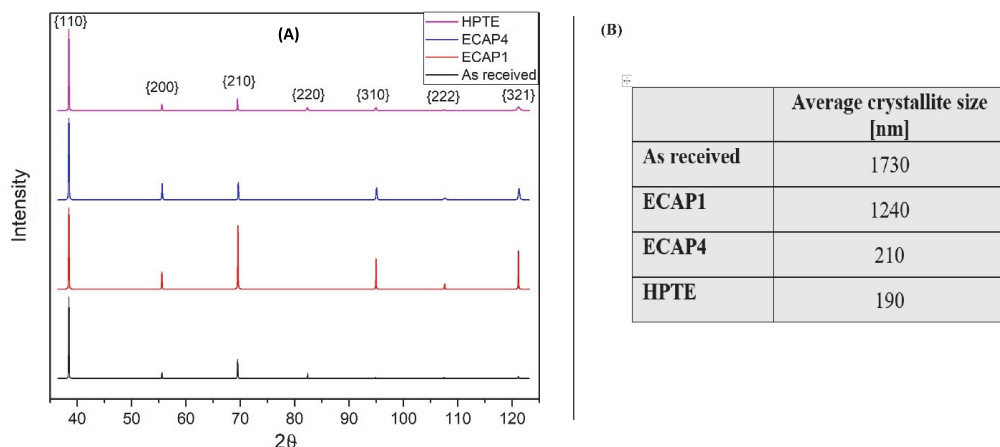


Fig. 2. XRD results: (A) Diffractogram of Niobium; (B) Estimated crystallite size obtained from XRD

**Mechanical properties.** Materials hardness in Vickers scale was measured for all samples. Results of hardness are presented in Fig. 3. According to this figure, as-received niobium with the initial hardness of 81 Hv improved  $\sim 35\%$  after one pass of ECAP (ECAP1) with an average value of 109 Hv; and ECAP4 improved by  $\sim 91\%$  with average value of 155 Hv. The hardness distribution in all samples of as-received and ECAP processed samples were homogeneous. However, in the case of

HPTE, since the applied strain in the sample varied from center to edge (*Table 1*), the resulting hardness in the sample showed a gradient in the graph. This gradient in hardness distribution is in compatible with the hardness results obtained previously from HPTE samples of copper [12] and aluminum [14]. In the present work, the lowest hardness value of 241 Hv was obtained in the center, and the maximum hardness value of 285 Hv was recorded close to the periphery of the sample. The hardness improvement rate, in compared with as-received sample, was about 198% at the center and 252% at the periphery zone of HPTE sample. It should also be noted that this improvement was achieved with one pass of HPTE.

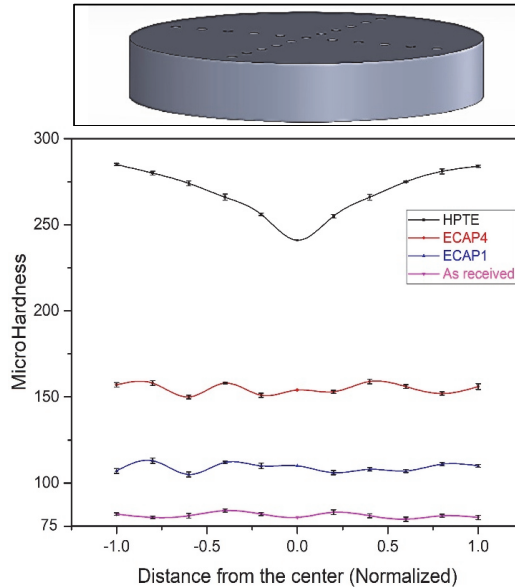


Fig. 3. Hardness testing: Illustration of micro indentation applied to the samples (above), and results of hardness (below)

**First hydrogenation kinetics.** Fig. 4 shows first hydrogenation (activation) of the samples. As it can be seen, as-received sample did not show any tendency for absorption after exposing to hydrogen for 24 hrs. On the other hand, the samples processed by HPTE and ECAP, absorbed hydrogen relatively fast but at different rates. Applying one pass of HPTE significantly enhanced the activation time. HPTE sample reached its maximum capacity ( $\sim 0.85\text{wt}\%$  of hydrogen in niobium) within  $\sim 8\text{hrs}$ . In comparison, ECAP4 reached its full capacity within  $\sim 18\text{hrs}$ . The ECAP1 sample showed much slower kinetics and possessed a capacity of  $\sim 0.7\%$  after 24hrs. This difference in hydrogen absorption can be explained by referring to material evolution during Severe Plastic Deformations. As mentioned earlier, the direct outcome of SPD is grain refinement. Reduction of grain size in materials leads to an increase in volumetric density of grain boundaries. In addition, applying severe deformation to the materials causes higher number of defects in the microstructure. In principle, hydrogenation starts with nucleation followed by diffusion. As indicated earlier, presence and accumulation of defects in materials may facilitate the process of nucleation. Furthermore, grain boundaries may act as a pathway for diffusion and enable hydrogen atoms to reach the grains faster. The higher the density of the boundaries, the more pathways for hydrogen to disperse throughout the material.

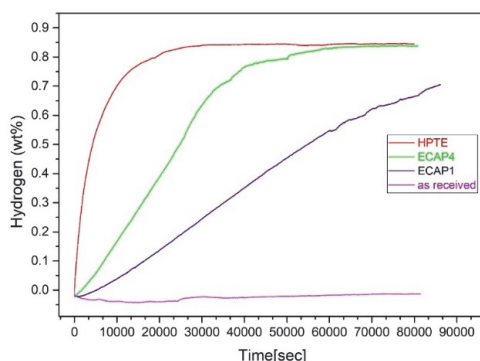


Fig. 4. First hydrogenation kinetics (activation)

As a result, due to massive accumulation of defects and significant grain refinement in HPTE sample, this sample was able to absorb hydrogen faster and easier than as-received and ECAP processed samples. This enhancement can be observed in ECAP4 and ECAP1, to a lesser extent, indicating the presence of defects and high grain-boundary density compared with as-received sample.

## Conclusions

This research, for the first time, evaluated the effect of a new Severe Plastic Deformation (SPD) technique called “HPTE” on first hydrogenation of niobium, and compared it with ECAP. The main outcomes of this work can be summarized as follows:

- HPTE as an effective technique was able to refine the microstructure, increase the hardness and enhance hydrogen-storage performance in materials.
- Hardness of niobium samples improved by 35% after one pass of ECAP and by 91% after four passes of ECAP, while this improvement surpassed 250% near to the periphery of the rod after one pass of HPTE.
- Kinetics of hydrogenation improved after SPD processing in the following order: ECAP1, ECAP4, and HPTE. ECAP4 and HPTE samples reached full capacity after ~18 h and ~10 h respectively. ECAP1 was only partially hydrided after 24hrs. On the other hand, as-received sample did not absorb hydrogen after 24 h, revealing the impact of SPD on hydrogenation.

## Acknowledgement

This project was sponsored in part by European social funds-DoraPlus- Estonia, in part by Quebec ministry of Higher Education-FRQNT- Canada, and in part by National Council of Science and Technology-Conacyt- Mexico.

## References

- [1] M. Zehetbauer, R. Grössinger, H. Krenn, M. Krystian, R. Pippan, P. Rogl, T. Waitz, R. Würschum, Bulk nanostructured functional materials by severe plastic deformation, *Adv. Eng. Mater.* 12 (2010) 692–700.
- [2] L. Schlapbach, A. Züttel, Hydrogen-storage materials for mobile applications, *Nature.* 414 (2001) 353–358.
- [3] J. Huot, Metal Hydrides, in: *Handb. Hydrog. Storage*, Wiley-VCH Verlag GmbH & Co. KGaA, Weinheim, Germany, 2010: pp. 81–116.
- [4] A. Grill, J. Horky, A. Panigrahi, G. Krexner, M. Zehetbauer, Long-term hydrogen storage in Mg and ZK60 after Severe Plastic Deformation, in: *Int. J. Hydrogen Energy*, Elsevier Ltd, 2015: pp. 17144–17152.

- 
- [5] J. Huot, Nanocrystalline Metal Hydrides Obtained by Severe Plastic Deformations, (2012) 22–40.
- [6] V. Skripnyuk, E. Rabkin, Y. Estrin, R. Lapovok, The effect of ball milling and equal channel angular pressing on the hydrogen absorption/desorption properties of Mg–4.95 wt% Zn–0.71 wt% Zr (ZK60) alloy, *Acta Mater.* 52 (2004) 405–414.
- [7] S. Løken, J.K. Solberg, J.P. Maehlen, R.V. Denys, M.V. Lototsky, B.P. Tarasov, V.A. Yartys, Nanostructured Mg–Mm–Ni hydrogen storage alloy: Structure–properties relationship, *J. Alloys Compd.* 446–447 (2007) 114–120.
- [8] D.R. Leiva, A.M. Jorge, T.T. Ishikawa, J. Huot, D. Fruchart, S. Miraglia, C.S. Kiminami, W.J. Botta, Nanoscale Grain Refinement and H-Sorption Properties of MgH<sub>2</sub> Processed by High-Pressure Torsion and Other Mechanical Routes, *Adv. Eng. Mater.* 12 (2010) 786–792.
- [9] K. Edalati, A. Yamamoto, Z. Horita, T. Ishihara, High-pressure torsion of pure magnesium: Evolution of mechanical properties, microstructures and hydrogen storage capacity with equivalent strain, *Scr. Mater.* 64 (2011) 880–883.
- [10] S. Couillaud, H. Enoki, S. Amira, J.L. Bobet, E. Akiba, J. Huot, Effect of ball milling and cold rolling on hydrogen storage properties of nanocrystalline TiV1.6Mn0.4 alloy, *J. Alloys Compd.* 484 (2009) 154–158.
- [11] S. Amira, S.F. Santos, J. Huot, Hydrogen sorption properties of Ti–Cr alloys synthesized by ball milling and cold rolling, *Intermetallics.* 18 (2010) 140–144.
- [12] Y. Ivanisenko, R. Kulagin, V. Fedorov, A. Mazilkin, T. Scherer, B. Baretzky, H. Hahn, High Pressure Torsion Extrusion as a new severe plastic deformation process, *Mater. Sci. Eng. A.* 664 (2016) 247–256.
- [13] K. Edalati, Z. Horita, A review on high-pressure torsion (HPT) from 1935 to 1988, *Mater. Sci. Eng. A.* 652 (2016) 325–352.
- [14] B. Omranpour, R. Kulagin, Y. Ivanisenko, E. Garcia Sanchez, Experimental and numerical analysis of HPTE on mechanical properties of materials and strain distribution, *IOP Conf. Ser. Mater. Sci. Eng.* 194 (2017) 012047.
- [15] F. Djavanroodi, B. Omranpour, M. Ebrahimi, M. Sedighi, Designing of ECAP parameters based on strain distribution uniformity, *Prog. Nat. Sci. Mater. Int.* 22 (2012) 452–460.
- [16] B. Omranpour, L. Kommel, V. Mikli, E. Garcia, J. Huot, Nanostructure development in refractory metals: ECAP processing of Niobium and Tantalum using indirect-extrusion technique, *Int. J. Refract. Met. Hard Mater.* 79 (2019).
- [17] R.Z. Valiev, T.G. Langdon, Principles of equal-channel angular pressing as a processing tool for grain refinement, *Prog. Mater. Sci.* 51 (2006) 881–981.
- [18] D.R. Leiva, A.M. Jorge, T.T. Ishikawa, J. Huot, D. Fruchart, S. Miraglia, C.S. Kiminami, W.J. Botta, Nanoscale grain refinement and H-sorption properties of MgH<sub>2</sub> processed by high-pressure torsion and other mechanical routes, *Adv. Eng. Mater.* 12 (2010) 786–792.
- [19] A.W. Burton, K. Ong, T. Rea, I.Y. Chan, On the estimation of average crystallite size of zeolites from the Scherrer equation: A critical evaluation of its application to zeolites with one-dimensional pore systems, *Microporous Mesoporous Mater.* 117 (2009) 75–90.
- [20] A.L. Ortiz, L. Shaw, X-ray diffraction analysis of a severely plastically deformed aluminum alloy, *Acta Mater.* 52 (2004) 2185–2197.
- [21] F. Khodabakhshi, A.P. Gerlich, Accumulative fold-forging (AFF) as a novel severe plastic deformation process to fabricate a high strength ultra-fine grained layered aluminum alloy structure, *Mater. Charact.* 136 (2018) 229–239.

**Article IV:**

L. Kommel, B. Omranpour, V. Mikli, Structuration of Refractory Metals Tantalum and Niobium Using Modified Equal Channel Angular Pressing Technique, Key Eng. Mater. 799 (2019) 103–108.





## Structuration of Refractory Metals Tantalum and Niobium Using Modified Equal Channel Angular Pressing Technique

Lembit Kommel<sup>1\*</sup>, Babak Omranpour Shahreza<sup>1,3,4</sup>, Valdek Mikli<sup>2</sup>

<sup>1</sup>Department of Mechanical and Industrial Engineering, Tallinn University of Technology, Ehitajate tee 5, 12618 Tallinn, Estonia

<sup>2</sup>Department of Materials and Environmental Technology, Tallinn University of Technology, Ehitajate tee 5, 12618 Tallinn, Estonia

<sup>3</sup>Faculty of Mechanical and Electrical Engineering, Universidad Autónoma de Nuevo León (UANL), 66455 San Nicolás de los Garza, Mexico

<sup>4</sup>Institute of Nanotechnology (INT), Karlsruhe Institute of Technology (KIT), 76021 Karlsruhe, Germany

Email: \*lembit.kommel@taltech.ee, omranpou@uqtr.ca, valdek.mikli@taltech.ee

**Keywords:** Tantalum, Niobium, Equal Channel Angular Pressing, Mechanical properties, Ultrafine-grained microstructure

**Abstract.** In the present work, we use a modified Equal Channel Angular Pressing technique for structure and properties change of Tantalum and Niobium at room temperature. The main advantage of this modified technique is the possibility to produce relatively large samples with ultrafine-grained microstructure in all volume of the workpiece by reduced deformation load up to 25% via friction decrease, and also to prevent the punch fracture under high compression stress during pressing. The various microstructures and properties were produced in metals by using different von Mises strain levels up to  $\varepsilon_{VM} = 13.8$ . The changes in microstructure were studied by using SEM and TEM techniques. The change of mechanical properties was measured by using various tension and hardness testing setups. We can conclude that during processing the ultrafine-grained microstructure in as-cast Nb and Ta was formed. The uniaxial tensile strength, Vickers hardness, and plasticity of Nb and Ta significantly increased as compared to coarse-grained counterparts. We believe that the relatively large workpieces of pure bulk Ta and Nb metals with improved microstructure and exploitation properties are suitable materials for the modern industry.

### Introduction

The Tantalum (Ta) and Niobium (Nb) are refractory metals like Tungsten (W), Rhenium (Re), and Molybdenum (Mo) [1]. Refractory metals Ta and Nb have high melting points over 2000°C, high density and chemical inertness, wear resistance, and so on. From the refractory metals, engineering objects with different shape and size can be produced, such as wire, ingots, rebar sheets or foil for industrial application [2]. Tantalum is also used for production of capacitors for portable telephones, computers, electronics, and photo cameras [3]. The high purity niobium is an important refractory metal for production of radiofrequency accelerating superconducting (SCRF) cavities, superconducting sheets, and pressure tubes in nuclear reactors [4-6]. These installations' performance is sensitive to the microstructure, physical and chemical properties of pure bulk Ta and Nb. The high purity metals for these applications can be processed by severe plastic deformation (SPD) techniques [7, 8]. It can be concluded, that Ta and Nb can be worked by deformation usually at room temperature as these metals are prone to oxidization at high temperatures at the presence of oxygen [9]. The Ta and Nb immediately after electron beam melting (EBM) have a specific (for this process) coarse microstructure and are not suitable for industrial usage in various advanced installations. For the production of large samples with needed microstructure and properties the ECAP technique can be used [7, 8]. For the production of small nanostructured samples for scientific research from these metals with needed physical, chemical, and mechanical properties the

high-pressure torsion (HPT) can be used [10]. The microfabrication on a desktop by HPT technique can be used to manufacture parts, characteristic dimensions of which range from 10 mm down to 10 microns [11]. For production of the sheets with UFG microstructure the accumulative roll bonding (ARB) can be used [12]. In the present work, we will study the possibilities of industrial production of the large samples of Ta and Nb using a modified ECAP or indirect-extrusion technique [13-15] and compare our results with others from the scientific literature. We propose that all these changes in microstructure and properties of relatively large (up to 50-100 kg) workpieces from refractory metals Ta and Nb can have a large influence on their effectiveness by using in modern industry. We also analyze in our work the influence of processing routines on the microstructure and properties evolution in-situ of the pure bulk metals of Nb and Ta.

### Materials and SPD Techniques

The materials for investigations were as-cast ingots of double EBM commercially pure Ta and Nb. These metals were obtained from Neo Performance Materials Silmet AS, Estonia. The as-cast ingots have diameters of 220 mm (Nb) and 120 mm (Ta), respectively. The chemical purity of Ta ingot was 99.95 wt% and the chemical purity of Nb ingot was 99.94 wt%, respectively. The chemical content of Nb and Ta ingots before and after processing was measured by the ELTRA ONH-2000 analyzer. The samples for experimental production in modified ECAP die were cut off from ingots with a cross-section of 12 x 12 mm and the length of 125 mm. The recrystallization of the structure was conducted in a vacuum furnace at a temperature of 1200 °C for 2 h [15-17]. The samples were covered with a copper film and molybdenum disulfide (MoS<sub>2</sub>) grease because the Nb and Ta under high pressure in sliding condition have the galling effect to steel channels of the ECAP die. The conventional SPD techniques, which are mainly used for the production of samples in the laboratory of Tallinn University of Technology, are presented in Fig. 1a,b,c. The scheme of the deformation in the shear region of conventional ECAP die is presented in Fig. 2a,b. The conventional ECAP [17, 20], PCAP [18] as well as ARB [12] (Fig. 1a,b,c) were used mainly for Al and Cu structurization.

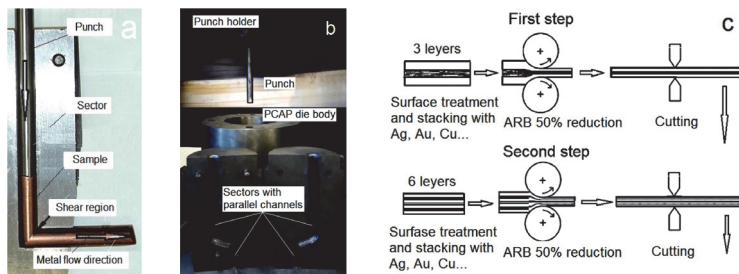


**Fig. 1.** Samples processing in conventional ECAP die (a), in parallel channel angular pressing (PCAP) die (b), and a sketch of the ARB technique (c) for UFG plates manufacturing.

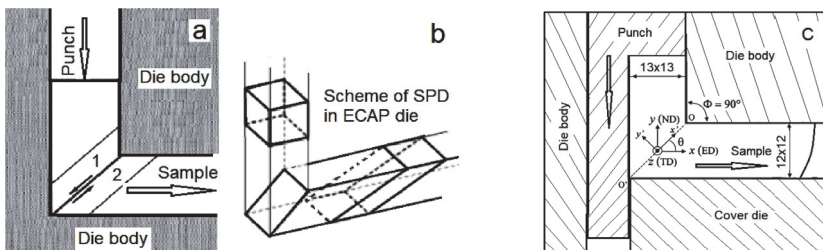


**Fig. 2.** Schemes of the deformation under shear stress in conventional ECAP die (a, b), and in proposed modified ECAP die (c).

The punch for conventional ECAP and PCAP processes was manufactured from highly alloyed instrumental steel with a diameter of 16 mm and length of 165 mm. During ECAP of hard to deformation Ta samples the punch lost stability and was fractured under uniaxial compression load of ~569 kN and corresponding uniaxial compression stress of ~2844 MPa.

**Procedures in modified ECAP die.** In the present work for the Ta and Nb processing, we use the modified ECAP die [16]. This modified ECAP die has punch with a cross-section which was increased up to ~3400 mm<sup>2</sup>. It means that the axial compression stress in the punch body was decreased to ~180 MPa. The inlet channel (for the sample in punch) was 13x13 mm in cross-section and an outlet channel in cross-section was 12x12 mm, respectively (Fig. 2c). The corner of channels section doesn't have radiuses. The sketch of modified ECAP die (initial stage, middle stage, and final stage) is presented in Fig. 3. The processing of samples was carried out at room temperature. The samples of Ta and Nb were processed up to 12 B<sub>c</sub> routes of ECAP. According to the 12 B<sub>c</sub> route, the billet was pressed 12 times by a punch through the channels and at the same time, after each pass, it was rotated by 90 degrees around the longitudinal axis. The two samples with as-cast microstructure were not ECAP processed and were used for comparison of received microstructure and properties. In present study the von Mises strain ( $\epsilon_{VM}$ ) of Ta samples was: S1 ( $\epsilon_{VM} = 0$ ); S2 ( $\epsilon_{VM} = 2.3$ ); S5 ( $\epsilon_{VM} = 5.75$ ), sample S12 ( $\epsilon_{VM} = 13.8$ ), and for Nb samples were S1 ( $\epsilon_{VM} = 0$ ); S6 ( $\epsilon_{VM} = 7.7$ ); S8 ( $\epsilon_{VM} = 9.2$ ); S10 ( $\epsilon_{VM} = 11.5$ ); and S12 ( $\epsilon_{VM} = 13.8$ ), respectively. The deformation scheme in the shear region of proposed modified ECAP die is shown in (Fig. 2c). The specimens were cut off for a measure of tension strength, elongation, and hardness, respectively. The microstructure was studied in cross-section of samples.

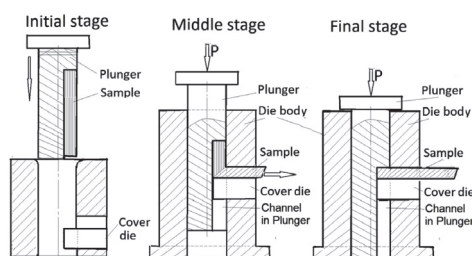


**Fig. 3.** Proposed modified ECAP processing stages: Initial, Middle, and Final.

**Changes in the microstructure.** The EBM Ta and Nb samples have an as-cast microstructure with grains in millimeter size which are connected by fully wetted [19] triple boundaries (Fig. 4a). Immediately after EBM, the metals contain a large number of pores (Fig. 4b). During ECAP in dependence on simple shear strain and compression stress, the grains size was decreased to UFG of microstructure, the pores were compressed and as result the gases concentration was decreased [16]. The microstructure forming during ECAP starts in the shear region (Fig. 4c) and under high hydrostatic compression stress. The deformation-induced formation of dislocations, shear bands, and grain boundaries occurred in the metal at the same time. The mechanism of grain sizes decrease at shear stress under high pressure is described in large amount of scientific articles in materials science during the last two decades [8, 10, and 13]. Such UFG and NC structures step-by-step forming are presented in SEM pictures (Fig. 5a,b,c) for Ta metal and in TEM pictures (Fig. 6a,b,c) for Nb, respectively. The diffraction reflections in pure Nb (see Fig. 6c) was not possible to separate in this study.

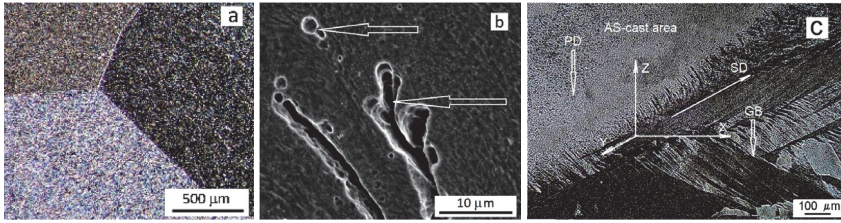


**Fig. 4.** EBM microstructure of the triple grain boundaries (GB) of sample S1 (a), pores in as-cast Nb (b) and microstructure in shear region forming at very first stage of processing (c).

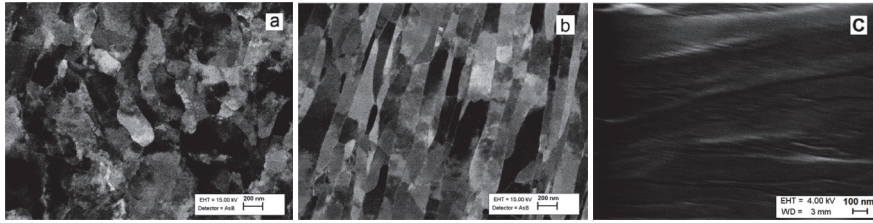


**Fig. 5.** SEM pictures of Ta produced during ECAP for samples S5 ( $\epsilon_{VM} = 5.7$ ) in cross-section (a), in extrusion direction (b), and sample S12 ( $\epsilon_{VM} = 13.8$ ) in longitudinal direction.

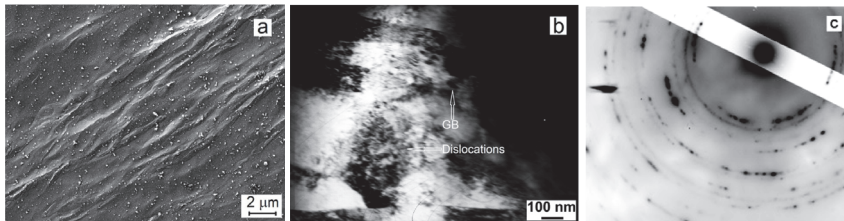


**Fig. 6.** SEM picture of Nb metal in SB region of sample S10 ( $\epsilon_{VM} = 11.5$ ) (a), dark field TEM micrographs of sample S12 ( $\epsilon_{VM} = 13.8$ ) with high density of dislocations induced by shear deformation under compression stress in-situ (b), and electron diffraction pattern of the NC pure Nb after ECAP of sample S12 (c).

**Mechanical properties of Ta and Nb.** The tensile strength of Ta was measured, and it was found that with increasing deformation of von Mises, the tensile strength Ta increased mainly during the first pressing (Fig. 7a). A similar rate of increase in hardness for Ta and Nb was shown in [15]. Fig. 7b shows that Martens hardness (maximum and plastic part) depends on the measurement of orientation to the sample; it is higher in cross section and lower in normal directions. As shown in Fig. 8a,b, the Vickers Ta hardness was increased by increasing the von Mises strain. The microhardness of Ta Vickers was increased from 95 HV<sub>0.2</sub> to 245 HV<sub>0.2</sub>, and for Nb from 80 HV<sub>0.2</sub> to 180 HV<sub>0.2</sub>. It should be noted that the methods for measuring hardness according to Martens and Vickers are different [21]. Marten's hardness is calculated from the difference between the maximum depth of indentation and after removal the load. Vickers hardness is calculated from the length of the diagonal, indentation load and only hardness is measured.



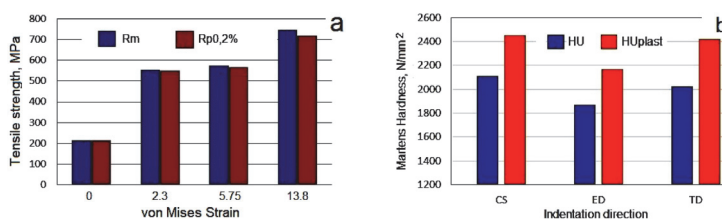


**Fig. 7.** The tensile strength of Ta processed in modified ECAP die (a) and Martens hardness of Ta in dependence on measuring orientation (b).

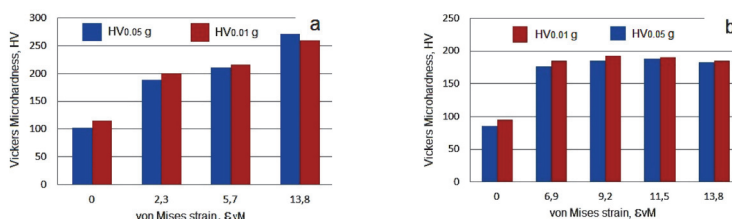


**Fig. 8.** The Vickers microhardness of Ta (a) and Nb (b) for various von Mises strain levels.

## Conclusions

The main advantage of this work is the designing of modified ECAP technique. By use this modified equipment the load of pressure is possible to reduce by 25% due to reducing of the friction. The stresses in the punch body decreased and the punch don't fracture as by conventional method. Was calculated that the using of this modified ECAP technique, it is possible to produce in industry relatively large samples weighing up to 50-100 kg from hard at deformation Ta and Nb on a hydraulic press with a maximal force of 1000 metric tons. The produced Nb and Ta samples have UFG microstructure and improved mechanical properties.

## Acknowledgements

This work was supported by the Estonian Research Council institutional research funding IUT 1929, IUT1928 and TK141. This project was sponsored in part by European social funds-DoraPlus-Estonia, in part by Quebec ministry of Higher Education-FRQNT- Canada, and in part by National Council of Science and Technology-Conacyt- Mexico.

## References

- [1] Information on [http:// www.Wikipedia](http://www.Wikipedia), the free encyclopedia, Refractory metals.
- [2] Commodity Report 2008: Tantalum. United States Geological Survey. Retrieved (2008) 10-24.
- [3] M. Filella, Tantalum in the environment. *Earth-Sci. Rev.* 173 (2017) 122-140.
- [4] A. Zamiri, F. Pourboghra, Characterization and development of an evolutionary yield function for the superconducting niobium sheet. *Int. J. Solids Struct.* 44 (2017) 8627-8647.
- [5] P. Kneisel, G. Ciovati, P. Dhakal, K. Saito, W. Singer, X. Singer, G.R. Myneni, Review of ingot niobium as a material for superconducting radiofrequency accelerating cavities. *Nucl. Instrum. Meth. A* 774 (2015) 133-150.
- [6] G. Ciovati, P. Dhakal, J. Matalевич, G. Myneni, A. Schmidt, J. Iversen, A. Matheisen, W. Singer, Mechanical properties of niobium radio-frequency cavities. *Mater. Sci. Eng. A* 642 (2013) 117-127.

- 
- [7] V.M. Segal, Equal channel angular extrusion: from macromechanics to structure formation. *Mater. Sci. Eng. A* 338 (1999) 322-333.
- [8] Vinogradov A, Estrin Y. Analytical and numerical approaches to modelling severe plastic deformation. *Prog. Mater. Sci.* 95 (2018) 172-242.
- [9] S. Shi, L. Zhu, H. Zhang, Z. Sun, Strength and ductility of niobium alloys with nonmetallic elements: A first-principles study. *Mater. Lett.* 189 (2017) 310-312.
- [10] N. Maury, N. X. Zhang, Y. Huang, A.P. Zhilyaev, T.G. Langdon, A critical examination of pure tantalum processed by high-pressure torsion. *Mater. Sci. Eng. A* 638 (2015) 174-182.
- [11] Y. Estrin, R. Kulagin, Y. Beygelzimer, Think big, manufacture small: microfabrication on a desktop by severe plastic deformation - *Materials Today. Information on <https://www.materialstoday.com/surface-science/comment/think-big-manufacture-small/>*.
- [12] A. Pramono, L. Kollo, R. Veinthal, Hot and cold regions during accumulative roll bonding of Al/Al<sub>2</sub>O<sub>3</sub> nanofibre composites. *Proc. Est. Acad. Sci.* 65 (2016) 132-137.
- [13] Z. Pan, F. Xu, S.N. Mathaudhu, L.J. Kecskes, W.H. Yin, X.Y. Zhang, K.T. Hartwig, Q. Wei, Microstructural evolution and mechanical properties of niobium processed by equal channel angularextrusion up to 24 passes. *Acta Mater.* 60 (2012) 2310-2323.
- [14] J.-P. Mathieu, S. Suwas, A. Eberhardt, L.S. Tóth, P. Moll, A new design for equal channel angular extrusion. *J. Mater. Process. Tech.* 173 (2006) 29-33.
- [15] B. Omranpour, L. Kommel, V. Mikli, E. Garcia, J. Huot, Nanostructure development in refractory metals: ECAP processing of Niobium and Tantalum using indirect-extrusion technique. *Int. J. Refract. Met. H.* 79 (2019) 1-9.
- [16] L. Kommel, Microstructure and properties that change during hard cyclic visco-plastic deformation of bulk high purity niobium. *Int. J. Refract. Met. H.* 79 (2019) 10-17.
- [17] L. Kommel, E. Kimmari, M. Saarna, M. Viljus, Processing and properties of bulk ultrafine-grained niobium. *J. Mater. Sci.* 48 (2013) 4723-4729.
- [18] A. Pramono, L. Kommel, L. Kollo, R. Veinthal, Hot and cold of pressing effect on ECAP-parallel channel composit based on Al/ANF material. *Adv. Mater. Res.* 1123 (2015) 343-347.
- [19] B.B. Straumal, O.A. Kogtenkova, A.S. Gornakova, V.G. Sursaeva, Review: grain boundary faceting-roughening phenomena. *J. Mater. Sci.* 51 (2016) 382-404.
- [20] L. Kommel, M. Saarna, R. Traksmaa, I. Kommel, Microstructure, properties and atomic level strain in severely deformed rare metal niobium. *Mater. Sci. (Medzd.)* 18 (2012) 330-335.
- [21] S.A. Shahdad, J.F. McCabe, S. Bull, S. Rusby, R.W. Wassell, Hardness measured with traditional Vickers and Martens hardness methods. *Dent. Mater.* 23 (2007) 1079-1085.

**Article V:**

B. Omranpour, R. Kulagin, Y. Ivanisenko, E. Garcia Sanchez, Experimental and numerical analysis of HPTE on mechanical properties of materials and strain distribution, IOP Conf. Ser. Mater. Sci. Eng. 194 (2017) 012047.





# Experimental and numerical analysis of HPTE on mechanical properties of materials and strain distribution

**B Omranpour**<sup>1,2,3\*</sup>, **R Kulagin**<sup>1</sup>, **Y Ivanisenko**<sup>1</sup>, **E Garcia Sanchez**<sup>2</sup>

1- Institute of Nanotechnology (INT), Karlsruhe Institute of Technology (KIT), Germany

2- Facultad de Ingeniería Mecánica y Eléctrica (FIME), Universidad Autónoma de Nuevo León (UANL), Mexico

3- Department of Materials Engineering, Tallinn University of Technology (TTU), Estonia

\* Email: babak.o@daad-alumni.de

**Abstract.** High Pressure Torsion Extrusion (HPTE) is a novel technique which has been recently introduced to the society of Nano-SPD researchers. HPTE exploits the deformation mechanics of HPT but in a larger scale using rod-shape samples and is capable of applying high values of strain to materials in one pass. This research aims to evaluate the effect of HPTE on mechanical properties of materials and also to study the effect of geometry of HPTE die on strain distribution in deformed samples by using Finite Element Method (FEM). Commercial pure Aluminium AA1050 was used for experimental work; and eccentric dies with parallel-misaligned channels were developed for evaluation by numerical modelling. Results of this research will help us better understand the effect of process parameters and also geometry of the die on materials.

**Keywords:** High Pressure Torsion Extrusion (HPTE); Die design; FEM; Eccentric dies

## 1. Introduction

Severe Plastic Deformations are very famous techniques in producing Ultra Fine-Grained materials (UFG) by imposing high strains on materials and subdividing original coarse grains into smaller subgrains. This reduction of grain size from micro-meters towards nanometers affects the mechanical properties of materials such as strength, hardness and ductility [1]. Basically in SPD processes, yield strength and hardness are improved, and ductility is reduced; although there are some reports about retaining ductility along with improving other mechanical properties [2].

High Pressure Torsion Extrusion, hereinafter called as HPTE, is a novel technique of Severe Plastic Deformation, introduced in 2015 [3] and has distinctive characteristics in deformation mechanism and properties. HPTE is composed of two separate upper and lower dies rotating relative to each other and a punch will extrude the sample through the die. HPTE approaches a combination of mechanisms of deformation including conventional High Pressure Torsion (HPT) [4] and Cyclic Expansion and Extrusion (CEE) [5] [6]. The major advantage of HPTE over HPT is the possibility of producing rod-shape samples, similar to ECAP; whereas in HPT, using a small disk with an average thickness of less than 1 mm restricts the applications to laboratory research [4] [7]. Plastic strain in this process is composed of torsion, expansion and extrusion (Figure1). Accumulated strain after one pass of HPTE can be calculated by the following equation:

$$E = 2 \ln \frac{D1}{D0} + 2 \ln \frac{D1}{D2} + \frac{\omega \cdot R \cdot D1}{\sqrt{3} \cdot v \cdot D2} \quad (1)$$

Where  $D_0$ ,  $D_1$ , and  $D_2$  are diameters of inlet channel, deformation chamber and the outlet channel, respectively;  $\omega$  is the rotational speed of the lower die,  $v$  is extruding speed and  $R$  is the desired distance from the center at the section of the sample. The first two terms of this equation correspond to expansion and extrusion, and the third term is referred to the plastic strain resulted by torsion [3].

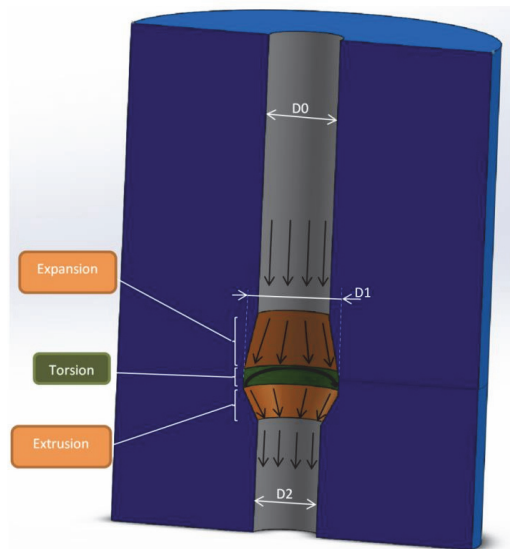


**Figure 1.** Schematic illustration of HPTE die

A key factor in HPTE die is concerned with the design of inner side of the die at the shear zone. Torsion at this zone is provided by rotating the lower die in order for twisting the workpiece and applying high amounts of shear strain to the specimen. Since the initial state of the material has a cylindrical shape, it is necessary to provide enough friction torque to prevent the materials from slippage. This issue is solved by using jutting surfaces inside the die. These jutting surfaces act as holding elements (resembling hexagon socket head cap screws) to constrain the material and apply torsion when the die is rotating (Figure 2.C).

This research in the first step tries to evaluate the effect of HPTE on mechanical properties of materials and in the second step, intends to propose a new design with eccentric channels using Finite Element Methods (FEM). Numerical modeling methods such as FEM are nowadays very common in metal forming processes either to study different aspects of a new technique or to optimize a process [8][9]. FEM as the most popular technique in numerical modeling is capable of assessing different parameters of a process including tool geometry, process conditions and materials properties [10]. The aim of simulation in this work is to devise a new design of HPTE die with eccentric channels towards manipulating strain distribution and adapting new properties in the materials. A theoretical concept of this idea firstly was introduced in an earlier work [3].

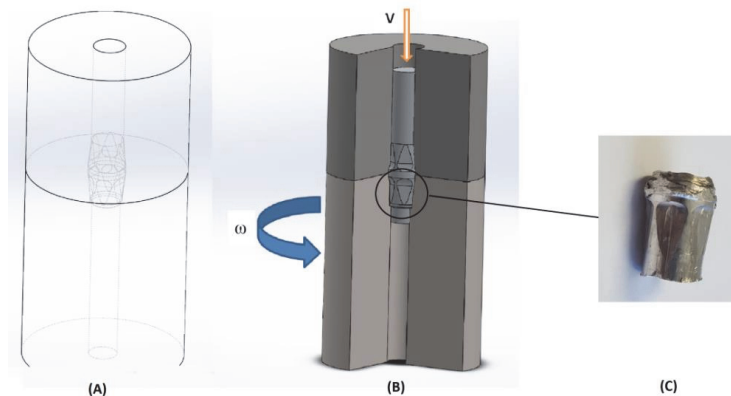


**Figure 2.** (A) Wireframe demonstration of HPTE die; (B) Process parameters of HPTE: Extruding speed,  $V$  and rotational speed,  $\omega$ ; (C) Small section of a workpiece extracted from the deformation zone of the die

## 2. Methodology

### 2.1. Experimental testing and evaluation

Processing of HPTE was performed on commercial pure Aluminium AA1050. Samples were prepared in the dimensions of 11.6 mm in diameter and 13.5mm in length. One specimen was considered as a reference and annealed at 350 °c for 30 minutes. Computer-controlled HPTE machine executed the process at room temperature with rotational speed of  $\omega=1$  rpm and extruding speed of  $V=7$ mm/min. Instant pressing force values together with extruding speed and rotational speed were monitored and recorded in real-time operating system to be used for validation of the simulations.

In order for mechanical testing of materials two testing methods of compression and hardness tests were conducted on the materials. A “SHIMADZU” universal testing machine performed the compression test on the samples with a compressive speed of 2 mm/min; Teflon sheet was used as a solid lubricant. Criterion of maximum length reduction of 66.67% ( $e=2/3$ ) was established in the test. “Buehler Micromet-5104” tester applied micro-indentation at the cross section of the specimens on 11 points at regular intervals to measure Vickers hardness. Pressing load of 0.2 Kg.F with a dwell time of 15 seconds was conducted into all samples.

### 2.2. FEM simulations:

In this study, DEFORM-Ver.11 was implemented for simulation of the process. Assumptions of simulation rest on using the same extruding and rotational speed as in the experiments ( $\omega=1$  rpm,  $V=7$ mm/min), friction coefficient of 0.4, neglecting the deformation heating and considering the die as rigid body.

### 2.3. Scheme of the new design

First and foremost, an FEM simulation of the base die with the exact dimensions was carried out to verify the simulations; thereafter, a new design with eccentric channels was modeled. This new die includes two channels with the same diameters as the base die, but they are misaligned in parallel lines. Therefore there is an eccentricity between the upper and lower channels. At the beginning of the process, there is no eccentricity ( $\Phi=0$ ) (Figure 3.A) but after rotation, it gradually increases to the maximum value of 2mm when the lower die is rotated 180 degrees ( $\Phi=180^\circ$ ) (Figure 3.B).

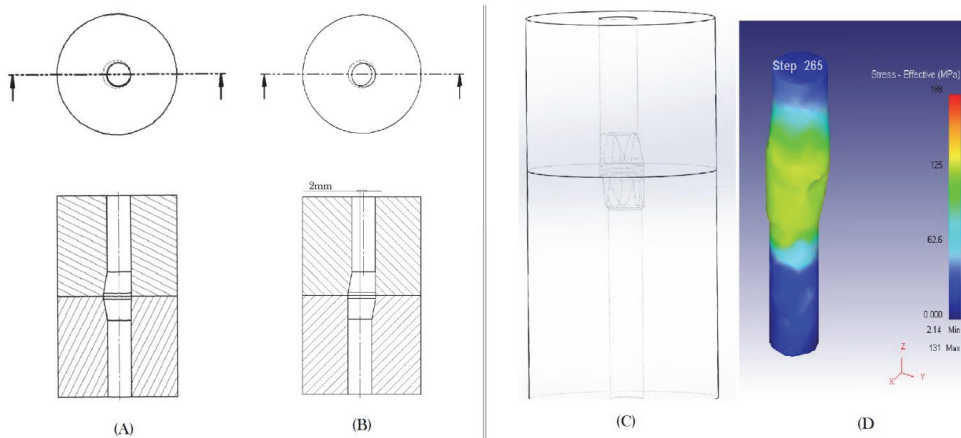


**Figure 3.** HPTE die with eccentric channels: (A) At the beginning of the process, both upper and lower dies are perfectly aligned and there is no eccentricity; (B) Maximum eccentricity appears after 180° of rotation; (C) Wireframe illustration of HPTE die with eccentric channels; (D) Numerical modeling of the process

### 3. Results and discussion:

#### 3.1. Mechanical testing

Following figures depict results of compression test and hardness test on the annealed and HPTE processed samples. Results of compression test are demonstrated in True stress-strain diagram in which yield strength of 44MPa as the initial case reached up to 141 MPa after processing.

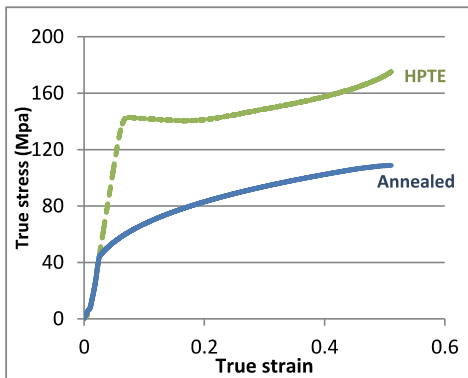


**Figure 4.** True stress-true strain diagram of HPTE processed and initial samples obtained by compression testing

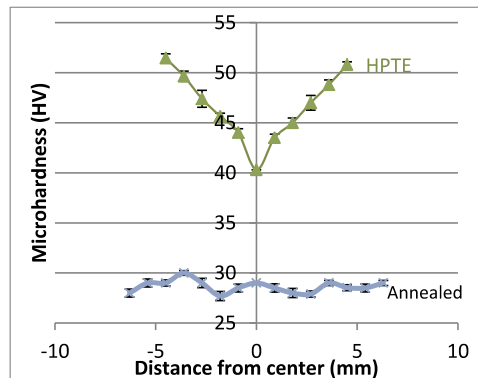


**Figure 5.** Results of Hardness testing

Results of hardness testing showed a sharp increase in hardness values after HPTE processing. One interesting point about this graph is that hardness distribution at the cross section of the samples is quite similar to that of HPT samples [11], that is to say lower values are located in the center and higher values are found near the periphery. The gradient of hardness varies from a minimum value of

40HV to the maximum value of 52 along the radius of the specimen, which implies a successful approach in improvement of mechanical properties of materials by means of HPTE.

### 3.2. Simulation results:

Simulated models were cut in the middle and then twenty nodes, evenly spaced apart, were selected from the cross section of the specimens.

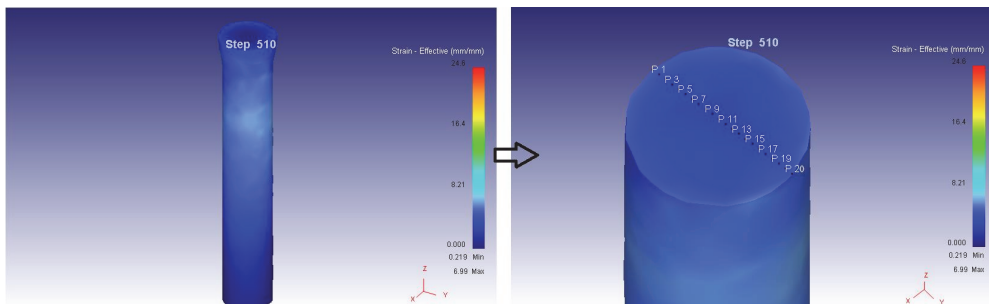


**Figure 6.** Selection of random nodes from the cross section of the models

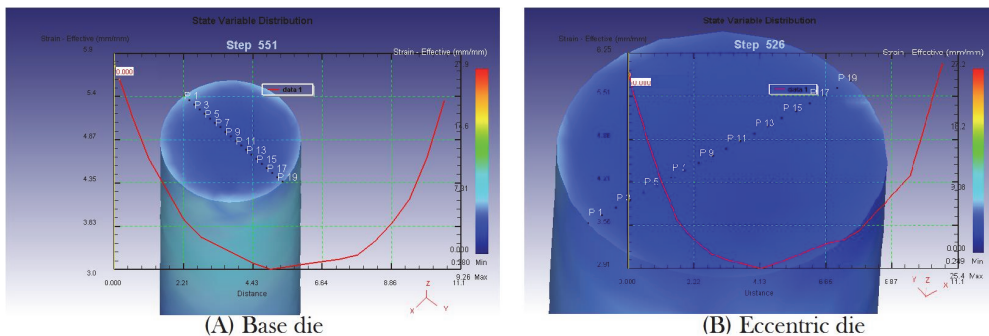


**Figure 7.** Strain distribution diagrams within the specimens for the base die (A) and eccentric die (B)

Figure 7 shows distribution of effective strain applied to the materials after HPTE. In this figure, strain distribution varies from 3 to 5.5 in base die, while in the eccentric die this variation changes from 2.9 to 6.1. Based on the results, there is no big difference in the minimum level of strain in the central part of both samples. But maximum values of strain in those areas which are close to the periphery, slightly increased in the presence of eccentricity.

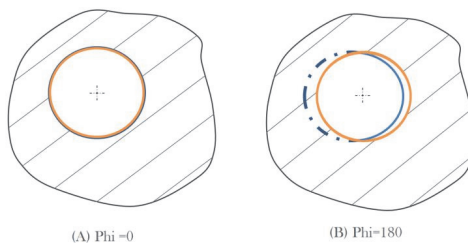


**Figure 8.** Cross section view of an eccentric die

(A) Both upper and lower channels are aligned; effective radius and nominal radius are equal.

(B) Eccentricity of two channels after rotation of the lower die at the phase of 180°; Effective radius in torsion is bigger than the nominal one

This phenomenon can be explained by considering the fact that strain in the central area of the specimens is mainly resulted from expansion and extrusion; and eccentricity does not really affect the strain at this area. On the other hand, at the outer parts of the specimen, when eccentricity reaches to its maximum value, effective radius at the deformation zone will be increased; and consequently strain which is caused by torsion will rise in value (Figure 8).

#### 4. Conclusion

A new SPD process was evaluated and analyzed using Aluminium specimens. Mechanical properties of materials by two different methods of hardness testing and compression testing were studied. Moreover, some modifications in die design were proposed by implementing FEM. Based on the experimental results, after one pass of HPTE hardness values increased by 79% from an initial state of 29 HV to the final state of 52HV near the edge of the samples; and yield strength in compression test improved by 220% from an initial value of 44MPa to 141MPa.

According to the simulation results, the new die with eccentric channels showed a gradual increase in the level of strain near the periphery of the sectioned samples.

#### 5. Acknowledgment

This project was sponsored in part by *Deutscher Akademischer Austauschdienst* (DAAD)- Germany and in part by *National Council of Science and Technology* (CONACYT)- Mexico. Technical and scientific support for running the compression test at CIDET-UANL is greatly appreciated.

#### References

- [1] Rosochowski A, Olejnik L and Richert M 2007 *Advanced Methods in Material Forming*; Banabic D (Heidelberg: Springer); pp215-221.
- [2] Wang Y, Chen M and Zhou F 2002 *Nature*; 419 pp 912-914.
- [3] Ivanisenko Y, et al 2016 *Materials science & Engineering A*; 664 pp 247-256.
- [4] Zhilyaev A and Langdon T 2008 *Progress in Materials science*; 53 pp 893-979.
- [5] Pardis N, et al 2011 *Materials science and Engineering A*; 528 pp 7537-7540.
- [6] Pardis N, et al 2015 *Materials science and engineering A*; 628 pp 423-432.
- [7] Estrin Y and Vinogradov A 2013 *Acta materialia*; 61 pp 782-817.
- [8] Djavanroodi F, Omranpour B and Sedighi M 2013 *Materials and Manufacturing processes*; 28 pp 276-281.
- [9] Djavanroodi F, Omranpour B, Sedighi M, Ebrahimi M. *Progress in natural science: Materials international*. 2012; 22: p. 452-460.
- [10] Rosochowski A and Olejnik L 2007 *Journal of materials: Design and Applications*; 221 pp 187-197.
- [11] Sabbaghianrad S and Langdon TG 2015 *Journal of materials science*; 50 pp 4357-4365.

**Article VI:**

F. Djavaanroodi, B. Omranpour, M. Sedighi, Artificial Neural Network Modeling of ECAP Process, *Mater. Manuf. Process.* 28 (2013) 276–281.





# Artificial Neural Network Modeling of ECAP Process

F. DJAVANROODI<sup>1</sup>, B. OMRANPOUR<sup>2</sup>, AND M. SEDIGHI<sup>2</sup>

<sup>1</sup>Department of Mechanical Engineering, Qassim University, Qassim, Saudi Arabia

<sup>2</sup>Department of Mechanical Engineering, Iran University of Science and Technology, Tehran, Iran

Equal channel angular pressing (ECAP) is a type of severe plastic deformation procedure for achieving ultra-fine grain structures. This article investigates artificial neural network (ANN) modeling of ECAP process based on experimental and three-dimensional (3D) finite element methods (FEM). In order to do so, an ECAP die was designed and manufactured with the channel angle of 90° and the outer corner angle of 15°. Commercial pure aluminum was ECAPed and the obtained data was used for validating the FEM model. After confirming the validity of the model with experimental data, a number of parameters are considered. These include the die channel angles (angle between the channels  $\Phi$  and the outer corner angle  $\Psi$ ) and the number of passes which were subsequently used for training the ANN. Finally, experimental and numerical data was used to train neural networks. As a result, it is shown that a feed forward back propagation ANN can be used for efficient die design and process determination in the ECAP. There is satisfactory agreement between results according to comparisons.

*Keywords* Aluminum; ANN; ECAP; FEM; Grain.

## INTRODUCTION

Artificial neural network technology enables the behavior of complicated processes to be modeled and predicted based on known data [1]. Recently, there has been increasing interest in neural network modeling in different fields of metal forming. [1–4].

There has been growing demand in Industry for the fabrication of nanostructured materials with high performance to weight ratio, such as Mg-, Al-, and Ti-based alloys. Currently, one of the most popular and economic ways for production of bulk nanostructured materials is the severe plastic deformation (SPD) approach. This approach allows the bulk material to undergo SPD and break up the original texture into ultra-fine grain (UFG) structure and finally nanostructure after a number of operations. ECAP is one of the most attractive processes of SPD to produce UFG materials. During ECAP, a sample is pressed through two intersecting channels with the same cross sections and material is subjected to an intense plastic strain through simple shear as shown in Fig. 1.  $\Phi$  is the angle between the channels and  $\Psi$  is the outer corner angle. In this process, extrusion routes creates different slip systems during the pressing operation so that various microstructure and mechanical properties can be achieved. For example, strong texture and anisotropic grain morphology is obtained by using routes A or B [5]. There are four fundamental routes: route A—no billet rotations between passes, route B<sub>A</sub>—90° billet rotations between passes in alternative direction between each pass, route B<sub>C</sub>—90° billet rotations between passes, and route C—that

the sample is rotated by 180° between passes [5, 6]. The magnitude of equivalent strain after N passes is given by the following relationship [7]:

$$\epsilon_{eq} = N/\sqrt{3} \left[ 2 \cot \left( \frac{\Phi + \Psi}{2} \right) + \Psi \operatorname{cosec} \left( \frac{\Phi + \Psi}{2} \right) \right]. \quad (1)$$

Equation (1) represents the average equivalent strain for frictionless conditions in the sample. Material structure evolution and mechanical property changes after the formation of nanostructure by ECAP has been investigated by many researchers [7–11]. The influence of process parameters on global and local deformation behavior of materials has also been studied using finite element methods [12–15]. Number of researchers have studied the influence of die design parameters on uniformity of strain distribution [14, 16, 17]. However, identifying the best design scenario to avoid inhomogeneous strain distribution requires complex calculations and expensive advanced computational analysis. In order to simplify this complex process, attempts have been made to combine the ANN and FEM simulation for ECAP process. Commercial pure aluminum was ECAPed up to 8 passes and the data obtained was used for validating simulations. After confirming the validity of the model with experimental data, a number of parameters that were subsequently used for training of the ANN were considered. Figure 2 presents the framework of the methodology used.

## EXPERIMENTAL PROCEDURES

An ECAP die with the channel angle of 90°, corner angle of 15°, and channel diameter of 20 mm was designed and manufactured. The material used for this

Received July 6, 2011; Accepted November 16, 2011

Address correspondence to F. Djavanroodi, Department of Mechanical Engineering, Qassim University, Qassim, Saudi Arabia; E-mail: roodi@qec.edu.sa

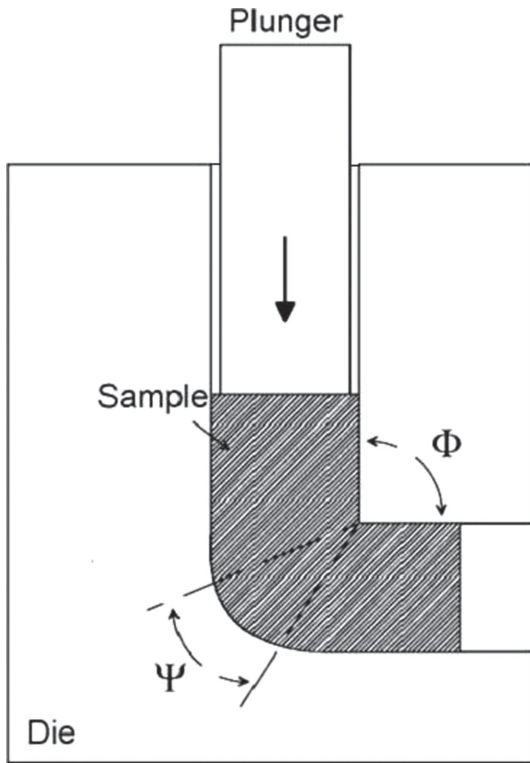


FIGURE 1.—Schematic views of an ECAP.

work is commercial pure Al (99.5% Al), which was homogenized at 345°C for 30 min and furnace cooled. All samples were well lubricated before pressing with  $MoS_2$ . The speed of the ram was constant and equal to 2 mm/s. All testing were performed at room temperature. Route A was used for the ECAP process. 12.5 mm round tension test specimens with 62.5 mm gauge length are used according to ASTM B557 M, 2010. These specimens were machined from the center of the billets after 0, 1, 2, 3, 4, and 8 ECAP passes with their longitudinal axes parallel to the pressing axis (see Table 1). Tensile tests were carried out with an initial strain rate of  $2e^{-3} S^{-1}$ . The tensile testing machine was controlled under constant crosshead speed condition. To verify refining of the grains, optical microscopy for initial samples and SEM for ECAPed samples was used to measure the grain size of materials. Figure 3 shows the experimental setup.

**FEM**

For this study, FEM simulations were carried out using Deform-3D™ V5.0. The sample model has the same geometry as the experimental specimen. The

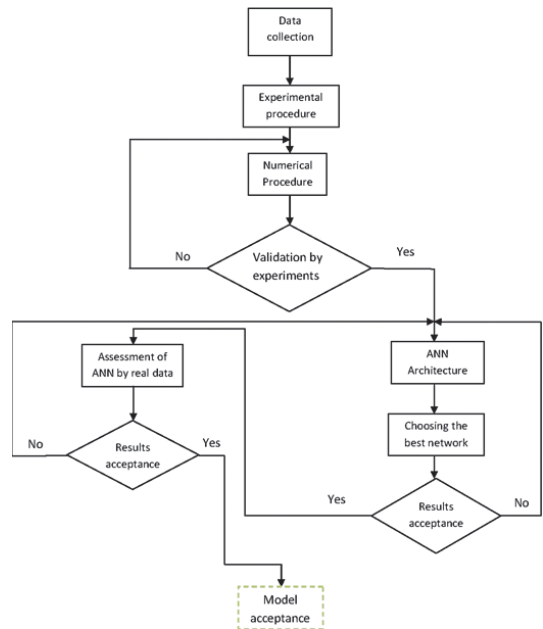


FIGURE 2.—Framework of the methodology used (color figure available online).

sample’s diameter and length was 19.7 mm and 180 mm, respectively. The plastic deformation of material was defined using equation  $\bar{\sigma} = K\bar{\epsilon}^n$ , where  $\bar{\sigma}$  is the effective von-mises stress,  $\bar{\epsilon}$  is the effective plastic strain, K is the strength coefficient (K = 143 MPa), and n is the strain hardening exponent (n = 0.208). These values were obtained from tensile tests. The number of elements after solid mesh generation was 10,000 and automatic re-meshing was used to accommodate large deformation during all of the analysis. The die and punch were assumed to be rigid so there is no deformation. The punch speed was  $2\text{ mms}^{-1}$ . Friction coefficient of 0.12 is used for all simulations. The various channel angle  $\Phi$  ( $60^\circ, 75^\circ, 90^\circ, 105^\circ, \text{ and } 120^\circ$ ) and outer corner angle  $\Psi$   $\{0, 15, (\pi - \phi)\}$  were simulated. A total number of 96 simulations were performed. To validate the simulated results, the calculated ECAP force is compared with experimental results. After validation, the magnitude of effective strain and in-homogeneity index at the cross-sectional of work pieces in the middle of the sample’s length were obtained. Figure 4 shows the

TABLE 1.—Material properties after ECAP.

No. of passes	Pass 0	Pass 1	Pass 2	Pass 3	Pass 4	Pass 8
YS (MPa)	39	87	118	136	145	153
UTS(MPa)	83	144	165	178	186	192
EL (%)	36	19	15	14	14	12



FIGURE 3.—Hydraulic press set-up, ECAP die, and sample (color figure available online).

simulated deformed sample after one pass with the effective strain contour for a die channel angle of 90°.

*ANN Architecture*

Neural network is characterized by important features such as the architecture, activation functions, and learning algorithm. The complexity level of the network depends on a number of hidden layer(s), number of neuron(s) in the input, and hidden and output layer [3]. Based on the experimental and numerical investigation,  $\phi$ ,  $\psi$ , and number of passes are the input variables and pressing force, magnitude of effective strain, and in-homogeneity index are the output variables. In this article, several networks with a different number of layers and neurons in the hidden layer have been designed and tested. Figure 5 schematically illustrates the architecture of the neural network.

Eighty-six data sets were used to develop and train the neural network model and 10 data sets were used to evaluate the performance of the resulting model. The data was normalized in the range [-1, 1] before the training of the network. The normalization ensures that ANN trains effectively without any deviation [18].

The ANN was built and trained using Matlab™ (Ver. 2008A). A feed forward-back propagation algorithm was used. The intensity of the signal passed between any two neurons depends on activation function and

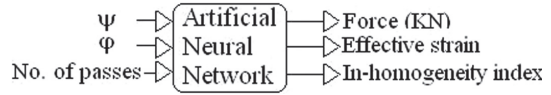


FIGURE 5.—Schematic of the ANN structure.

the weight of the connection. A tangent sigmoid function was used as a transfer function to transmit the data from input layer to hidden layer. The single neuron carries out a weighted sum of the inputs that is by and large the output of the neurons of the previous layer, adding threshold value and producing an output as shown:

$$a_k = f \left( \sum_{i=1}^n W_{ik} \cdot p_i + b_k \right), \tag{2}$$

where  $a_k$  = final output from  $k_{th}$  neuron,  $f$  = transfer function,  $n$  = number of neurons in the previous layer,  $W_{ik}$  = connection weight between  $i_{th}$  and  $k_{th}$  neuron,  $P_i$  = output from  $i_{th}$  neuron of previous layer, and  $b_k$  = bias of  $k_{th}$  neuron. The selection of the number of hidden neurons depends on number of input and output units, number of training cases, amount of noise in the targets, complexity of the function or classifications to be learnt, architecture, type of activation function, and training algorithm regularization. A low number of hidden neurons may cause high training error and high generalization error due to under fitting and high statistical bias. Conversely, a high number of hidden neurons may cause low training error but still have high generalization error due to overfitting and high variance [3]. In most cases, the optimum number of hidden neurons can be obtained by training several networks and estimating the generalization error of each. The network is trained by using the Levenberg–Marquardt back-propagation algorithm. After the training session was completed, the performance of the trained ANN was tested by evaluating the MSE (Mean Squared Error), as shown:

$$MSE = \frac{1}{M} \sum_{i=1}^M (t_k - a_k)^2, \tag{3}$$

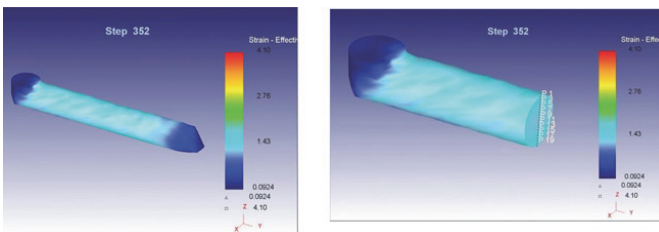


FIGURE 4.—Deformed sample after one pass for  $\Phi=90^\circ$ (color figure available online).

where  $a_k$  is the output value,  $t_k$  is the target value, and  $M$  is total number of training patterns. The prediction error in each output nodes are defined as:

$$\text{Prediction error}\% = \frac{(\text{Experimental value} - \text{Prediction value})}{\text{Experimental value}} \times 100. \quad (4)$$

RESULTS AND DISCUSSIONS

Table 1 lists the magnitudes of yield and ultimate tensile strengths and elongation for pure aluminum up to eight passes by route A. As can be seen, significant changes in the magnitudes were achieved for the first pass before gradual changes were observed for subsequent passes [11]. The yield and ultimate tensile strength increased by 300% and 200%, respectively, after ECAP. The elongation was reduced by 60% during the ECAP. The average grain sizes measured before and after the ECAP process were 2 μm and 257 nm, respectively.

To validate simulation results, the magnitudes of ECAP pressing force were measured in laboratory and compared with FEM results. After one pass, the pressing force magnitudes obtained from the experimental and the simulation work was 121.5 KN and 113 KN, respectively. This represents a 7% discrepancy between the experimental and numerical results, which for all practical purposes is acceptable. After validation, the effect of channel angle  $\Phi$ , the outer corner angle  $\Psi$ , and number of passes on pressing force, magnitude of effective strain, and uniformity of strain distribution were investigated. Route A was chosen as it gives the least homogeneity [5, 19]. In-homogeneity index ( $C_i$ ) was used to examine the uniformity of strain distribution at the

cross-section of the work piece [14, 15]. The  $C_i$  is defined as:

$$C_i = \frac{\epsilon_{\max} - \epsilon_{\min}}{\epsilon_{\text{ave}}}, \quad (5)$$

where  $\epsilon_{\max}$ ,  $\epsilon_{\min}$ , and  $\epsilon_{\text{ave}}$  are maximum, minimum, and average magnitudes of effective strain. Lower magnitude of  $C_i$  indicates higher homogeneity of strain. The results are shown in Table 2. As can be seen, for one pass ECAP with outer corner angle  $\Psi = 0^\circ$ , an increase in the die channel angle to  $120^\circ$  from  $60^\circ$  causes the effective strain magnitude to decrease from 2.01 to 0.68. In contrast, for one pass ECAP with channel angle  $\Phi = 90^\circ$ , an increase in the outer corner angle to  $(\pi - \varphi)^\circ$  from  $0^\circ$  makes the effective strain magnitude decrease to 0.94 from 1.24. Route A gives the least uniformity of strain distribution because strain difference between the maximum and minimum continues to increase with pass number [19], on the other hand, as shown in Table 2, the value of  $C_i$  decreases (i.e., strain homogeneity increases) as the number of passes increases for similar die geometry, indicating that perhaps this is not good parameter for examining the uniformity of strain distribution for this route since. On the whole, with an increase in die channel angle or outer corner angle the magnitude of effective strain decreases.

One of the objectives of the present work is to explore the use of ANN for efficient die design and process determination in the ECAP process. The experimental and numerical results were used to train the ANN. Based on these results, three inputs and three outputs in the networks was decided to be sufficient for this study, as shown in Figure 5. In this article, the activation function calculations performed at each neuron in the

TABLE 2.—Selected data sets of different ECAP conditions.

Input			Target			Input			Target		
$\Phi^0$	$\Psi^0$	No. of Passes	Strain	Force (KN)	$C_i$	$\Phi^0$	$\Psi^0$	No. of Passes	Strain	Force (KN)	$C_i$
60	0	1	2.01	154	0.226	105	0	1	0.91	82	0.539
60	0	2	4.04	191	0.113	105	0	2	1.78	90	0.238
60	0	3	5.99	195	0.074	105	0	3	2.69	91	0.202
60	0	4	8.14	199	0.058	105	0	4	3.59	92	0.195
60	0	5	9.95	202	0.033	105	0	5	4.56	93	0.165
60	15	6	11.12	196	0.014	105	15	6	5.34	91	0.199
60	15	7	12.57	207	0.008	105	15	7	6.17	91	0.186
60	120	4	4.89	140	0.350	105	75	4	3.1	81	0.442
60	120	5	6.24	141	0.268	105	75	5	3.92	82	0.378
60	120	6	7.42	144	0.156	105	75	6	4.8	83	0.307
90	0	4	4.59	123	0.091	120	0	4	2.69	71	0.340
90	0	5	5.79	124	0.062	120	0	5	3.48	77	0.327
90	0	6	6.9	125	0.076	120	0	6	4.11	81	0.315
90	15	4	4.36	115	0.159	120	15	4	2.55	74	0.408
90	15	5	5.56	116	0.137	120	15	5	3.29	77	0.405
90	15	6	6.59	117	0.133	120	15	6	4.02	80	0.373
90	90	6	5.64	95	0.282	120	60	6	3.64	68	0.287
90	90	7	6.48	96	0.256	120	60	7	4.33	69	0.271
90	90	8	7.44	98	0.249	120	60	8	4.85	70	0.222

TABLE 3.—Selected data sets of MSE for different networks.

One-layer Networks with different neuron No.		Two-layers Networks with different neuron No.			Three-layers Networks with different neuron No.			
1st Layer	MSE	1st Layer	2nd Layer	MSE	1st layer	2nd layer	3rd layer	MSE
3	0.03	2	1	0.03	4	2	1	0.03
4	0.04	3	2	0.02	4	3	2	0.1
5	0.01	4	3	0.08	5	4	3	0.02
6	0.2	5	4	0.02	6	5	4	0.1
7	0.009	6	2	0.04	7	6	2	0.3
8	0.0058	7	3	0.1	8	7	3	0.1
9	0.01	8	4	0.09	9	8	4	0.5
10	0.009	9	5	0.0068	10	9	5	0.06
11	0.2	2	6	0.02	11	2	6	0.02
12	0.08	3	3	0.01	12	3	3	0.06
13	0.09	4	4	0.03	13	4	4	0.03
14	0.05	5	4	0.06	14	5	4	0.1
15	0.07	6	4	0.05	15	6	4	0.3
16	0.1	7	5	0.1	16	7	5	0.2
17	0.03	8	5	0.03	17	8	5	0.04

hidden layer and in the output layer is tangent sigmoid and linear respectively. A minimum error was observed with the Levenberg-Marquardt back-propagation algorithm. Therefore, the L-M back-propagation training was repeatedly applied until satisfactory training is achieved. For determining the optimal architecture, 99 different networks with a different number of neurons in the

hidden layer were designed and tested with their performance capability examined based on MSE (see Table 3). The number of neurons in the hidden layer determines the amount of connections and weights to be fitted. Although the neural network can still be trained, if this number (connections) is larger than the number of the data pairs available for training, the case is mathematically undetermined. The minimum learning inputs is [3]:

$$C = 1 + (N(I + T + 1))/T \tag{6}$$

TABLE 4.—Comparison of ANN output with target data.

	Effective Strain	Force (KN)	C <sub>i</sub>
Target	5.99	195	0.074
	4.89	140	0.350
	4.59	123	0.091
	5.56	116	0.137
	5.64	95	0.282
	4.56	93	0.165
	6.17	91	0.186
	4.8	83	0.307
	4.11	81	0.315
	3.29	77	0.405
Output	6.221748	187.3827	0.071686
	4.941233	140.9989	0.342978
	4.464847	122.9133	0.086657
	5.441037	116.538	0.126576
	5.557725	96.48901	0.302745
	4.45415	92.80365	0.159356
	6.021931	92.07106	0.184875
	4.624649	82.50429	0.313333
	4.055454	78.53132	0.274063
	3.340591	75.41962	0.395326
%error	3.87	3.91	2.72
	1.05	0.71	1.92
	2.73	0.07	4.77
	2.14	0.46	7.61
	1.46	1.57	7.36
	2.32	0.21	3.42
	2.4	1.18	0.61
	3.65	0.6	1.9
	1.33	3.05	12.99
	1.54	2.05	2.39

where C = the minimum learning inputs, N = neurons in hidden layer, and T and I are output and input parameters, respectively. According to Eq. (6), there can be up to 37 numbers of neurons in the hidden layer. Table 3 demonstrates that the networks with one hidden layer of eight neurons produced the best performance (3-8-3). To verify the validity of the network, ten data points were given to the network as inputs. This data was completely unknown to the network (gray rows in Table 2). The correlation between the predicted values of the neural network model (Eq. (4)) and the data is shown in Table 4. The average error was 2.83%, which indicates a good conformity between numerical and ANN prediction. Thus, the optimum network selected is that of a network having one hidden layers of eight neurons trained with Levenberg-Marquardt back-propagation algorithm. However, it is possible to use multi-objective genetic algorithms for training and optimizing the neural network. In this method, the number of nodes in the hidden layer, architecture of the network, and weights can be taken as variables, and a Pareto front can be constructed by minimizing the training error along with the network size [20, 21].

CONCLUSION

In this article, the deformation behavior of a pure aluminum processed by ECAP was investigated by using 3D FEM and experimental method. The material was



successfully ECAPed up to eight passes. An ANN model was developed for predicting the process parameters. Based upon results, the following conclusions have been drawn.

1. In comparison to un-ECAPed alloy, improvements of more than three times yield strength and more than twice in ultimate tensile strength are seen in ECAPed alloy. The elongation of the alloy reduced 60% during the ECAP. The average grain size was also reduced from 2  $\mu\text{m}$  to 257 nm during ECAP.
2. With an increase in die channel angle or outer corner angle, the magnitude of effective strain decreases. Conversely, a better strain homogeneity distribution has been obtained with an increase in die channel angle.
3. Ninety-nine different architectures are trained/analyzed using numerical and experimental data. Based upon the MSE, an optimum architecture is identified. Data demonstrated that a network with one hidden layer having eight neurons can be used to model the ECAP process.
4. This study provides guidelines for efficient die design and process determination in the ECAP. To avoid performing expensive simulation or experimental work, a new technique has been suggested combining FEM and ANN. This technique can also be viewed as a tool to perform virtual experiments or simulations whereby the effect of various variables can be assessed. All the validation results show that the estimation of ANN can achieve a satisfactory level.

#### REFERENCES

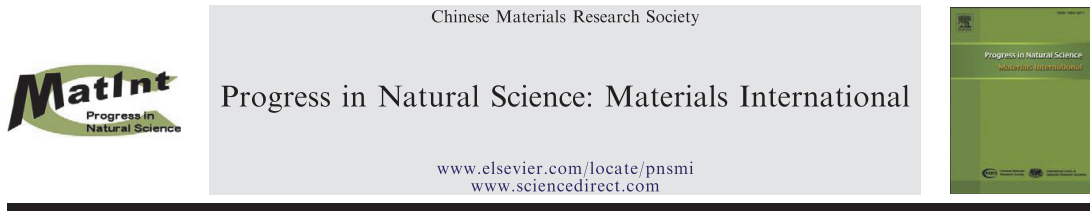
1. Chan, W.L.; Fu, M.W.; Lu, J. An integrated FEM and ANN methodology for metal-formed product design. *Engineering Applications of Artificial Intelligence* **2008**, *21*, 1170–1181.
2. Cheng, L.; Zhao, G.; Cheng, C.; Zhao, X. Application of neural network in complex forging design. *International Journal of Materials and Product Technology*, **2010**, *38* (2/3), 237–247.
3. Derogar, A.; Djanroodi, F. Artificial neural network modeling of forming limit diagram. *Materials and Manufacturing Processes* **2011**, *26*, 1415–1422.
4. Djanroodi, F.; Pirgholi, A.; Derakhshani, E. FEM and ANN analysis in fine-blanking process. *Materials and Manufacturing Processes* **2010**, *25*, 864–872.
5. Barber, R.E.; Dudo, T.; Yasskin, P.B.; Hartwig, K.T. Product yield for ECAE processing. *Scripta Materialia* **2004**, *51*, 373–377.
6. Stolyarov, V.V.; Zhu, Y.T.; Alexandrov, I.V.; Lowe, T.C.; Valiev, R.Z. Influence of ECAP routes on the microstructure and properties of pure Ti. *Materials Science and Engineering* **2001**, *A299*, 59–67.
7. Fu, M.W.; Yong, M.S.; Pei, Q.X.; Hng, H.H. Deformation behaviour of multi-pass ECAE process for fabrication of ultrafine or nanostructured bulk materials. *Materials and Manufacturing Processes* **2006**, *21*, 507–512.
8. Tham, Y.W.; Fu, M.W.; Hng, H.H.; Pei, Q.X.; Lim, K.B. Microstructure and properties of Al-6061 alloy by equal channel angular extrusion for 16 Passes. *Materials and Manufacturing Processes* **2007**, *22*, 819–824.
9. Cherukuri, B.; Srinivasan, R. Properties of AA6061 processed by multi-axial compressions/forging (MAC/F). *Materials and Manufacturing Processes* **2006**, *21*, 519–525.
10. Reihanian, M.; Ebrahimi, R.; Tsuji, N.; Moshksar, M.M. Analysis of the mechanical properties and deformation behavior of nanostructured commercially pure Al processed by equal channel angular pressing (ECAP). *Materials Science and Engineering A* **2008**, *473*, 189–194.
11. Djanroodi, F.; Ebrahimi, M.; Rajabifar, B.; Akramizadeh, S. Fatigue design factors for ECAPed materials. *Materials Science and Engineering A* **2010**, *528*, 745–750.
12. Luis, C.J.; Garcés, Y.; González, P.; Berlanga, C. FEM analysis of equal channel angular processes. *Materials and Manufacturing Processes* **2002**, *17* (2), 223–250.
13. Patil Basavaraj, V.; Chakkingal, U.; Prasanna Kumar, T.S. Study of channel angle influence on material flow and strain in homogeneity in equal channel angular pressing using 3D finite element simulation. *Journal of Materials Processing Technology* **2009**, *209*, 89–95.
14. Djanroodi, F.; Ebrahimi, M. Effect of die parameters and material properties in ECAP with parallel channels. *Materials Science and Engineering A* **2010**, *527*, 7593–7599.
15. Djanroodi, F.; Ebrahimi, M. Effect of die channel angle, friction and back pressure in the equal channel angular pressing using 3D finite element simulation. *Materials Science and Engineering A* **2010**, *527*, 1230–1235.
16. Yoon, S.C.; Quang, P.; Hong, S.I.; Kim, H.S. Die design for homogeneous plastic deformation during equal channel angular pressing. *Journal of Materials Processing Technology* **2007**, *187–188*, 46–50.
17. Chao Duan, Z.; Langdon, T.G. An experimental evaluation of a special ECAP die containing two equal arcs of curvature. *Materials Science and Engineering A* **2011**, *528*, 4173–4179.
18. Qin, Y.J.; Pan, Q.L.; He, Y.B.; Li, W.B.; Liu, X.Y.; Fan, X. Artificial neural network modeling to evaluate and predict the deformation behavior of ZK60 magnesium alloy during hot compression. *Materials and Manufacturing Processes* **2010**, *25*, 539–545.
19. Kim, W.J.; Namkung, J.C. Computational analysis of effect of route on strain uniformity in equal channel angular extrusion. *Materials Science and Engineering A* **2005**, *412*, 287–297.
20. Pettersson, F.; Biswas, A.; Sen, P.K.; Saxn, H.; Chakraborti, N. Analyzing leaching data for low-grade manganese ore using neural nets and multi objective genetic algorithms. *Materials and Manufacturing Processes* **2009**, *24*, 320–330.
21. Pettersson, F.; Suh, C.; Saxn, H.; Rajan, K.; Chakraborti, N. Analyzing sparse data for nitride spinels using data mining, neural networks, and multiobjective genetic algorithms. *Materials and Manufacturing Processes* **2009**, *24*, 2–9.

**Article VII:**

F. Djavanroodi, B. Omranpour, M. Ebrahimi, M. Sedighi, Designing of ECAP parameters based on strain distribution uniformity, *Prog. Nat. Sci. Mater. Int.* 22 (2012) 452–460.







ORIGINAL RESEARCH

# Designing of ECAP parameters based on strain distribution uniformity

F. Djavaanroodi, B. Omranpour, M. Ebrahimi\*, M. Sedighi

Department of Mechanical Engineering, Iran University of Science and Technology, Tehran, Iran

Received 21 May 2012; accepted 5 August 2012  
Available online 30 October 2012

**KEYWORDS**

ECAP;  
FEM;  
Die design;  
Strain distribution

**Abstract** Equal Channel Angular Pressing (ECAP) is currently one of the most popular methods for fabricating Ultra-Fine Grained (UFG) materials. In this work, ECAP process has been performed on commercial pure aluminum up to 8 passes by route *A*. After verification of FEM work, the influences of four die channel angles, three outer corner angles and pass number up to 8 have been analyzed to investigate strain distribution behavior of ECAPed material. Two methods for quantifying the strain homogeneity namely inhomogeneity index ( $C_i$ ) and standard deviation (S.D.) are compared. It is shown that  $C_i$  is not a good candidate for examining the strain distribution uniformity. Moreover, it is suggested that designing of ECAP die geometry to achieve optimum strain distribution homogeneity is more suitable than the optimum effective strain magnitude. The best strain distribution uniformity in the transverse plane is obtained with  $\Phi=60^\circ$  and  $\Psi=15^\circ$  and for the bulk of the sample,  $\Phi=120^\circ$  and  $\Psi=15^\circ$  or  $60^\circ$ , gives the highest strain dispersal uniformity.

© 2012 Chinese Materials Research Society. Production and hosting by Elsevier Ltd. All rights reserved.

## 1. Introduction

Equal Channel Angular Pressing developed by Segal [1] is the most popular Severe Plastic Deformation (SPD) techniques for enhancement of mechanical properties and superplastic behavior with respect to the grain size reduction [2–4]. As a principle, material grain size is one of the prominent parameters influencing mechanical behavior of base metals and alloys concentrated in all of the SPD techniques like ECAP [5], High Pressure Torsion (HPT) [6], Accumulative Roll Bonding (ARB) [7], Constrained Groove Pressing (CGP) [8], Accumulative Back Extrusion (ABE) [9], Tubular Channel Angular

\*Corresponding author. Tel.: +98 217 724 0203.

E-mail addresses: javanroodi@iust.ac.ir (F. Djavaanroodi), omranpour@yahoo.com (B. Omranpour), mebrahimi@iust.ac.ir (M. Ebrahimi), sedighi@iust.ac.ir (M. Sedighi).

Peer review under responsibility of Chinese Materials Research Society.



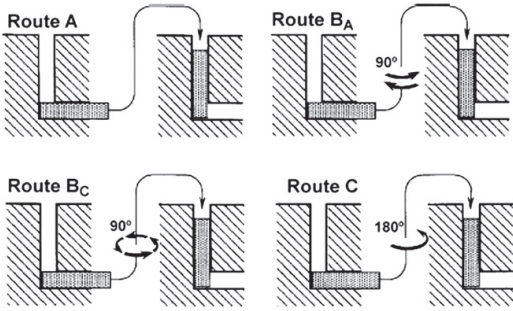


Fig. 1 Four fundamental routes in the ECAP process [12].

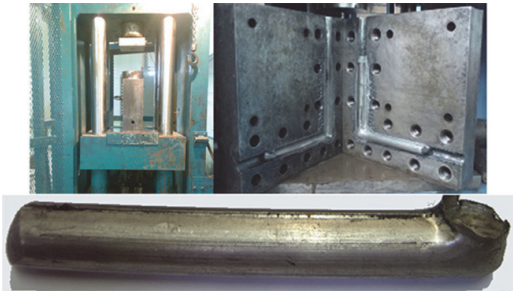


Fig. 2 Hydraulic press, ECAP die and AL billet after one pass pressing.

Pressing (TCAP) [10], etc. During ECAP, a sample is pressed through two intersecting channels having the same cross-sections with a die channel angle of  $\Phi$  and an outer corner angle of  $\Psi$ . During this process, billet with high value of plastic strain can be produced because of accumulative shear strain at each pass. The magnitude of shear strain after one pass ECAP in the frictionless condition is determined with [11]:

$$\gamma = 2 \cot \left( \frac{\Phi + \Psi}{2} \right) + \Psi \operatorname{cosec} \left( \frac{\Phi + \Psi}{2} \right) \quad (1)$$

Also, the magnitude of equivalent effective plastic strain ( $\epsilon_{eq}$ ) after  $N$  passes is given by the following relationship:

$$\epsilon_{eq} = N / \sqrt{3} \left[ 2 \cot \left( \frac{\Phi + \Psi}{2} \right) + \Psi \operatorname{cosec} \left( \frac{\Phi + \Psi}{2} \right) \right] \quad (2)$$

In the ECAP process, there are four fundamental routes between each repetitive pressing as shown in Fig. 1 [12]. These are as follows: route  $A$  by which the sample is repetitively pressed without any rotation, route  $B_A$  by which the sample is rotated by  $90^\circ$  in the alternative direction between each pass, route  $B_C$  by which the sample is rotated in the same direction by  $90^\circ$  and route  $C$  by which the sample is rotated by  $180^\circ$  between consecutive passes. These routes result in different slip systems in the specimen and so, various microstructures and mechanical properties can be obtained by them [12,13].

So far, many experimental studies have been performed to investigate the influence of different pressing routes on the microstructure, texture and so, mechanical properties of the final work-piece [14,15]. Investigations of Komura et al. [16]

Table 1 Mechanical properties of pure Al before and after ECAP process up to 8 passes by route A.

No. of passes	Pass 0	Pass 1	Pass 2	Pass 3	Pass 4	Pass 8
YS (MPa)	39	87	118	136	145	153
UTS (MPa)	83	144	165	178	186	192
EL (%)	36	19	15	14	14	12

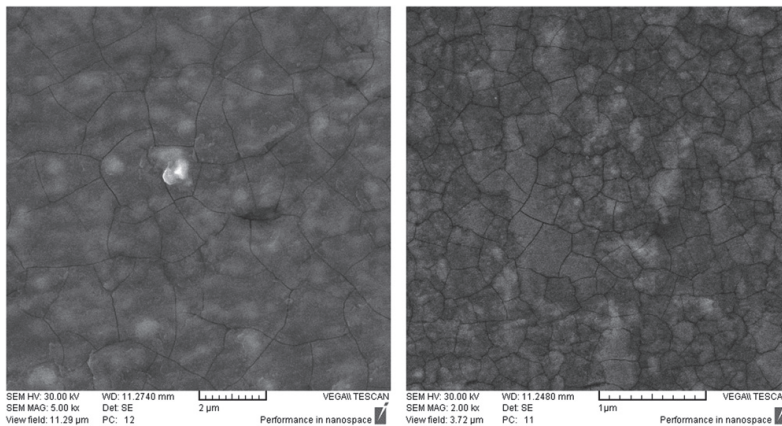


Fig. 3 Microstructure observations for initial and ECAPed Al after 8 passes by route A using SEM.

had been shown that the optimum superplastic ductility is achieved by route  $B_C$  because of the most expeditious generation of equiaxed grains with high angle grain boundaries (HAGBs). The results of Stolyarov et al. [17] indicated that route  $B_C$  is the most effective and route  $B_A$  is the least efficient in grain refinement. Also, routes  $B_A$  and  $C$  lead to elongated

grains. Tong et al. [18] had surveyed the influence of ECAP routes on the microstructure and mechanical properties of Mg alloys. The results revealed that route  $B_C$  is the most capable in grain refinement and production of HAGBs, while route  $A$  is the least capable. In addition, Kim and Namkung [19] illustrated that routes  $A$  and  $B_A$  cause the lowest strain

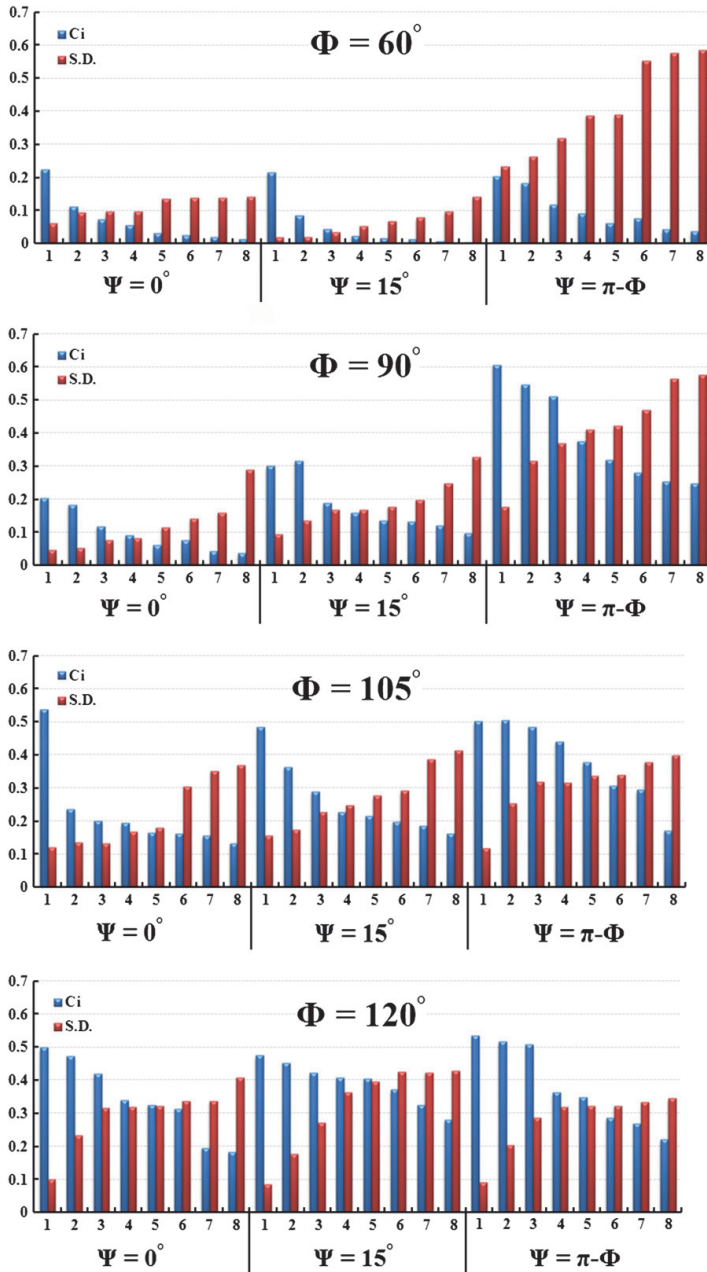


Fig. 4 The magnitudes of  $C_i$  and S.D. versus pass numbers in transverse direction.

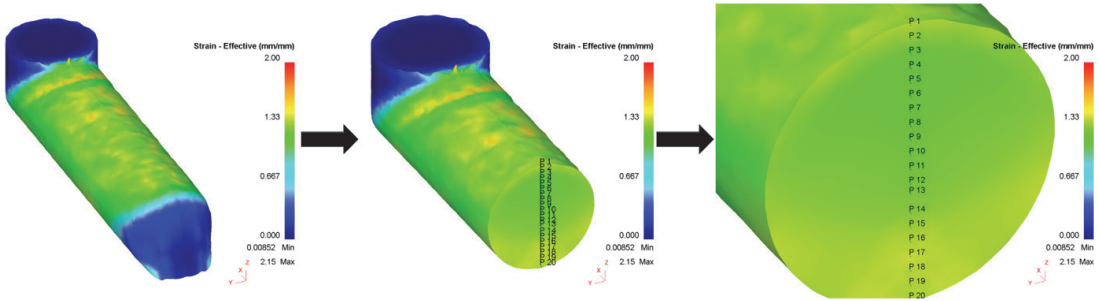


Fig. 5 Locations of 20 different nodes in the vertical centerline at the transverse direction of the work-piece.

distribution homogeneity and routes  $C$  and  $B_C$  give the highest strain dispersal uniformity.

On the other hand, several numerical researches have been performed to investigate the effects of different ECAP parameters including die channel angle, outer corner angle, friction coefficient, material properties, ram speed and temperature on the effective strain value, strain distribution uniformity, required pressing force value and material flow [20–23].

Although Eq. (2) represents the average effective strain magnitude induced to the specimen during each pass, different locations of the sample (in the transverse and longitudinal directions) experience different strain values depending on various parameters in the process. In general, there are two methods to quantify the degree of strain distribution homogeneity. One is inhomogeneity index ( $C_i$ ) defined by Li et al. [24]:

$$C_i = \frac{\epsilon_{\max} - \epsilon_{\min}}{\epsilon_{\text{avg}}} \quad (3)$$

where  $\epsilon_{\max}$ ,  $\epsilon_{\min}$  and  $\epsilon_{\text{avg}}$  denote the maximum, minimum and average of the plastic strain, respectively. A number of researchers have used inhomogeneity index ( $C_i$ ) for investigating the strain distribution uniformity [24–29]. Less magnitude for  $C_i$  leads to better strain dispersal uniformity. According to Eq. (3), this factor depends only on the maximum, minimum and average magnitudes of plastic strain. The second method is a mathematical coefficient called standard deviation (S.D.) [30]. In addition, this parameter is utilized in statistical analyses in variant fields of sciences and humanities. In this study, S.D. has been employed to measure strain distribution uniformity expressed by

$$S.D. = \sqrt{\frac{\sum_{i=1}^n (\epsilon_i - \epsilon_{\text{avg}})^2}{n}} \quad (4)$$

where  $\epsilon_i$  is the plastic strain magnitude in  $i$ th node,  $\epsilon_{\text{avg}}$  is the average value of plastic strain extracted from all nodes and  $n$  is the number of nodes in the billet. As is known, high value for S.D. indicates strain distribution non-uniformity.

Although a number of researches have been carried out on the efficiency of ECAP process routes and influences of various ECAP parameters on the strain behavior, there is no work up to now to design ECAP die based on the optimum strain behavior. In this paper, ECAP process strain distribution uniformity for different passes were compared using two factors inhomogeneity index ( $C_i$ ) and standard deviation (S.D.). Furthermore, route  $A$  was used for examining these two strain distribution factors since this route gives the worst

Die design	Pass number	S.D.	$\Phi$ & $\Psi$
	1	0.02	60° & 15°
	2	0.022	60° & 15°
	3	0.035	60° & 15°
	4	0.055	60° & 15°
	5	0.069	60° & 15°
	6	0.08	60° & 15°
	7	0.097	60° & 15°
	8	0.141	60° & 15°

Fig. 6 ECAP die design based on strain distribution uniformity in transverse direction for 8 passes.

strain distribution homogeneity and the magnitude of strain heterogeneity increases by adding pass numbers. Also, ECAP process is experimentally performed on the commercial purity aluminum up to 8 passes by route  $A$ . The improvement of ECAPed Al properties has been demonstrated by accomplishing tensile test and microstructure observation. Influences of various die channel angles (60°, 90°, 105° and 120°) and outer corner angles (0°, 15° and  $\pi - \Psi$ ) up to 8 passes on the strain behavior have been investigated numerically (96 different simulations). Finally, ECAP die design has been carried out based on the optimum strain distribution uniformity.

## 2. Experimental procedure

The material used in this study was commercial purity aluminum (chemical composition wt%: 99.5Al, 0.258Fe, 0.156Si, 0.0001Cu, 0.027Mg, 0.003Mn, 0.003V) annealed at 375 °C for 1 h and cooled slowly in furnace. Samples were prepared with diameter of 19.7 mm same as the ECAP die channel diameter and 180 mm length well lubricated in MoS<sub>2</sub> before pressing. An ECAP die with the channel angle of 90°, outer corner angle of 15° and channel diameter of 19.8 mm was designed and manufactured. The hydraulic press, ECAP die setup and billet after one pass

pressing are shown in Fig. 2. The ram speed was constant (equal to 2 mm/s) and ECAP process was performed at room temperature by route *A* up to 8 passes.

To prepare tensile test, specimens were machined with their longitudinal axes parallel to the pressing axis from the billet center according to ASTM B557M. To verify refining of the grain size during ECAP process, optical microscopy (OM) for initial billet and scanning electron microscopy

(SEM) for ECAPed billet were applied to ensure the grain size reduction.

### 3. Finite element modeling

Simulations were carried out using commercial FEM software, DEFORM3D™. The work-piece was assumed to be plastic

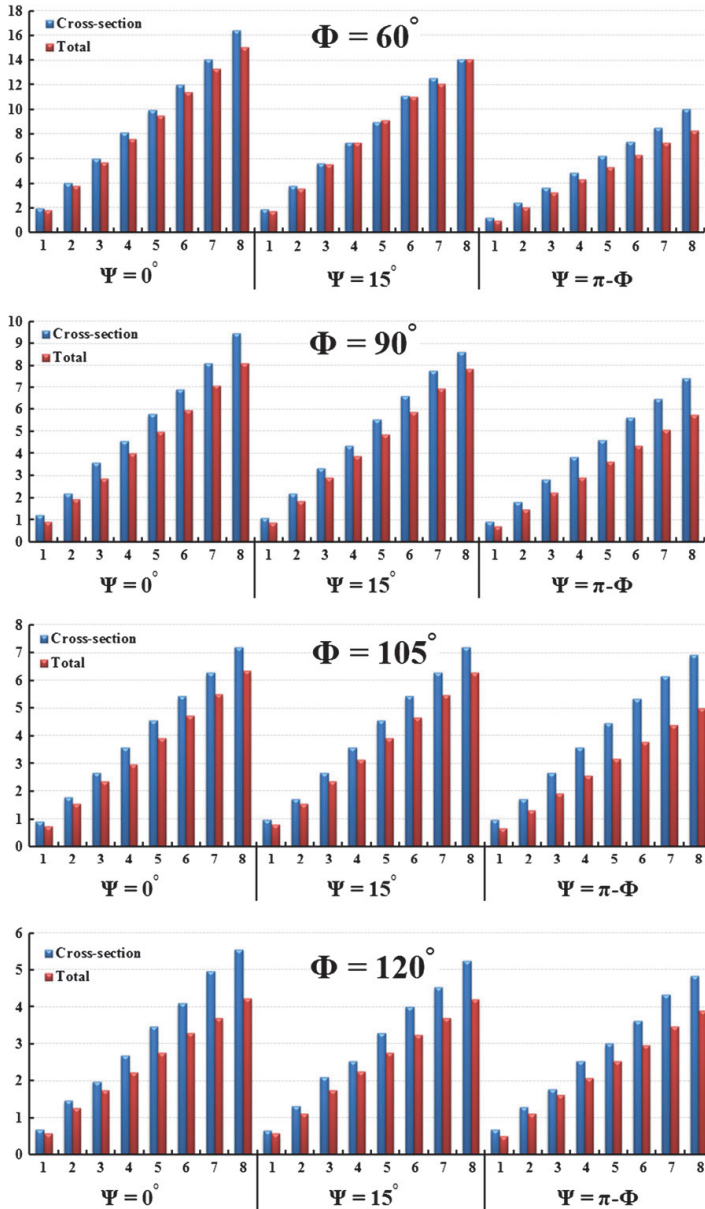


Fig. 7 The effective strain values for the 4 die channel angles and 3 outer corner angles up to 8 passes by route A.



having the same geometry with the experimental work. For the FEM analysis, the magnitudes of strain hardening coefficient ( $K=143$  MPa) and strain hardening exponent ( $n=0.208$ ) were obtained from true stress–true strain relationship in tensile test. The die and punch were supposed to be rigid. The value of  $2\text{ mm s}^{-1}$  was assigned to the ram speed. In order to determine the optimum mesh size, mesh sensitivity diagram was plotted to investigate the convergence of results and selection of proper mesh element size. The optimum mesh element numbers were chosen as 10,000 and automatic re-meshing was used to accommodate large deformation in analyses. The value of 0.12 was selected as a friction coefficient [31] and all analyses were performed at the ambient temperature.

The pressing force is an important factor in metal forming and so, other significant parameters can affect this factor during the process. Hence as a validation of the FEM results, the required pressing force can be compared with the experimental work. If the punch force in the simulation meets well with that in the experiment at the same punch position with all similar conditions, the outputs in the FEM are considered as agreeable values.

After verification, various die channel angles ( $\Phi=60^\circ, 90^\circ, 105^\circ$  and  $120^\circ$ ) and outer corner angles ( $\Psi=0^\circ, 15^\circ$  and  $\pi-\Psi$ ) were simulated up to 8 passes via route *A*. Combination of these situations yields a total number of 96 runs. The effects of die channel angle, outer corner angle and pass number have been investigated on effective strain magnitude and strain distribution uniformity. Finally, the die design has been considered based on these parameters to achieve the optimum strain distribution homogeneity.

**4. Results and discussion**

*4.1. Verification of FEM*

To verify FEM work, the magnitude of pressing force has been measured in laboratory and compared with the FEM results. For one pass ECAP with commercial purity Al, the required pressing force magnitudes acquired from the experimental and the simulated works are 121.5 kN and 113 kN, respectively. This represents about 7% discrepancy between the experimental and numerical outcomes which is acceptable for all practical purposes.

*4.2. Experimental results*

Table 1 illustrates the magnitudes of yield strength (YS) and ultimate tensile strength (UTS) and also elongation to failure for commercial purity aluminum up to eight passes by route *A*. As can be seen, significant enhancements in the magnitudes of YS and UTS are obtained for the 1st pass and then, gradual increases are observed for subsequent passes. The same trend had been reported earlier [32,33]. YS and UTS values have been improved by 125%, 75% and 290%, 130% after 1st and 8th passes, respectively. The elongation to failure has been reduced by 45% and 65% after the 1st and 8th passes, respectively. This indicates that by increasing pass numbers, the ductility of aluminum tends to be dropped. Also, the average grain sizes measured before and after 8 pass ECAP are about  $2\ \mu\text{m}$  and  $240\ \text{nm}$ , respectively; see Fig. 3. As is known, the ECAP process consists of production, multiplication and locking of dislocations, making of low angle grain boundaries

(LAGBs), HAGBs and finally, formation of UFG materials [32–34].

*4.3. Numerical results*

*4.3.1. Strain distribution uniformity parameters*

Two parameters (inhomogeneity index ( $C_i$ ) and standard deviation (S.D.)) have been applied to measure and investigate strain distribution homogeneity. Increasing pass number by route *A* results in decrease of strain distribution uniformity [19]. So, it is anticipated that  $C_i$  and S.D. values would increase by increasing pass number. The magnitudes of inhomogeneity index and standard deviation are presented in Fig. 4 for all 96 ECAP circumstances. These conditions are the combinations of 4 die channel angles ( $\Phi=60^\circ, 90^\circ, 105^\circ$  and  $120^\circ$ ) and 3 outer corner angles ( $\Psi=0^\circ, 15^\circ$  and  $\pi-\Psi$ ) up to 8 passes by route *A*. These values have been calculated from the 20 effective strain magnitudes at the cross-sectional area in the mid-length of the billet as shown in Fig. 5.

As can be observed in Fig. 4, the inhomogeneity index is reduced with increasing pass number. It means that ECAPed aluminum with uniform strain distribution is obtained by increasing pass number. This is inconsistent with the previous experimental and numerical investigations where the pass number increase by route *A* leads to non-uniformity in the strain dispersal [19]. Also, it has been demonstrated that the volume of fully worked material is continuously reduced by increasing the number of passes and as a result, ECAPed material with a strong texture or anisotropic grain morphology is obtained by this route [35]. So, for route *A* ECAPed materials, the degree of strain inhomogeneity cannot be quantified with  $C_i$  factor. On the other hand, S.D. value indicates that strain distribution heterogeneity is increasing as the number of passes increases. It can thus be said that at least for route *A*, the S.D. is a better indication of quantifying the strain distribution homogeneity of ECAPed materials than  $C_i$ .

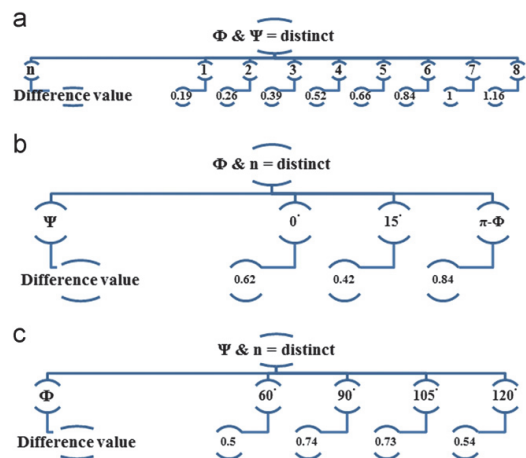


**Fig. 8** The magnitudes of effective strain differences between the cross-section and whole of the work-piece.

4.3.2. Die design based on the strain distribution homogeneity in the transverse direction

The optimum combinations of  $\Phi$  and  $\Psi$  to achieve minimum S.D. value in the transverse direction for 8 passes are listed in Fig. 6.

As can be seen, the best strain dispersal homogeneity can be obtained with  $\Phi=60^\circ$  and  $\Psi=15^\circ$ . In addition, the die channel angle of  $60^\circ$  leads to a higher magnitude of effective strain than the other 3.

4.3.3. Die design based on the strain distribution homogeneity in the sample

Up to now, most of the ECAP die design has been based on the effective strain magnitude. Achieving a certain amount of

grain refinement or effective strain value can be obtained with increasing pass number, but, the authors believe that the most prominent factor in this process is the strain distribution uniformity which leads to homogenous ECAPed materials. Fig. 7 represents the effective strain magnitude for the 4 die channel angles and 3 outer corner angles up to 8 passes by route A at the cross-section and in the bulk of the samples. The position of the cross-section is indicated in Fig. 5.

As a first result, the effective strain value at the cross-section is higher or at least equal to that of the entire billet. It may be related to the undeformed regions of the ECAPed material in the head and tail parts of the sample. The existence of these sections reduces the effective strain magnitude in the whole of the sample. The minimum and maximum differences between the effective strain at the cross-section and entirety of

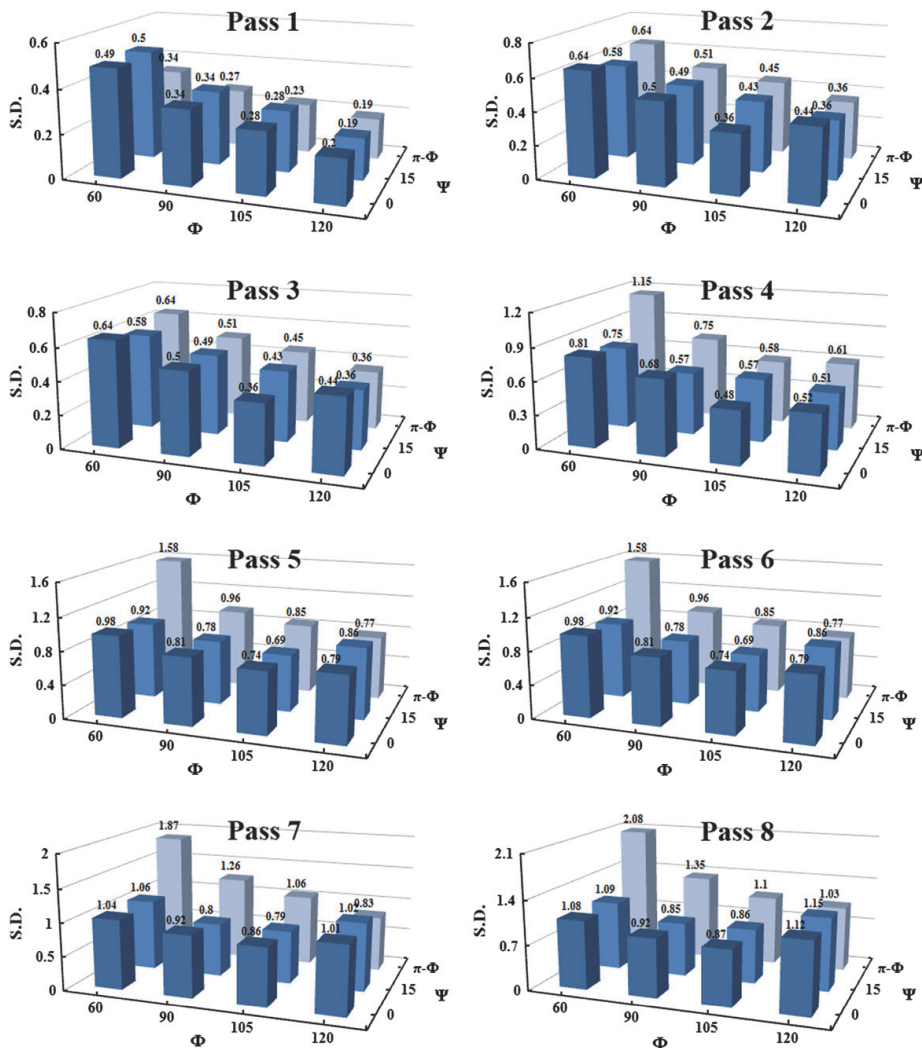


Fig. 9 The S.D. magnitudes for the different values of die channel and outer corner angles from 1 to 8 passes.

the billet are 0.01 and 1.93 referred to the cases of  $\Phi=60^\circ$ ,  $\Psi=15^\circ$  and 4th pass and  $\Phi=105^\circ$ ,  $\Psi=75^\circ$  and 8th pass, respectively. Also, the dissimilarity value between the effective strain at the cross-section and whole of the sample intensifies by increasing pass number irrespective of the die parameters ( $\Phi$  and  $\Psi$ ), as exhibited in Fig. 8a. These values are averaged magnitudes calculated from the effective strain differences at the cross-section and whole of the sample for the 4 die channel angles and 3 outer corner angles. The average difference between the effective strain at the cross-section and entity of the billet for the 4 die channel angle and 8 passes versus outer corner angles is represented in Fig. 8b. It is observed that less disparity is obtained when the outer corner angle is equal to  $15^\circ$ . Finally for different die channel angles, the magnitude of effective strain differences at the cross-section and whole of sample is expressed in Fig. 8c. In this circumstance, the differences are averaged for the 3 outer corner angles and 8 passes. As a conclusion of this figure, 1st pass,  $\Psi=15^\circ$  and  $\Phi=60^\circ$  gives the least effective strain differences between the cross-section and whole of the ECAPed Al.

Fig. 9 shows the S.D. values for different die channel angles, outer corner angles and pass numbers.

Firstly, the magnitude of S.D. increases with increasing pass numbers for every die channel and outer corner angles. This means that increasing pass number results in a lower strain distribution uniformity in materials. The average magnitudes of S.D. are listed in Fig. 10 for each pass number (up to 8 passes) calculated from the 4 die channel angles and 3 outer corner angles.

Secondly as mentioned earlier, we believe that the die which produces more isotropic ECAP material is more suitable and important than the one which produces higher effective strain value. For this consideration, the suitable combination of  $\Phi$  and  $\Psi$  are ( $\Phi=120^\circ$  and  $\Psi=15^\circ$ ) and ( $\Phi=120^\circ$  and  $\Psi=60^\circ$ ), together. It is noted that for the die channel angle of  $120^\circ$ , the magnitude of S.D. is virtually independent on the outer corner angle. Finally for ECAPing of Al, the optimum parameters for die design depend on the pass number as listed in Table 2.

As indicated in Table 2, the optimum values of die design parameters are  $\Phi=120^\circ$  and  $\Psi=15^\circ$  or  $60^\circ$ . Although material in these die design conditions gives better strain distribution homogeneity, the effective strain magnitude is not the highest. However, increasing pass numbers can produce the desire amount of effective strain.

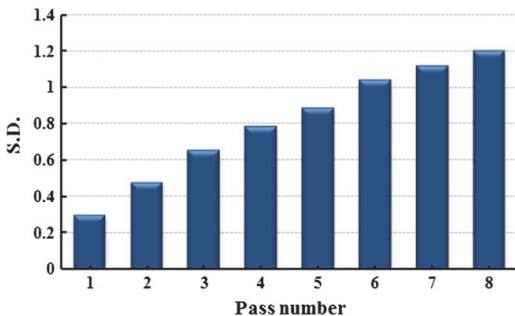


Fig. 10 The average S.D. values for each pass number up to 8 passes irrespective of die channel and outer corner angles.

Table 2 The magnitudes of die design parameters to achieve the optimum strain distribution uniformity in the ECAPed sample.

No. of passes	S.D.	ECAP die design parameters	
		$\Phi$	$\Psi$
1	0.19	120	15 and $\pi-\Psi$
2	0.36	120	15 and $\pi-\Psi$
3	0.48	105	0
4	0.61	105	0
5	0.69	105	15
6	0.79	105	15
7	0.85	90	15
8	0.87	105	15

## 5. Conclusion

In the current study, combinations of 4 die channel angles ( $\Phi=60^\circ$ ,  $90^\circ$ ,  $105^\circ$  and  $120^\circ$ ), 3 outer corner angles ( $\Psi=0^\circ$ ,  $15^\circ$  and  $\pi-\Psi$ ) and pass numbers (up to 8 passes) have been simulated by route A. The influences of above factors on the effective strain magnitude and strain distribution behavior via two parameters (inhomogeneity index and standard deviation) at the transverse direction and whole of the samples are investigated. The prominent conclusions can be drawn as follows:

- For route A ECAP, the magnitude of S.D. increases with increasing pass number; i.e. less strain distribution homogeneity is achieved using route A by increasing pass numbers.
- Considering that the increasing pass number causes high strain distribution heterogeneity, inhomogeneity index ( $C_i$ ) is not a suitable candidate to quantify the strain dispersal homogeneity. On the other hand, standard deviation (S.D.) is a better factor for quantifying the strain distribution uniformity of ECAPed materials.
- 1st pass,  $\Psi=15^\circ$  and  $\Phi=60^\circ$  are the general guidelines to obtain the least effective strain differences between the transverse plane and whole of the ECAPed Al.
- $\Phi=60^\circ$  and  $\Psi=15^\circ$  are the values of optimum parameters to design ECAP die based on the best strain distribution uniformity at the cross-section of the sample.
- $\Phi=120^\circ$  and  $\Psi=15^\circ$  or  $60^\circ$  are the magnitudes of die channel angle and outer corner angle for designing ECAP die to achieve optimum strain dispensation homogeneity at the bulk of the work-piece.

In the experimental work, pure Al was subjected to ECAP die with the channel angle of  $90^\circ$  and outer corner angle of  $15^\circ$  up to 8 passes by route A. Improvement of the ECAPed aluminum properties was confirmed with increasing YS and UTS (about 4 and 2 times, respectively) and also, reduction of the grain size (about 8 times).

## Acknowledgment

The authors wish to thank Mr. H. Nomoradi for providing the SEM micrographs used in this work.



## References

- [1] V.M. Segal, Equal channel angular extrusion: from macromechanics to structure formation, *Materials Science and Engineering A* 271 (1999) 322–333.
- [2] S.L. Semiatin, D.P. DeLo, Equal channel angular extrusion of difficult-to-work alloys, *Materials and Design* 21 (2000) 311–322.
- [3] L. Kommel, I. Hussainova, O. Volobueva, Microstructure and properties development of copper during severe plastic deformation, *Materials and Design* 28 (2007) 2121–2128.
- [4] Ruslan Z. Valiev, Terence G. Langdon, Principles of equal-channel angular pressing as a processing tool for grain refinement, *Progress in Materials Science* 51 (2006) 881–981.
- [5] Minoru Furukawa, Yoshinori Iwahashi, Zenji Horita, Minoru Nemoto, Terence G. Langdon, The shearing characteristics associated with equal-channel angular pressing, *Materials Science and Engineering A* 257 (1998) 328–332.
- [6] Alexander P. Zhilyaev, Terence G. Langdon, Using high-pressure torsion for metal processing: fundamentals and applications, *Progress in Materials Science* 53 (2008) 893–979.
- [7] Y. Saito, N. Tsuji, H. Utsunomiya, T. Sakai, R.G. Hong, Ultra-fine grained bulk aluminum produced by accumulative roll-bonding (ARB) process, *Scripta Materialia* 39 (9) (1998) 1221–1227.
- [8] Dong Hyuk Shin, Jong-Jin Park, Yong-Seog Kim, Kyung-Tae Park, Constrained groove pressing and its application to grain refinement of aluminum, *Materials Science and Engineering A* 328 (2002) 98–103.
- [9] S.M. Fatemi-Varzaneh, A. Zarei-Hanzaki, Accumulative back extrusion (ABE) processing as a novel bulk deformation method, *Materials Science and Engineering A* 504 (2009) 104–106.
- [10] Ghader Faraji, Mahmoud Mosavi Mashhadi, Hyoung Seop Kim, Tubular channel angular pressing (TCAP) as a novel severe plastic deformation method for cylindrical tubes, *Materials Letters* 65 (2011) 3009–3012.
- [11] I. Balasundar, M.Sudhakara Rao, T. Raghu, Equal channel angular pressing die to extrude a variety of materials, *Materials and Design* 30 (2009) 1050–1059.
- [12] Terence G. Langdon, The principles of grain refinement in equal-channel angular pressing, *Materials Science and Engineering A* 462 (2007) 3–11.
- [13] F. Djavanroodi, M. Ebrahimi, B. Rajabifar, S. Akramizadeh, Fatigue design factors for ECAPed materials, *Materials Science and Engineering A* 528 (2010) 745–750.
- [14] Cheng Xu, Minoru Furukawa, Zenji Horita, Terence G. Langdon, Severe plastic deformation as a processing tool for developing superplastic metals, *Journal of Alloys and Compounds* 378 (2004) 27–34.
- [15] Irene J. Beyerlein, László S. Tóth, Texture evolution in equal-channel angular extrusion, *Progress in Materials Science* 54 (2009) 427–510.
- [16] Shogo Komura, Minoru Furukawa, Zenji Horita, Minoru Nemoto, Terence G. Langdon, Optimizing the procedure of equal-channel angular pressing for maximum superplasticity, *Materials Science and Engineering A* 297 (2001) 111–118.
- [17] Vladimir V. Stolyarov, Y.Theodore Zhu, Igor V. Alexandrov, Terry C. Lowe, Ruslan Z. Valiev, Influence of ECAP routes on the microstructure and properties of pure Ti, *Materials Science and Engineering A* 299 (2001) 59–67.
- [18] L.B. Tong, M.Y. Zheng, X.S. Hu, K. Wu, S.W. Xu, S. Kamado, Y. Kojima, Influence of ECAP routes on microstructure and mechanical properties of Mg–Zn–Ca alloy, *Materials Science and Engineering A* 527 (2010) 4250–4256.
- [19] W.J. Kim, J.C. Namkung, Computational analysis of effect of route on strain uniformity in equal channel angular extrusion, *Materials Science and Engineering A* 412 (2005) 287–297.
- [20] Z.J. Zhang, I.H. Son, Y.T. Im, J.K. Park, Finite element analysis of plastic deformation of CP-Ti by multi-pass equal channel angular extrusion at medium hot-working temperature, *Materials Science and Engineering A* 447 (2007) 134–141.
- [21] Roberto Braga Figueiredo, Maria Teresa Paulino Aguiar, Paulo Roberto Cetlin, Finite element modelling of plastic instability during ECAP processing of flow-softening materials, *Materials Science and Engineering A* 430 (2006) 179–184.
- [22] F. Djavanroodi, M. Ebrahimi, Effect of die parameters and material properties in ECAP with parallel channels, *Materials Science and Engineering A* 527 (2010) 7593–7599.
- [23] P. Karpuz, C. Simsir, C. Hakan Gür, Investigating the effects of hardening of aluminium alloys on equal-channel angular pressing—a finite-element study, *Materials Science and Engineering A* 503 (2009) 148–151.
- [24] S. Li, M.A.M. Bourke, I.J. Beyerlein, D.J. Alexander, B. Clausen, Finite element analysis of the plastic deformation zone and working load in equal channel angular extrusion, *Materials Science and Engineering A* 382 (2004) 217–236.
- [25] Tao Suo, Yulong Li, Yazhou Guo, Yuanyong Liu, The simulation of deformation distribution during ECAP using 3D finite element method, *Materials Science and Engineering A* 432 (2006) 269–274.
- [26] Tao Suo, Yulong Li, Qiong Deng, Yuanyong Liu, Optimal pressing route for continued equal channel angular pressing by finite element analysis, *Materials Science and Engineering A* 466 (2007) 166–171.
- [27] V. Patil Basavaraj, Uday Chakkingal, T.S. Prasanna Kumar, Study of channel angle influence on material flow and strain inhomogeneity in equal channel angular pressing using 3D finite element simulation, *Journal of Materials Processing Technology* 209 (2009) 89–95.
- [28] Hong-jun Hu, Ding-fei Zhang, Fu-sheng Pan, Die structure optimization of equal channel angular extrusion for AZ31 magnesium alloy based on finite element method, *Transactions of the Nonferrous Metals Society of China* 20 (2010) 259–266.
- [29] Nahed El Mahallawy, Farouk A. Shehata, Mohamed Abd El Hameed, Mohamed Ibrahim Abd El Aal, Hyoung Seop Kim, 3D FEM simulations for the homogeneity of plastic deformation in Al–Cu alloys during ECAP, *Materials Science and Engineering A* 527 (2010) 1404–1410.
- [30] F. Zari, B. Aour, J.M. Gloaguen, M. Nat-Abdelaziz, J.M. Lefebvre, Numerical modelling of elastic–viscoplastic equal channel angular extrusion process of a polymer, *Computational Materials Science* 38 (2006) 202–216.
- [31] F. Djavanroodi, M. Ebrahimi, Effect of die channel angle, friction and back pressure in the equal channel angular pressing using 3D finite element simulation, *Materials Science and Engineering A* 527 (2010) 1230–1235.
- [32] M. Reihanian, R. Ebrahimi, N. Tsuji, M.M. Moshksar, Analysis of the mechanical properties and deformation behavior of nanostructured commercially pure Al processed by equal channel angular pressing (ECAP), *Materials Science and Engineering A* 473 (2008) 189–194.
- [33] K.J. Kim, D.Y. Yang, J.W. Yoon, Microstructural evolution and its effect on mechanical properties of commercially pure aluminum deformed by ECAE (Equal Channel Angular Extrusion) via routes A and C, *Materials Science and Engineering A* 527 (2010) 7927–7930.
- [34] Zubear Ahmed Khan, Uday Chakkingal, P. Venugopal, Analysis of forming loads, microstructure development and mechanical property evolution during equal channel angular extrusion of a commercial grade aluminum, *Journal of Materials Processing Technology* 135 (2003) 59–67.
- [35] R.E. Barber, T. Dudo, P.B. Yasskin, K.T. Hartwig, Product yield for ECAE processing, *Scripta Materialia* 51 (2004) 373–377.



**Article VIII:**

L. Kommel, B.O. Shahreza, V. Mikli, Microstructure and physical-mechanical properties evolution of pure tantalum processed with hard cyclic viscoplastic deformation, *Int. J. Refract. Met. Hard Mater.* 83 (2019) 104983.





ELSEVIER

Contents lists available at ScienceDirect

# International Journal of Refractory Metals & Hard Materials

journal homepage: [www.elsevier.com/locate/IJRMHM](http://www.elsevier.com/locate/IJRMHM)

## Microstructure and physical-mechanical properties evolution of pure tantalum processed with hard cyclic viscoplastic deformation

Lembit Kommel<sup>a,\*</sup>, Babak Omranpour Shahreza<sup>a,c,d</sup>, Valdek Mikli<sup>b</sup><sup>a</sup> Department of Mechanical and Industrial Engineering, Tallinn University of Technology, Ehitajate tee 5, 12618 Tallinn, Estonia<sup>b</sup> Department of Materials and Environmental Technology, Tallinn University of Technology, Ehitajate tee 5, 12618 Tallinn, Estonia<sup>c</sup> Faculty of Mechanical and Electrical Engineering, Universidad Autónoma de Nuevo León (UANL), 66455 San Nicolás de los Garza, Mexico<sup>d</sup> Institute of Nanotechnology (INT), Karlsruhe Institute of Technology (KIT), 76021 Karlsruhe, Germany

## ARTICLE INFO

## Keywords:

Tantalum  
Severe plastic deformation  
Hard cyclic viscoplastic deformation  
Microstructure  
Mechanical properties  
Physical properties

## ABSTRACT

The techniques of equal channel angular pressing and hard cyclic viscoplastic deformation were used to make changes in the microstructure and physical-mechanical properties of commercially pure tantalum. For the experiments, we used double electron beam melted oligocrystalline tantalum billet that was previously heat treated at 1100 °C for 1 h and processed by equal channel angular pressing with a wide range of equivalent von Mises strain ( $\epsilon_{VM} = 0 \div 13.8$ ) imposed on materials. At follows, the samples with stepped cross sections were tested on a materials testing setup Instron-8516 at room temperature. These changes in tantalum were determined depending on the tension-compression strain amplitude, strain rate, cycling frequency and number of cycles. The effects of processing routines on changes in the microstructure were investigated using scanning electron microscope and X-ray techniques. The mechanical and physical properties changes were characterized using hardness, density and electrical conduction measure techniques. The fracture mechanics change was studied by mini samples tensile testing up to fracture. The results show that during hard cyclic viscoplastic deformation of equal channel processed samples, with different processing histories, the tensile strength, hardness, plasticity, density, electrical conductivity, Young's modulus, etc. are changed. These changes in tantalum were characterized and analyzed.

## 1. Introduction

Tantalum (Ta) is a refractory metal with a high melting point ( $T_m = 5731 \text{ K } 3017 \text{ }^\circ\text{C}, 5463 \text{ }^\circ\text{F}$ ) [1]. Tantalum is dark (blue-gray), highly dense ( $16.65 \div 16.69 \text{ g/cm}^3$ ), and ductile metal. This metal is conductive to heat and electricity. Tantalum is highly resistant to corrosion by acids and used in the chemical industry for production of lining, claddings, tanks, valves, heat exchangers and so on [2]. Tantalum can be found in two different crystal structures: bulk  $\alpha$ -Ta with body-centered cubic (bcc) structure [3] and thin film  $\beta$ -Ta with tetragonal crystal structure [4]. Tantalum capacitors are attractive for portable telephones, personal computers, automotive electronics, and photo cameras. Tantalum usage estimated to account for > 66% in electronic industry in the world [5]. The methods for production of bulk ultrafine-grained (UFG) and nano-crystalline (NC) microstructures in the metals by severe plastic deformations (SPD) methods are described in [6–14]. According to continuum theory of plasticity [15] the polycrystalline metals are aggregate of a great number of single-crystal

grains with different orientations. The internal stresses, which are induced by SPD, include texture development due to large plastic deformation, and the evolution of grain size and shape [16,17]. Nowadays fatigue testing of metallic materials has been studied in different forms with a wide range of frequencies of cycling, number of cycles and with levels of strains-stresses imposed on the materials [18,19]. For an in-depth study of these changes in material during thermo-mechanical processing, the powerful X-ray analysis technique can be used [20,21]. It is common knowledge that the peak intensities of X-ray diffractions depend on material microstructure, density, and grain size, all of which determine how X-rays penetrate, dissipate, absorb, and deflect. In the present work, we use hard cyclic viscoplastic deformation (HCVD) technique [22–24] for the study and change of the microstructure, physical and mechanical properties. The fracture mechanics differences of the minisamples are studied by tensile testing. The experimental and theoretical results presented here, which may enrich the material science and engineering, can be used for design and manufacturing of advanced materials in industry as well.

\* Corresponding author.

E-mail addresses: [lembit.kommel@taltech.ee](mailto:lembit.kommel@taltech.ee) (L. Kommel), [omranpou@uqtr.ca](mailto:omranpou@uqtr.ca) (B.O. Shahreza), [valdek.mikli@taltech.ee](mailto:valdek.mikli@taltech.ee) (V. Mikli).<https://doi.org/10.1016/j.ijrmhm.2019.104983>

Received 10 May 2019; Accepted 10 June 2019

Available online 11 June 2019

0263-4368/ © 2019 Elsevier Ltd. All rights reserved.

**Table 1**  
Chemical composition of Ta sample.

Method	Al	Mg	Pb	Cu	Fe	Mo	Nb	W	Bi	Mn	Na	Si	Se	Sn	Ti
ICP-OES	< 5	< 5	< 5	< 5	5	< 5	20	< 10	< 1	< 5	< 5	< 10	< 2	< 5	< 5
Method	–	N	O	H	–	S	C	–	–	–	–	–	–	–	–
LECO	–	< 20	< 30	< 10	–	< 10	< 10	–	–	–	–	–	–	–	–

## 2. Experimental procedures

### 2.1. Material

In this work, we used commercially pure tantalum ingots which were manufactured by double electron beam melting (EBM) technique at Neo Performance Materials (NPM) Silmet AS, Estonia. The ingot diameter was 120 mm and had an oligocrystalline microstructure [24,25] with grain sizes up to 6–8 cm in length and about 2–4 cm in width. The chemical composition of Ta was 99.98% purity and other elements are presented in Table 1. The content (in ppm) of metals inclusions were studied according to method of МВИ 58.261–14 (ICP-OES Agilent 730) and gases concentration according to method of МВИ 58.266–16 (LECO ONH-836) and S according to method of МВИ 58.267–16 (LECO CS-844). Twenty pieces of samples with dimensions of 12 × 12 mm in cross section and 130 mm in length were cut for further processing by ECAP. The samples were heat-treated in a vacuum oven for one hour at 1100 °C. The heat treatment in such conditions was applied in order to change the as-cast oligocrystalline microstructure to annealed conditions without oxidation of samples' surfaces.

### 2.2. ECAP procedure

Alpha-tantalum with a body-centered cubic (BCC) structure is difficult to extrude at room temperature. Using a conventional ECAP die, the punch was broken during the second or third pass of extrusion under a compression load raised up to ~570 kN before fractions. Therefore, to reduce the load a new die design for ECAP was proposed [23,26] by following the principles of indirect-extrusion technique [9] to process Ta towards UFG microstructure. The processing stages of modified ECAP die are shown in Fig. 1. The punch in this modified die has a cross section of 3400 mm<sup>2</sup>. The inlet and outlet channels have cross sections of 13 × 13 mm and 12 × 12 mm, respectively. According to previous work [9], due to the reduction of friction, the deformation force decreases by about 25% and thereby, the punch did not collapse during the process even up to 12 passes of extrusion. Molybdenum disulfide (MoS<sub>2</sub>) based lubricant was used in all experiments to reduce the friction. Samples were processed by B<sub>C</sub> route for 5, and 12 times at room temperature. Samples with the following ID numbers of S1, S2,

and S3 were processed and analyzed by exposing to the following equivalent Von Mises strains ( $\epsilon_{VM}$ ): Sample S1 ( $\epsilon_{VM} = 0$ , annealed sample); sample S2 ( $\epsilon_{VM} = 5.7$  after five passes of ECAP) and sample S3 ( $\epsilon_{VM} = 13.8$  after twelve passes). The sample S1 with a homogenized microstructure was used as a reference to compare the results with the processed ones. All samples were prepared with the dimensions of 12 × 12 mm in cross section and about 120 ÷ 130 mm in length (Fig. 2a).

### 2.3. HCVD procedure

The workpiece with stepped cross-section in HCVD is subjected to tension and compression by tensile and compressive forces; these forces are not necessarily of the same absolute values. It will be mentioned that the HCVD technique of metals testing base on Bauschinger effect [27]. The deformation forces at HCVD are controlled by constant tension-compression strain amplitude during cycling. The following strain amplitudes were applied to the specimens in this study:  $\epsilon_1 = \pm 0.05\%$ ,  $\epsilon_2 = \pm 0.2\%$ ,  $\epsilon_3 = \pm 0.5\%$ ,  $\epsilon_4 = \pm 1.0\%$  and  $\epsilon_5 = \pm 1.5\%$ . The number of cycles was selected twenty (for constant strain amplitude) in all experiments. It should be noted that an increase in the strain amplitude leads to an increase in the strain rate ( $\dot{\epsilon}$ ), since the frequency of the cycling is constant. The optimal cycling frequency of  $f_{-1} = 0.5$  Hz was experimentally chosen in this work. In this case, the strain rate varied from  $\dot{\epsilon} = 0.02 \text{ s}^{-1}$  to  $\dot{\epsilon} = 0.3 \text{ s}^{-1}$ . Using a turning machine, we cut the ECAP processed samples (Fig. 2a) to prepare stepped cross-section samples (Fig. 2b) for HCVD testing. More details about the experimental procedure of HCVD can be found in an earlier report [23]. The cross-sectional areas of these samples in HCVD specimen with stepped cross-sections were:  $A_1 = 38.5 \text{ mm}^2$ ,  $A_2 = 50 \text{ mm}^2$ ,  $A_3 = 84 \text{ mm}^2$  and  $A_4 = 144 \text{ mm}^2$ , respectively. Then mini-samples (MS) were cut off by using electrical discharge installation in a thickness of 0.5 mm and a length of 13 mm (Fig. 2c, e). The corresponding mini-samples (MS1 ÷ MS4) before HCVD (Fig. 2c) had absolute identical microstructure and properties. The mini sample MS5 was cut off from the as-cast sample (S1), and the mini sample MS6 was cut off from the ECAP processed sample S3 (12 passes of ECAP,  $\epsilon_{VM} = 13.8$ ), but these mini samples were not processed by HCVD, for comparison reasons (Fig. 2b, c). The strain amplitude during HCVD was measured by

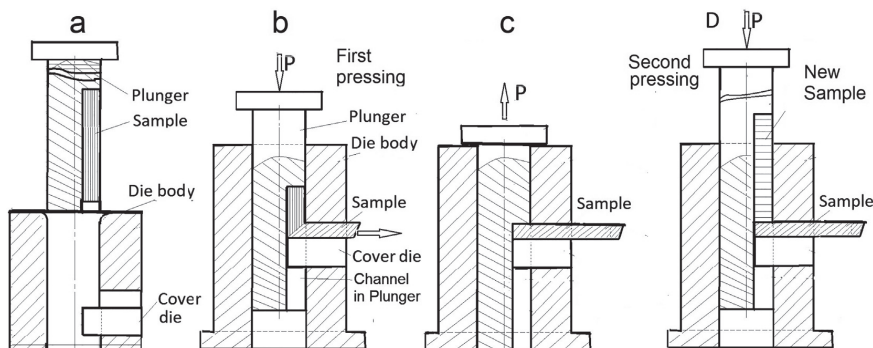
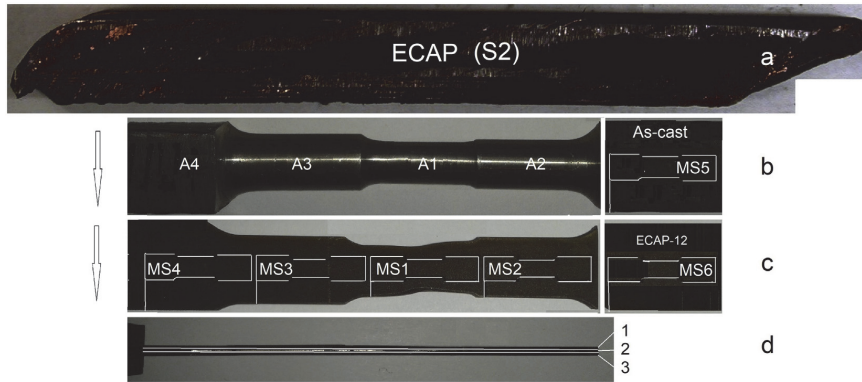


Fig. 1. Sketch of processing stages of samples in modified ECAP die.



**Fig. 2.** ECAP-treated specimen S2 ( $\epsilon_{VM} = 5.7$ ) after 5 ECAP passes (a), HCVD test specimen with stepped cross section and a piece of the cast specimen (right) (b), mini samples (MS) cut off points after HCVD and a piece of the sample S3 (right) (c), side view of the three layers (1, 2, 3) of mini-samples in a longitudinal section (d). A sketch of the mini-sample (with dimensions in mm) is shown in (d).

an extensometer with a base length of 10 mm and with a minimal cross-section of ( $A_1 = 38.5 \text{ mm}^2$ ). The HCVD samples were tested in the strain-controlled mode [23] using an Instron-8516 material testing system. Young's modulus was measured during tension in two strain ranges of  $\epsilon = (0 \text{ to } 0.06) \%$  and  $\epsilon = (0 \text{ to } 0.1) \%$ . These intervals were chosen for studying interatomic interaction change in materials. The load of compression-tension was measured for all cycles on the minimal cross-section ( $A_1$ ) of sample. For other sections the load was calculated.

#### 2.4. Characterization of microstructure

For microstructure studies, samples were mechanically grinded by silicon paper and then they were polished by diamond paste. We did not use chemical etching. After such grinding/polishing procedures, samples surface for microstructure study were treated by ion milling using a Precision Etching System at 30 kV for 30 min in a protective argon (Ar) atmosphere. Microstructure and grain boundaries (GB) were studied by means of scanning electron microscopy technique (Zeiss EVO MA-15, Gemini LEO Supra 35). Chemical composition was analyzed by SEM-EDS technique. X-ray diffraction of samples was studied by Bruker D5005 AXS.

#### 2.5. Mechanical and physical property testing

The ECAP processed samples with various imposed strain values ( $\epsilon_{VM} = 0$ ,  $\epsilon_{VM} = 5.7$  and  $\epsilon_{VM} = 13.8$ ) were evaluated by Instron-8516 materials testing installation. Hardness of samples was measured by Micrometer 2001 under the loads of 50 g and 100 g at dwell time for 12 s. A modified MDD Manual Test Stand-UK, performed the tensile test on the mini samples. Three pieces of mini samples with identical properties (three layers) were tested for reliability of the results (see Fig. 2d). Density of the samples after ECAP were measured by METTLER Toledo Me 204 balances at 23.5 °C. Electrical conductivity of the samples was measured by a Sigmatest 2.069, Foerster, according to the standards of the National Physics Laboratory (NPL, United Kingdom). All samples' electrical conductivities were measured 30 times automatically and results were presented as mean values in the tables.

### 3. Results and discussion

#### 3.1. Mechanical properties

Yield strength ( $Rp_{0.2\%}$ ), Ultimate tensile strength ( $Rm$ ) and elongation of the samples were measured after ECAP (Fig. 3a) and also after

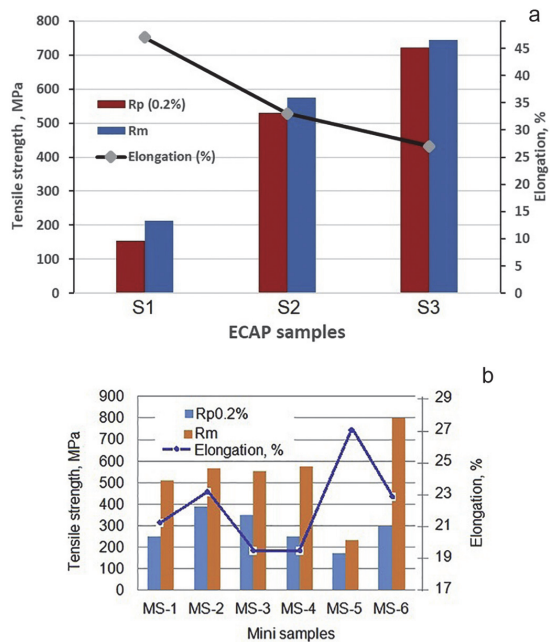


**Fig. 3.** Tensile strength ( $Rp_{0.2\%}$  and  $Rm$ ) and elongation values (in %) of samples after ECAP (a) and of mini samples after HCVD (b).

HCVD (Fig. 3b). According to these graphs, mechanical properties changed by ECAP and HCVD. The maximal tensile strength of Ta sample after 12 passes by B<sub>C</sub> route ( $\epsilon_{VM} = 13.8$ ) was 773 MPa, but the maximal elongation was 34% which was received after 5 passes of ECAP ( $\epsilon_{VM} = 5.7$ ). The tensile strength and elongation of mini-samples are presented in Fig. 3b. Results of HCVD processed samples at different stress-strain amplitudes and strain rates are presented in Fig. 4.

As it can be seen in Fig. 4a, the tensile-compression stress amplitudes' values depend on von Mises strain at ECAP induced by simple shear strain under hydrostatic compression stress as well as strain amplitude and cycles' number increased during HCVD, respectively. It will be mentioned that the samples (S1, S2 and S3) for HCVD had a step-by-step increase of the cross-sections and corresponding mini

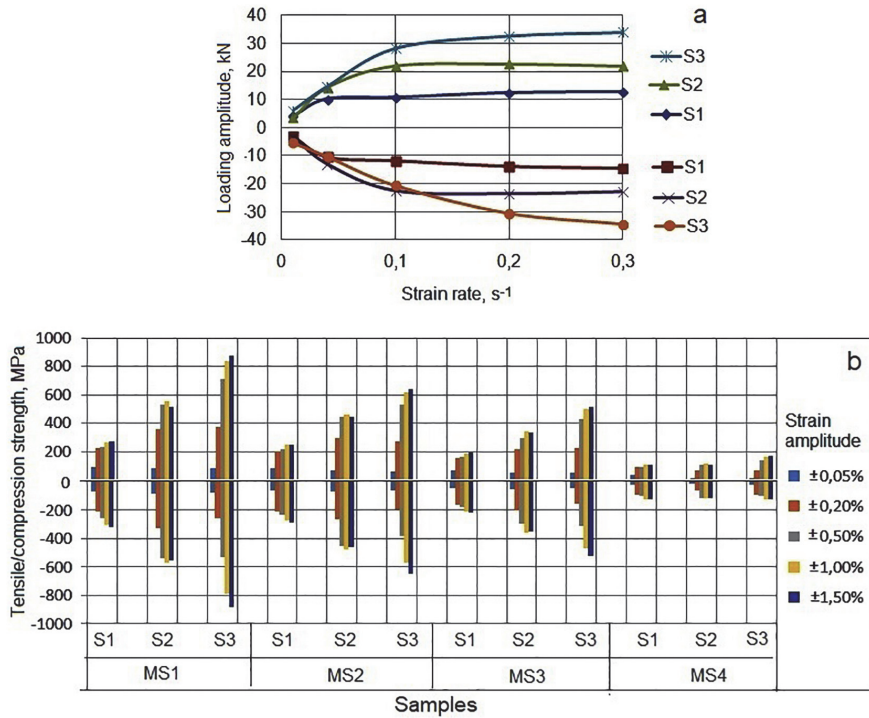


Fig. 4. The load amplitudes in different HCVD samples which were formed at different strain rates (a), tensile and compression amplitude values in the mini samples during HCVD with constant strain amplitude for 40 s and 20 cycles (b).

samples (see Fig. 2), which were cut off from these large samples, were loaded at different strain, strain rates, and load-stress amplitudes during HCVD (Fig. 4b), respectively. The increase in tensile and compression amplitudes for all mini samples by strain amplitude increase is presented in Fig. 5a. As you can see in Fig. 5a, the mean values of tensile and compression stresses during HCVD increased by strain amplitude increasing. By this, the tensile and compression strength increase influenced on the hardening and softening of Ta during HCVD (Fig. 5b). The stress amplitudes' values for all samples with different von Mises strain levels during HCVD changed. The rate of these changes of stress depended on Bauschinger effect [28]. According to this effect, the conventional metal with a coarse grained (CG) microstructure took stronger at compression cycle. In this study the sample S1 has recrystallized CG microstructure and its strength was increased during HCVD. The samples S2 and S3 have UFG microstructure and their behavior at HCVD was differed with sample S1. During 20 cycles, mainly at increased strain amplitude, the softening was maximal (Fig. 5b). This effect is related to the changes of mechanical properties as well as in the changes in microstructure in the metal. This standpoint is shown graphically in Fig. 5b at tension (high) and at compression (low) cycles. In this graph we see tensile strength at second cycle and it increase or decrease during twenty cycles of straining by no changes in strain amplitude at tension and compression on this level. For low strain amplitudes  $\epsilon = \pm 0.1\%$ , and  $\epsilon = \pm 0.2\%$  the stress changes are minimal and the microstructure didn't change. At strain  $\epsilon = \pm 0.5\%$  these changes in the stress lowering increased at increasing the strain amplitude. When the strain amplitude was increased to  $\epsilon = \pm 1.0\%$ , and exactly to  $\epsilon = \pm 1.5\%$  during HCVD of sample S3 we see that the softening rate during 20 cycles was maximal (Fig. 5b, S3, curves  $\pm 1.0\%$  and  $\pm 1.5\%$ ), respectively.

### 3.2. Physical properties

A well-known fact from the scientific literature is that the Young's modulus is constant in materials at room temperature [1]. This modulus decreases with increasing the temperature and increases with increasing the density in materials. The Young's modulus of Ta is about 186 GPa at room temperature and the maximum value is 193 GPa at  $10^{-6}$  K [1]. As it can be seen in this paper (Fig. 6), this modulus may also be affected by the amount of strain applied to the material (or the number of passes in ECAP) and the change in equivalent strain-stress amplitude during HCVD. The changes of Young's modulus in the samples S1, S2 and S3 are shown in Fig. 6. It should be mentioned that Young's modulus of each mini-sample was measured three times in the intervals of strains from  $0 \div 0.06\%$  and from  $0 \div 0.1\%$  to ensure about the reliability of results. This modulus depends on von Mises strain (E0, E5 and E12), strain rate as well on the interval of strain, at which this parameter was measured. When the material is harder, the Young's modulus is higher at tension in the interval of strain of  $0-0.1\%$  (S2) and when the material is softer, Young's modulus is higher for  $0 \div 0.06\%$  strain interval (S1), and lowers at  $0 \div 0.1\%$ , respectively.

Changes in electrical conductivity and Vickers microhardness in ECAP samples (S1, S2, and S3) were measured with different orientations (Fig. 7). These values vary depending on the strain applied during processing or hardness, as well as on the orientation of the measurement, in cross-section (CS) or transverse (TD) direction. As you can see (Fig. 7), when the Vickers microhardness is higher, the conductivity is lower when the heating rate is low. In works [28–30] is shown, that the electrical conductivity depend on harness and strength properties of CuCr-alloys. In the works [31,32] is shown, that the electrical conductivity and Vickers microhardness of CuCr-alloys increase by



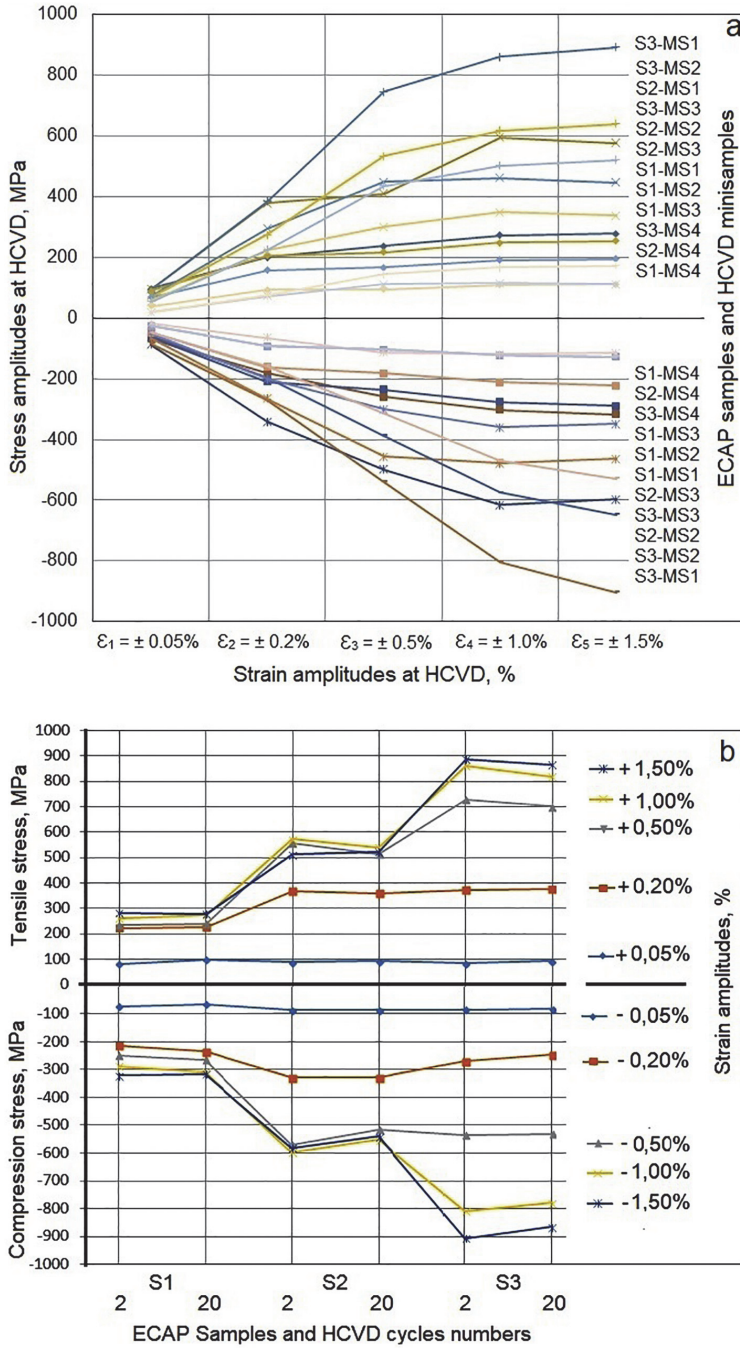


Fig. 5. The tensile and compression stress amplitudes in MS during HCVD (a) and the softening and hardening of MS during 19 cycles (from second to twenty) of HCVD (b).

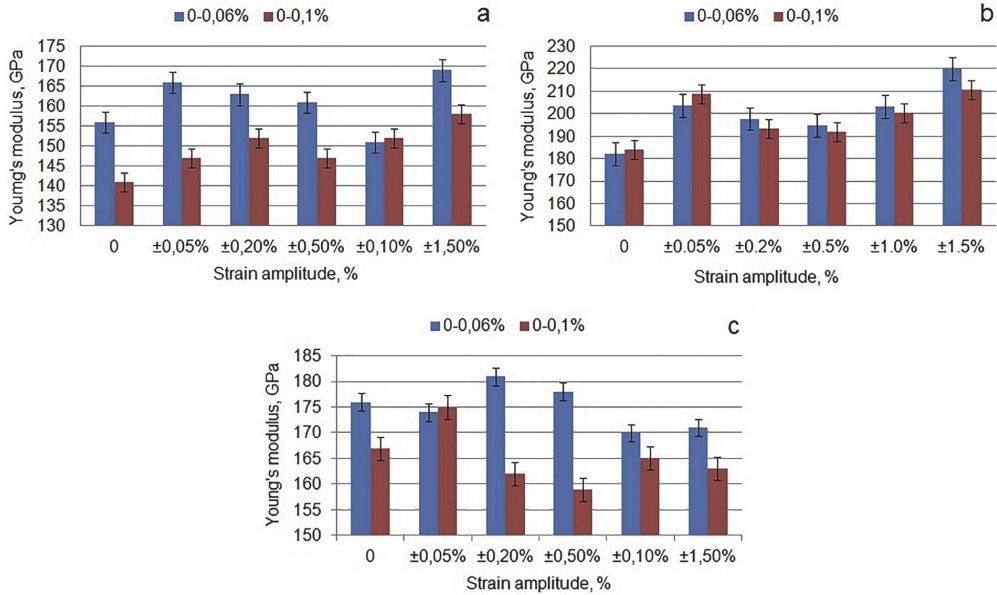


Fig. 6. Change of Young's modulus in Ta at uniaxial tension at strain of 0–0.06% and of 0–0.1% of samples S1 (a), S2 (b) and S3 (c), respectively.

temperature increase and revealed maximal values at ~450 °C. Accordingly, these parameters depends not only on the microhardness because the density of dislocations was lowered during heat treatment. In the present work the Ta samples were heat treated at a very low heating rate of 1 °C·min<sup>-1</sup>, and the Vickers microhardness and electrical conductivity increase in sample S2 and decrease in sample S3, respectively. The conductivity is expressed as a percentage of the International Standard Annealed Copper (%IACS), which is 5.80 × 10<sup>7</sup> Siemens/m at 20 °C. Results show, that the electrical conductivity varied in dependence on energy associated with dislocations, grain boundaries state and vacancy concentration [33] in Ta samples during ECAP and HCVD, respectively.

The physical properties of metals under very high pressure were studied previously by P.W. Bridgman [34]. He show that the density don't change unde compression stress when metal is defect free. The theoretical density of nanocrystalline material free from excess dislocations and deformation-induced defects was studied in [35]. In the present study the samples (see Fig. 2b, A1, A2, A3, and A4) for density study were cut off from HCVD samples S1, S2 and S3, respectively. The pieces densities were measured at least 10 ÷ 12 times to assure reliable results. It was established that the density of Ta (as well as other metals

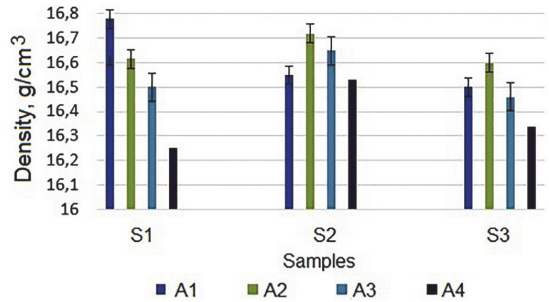


Fig. 8. Density of pure Ta of ECAP (A4) sample and of HCVD (A1, A2, and A3) samples (see Fig. 2b).

processed by SPD) depends on processing routines as well as on microstructure, dislocation density and microdefects increase as well as softening during SPD processing of the metal. These changes in the density of Ta are shown in Fig. 8. It has been shown [1] that the density

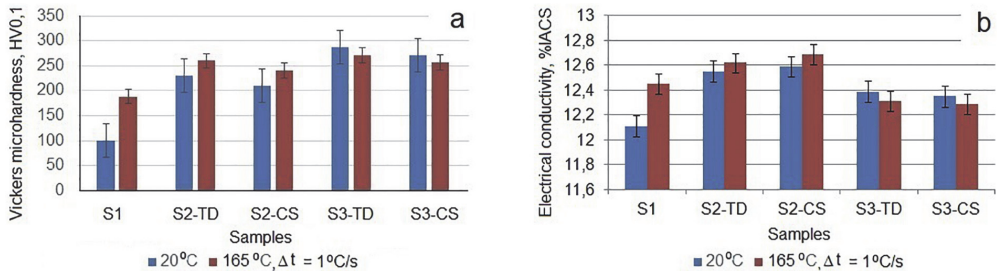


Fig. 7. Evolution of Vickers microhardness (a), and electrical conductivity (b) depends on measuring orientation and heat treatment from 20 °C to 165 °C with a heating rate of 1 °C·min<sup>-1</sup>. TD - transverse direction and CS - cross-section.

of Ta (near r.t.) is  $d = 16.70 \text{ g}\cdot\text{cm}^{-3}$ , and in liquid phase is  $d = 15 \text{ g}\cdot\text{cm}^{-3}$ . In our previous study [23], we explored the density of EBM Nb ingots depending on the defects in metal bulks. During ECAP these defects (pores) were compressed under the hydrostatic pressure and simple shear strain during ECAP processing. As a result, the density of samples increased by increasing the amount of von Mises strain during ECAP. In the present study, the density of Ta increased by increasing the amount of strain only up to  $\epsilon_{\text{VM}} = 5.7$  during ECAP (see Fig. 8, S2, A4). During HCVD the density of samples A2 and A3 was increased for all samples. By strain rate increase during HCVD the density of A1, which were cut off from S2 and S3, was decreased. The sample A1 from sample S1 (with recrystallized microstructure before HCVD) shows maximal rate of increasing of density. The density was increased from  $16.26 \text{ g}\cdot\text{cm}^{-3}$  to  $16.80 \text{ g}\cdot\text{cm}^{-3}$  during HCVD. This value of density for Ta is maximal in this experimental study. The Ta density was decreased during HCVD at strain rate increase as a result of the supersaturation of metal in samples A1, which was cut off from samples S2 and S3, respectively. The sample S1 was not by ECAP processed and the supersaturation was not yet start at strain amplitude of 1.5%, which was maximal in this study.

### 3.3. X-ray investigation

Anisotropic deformation during ECAP and HCVD processes, as well as anisotropic properties in samples (Figs. 6, 8) can lead to the formation of anisotropic crystallites and, therefore, anisotropic peak intensities [20]. The X-ray diffraction patterns of the three samples (S1, S2, and S3) after ECAP and sample S1 + 5HCVD (only after HCVD) are presented in Fig. 9. As seen in Fig. 9, X-ray diffraction patterns of the treated HCVD Ta differ significantly from other samples. It should be noted that this sample (S1 + 5HCVD) had a recrystallized microstructure before HCVD. During HCVD, the microstructure changed, and only one peak appeared in the X-ray diagram at  $\sim 55.6^\circ$ . Such X-ray pattern with a single peak is characteristic of a single-crystal metal [20,21] and a single-crystal Ni-based superalloy [36].

### 3.4. Microstructural evolution in Ta

Microstructural evolution in bulk Ta samples during ECAP (Fig. 10) with different routines of ECAP and HCVD (Fig. 11) are presented. The EBM as-cast microstructure (sample S1) in the GB triple junction is shown in Fig. 10a. The grain boundaries of EBM Ta are fully faceted [37] since the material is of high purity and dense. Such structure can

be changed during ECAP. These changes during ECAP are shown in Fig. 10b for sample S2 and in Fig. 10c for sample S3. The trace of this change can be noticed in corresponding X-ray patterns (S2 and S3) shown in Fig. 9. The microstructure evolution of sample S1 during HCVD, with a number of 100 cycles is shown in Fig. 11. The microstructure has GB-s on atomic level [38].

### 3.5. Fractured surfaces peculiarities analysis

The fracture surfaces of the samples were studied and received SEM images are presented in Fig. 12. As you can see the fracture surfaces are very different and consequently, depend on the loading history and processing routes during ECAP and followed HCVD, respectively.

The microstructural analysis of fractured surfaces at tension of Ta samples shows the very different mechanisms of fracture. For example, the MS5 was cut off from sample S1 was not via ECAP processed before. During HCVD for 100 cycles in summary the MS5 shows the evidence of ductile fracture via laminating by grain boundaries by atomic level (see Figs. 11 and 12a). This sample shows maximal density revealed to  $\sim 16.79 \text{ g}\cdot\text{cm}^{-3}$  (Fig. 8) and also maximal elongation revealed to 27%. With compare to other mini samples this elongation is highest. The MS1 was cut off from S2 sample which was ECAP processed by von Mises strain at  $\epsilon_{\text{VM}} = 5.7$  and was at follows HCVD processed up to maximal strain amplitude of  $\epsilon = \pm 1.5\%$  as well as deformation rate of  $\dot{\epsilon} = 0.3 \text{ s}^{-1}$ . Metal in MS1 is saturated by deformation at high strain rate, softening and show the pre-destructive behavior of surface before fracture [39]. As result, the fractured surface is characterized as the saturated fracture surface before destruction. The MS6 (after 12 passes of ECAP with  $\epsilon_{\text{VM}} = 13.8$ ) shows maximal tensile strength up to  $\sim 800 \text{ MPa}$  and Vickers hardness of  $\sim 260 \text{ HV}_{0.05}$ , respectively. The fractured surface is a finest with compare to other samples [40]. The MS2 (from S2,  $\epsilon_{\text{VM}} = 5.7$ ) shows maximal Young's modulus of  $210 \div 220 \text{ GPa}$ , maximal Rp0.2% of  $\sim 388 \text{ MPa}$  and Rm of  $\sim 565 \text{ MPa}$ , the density of  $\sim 16.7 \text{ g}\cdot\text{cm}^{-3}$  and maximal electrical conductivity of  $\sim 12.65\% \text{ ICAS}$ , but the Vickers hardness was lowered to  $\sim 245 \text{ HV}_{0.05}$ , respectively. The MS3 (from S2) was HCVD tested at high stress and compression strain amplitudes and it shows softening behavior. The tension strength and compression strength as well Young's modulus were lowered at the end of HCVD during latest 5–6 cycles. The MS4 (from S2,  $\epsilon_{\text{VM}} = 5.8$ ) during HCVD has lowest tensile and compression stress amplitudes (see Fig. 4b), with minimal strain rate and low load. As result in the fractured surface at tension, the pores were formed [41]. The sample MS4 from S2 was a fractured surface fulfilled with an abundance of pores and dimples which were formed at tension straining. The microstructures before tension don't have the pores and dimples. These pores were formed at tension but were initiated during HCVD. As it is shown above, the density of metal changed in dependence on the defects forming on pre-destruction state of metal (Fig. 8).

## 4. Summary and concluding remarks

A large number of experiments were performed on the basis of high-purity Ta to study changes in the microstructure, mechanical and physical properties during ECAP and during subsequent HCVD. The tests were carried out on samples with a stepped cross-section along the length. The following conclusions can be drawn from this study:

1. During ECAP, depending on the von Mises strain, the tensile strength was increased from 200 MPa in EBM sample with oligocrystalline microstructure to 798 MPa after ECAP for 12 passes by  $B_C$  route, and Vickers microhardness was increased from  $100 \text{ HV}_{0.05}$  to  $280 \text{ HV}_{0.05}$ , respectively.
2. During HCVD, depending on the cycle's number, strain amplitude and strain rate the Young's modulus was increased from  $\sim 140 \text{ GPa}$  (as-cast Ta with recrystallized microstructure) up to  $\sim 220 \text{ GPa}$  (ECAP with  $\epsilon_{\text{VM}} = 5.7$  and HCVD up to  $\epsilon = \pm 1.5\%$ , for 100 cycles,

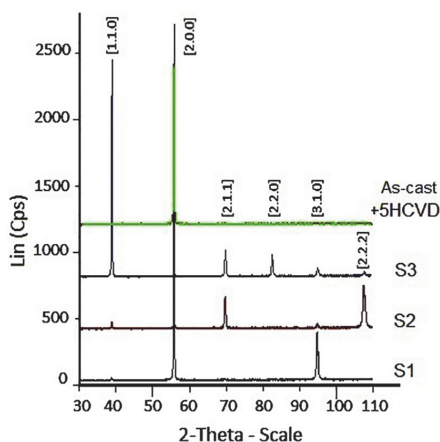


Fig. 9. X-ray diffractograms of the samples S1, S2, and S3 after ECAP and S1 + 5HCVD after HCVD, respectively.



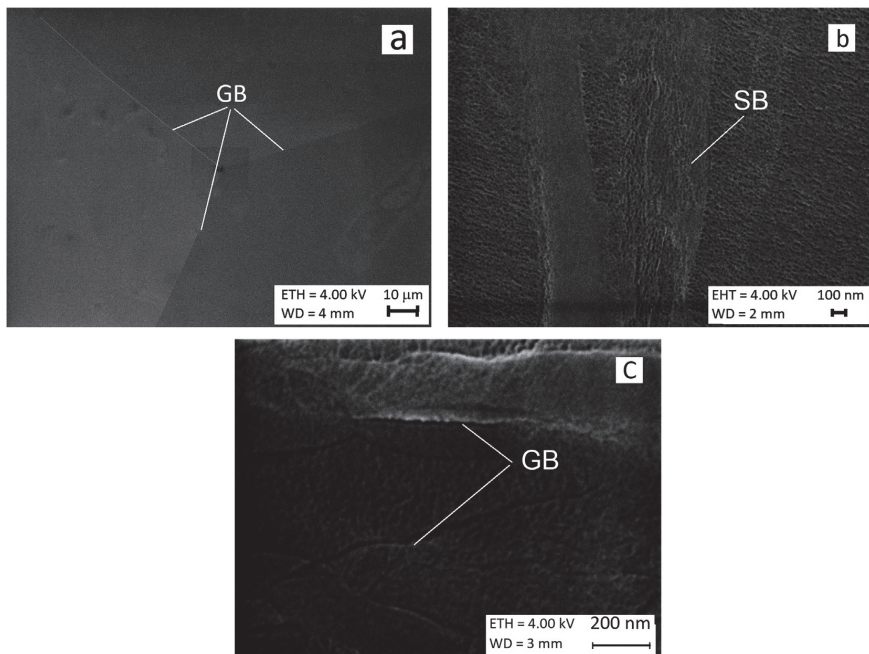


Fig. 10. Microstructure of tantalum EBM as-cast ingot (S1) demonstrating the triple junction of grain boundaries (a), banded microstructure of sample (S2) after 5 passes of ECAP (b), and formed shear bands with GB in sample S3 after 12 passes of ECAP (c).

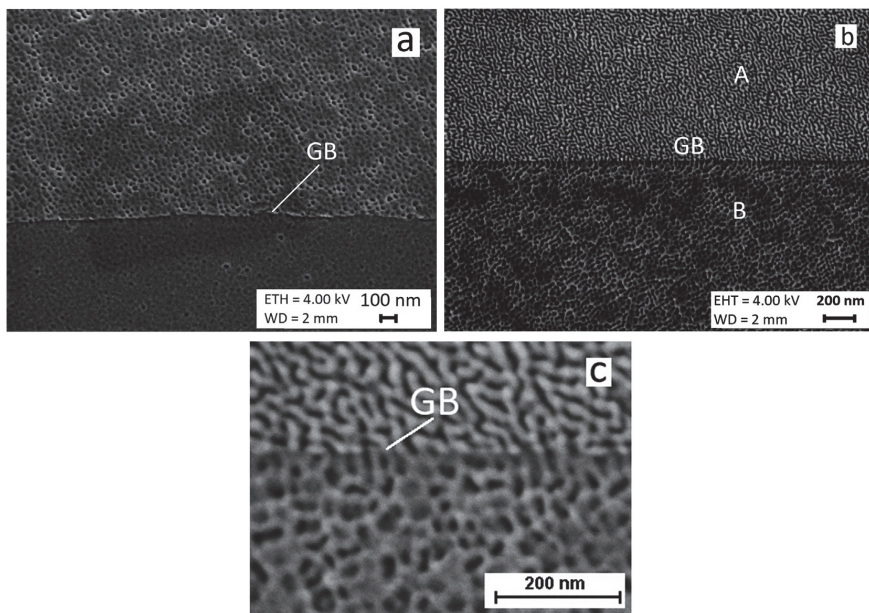
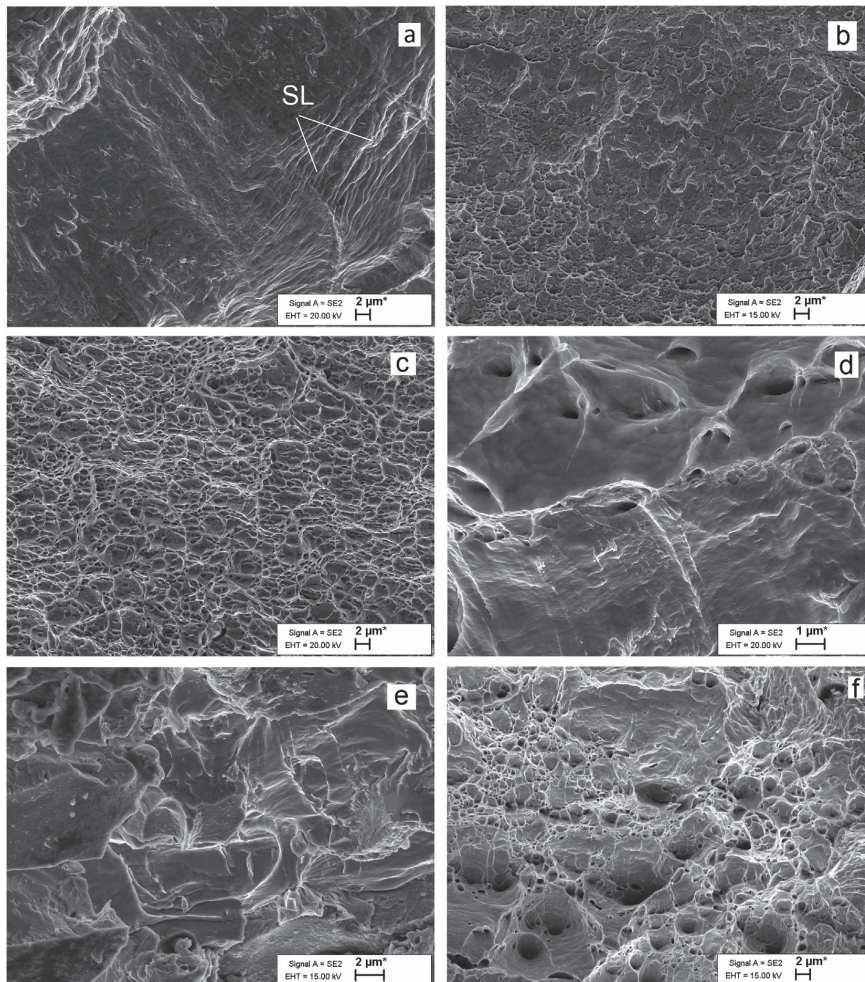


Fig. 11. Microstructure evolution of pure Ta processed by HCVD at 5 test series for 100 tension-compression cycles in sum. The atomic level GB-s with different orientations of two grains is presented.



**Fig. 12.** Surfaces of pure Ta after tension testing up to fracture: a) MS5 after HCVD, taken from sample S1; b) MS1, taken from a 5-fold ECAP-ed sample S2, and 100 cycles of the HCVD sample, section A1 (see Fig. 2b, c); c) MS6 is from a 12-fold ECAP-ed sample; d) MS2 after ECAP and HCVD taken from S2 sample, section A2; e) MS3 after ECAP and HCVD taken from S2, section A3; f) MS4 after ECAP and HCVD taken from S2, section A4, respectively.

in summary).

3. During HCVD, depending on the increase in the amplitude of the strain and strain rate, the tensile stress and the compressive stress increased. These parameters were maximum at average values of strain and strain rate. With an increase of strain amplitude is over  $\pm 1.0\%$  and number of cycles over 80, the Ta loses tensile and compressive strength. According to the Bauschinger effect, the material is strengthened or loses strength because of the interatomic forces in the material change during HCVD.
4. During processing the Vickers microhardness and electrical conductivity depend on measuring orientation and heat treatment temperature from  $20\text{ }^{\circ}\text{C}$  to  $165\text{ }^{\circ}\text{C}$  with a heating rate of  $1\text{ }^{\circ}\text{C}\cdot\text{min}^{-1}$ . The electrical conductivity was increased from  $12.1\%$ IACS up to  $12.8\%$ IACS, but it was decreased to  $12.3\%$ IACS with increasing of the dislocation density as well as an increase of hardness. The Vickers microhardness and electrical conductivity of UFG Ta are inversely proportional in magnitude.
5. During HCVD the tantalum density was increased from

$16.35\text{ g}\cdot\text{cm}^{-3}$  to a maximal value of  $16.79\text{ g}\cdot\text{cm}^{-3}$  at room temperature of  $23.5\text{ }^{\circ}\text{C}$ .

6. By the X-ray investigation, it was revealed, that Ta with re-crystallized microstructure is possible to change to like single crystalline as the atomic level grain boundaries were formed.
7. At uniaxial tension of Ta mini-samples, depending on processing routines and parameters the corresponding fracture surfaces are formed. These surfaces are much differed and are characterized by the formed microstructure, physical and mechanical properties, respectively.

#### Acknowledgements

This work was supported in part by the Estonian Research Council institutional research funding IUT 1929, IUT1928 and TK141, in part by European social funds-DoraPlus-Estonia, and in part by National Council of Science and Technology-Conacyt-Mexico.



## References

- [1] Information on <https://en.wikipedia.org/wiki/Tantalum>.
- [2] A.A. Navid, A.M. Hodge, Nanostructured alpha and beta tantalum formation-relationship between plasma parameters and microstructure, *Mater. Sci. Eng. A* 536 (2012) 49–56, <https://doi.org/10.1016/j.msea.2011.12.017>.
- [3] M. Magnuson, G. Greczynski, F. Eriksson, L. Hultman, H. Högberg, Electronic structure of  $\beta$ -Ta films from X-ray photoelectron spectroscopy and first-principles calculations, *Appl. Surf. Sci.* 470 (2019) 607–612, <https://doi.org/10.1016/j.apsusc.2018.11.096>.
- [4] R.W. Buckmann Jr., New application for tantalum and tantalum alloys, *JOM* 52 (3) (2000) 40–41, <https://doi.org/10.1007/s11837-000-0100-6>.
- [5] M. Filella, Tantalum in environment, *Earth Sci. Rev.* 173 (2017) 122–140, <https://doi.org/10.1016/j.earscirev.2017.07.002>.
- [6] A. Vinogradov, Y. Estrin, Extreme grain refinement by severe plastic deformation: a wealth of challenging science, *Acta Mater.* 61 (2013) 782–817, <https://doi.org/10.1016/j.actamat.2012.10.038>.
- [7] A. Vinogradov, J. Estrin, Analytical and numerical approaches to modelling severe plastic deformation, *Prog. Mater. Sci.* 95 (2018) 172–242, <https://doi.org/10.1016/j.pmatsci.2018.02.001>.
- [8] N. Maury, N.X. Zhang, Y. Huang, A.P. Zhilyaev, T.G. Langdon, A critical examination of pure tantalum processed by high-pressure torsion, *Mater. Sci. Eng. A* 638 (2015) 174–182, <https://doi.org/10.1016/j.msea.2015.04.053>.
- [9] B. Omeranovic, L. Kommel, V. Mikli, E. Garcia, J. Huot, Nanostructure development in refractory metals: ECAP processing of niobium and tantalum using indirect-extrusion technique, *Int. J. Refract. Met. Hard Mater.* 79 (2019) 1–9, <https://doi.org/10.1016/j.ijrmhm.2018.10.018>.
- [10] Q. Wei, K.T. Ramesh, L.J. Kecskes, S.N. Mathaudhu, K.T. Hartwig, Ultrafine and nanostructured refractory metals processed by SPD: microstructure and mechanical properties, *Mater. Sci. Forum* (TTP) 579 (2008) 75–90, <https://doi.org/10.4028/0-87849-384-075>.
- [11] Y. Wang, S. Goej, J.L. Sun, Y.M. Zhu, H. Yuan, J.T. Wang, The effect of temperature on activation volume of ultrafine grained tantalum, *Int. J. Refract. Met. Hard Mater.* 71 (2018) 232–238, <https://doi.org/10.1016/j.ijrmhm.2017.11.029>.
- [12] N. Lin, S. Liu, Y. Liu, H. Fan, J. Zhu, C. Deng, Q. Liu, Effects of a symmetrical rolling on through-thickness microstructure and texture of body-centered cubic (BCC) tantalum, *Int. J. Refract. Met. Hard Mater.* 78 (2019) 51–60, <https://doi.org/10.1016/j.ijrmhm.2018.08.012>.
- [13] Z. Zhang, D. Chen, H. Zhang, S. Liu, A comparative study of clock rolling and unidirectional rolling on deformation/recrystallization microstructure and texture of high purity tantalum plates, *Int. J. Refract. Met. Hard Mater.* 41 (2013) 453–460, <https://doi.org/10.1016/j.ijrmhm.2013.06.003>.
- [14] C. Deng, S.F. Liu, J.L. Ji, X.B. Hao, Z.Q. Zhang, Q. Liu, Texture evolution of high purity tantalum under different rolling paths, *J. Mater. Process. Technol.* 214 (2014) 462–469, <https://doi.org/10.1016/j.jmatprotec.2013.09.026>.
- [15] A.S. Khan, S. Huang, Continuum Theory of Plasticity, John Wiley & Sons, INC, 1995, [https://doi.org/10.1016/0008-6215\(95\)00257-X](https://doi.org/10.1016/0008-6215(95)00257-X) (421 p).
- [16] S.F. Liu, H.Y. Fan, C. Deng, X.B. Hao, Y. Guo, Q. Liu, Through-thickness texture in clock-rolled tantalum plate, *Int. J. Refract. Met. Hard Mater.* 48 (2015) 194–200, <https://doi.org/10.1016/j.ijrmhm.2014.08.019>.
- [17] N. Lin, S. Liu, Y. Liu, H. Fan, J. Zhu, C. Deng, Q. Liu, Effects of asymmetrical rolling on through-thickness microstructure and texture of body-centered cubic (BCC) tantalum, *Int. J. Refract. Met. Hard Mater.* 78 (2019) 51–60, <https://doi.org/10.1016/j.ijrmhm.2018.08.012>.
- [18] W. Muhammad, A.P. Brahma, J. Kang, R.K. Mishra, Experimental and numerical investigation of texture evolution and the effects of intergranular back stresses in aluminum alloys subjected to large strain cyclic deformation, *Int. J. Plast.* 93 (2017) 137–163, <https://doi.org/10.1016/j.ijplas.2016.11.003>.
- [19] R.A. Barrett, P.E. O'Donoghue, S.B. Leen, A physically-based constitutive model for high temperature microstructural degradation under cyclic deformation, *Int. J. Fatigue* 100 (2017) 388–406, <https://doi.org/10.1016/j.ijfatigue.2017.03.018>.
- [20] T. Ungár, E. Schafer, J. Gubicza, Microstructure of bulk nanomaterials determined by X-ray line-profile analysis, in: M.L. Zehetbauer, Y.T. Zhu (Eds.), *Bulk Nanostructured Materials*, WILEY-VCH Verlag GmbH & Co. KGaA, Weinheim, 2009.
- [21] R. Kishor, L. Sahu, K. Dutta, A.K. Mondal, Assessment of dislocation density in asymmetrically cyclic loaded non-conventional stainless steel using X-ray diffraction profile analysis, *Mater. Sci. Eng. A* 598 (2014) 299–303, <https://doi.org/10.1016/j.msea.2014.01.043>.
- [22] L. Kommel, Properties development of ultrafine-grained copper under hard cyclic viscoplastic deformation, *Mater. Lett.* 64 (2010) 1580–1582, <https://doi.org/10.1016/j.matlet.2010.04.056>.
- [23] L. Kommel, Microstructure and properties that change during hard cyclic viscoplastic deformation of bulk high purity niobium, *Int. J. Refract. Met. Hard Mater.* 79 (2019) 10–17, <https://doi.org/10.1016/j.ijrmhm.2018.10.009>.
- [24] M.F. Hupaló, H.R.Z. Sandim, The annealing behavior of oligocrystalline tantalum deformed by cold swaging, *Mater. Sci. Eng. A* 318 (2001) 216–223, [https://doi.org/10.1016/S0921-5093\(01\)01323-5](https://doi.org/10.1016/S0921-5093(01)01323-5).
- [25] H.R.Z. Sandim, J.P. Martins, A.L. Pinto, A.F. Padilha, Recrystallization of oligocrystalline tantalum deformed by cold rolling, *Mat. Sci. Eng. A* 392 (2005) 209–221, <https://doi.org/10.1016/j.msea.2004.09.032>.
- [26] J.-P. Mathieu, S. Suwas, A. Eberhardt, L.S. Tóth, P. Moll, A new design for equal channel angular extrusion, *J. Mater. Process. Technol.* 173 (1) (2006) 29–33, <https://doi.org/10.1016/j.jmatprotec.2005.11.007>.
- [27] X. Hu, S. Jin, H. Zhou, Z. Yin, J. Yang, Y. Gong, Y. Zhu, G. Sha, X. Zhu, Bauschinger effect and back stress in gradient Cu-Ge alloy, *Metal Mater. Trans. A* 48 (9) (2017) 3943–3950, <https://doi.org/10.1007/s11661-017-4176-9>.
- [28] S.V. Dobatkin, J. Gubicza, D.V. Shangina, N.R. Bochvar, N.Y. Tabachkova, High strength and good electrical conductivity in Cu-Cr alloys processed by severe plastic deformation, *Mater. Lett.* 153 (2015) 5–9, <https://doi.org/10.1016/j.matlet.2015.03.144>.
- [29] R.K. Islamgaliev, K.M. Nesterov, J. Bourgon, Y. Champion, R.Z. Valiev, Nanostructured Cu-Cr alloy with high strength and electrical conductivity, *J. Appl. Phys.* 115 (2014) 194301, <https://doi.org/10.1063/1.4874655>.
- [30] M.Yu. Murashkin, I. Sabirov, X. Sauvage, R.Z. Valiev, Nanostructured Al and Cu alloys with superior strength and electrical conductivity, *J. Mater. Sci.* (2015) 1–19, <https://doi.org/10.1007/s10853-015-9354-9>.
- [31] L. Kommel, A. Pokatilov, Electrical conductivity and mechanical properties of Cu-0.7wt% Cr and Cu-1.0wt% Cr alloys processed by severe plastic deformation, *IOP Conf. Ser.* 63 (2014) 012169, <https://doi.org/10.1088/1757-899X/63/1/012169>.
- [32] L. Kommel, Tribological behavior at dry sliding by electric current of Cu-Cr-S alloy after equal channel angular pressing, *TTP Key Eng. Mater.* 721 (2016) 430–435, <https://doi.org/10.4028/www.scientific.net/KEM.721.430>.
- [33] O.F. Higuera-Cobos, J.M. Cabrera, Mechanical microstructural and electrical evolution of commercially pure copper processed by equal channel angular extrusion, *Mater. Sci. Eng. A* 571 (2013) 103–114, <https://doi.org/10.1016/j.msea.2013.01.076>.
- [34] P.W. Bridgman, *Book: Studies in Large Plastic Flow and Fracture: With Special Emphasis on the Effects of Hydrostatic Pressure*, Harvard University Press, Cambridge, Mass, 1964.
- [35] T.D. Shen, J. Zhang, Y. Zhao, What is the theoretical density of a nanocrystalline material? *Acta Mater.* 56 (2008) 3663–3671, <https://doi.org/10.1016/j.actamat.2008.04.003>.
- [36] L. Kommel, Phase equilibrium evolution in single-crystal Ni-based superalloys, *Superalloys*, IntechOpen, 2015, <https://doi.org/10.5772/61102> Chapter 8.
- [37] B.B. Straumal, O.A. Kogtenkova, A.S. Gornakova, V.G. Sursava, B. Baretzky, Review: grain boundary faceting-roughening phenomena, *J. Mater. Sci.* 51 (2016) 382–404, <https://doi.org/10.1007/s10853-015-9341-1>.
- [38] H.J. Fecht, H. Gleiter, A lock-in model for the atomic structure of interphase boundaries between metals and ionic crystals, *Acta Metall.* 33 (1985) 557, [https://doi.org/10.1016/0001-6160\(85\)90019-7](https://doi.org/10.1016/0001-6160(85)90019-7).
- [39] Y. Tang, E.M. Bringa, M.A. Meyers, Inverse hall-petch relationship in nanocrystalline tantalum, *Mater. Sci. Eng. A* 580 (2013) 414–426, <https://doi.org/10.1016/j.msea.2013.05.024>.
- [40] Z. Pan, Y. Li, Q. Wei, Tensile properties of nanocrystalline tantalum from molecular dynamic simulations, *Acta Mater.* 56 (2008) 3470–3480, <https://doi.org/10.1016/j.actamat.2008.03.025>.
- [41] Z.S. Levin, X. Wang, M. Kaynak, I. Karaman, K.T. Hartwig, Strength and ductility of powder consolidated ultrafine-grain tantalum, *Int. J. Refract. Met. Hard Mater.* 80 (2019) 73–84, <https://doi.org/10.1016/j.ijrmhm.2018.12.017>.

## **CURRICULUM VITAE**

### **Personal data**

Name& surname	Babak Omranpour Shahreza
Date of birth	21.0.3.1985
Place of birth	Esfahan
Nationality	Iranian
Contact data	<u><a href="mailto:babak.o@daad-alumni.de">babak.o@daad-alumni.de</a></u> <u><a href="mailto:omranpou@uqtr.ca">omranpou@uqtr.ca</a></u>

### **Education**

2008–2011	M.Sc. Iran University of Science and Technology, IRAN
2003–2008	B.Sc. Iran University of Science and Technology, IRAN

### **Language competence**

Persian	Native
English	Fluent
Spanish	Basic

### **Professional employment**

2016–Onward	Post-graduate research assistant, Nuevo Leon State University – Mexico
2017	Visiting research fellow, University of Quebec-Trois Rivieres (UQTR) – Canada
2016–Onward	Research partner, Karlsruhe Institute of Technology – Germany
2014–2015	Research assistant – Italy
2011–2013	Lecturer, University of Applied Sciences and Technology (UAST) – Iran

### **Scholarship & grant awards**

Mexico, National Council of Science and Technology (CONACYT), 2016

Germany, German Academic Research Service (DAAD), 2016

Estonia, Archimedes Foundation, 2015

IRAN, Iranian Nano Technology Initiative Council, 2010

## ELULOOKIRJELDUS

### Isikuandmed

Nimi: Babak Omranpour Shahreza  
Sünniaeg: 21.0.3.1985  
Sünnikoht: Esfahan  
Kodakondsus: Iraani  
E-post: [babak.o@daad-alumni.de](mailto:babak.o@daad-alumni.de)  
[omranpou@uqtr.ca](mailto:omranpou@uqtr.ca)

### Hariduskäik

2008–2011 MSC Iran University of Science and Technology-Iraan  
2003–2008 BSC Iran University of Science and Technology-Iraan

### Keelteoskus

Pärsia emakeel  
Inglise kõrgtase  
Hispaania algtase

### Teenistuskäik

2016-aastast Teadusassistent, Nuevo Leon State University – Mehhiko  
2017 Külalisteadur, Quebec-Trois Rivieresi ülikool (UQTR) – Kanada  
2016-aastast Uurimispartner, Karlsruhe tehnoloogiainstituut (KIT) – Saksamaa  
2014–2015 Teadusassistent, Trento ülikool – Itaalia  
2012–2013 Lektor, Rakendusteaduste ja Tehnoloogiaülikool (UAST) – Iraan

### Stipendium ja anda auhinnad

Mehhiko, riiklik teaduse ja tehnoloogia nõukogu (CONACYT), 2016  
Saksamaa, Saksa akadeemiline uurimisteenistus (DAAD), 2016  
Eesti, Archimedese Euroopa Sotsiaalfond, 2015  
Iraan, Iraani nanotehnoloogiaalgatuse nõukogu, 2010